Controls on the sulfur isotopic composition of carbonate-associated sulfate

Thesis by

Theodore Michael Present

In Partial Fulfillment of the Requirements for

the degree of

Doctor of Philosophy in Geochemistry

CALIFORNIA INSTITUTE OF TECHNOLOGY

Pasadena, California

2018

(Defended May 11, 2018)

To my family and Kate, who made this possible with constant love and support from near and far.

Theodore Michael Present
ORCID: 0000-0002-4747-2174

ACKNOWLEDGEMENTS

I sincerely thank my advisors, Jess Adkins and John Grotzinger, for supporting my zig-zagging path learning both sedimentology and geochemistry. Both of you have encouraged and invested in my education with many opportunities well beyond the scope of this thesis. Fieldwork in Namibia and coring in the North Atlantic were among the most spectacular, but I appreciate the daily freedom to work on whatever seemed interesting and promising. I thank my committee members, Woody Fischer and Joe Kirschvink, for the endless stream of ideas and motivation. I also greatly appreciate how accessible all of you were. You all have had open doors and made time to talk about both scientific problems and my professional development, and I have always felt that I could get the help or feedback I needed.

A humungous portion of my training came from Ge 121 classes, Agouron Institute field trips, and division trips led by John, Andy Knoll, Charlie Kerans, Woody, Joe, Jason Saleeby, and Jean-Philippe Avouac. Every single trip was the experience of a lifetime, was a critical part of my education, and couldn't have been more fun. Thank you for including me. On these trips, I have met some of the most amazing geologists and geochemists that I am honored to work with. Thank you, especially, Ken Williford, Maya Gomes, and Cori Meyers.

I couldn't imagine a better friend, roommate, and colleague than Frank Sousa. Nothing beats lighting the grill and looking at maps. Frank, Brian Kohan, Jason Price, and Stephen Cox—it's always grill season! I thank everyone in my first year pit and the Open Pit regulars—Frank, Jason, Sophie Hines, Kirsten Siebach, Vicky Stevens, Adam Subhas, Renata Cummins, Jen Hamon, Luca Malatesta, Kristel Chanard, and Chris Rollins—for being such great friends and colleagues. After weeks and weeks with you at work, it was still always great to meet up at barbeques, bars, and campsites. I win the tontine… Cody Finke, Hayden Miller, Jeff Prancevic, Alison Piasecki, Jen Buz, Max Loyd, Daven Quinn, Nathan Stein, and Usha Lingappa, thank you for your friendship and adventures. Daven, thanks for bringing me with you to Namibia—that was an amazing trip.

I have been privileged to fall under the wings of Guillaume Paris, Andrea Burke, James Rae, Kristin Bergmann, and Maggie Osburn. Thank you for being the best mentors, friends, advisors, motivators, and distractors. None of your future students can be as lucky as I was to get days with coffee and nights with whisky for your advice and friendship. Katie Snell, Lizzy Trower, Jessica Creveling, Nithya Thiagarajan, Morgan Raven, Sarah Slotznick, Daniel Stolper, Kat Dawson, Steve Skinner, and Joel Scheingross, thank you too for your guidance, thoughtfulness, and friendship.

Adam, Sophie, Guillaume, James, Andrea, Dan Johnson, Sang Chen, John Naviaux, Grace Lopez, Yoni Goldsmith, Preston Kemeny, Jared Marske, Alex Phillips, Paula Mateo, Antoine Cremiere, and Eric Praske, thank you for keeping the office and lab fun, interesting, invigorating, and super weird. Guillaume, Jared, Fenfang Wu, Nathan Dalleska, Nami Kitchen, and Lindsay Hedges, I am forever indebted to the time you have put in to helping with my lab work and the instruments. Katie, Dan, Guillaume, Kristin, and Jess, thank you

for helping me in the Guadalupe Mountains. Jonena Hearst, thank you for your patience and help showing me some hidden gems in McKittrick Canyon and the Patterson Hills. Melissa Gutierrez, thank you for all of your help preparing samples from the Guadalupe Mountains. It was an honor to help mentor such a talented and curious student and I really enjoyed working with you. Nora Oshima, Janice Grancich, Mark Garcia, Jen Shechet, Kathy Young, Heather Steele, Julie Lee, Dian Buchness, Liz Boyd, Marcia Hudson, Leticia Calderon, Aleen Boladian, and Tony Diaz, thank you for everything you all do to make sure our experience as graduate students is comfortable and successful.

I ended up at in geology and at Caltech because of the spectacular program at Penn State. I very much thank Dave Bice, Lee Kump, Matt Fantle, Kate Freeman, and Rudy Slingerland for your support, advice, and the encouragement and opportunity to pursue a Ph.D.

My mom, dad, and Sam—thank you so much for supporting me for decades, helping me in small ways and large every day, and your generosity all of the time. I wish I could be closer to home and see you all more. Thank you for encouraging me and helping me be successful while so far away.

Nobody has been kinder, more loving, and perfect than my wife Kate. I love coming home to you every day. Thanks for your patience when I disappeared for weeks, your help sorting everything out when I get home too late, and for being my motivation to get everything done so that we can spend more unbelievable time together.

ABSTRACT

Sulfate in the modern ocean has a homogenous concentration and sulfur isotopic composition. It is well-mixed because rivers and mantle degassing deliver small amounts relative to its mass in the ocean. A similar small amount of sulfate is removed as biologic, sedimentary, and hydrothermal processes oxidize and reduce sulfur, carbon, and iron. These sulfur fluxes may have changed along with the carbon and oxygen cycles during ancient evolutionary, extinction, climatic, and tectonic transitions. The changing budget of marine sulfate is therefore key to understanding biogeochemical processes that control Earth's surface environment. The sulfur isotopic composition of marine sulfate reflects the proportion of sulfur partitioned into reduced minerals, especially pyrite, in marine sediments and weathering rocks.

In this thesis, I examine how the sulfur isotopic compositions of ancient oceans is recorded in the sedimentary rock record and examine local and global effects on the sulfur isotopic composition of Paleozoic and the Mesoproterozoic sedimentary rocks. Carbonate minerals form in many depositional environments throughout Earth history and their chemical compositions relate to that of the fluid in which they formed. Much of my thesis focuses on the sulfur isotopic composition of minor amounts of sulfate incorporated into calcite, dolomite, and aragonite called carbonate-associated sulfate. Unpacking the local biogeochemical processes and global budgets affecting the sulfur isotopic composition of ancient carbonates enriches and clarifies the paleoenvironmental information preserved in the sedimentary record.

Chapter 1 is a compilation and critical comparison of proxy records of the sulfur isotopic composition of Phanerozoic seawater sulfate. I compared data from marine evaporites, barite, and carbonate-associated sulfate and showed where each record is prone to biases and which processes create variance. Only carbonate-associated sulfate data fills critical periods of biogeochemical change, but it is the most susceptible to sources of variance other than passively recording the composition of ancient oceans. However, this additional variance

reflects changes in the biogeochemical processes during early diagenesis in penecontemporaneous sediments, which are the locus of the pyrite burial and sulfide reoxidation fluxes pulling on the global sulfur budget.

Chapter 2 utilizes a recently-developed analytical technique to compare the carbonate-associated sulfate of diagenetic carbonates and primary marine biogenic carbonates from latest Ordovician and earliest Silurian strata on Anticosti Island, Quebec. These samples span the duration of the Hirnantian Stage glaciation of Gondwana, which coincided with and possibly caused the Late Ordovician Mass Extinction. Much of the variance observed in bulk carbonate-associated sulfate is imparted during early diagenesis and burial diagenesis, and the best-preserved calcite from ancient brachiopods faithfully reflects seawater's sulfur isotopic composition. Seawater sulfate's isotopic composition did not change during the glaciation and extinction, supporting prior constraints on the mass of the marine sulfate reservoir and the magnitude of sulfur flux changes.

In Chapter 3, we extended the record of seawater sulfate's sulfur isotopic composition from well-preserved brachiopod calcite from the Cincinnati Arch, Indiana-Ohio-Kentucky and Gotland, Sweden. We demonstrated that marine sulfate likely remained globally well-mixed with a constant isotopic composition for at least 30 Myr, from the earliest Late Ordovician through the late Silurian. The ocean's sulfur isotope composition likely changed little during multiple biotic crises, periods of basin restriction, oceanographic circulation changes, and sea level and climate changes. However, the first replicate carbonate-associated sulfate measurements of individual brachiopods indicate that even the best-preserved calcite is prone to diagenetic alteration that may obscure small changes in the ocean sulfate budget.

Exquisitely-preserved biogenic calcite is rare in the rock record and absent in Precambrian strata, but bulk limestones and dolomites may record changes in the composition of ancient oceans. Chapter 4 compares the sulfur isotopic composition of carbonate-associated sulfate from limestones and dolostone deposited in peritidal to basinal environments on the Capitan Reef carbonate platform in the Guadalupe Mountains, west Texas. Rocks formed in different environments at the same time have carbonate-associated sulfate with different sulfur isotope

compositions. Carbonate-associated sulfate is incorporated into bulk limestone and dolostone during early marine diagenesis, and its sulfur isotopic composition reflects the diagenetic and depositional environment. Carbonates recrystallizing in low-energy environments may incorporate marine pore fluids whose sulfur isotopic compositions evolved by the action of microbial sulfate reducing organisms. The sulfur isotopic composition of rocks deposited in high-energy environments, however, reflects that of seawater sulfate because the diagenetic fluid is open to the ocean and has the same sulfur isotopic composition of seawater. Later meteoric and burial diagenetic processes to which other geochemical tracers, such as carbon and oxygen isotopes, are sensitive do not greatly affect carbonate-associated sulfate. Thus, a record of the evolution of the sulfur, carbon, and oxygen isotopic composition of ancient oceans cannot come from the same sedimentary archives.

Chapter 5 considers the range of hydrothermal and sedimentary reactions that fractionate sulfur isotopes to understand the origin of unusual millimeter-scale pyrite tubes associated with a Mesoproterozoic massive sulfide deposit in the Newland Formation, Belt Supergroup, Meagher County, Montana. The petrography and sedimentology of the tubes indicates that they formed on the seafloor or in the uppermost unlithified sediments from the effluence of metalliferous fluids into euxinic seawater. The texture-specific sulfur isotopic compositions of diagenetic barite, carbonate-associated sulfate, and diagenetic and hydrothermal pyrite indicates that there was an active microbial sulfate reducing community in the sediments and possibly colonizing the vents. A dynamic set of oxidation and reduction interactions between hydrothermal fluids and seawater were controlled by this community, leading to the novel morphology and texture of vent structures.

This work indicates that combining sedimentological and petrographic observations with sulfur isotope data can constrain a wide range of biogeochemical processes. It guides future sulfur geochemical examination of parts of the rock record, especially the Precambrian, with few traditional archives of ancient seawater sulfate's chemistry. Information on both local and global controls on the sulfur isotopic composition of carbonate-associated sulfate, barite, and pyrite helps to resolve paleoenvironmental change.

PUBLISHED CONTENT AND CONTRIBUTIONS

Present, Theodore M., Guillaume Paris, Andrea Burke, Woodward W. Fischer, and Jess F. Adkins. "Large Carbonate Associated Sulfate Isotopic Variability between Brachiopods, Micrite, and Other Sedimentary Components in Late Ordovician Strata." *Earth and Planetary Science Letters* 432 (2015): 187–98. https://doi.org/10.1016/j.epsl.2015.10.005.

T.M.P. participated in the conception of the project, prepared and analyzed previously-collected samples, analyzed the data, and wrote the manuscript. As the author of this article, T.M.P. retains the rights to include it in a dissertation from the copyright holder, Elsevier.

Present, Theodore M., Kristin D. Bergmann, Corinne Myers, Sarah P. Slotznick, Jessica R. Creveling, Jerry Zieg, Woodward W. Fischer, Andrew H. Knoll, and John P. Grotzinger. "Pyrite-Walled Tube Structures in a Mesoproterozoic Sediment-Hosted Metal Sulfide Deposit." *Geological Society of America Bulletin* 130, no. 3–4 (2017): 598–616. https://doi.org/10.1130/B31504.1.

T.M.P. participated in an Agouron Institute field trip to develop the project and collect samples. T.M.P. helped describe the drill core and hand samples, helped describe the petrography and mineralogy of the samples, performed the reflected light petrography, acquired the barite and carbonate-associated sulfate isotope data, helped acquire the SIMS sulfur isotope data, analyzed and processed all sulfur isotope data, helped interpret all sulfur isotope, petrographic, and sedimentological, and wrote the manuscript. This article is included in a dissertation with permission from the copyright holder, the Geological Society of America.

TABLE OF CONTENTS

LIST OF ILLUSTRATIONS

Page

Chapter I

Chapter II

Chapter V

LIST OF TABLES

Page

Chapter 1

INTRODUCTION: COMPILATION AND COMPARISON OF PROXIES FOR THE SULFUR ISOTOPIC COMPOSITION OF PHANEROZOIC SEAWATER SULFATE

Theodore M. Present[1], Woodward F. Fischer[1], Jess F. Adkins[1]

[1]California Institute of Technology, Pasadena, California, USA

Abstract

The sulfur isotopic composition ($\delta^{34}S$) of marine sulfate reflects weathering, carbon, and oxygen fluxes. Therefore, much effort has gone towards reconstructing the history of Phanerozoic seawater sulfate to examine how these fluxes changed during reorganizations of the biosphere and climate. Compiled here are 4877 $\delta^{34}S$ measurements from three different sedimentary archives used as proxies for Phanerozoic seawater's composition: marine barite, evaporites, and carbonate associated sulfate (CAS). The proxy records are collated onto a consistent geologic time scale to compare robust features and critically examine sources of variance.

The time-windowed variance of all records increases with age and at major biogeochemical events such as mass extinctions. Some of this variance reflects spatial and temporal variability in the $\delta^{34}S$ of ancient oceans, but each record is prone to additional biases and diagenetic imprints. Marine barite is likely the most accurate proxy of ancient seawater's $\delta^{34}S$, but the record is unlikely to have further increases in temporal extent or resolution. Evaporites represent a major sulfur reservoir but are limited to deposition during periods of propitious tectonic and climatic arrangement and sometimes reflect local fluid compositions in restricted basins. CAS has the most complete spatial and temporal resolution, but is the most susceptible to diagenetic sources of variance by interaction with modified pore fluids. The biogenic CAS record resolves sulfur cycle dynamics during the Toarcian Ocean Anoxic Event, the Carboniferous Period, and the Late Ordovician Mass Extinction, but disagrees

with other archives during the other Phanerozoic mass extinctions. Sulfur isotope variability of multiple fossil specimens can quantify the effect of diagenesis on the biogenic CAS archive. The distribution of $\delta^{34}S$ compositions recorded by bulk rock CAS is statistically distinct from that recorded by other archives, and a major component of this variance reflects diagenetic processes. However, careful assessment of the timing and style of early diagenesis can inform both primary spatial and temporal changes in seawater sulfate $\delta^{34}S$ and changes in biogeochemical processes such as sulfide oxidation and pyrite burial occurring in marine sediments. Critical appraisal of proxies for ancient seawater sulfate's $\delta^{34}S$ composition guides interpretation of data from periods of Earth history, including the Precambrian, for which fewer sedimentary archives are available.

Introduction

Understanding how Earth's climate and ocean chemistry shape and respond to life requires tracking biogeochemical processes that drive the oxidation and reduction of carbon, oxygen, iron, and sulfur. In the Phanerozoic, sulfate in seawater acts as a major oxidant of organic carbon, controlling the accumulation of organic matter in many sediments (Bowles et al., 2014; Jørgensen, 1982). Sedimentary sulfur cycling, including the microbial reduction of sulfate, the reoxidation of the produced sulfide, and the anaerobic oxidation of methane by remaining sulfate, is a major control on alkalinity fluxes in marine sediments (Froelich et al., 1979). Sulfide, once fixed as pyrite with available iron, may be uplifted, exposed, and oxidized during weathering, controlling the oxygen budget on tectonic timescales (Kump and Garrels, 1986). For the oceans to have remained habitable throughout the Phanerozoic, burial of reduced sulfur as sulfide minerals must, on some timescale, balance the acid produced and oxygen consumed during the terrestrial weathering of pyrite. Therefore, tracking ancient sulfate fluxes illuminates when, how, and where the Earth system achieves this balance, and what happens during unsteadiness.

The enzymes responsible for microbial sulfate reduction (MSR) impart a kinetic isotopic fractionation on the sulfate reduction reaction, which preferentially enriches the light isotopes in the sulfide product (Harrison and Thode, 1958). When more of this sulfide is

fixed as pyrite, removing more light sulfur isotopes from the ocean for the next rock cycle, the remaining sulfate in the ocean becomes enriched in the heavy isotopes. Ault and Kulp (1959) first recognized that a record of ancient oceans' sulfur isotopic compositions would inform changes to Earth's biogeochemical cycles. Holland (1973) first attempted to calculate the change in oxygen flux from the sulfur cycle and Holser (1977) further recognized that rapid changes in the composition of the ancient oceans' reflect biotic crises and dramatic reorganizations of Earth's climate and life systems on short periods of time.

Three materials serve as proxies for the sulfur isotopic composition of Phanerozoic oceans: marine evaporites, which include sulfate salts precipitated from drying seas; marine barite, which forms in pelagic waters; and carbonate-associated sulfate (CAS), which is minor sulfate incorporated into the crystal lattice of calcite, aragonite, and dolomite. Important reviews (Bottrell and Newton, 2006; Claypool et al., 1980; Holser et al., 1989; Strauss, 1997) on the evolution of the Phanerozoic sulfur cycle have assumed that these proxies each accurately preserve the isotopic composition of ancient seawater sulfate. In an effort to extract the most complete biogeochemical information from the rock record, this review attempts to highlight the differences recorded by each archive and attribute them to temporal and spatial controls on the incorporation and preservation of sulfur isotopes in sulfate in sedimentary rocks.

Sulfur isotope notation and fractionating processes

Sulfur has four stable isotopes. In the solar system, ^{32}S is the major isotope (95%) and ^{34}S is the most abundant minor isotope (4%). The isotopic composition of sulfur is expressed in delta-notation as parts-per-thousand changes in the $^{34}S/^{32}S$ ratio relative to a defined standard similar in composition to the Cañon Diablo troilite, the Vienna-Cañon Diablo Troilite (V-CDT, Beaudoin et al., 1994; Coplen and Krouse, 1998):

$$\delta^{34}S(‰) = \left[\frac{\left({}^{34}S/_{32}S\right)_{sample}}{\left({}^{34}S/_{32}S\right)_{V-CDT}} - 1\right] * 1000$$

Dissimilatory MSR is the dominant process that fractionates sulfur isotopes at Earth's surface conditions by anaerobically oxidizing simple organic electron donors. Organisms performing MSR often incompletely oxidize the organic material (e.g., lactate), producing acetate (Goldhaber and Kaplan, 1980):

$$2CH_3COHCOO^- + SO_4^{2-} \rightarrow 2HCO_3^- + 2CH_3COO^- + HS^-$$

MSR is controlled by enzymatic pathways that preferentially react sulfate ions containing the lighter ^{32}S isotope (Harrison and Thode, 1958). The amount of discrimination against ^{34}S is also expressed in parts-per-thousand:

$$\epsilon_{product-reactant} = \left(\frac{\delta^{34}S_{\ product} + 1000}{\delta^{34}S_{\ reactant} + 1000} - 1\right) * 1000$$

The discrimination depends on the microbial culture, the organic substrate mixture, the rate of sulfate reduction, and the enzymatic pathway used (Brunner and Bernasconi, 2005; Canfield, 2001; Habicht and Canfield, 1997; Harrison and Thode, 1958; Sim et al., 2011b). It is typically $\varepsilon_{H2S\text{-}SO4} \approx$ -30 – -40‰ in marine sediments (Canfield, 2001), though much larger fractionations of up to $\varepsilon_{H2S\text{-}SO4} \approx$ -70‰ are possible (Brunner and Bernasconi, 2005; Sim et al., 2011a). The observed difference between the substrate sulfate in seawater and the produced sulfide often differs from the discrimination (Canfield and Teske, 1996; Goldhaber and Kaplan, 1980). This difference is also expressed in parts-per-thousand:

$$\Delta^{34}S = \delta^{34}S_{\ HS^-} - \delta^{34}S_{\ SO_4^{2-},sw}$$

Sulfide may be lighter than the MSR discrimination (i.e., $\Delta^{34}S<\varepsilon_{H2S\text{-}SO4}$) if a fraction of the original product sulfide is partially re-oxidized to S^0 or thiosulfate and then disproportionated (Canfield and Thamdrup, 1994; Jørgensen, 1990). Disproportionation produces sulfate with higher $\delta^{34}S$ than the S^0 or thiosulfate but lower $\delta^{34}S$ than the original sulfate, which can then be cyclically reduced by MSR and iteratively fractionated.

Alternatively, sulfide may be much less ^{34}S-depleted than the discrimination (i.e., $\Delta^{34}S > \varepsilon_{H2S\text{-}SO4}$) if the rate of sulfate supply to the anoxic site of MSR is slower than the rate of reduction (Jørgensen, 1979). Such a closed-system occurs in marine sediments with deep oxygen penetration, high amounts of sulfide reoxidization, or high sedimentation rates relative to sulfate's diffusive length-scale (Jørgensen, 1979). Reservoir effects on the residual sulfate in euxinic seawater similarly lead to higher (more positive) values of $\Delta^{34}S$, which is more pronounced at lower sulfate concentrations (Gomes and Hurtgen, 2015).

If ferrous iron is available, aqueous sulfide precipitates as iron monosulfides (Berner, 1984; Rickard, 1995). These iron monosulfides ultimately form pyrite with additional aqueous sulfide (Rickard and Luther, 1997). These reactions generally do not significantly fractionate sulfur isotopes (Bottcher et al., 1998; Price and Shieh, 1979). However, up to 30‰ differences between the $\delta^{34}S$ of pyrite and coexisting aqueous sulfide have been observed; this is likely caused by the cycling of sulfide between mineral, aqueous, and organic sulfur phases (Raven et al., 2016).

Most sulfide produced by MSR is reoxidized back to sulfate (Bowles et al., 2014; Jørgensen, 1982). Aqueous or mineral sulfides may be reoxidized by free oxygen (Gartman and Luther, 2014; Schippers and Jørgensen, 2002). Aqueous sulfide and iron monosulfides, but not pyrite, may also be oxidized microbially using oxygen, manganese, nitrate, or ferric iron (Schippers and Jørgensen, 2002). These reactions produce sulfate or intermediate sulfur species such as S^0 and thiosulfate with slight discrimination against ^{34}S. Measured discriminations are $\varepsilon_{SO4\text{-}H2S} \approx 0 - -5‰$ (Brabec et al., 2012; Fry et al., 1988), and are typically neglected in diffusion-advection-reaction models of pore fluid sulfur reactions. However, the fraction of sulfide that is reoxidized affects the openness of the pore fluid system, and therefore the observed $\Delta^{34}S$; more sulfide reoxidation leads to a smaller difference between seawater sulfate and sulfide $\delta^{34}S$ (less negative value of $\Delta^{34}S$) (Jørgensen, 1979).

Gypsum precipitation from evaporating seawater slightly discriminates against ^{32}S. The $\delta^{34}S$ of gypsum precipitating from solution at equilibrium is $\varepsilon_{gypsum\text{-}SO4} \approx 2‰$ higher than its parent brine (Raab and Spiro, 1991). Consequently, the $\delta^{34}S$ of sulfate in a given batch of

evaporating seawater—and the gypsum precipitating from the evolved seawater—decreases as salinity increases. Evaporites that reach halite saturation are therefore less than 1‰ heavier than the original seawater (Raab and Spiro, 1991).

Fluxes and reservoirs in the sulfur cycle

Sulfur available to biogeochemical processes at the surface of the earth, as measured in sulfide minerals in mid-ocean ridge basalts, has an isotopic composition similar to that of the solar system (i.e., ~0‰) (Alt, 1995). Sulfate in the modern ocean has a well-mixed sulfur isotopic composition of 21‰ (Johnston et al., 2014; Paris et al., 2013; Rees et al., 1978), indicating that there must be a net accumulation of light sulfur isotopes in the crust and mantle (Ault and Kulp, 1959). This reflects the growth of a low $\delta^{34}S$ crustal pyrite reservoir, some of which returns to the mantle during subduction (Canfield, 2004).

The oxic Phanerozoic atmosphere permits weathering of sedimentary sulfide and evaporate minerals and the accumulation of aqueous sulfate in the ocean (Canfield, 2004; Canfield and Raiswell, 1999; Canfield and Teske, 1996). The modern ocean, which contains $37 \cdot 10^6$ Tmol of sulfate, is fed by 3.4 Tmol/yr sulfate from rivers and 0.34 Tmol/yr of sulfur from volcanoes (Berner and Berner, 2012; Burke et al., 2018; Meybeck, 2003). Sulfur in the modern ocean therefore has a residence time of ~10 Myr (Walker, 1986).

The influx of sulfate from rivers is balanced primarily by the precipitation of sulfide minerals in marine sediments with MSR. Because as much as 95% of sulfate that is reduced by MSR is reoxidized (Jørgensen, 1982), sulfate molecules have a residence time in the ocean of ~1 Myr, much shorter than that of sulfur atoms in the ocean (Turchyn and Schrag, 2004). Additional sulfur is removed from the ocean by sulfate deposition in evaporite minerals and by reduction in hydrothermal systems, but these fluxes are difficult to constrain. Estimates of the proportion of sulfur buried as pyrite vary widely between 30% and 90% of the riverine and volcanic influx to the oceans (Burke et al., 2018; Garrels and Lerman, 1981; Halevy et al., 2012; Tostevin et al., 2014).

Proxies for Phanerozoic seawater sulfate

Evaporites

Extensive deposits of carbonate, sulfate, and halide salts form as seawater evaporates in restricted basins. Throughout the Phanerozoic, bedded marine evaporites formed subaqueously in salinas (hypersaline lagoons) and salt pans, and supratidal sabkha environments, especially in arid climates or in marine embayments into craton interiors. Modern analogs for such deposits include marginal-marine environments of the Arab sabkhas and salt pans in Mexico (Lowenstein and Hardie, 2006; Schreiber and Tabakh, 2000). Additionally, extremely thick (>100s of meters) evaporite deposits have formed in deeper-water environments (Warren, 2010). Because there is no modern analog for formation of deep-water evaporites, their genesis is inferred from sedimentological and geochemical data (Schmalz, 1969). Seawater must have evaporated from the surface of the water body or a marginal environment, after which the brine may have flowed down slope and displaced fresher overlying water, or gypsum crystals may have been transported by mass flow or dropped out of suspension from a super-saturated surface layer (Schmalz, 1969). Deposition and preservation of evaporites require favorable climatic and tectonic conditions where restricted basins experience net evaporation (Warren, 2010). Therefore, the evaporite record has limited spatial and temporal continuity (Claypool et al., 1980; Strauss, 1997).

Evaporites are massive products of seawater sulfate, but because they form in marginal marine environments with biologically-adverse salinities, it is difficult to constrain their geologic age with biostratigraphy. In many deposits, it is also difficult to discern between lacustrine or marine depositional environments, the influence of non-marine groundwater and continental runoff, and the signature of remobilized older evaporites in the local hydrological catchment (Hardie, 1984; Kendall and Harwood, 1989; Lu and Meyers, 2003). The restricted, marginal marine settings in which evaporites form are particularly prone to changes in fluid source or depositional environment with minor sea level changes (Playà et al., 2007). Additionally, evaporites form diapirs that drive salt tectonics, which may complicate a deposit's internal stratigraphy (Nielsen, 1989).

The $\delta^{34}S$ of evaporites varies by 1‰ – 6‰ in a given formation (Thode and Monster, 1965). This variability cannot be attributed to fractionation during gypsum crystallization, which produces evaporites that have $\delta^{34}S$ compositions 1‰ – 2‰ higher than the unevaporated seawater (Raab and Spiro, 1991). Salinity stratification in evaporating basins promotes water-column anoxia and allows MSR to distill sulfate to higher $\delta^{34}S$ compositions than the original seawater. Consequently, early workers suggested that the isotopic composition of ancient seawater was best reflected by the lowest $\delta^{34}S$ in an evaporite succession (Ault and Kulp, 1959; Davies and Krouse, 1975; Thode and Monster, 1965), and in some cases, evaporite $\delta^{34}S$ compositions are higher than other proxies from the same depositional basin (Fike and Grotzinger, 2010). However, evaporite basins in marginal marine environments are recharged not only by unadulterated seawater, but by groundwater and runoff as well. These fluids may contain sulfate with dramatically different $\delta^{34}S$ compositions from remobilized older evaporite deposits or weathered sedimentary sulfides (Utrilla et al., 1992).

Marine Barite

Barite precipitates from hydrothermal fluids, sediment pore fluids, and from the marine water column (Paytan et al., 2002, 1993). Barite is under-saturated in most of the ocean (Chow and Goldberg, 1960; Church and Wolgemuth, 1972). However, marine barite has been observed in sediment traps in the upper 200 m in the water column, especially in high-productivity regions, and is associated with sulfate enrichment from decaying organic matter and barite enrichment in dissolving siliceous plankton, especially Acantharian radiolarians (Bishop, 1988). While barite super-saturation is achieved predominately by the addition of sulfate from oxidizing organic sulfur (Horner et al., 2017; Jacquet et al., 2007), marine barite apparently precipitates predominately from seawater sulfate and has the $\delta^{34}S$ of modern seawater (Paytan et al., 2002, 1998). It is transported to sediments by fecal pellets and marine snow (Bishop, 1988). Barite is therefore preserved in oxic marine sediments in high-productivity regions where enough barite is delivered to saturate pore fluids (Church and Wolgemuth, 1972). Sulfate reduction in anoxic sediments causes dissolution of barite, which re-precipitates at the base of the sulfate reduction zone with extremely high $\delta^{34}S$ compositions (Torres et al., 1996).

Carbonate Associated Sulfate

Limestones and dolomites have deposited nearly continuously throughout the Phanerozoic, accumulating in marginal marine and open-ocean environments. A minor amount of sulfate is incorporated into biogenic and inorganic carbonates. Biogenic carbonates typically contain part-per-thousand sulfate by mass, while inorganic cements typically contain hundreds of parts-per-million (Busenberg and Plummer, 1985; Staudt and Schoonen, 1995). In modern and cultured biogenic carbonates, the incorporated sulfate has an isotopic composition within 2‰ of the seawater from which it precipitated (Burdett et al., 1989; Kampschulte et al., 2001; Kaplan et al., 1963; Mekhtiyeva, 1974; Paris et al., 2014b, 2013; Present et al., 2015). Recent bulk carbonate sediments from various peritidal carbonate platform environments also include CAS with an isotopic composition similar to modern seawater (Lyons et al., 2004). Further, sedimentological and geochemical context is abundant in most carbonates, allowing for robust constraints on the depositional environment, and, in many cases, the diagenetic history of the rock. CAS, therefore, has the potential to exceed the temporal resolution and completeness of the evaporite and barite records (Strauss, 1997).

Various experimental methods suggest that sulfate is incorporated as a solid solution into the crystal lattice of calcite, aragonite, and dolomite. Tetrahedral sulfate ions substitute for a trigonal carbonate group, with three oxygen atoms replacing the carbonate and the fourth in the interstitial space between calcium and other coordinated carbonate groups (Balan et al., 2014; Fernández-Díaz et al., 2010; Kontrec et al., 2004). This distorts both the crystal lattice of the carbonate mineral and the sulfate tetrahedral, creating predictable infrared absorption features (Takano, 1985). Further, increase of the crystal unit cell volume is observable by X-ray diffraction (Busenberg and Plummer, 1985; Kontrec et al., 2004). Coordination between the interstitial oxygen of the sulfate tetrahedral and cations in the carbonate mineral creates observable X-ray absorption features, as well (Pingitore et al., 1995). X-ray absorption features vary between calcite, aragonite, and dolomite but are consistent between samples of the same mineralogy, suggesting that the sulfate is coordinated with the carbonate mineral and is not a trace impurity (Pingitore et al., 1995). Sulfate enrichment in biogenic

and inorganic carbonate is consistently correlated with magnesium content (Fichtner et al., 2018; Paris et al., 2014b; Takano, 1985).

Sulfate from other phases in carbonate samples may contaminate CAS measurements. In biogenic carbonates, sulfur may be incorporated into organic material as amino acids or sulfate-containing polysaccharides and the relative proportion of organic to inorganic sulfate is variable and difficult to discern (Balan et al., 2017; Cuif et al., 2003; Cusack et al., 2008; Dauphin et al., 2005; Perrin et al., 2017). Additionally, limestone and dolostone rocks contain other sulfur-bearing minerals, especially pyrite, that may contaminate CAS during laboratory extraction (Marenco et al., 2008a; Present et al., 2015; Theiling and Coleman, 2015; Wotte et al., 2012a).

Unlike evaporites and barite, sulfate is a minor to trace constituent in carbonates (Staudt and Schoonen, 1995). Diagenetic fluids may exchange sulfate with the primary carbonate and alter its isotopic composition: incorporation of reoxidized sulfide may alter CAS towards lower $\delta^{34}S$, or incorporation of sulfate distilled by MSR in a closed pore fluid environment may alter CAS towards higher $\delta^{34}S$ (Kampschulte and Strauss, 2004). Kampschulte & Strauss (2004) suggested that the variability of multiple $\delta^{34}S$ analyses from contemporaneous stratigraphic successions can be used to quantify the effect of diagenesis on the CAS record. However, rapidly-changing and disparate CAS $\delta^{34}S$ compositions have since been interpreted, especially in Paleozoic studies, to reflect intervals of heterogeneous seawater sulfate $\delta^{34}S$ reflecting periods of low sulfate concentrations and low marine sulfate residence times (e.g., Gill et al., 2011b; Kah et al., 2004). Although this may certainly be the case, the effect of diagenesis on the CAS record has gone largely unquantified.

Limestones and dolomites are comprised of mud or grains that precipitated both biologically and abiotically from seawater and of cements binding them together. All of these components may recrystallize in pore fluids whose chemical composition reflects marine, meteoric, and burial diagenetic processes. A combustion CAS analysis typically requires 10-100 g of carbonate (Wotte et al., 2012a) and therefore may reflect a physical mixture of components precipitated or recrystallized at different times. Recent application of plasma-

source mass spectrometry for sulfur isotope analysis has permitted $\delta^{34}S$ analyses on less than one-thousandth as much sulfate, corresponding to 5-50 mg of carbonate (Paris et al., 2013, 2014a; Present et al., 2015). In Chapter 2 of this thesis, it is demonstrated that well-preserved biogenic grains, recrystallized grains, and matrix from latest Ordovician and earliest Silurian limestones each contain CAS with different $\delta^{34}S$ compositions. Fine-grained skeletal wackestone matrix contains CAS with $\delta^{34}S$ as low as 10‰, and grains recrystallized during burial diagenesis contain CAS $\delta^{34}S$ as high as 35‰ (Present et al., 2015), which spans the range of CAS analyses from the entire Ordovician. Therefore, much of the variability of CAS $\delta^{34}S$ data cannot reflect the $\delta^{34}S$ composition of ancient seawater sulfate. Further, diagenetic processes impart different $\delta^{34}S$ signatures at different times, which could create major systematic biases between primary seawater $\delta^{34}S$ compositions and CAS $\delta^{34}S$ compositions. Identifying components that retain the $\delta^{34}S$ of sulfate incorporated from syndepositional seawater is critical to successfully exploit the CAS $\delta^{34}S$ archive.

Phosphate Associated Sulfate

Part-per-thousand to weight-percent sulfate is incorporated into the phosphate mineral apatite and its carbonate-rich variety, francolite (Jarvis et al., 1994). Authigenic phosphorite forms in organic-rich sediments where phosphate adsorbed onto iron-manganese oxy-hydroxide coatings is released during suboxic iron and manganese reduction (Föllmi, 1996). Some phosphorite deposits have been reworked by sedimentary processes or bioturbation into granular phosphorites, indicating that the phosphate authigenesis likely occurred during early diagenesis in contact with seawater sulfate above the zone of MSR (Glenn et al., 1994; Jarvis et al., 1994). The $\delta^{34}S$ of sulfate substituted into francolite has therefore been measured as a proxy for Neoproterozoic and early Cambrian seawater sulfate (Goldberg et al., 2005; Hough et al., 2006; Shields et al., 2004, 1999). Additionally, Wu et al. (2014) reports the $\delta^{34}S$ of sulfate incorporated into Paleozoic and Mesozoic conodont apatite.

Compilation of Phanerozoic seawater sulfate $\delta^{34}S$ proxy data

This compilation includes 4877 measurements from 76 references that analyzed $\delta^{34}S$ in marine evaporites, bulk-rock CAS, biogenic CAS, or marine barite. Most data is from references studying Phanerozoic successions, but data from references spanning the

Cambrian-Precambrian boundary are included; the oldest analysis is 607 Ma. Some older evaporite $\delta^{34}S$ compilations included data from salt diapirs, secondary veins in non-sedimentary rocks, aqueous brines that had dissolved nearby evaporite-bearing formations, or brackish or non-marine depositional environments; these data are excluded from this compilation. Bulk rock CAS includes data from sedimentary carbonates, although the extraction procedure varies between references. Biogenic CAS includes data from brachiopods, belemnites, conodonts (which are composed of biomineralized phosphate, not carbonate), bivalves, and foraminifera. Although differential preservation of biogenic and bulk-rock CAS is addressed in each reference, all data is included in the compilation and differences between datasets are discussed below. Other than conodont apatite, sulfur isotope data from authigenic phosphorites are not included in this compilation. Figure 1 includes histograms of the $\delta^{34}S$ of all data for each proxy material.

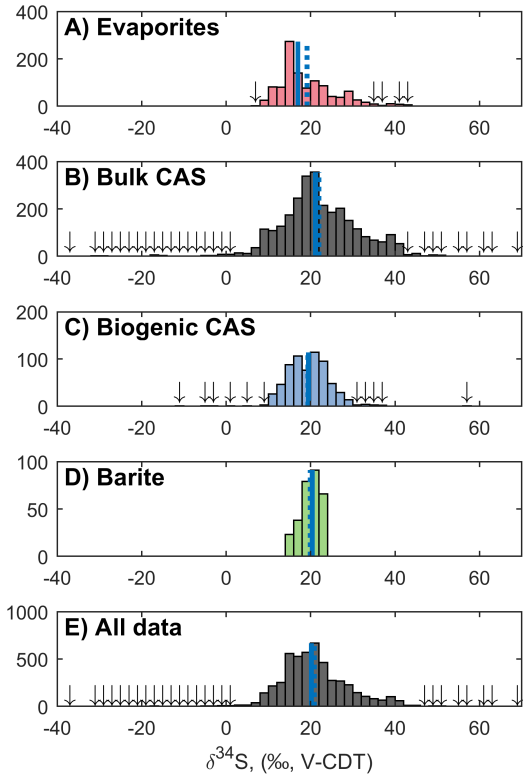

Figure 1: Histograms of $\delta^{34}S$ of sulfate in each proxy for ancient seawater sulfate. Arrows mark occupied histogram bins with less than 10 counts. The solid line marks the medians and the broken line marks the means reported in Table 1.

Each sample is assigned an age using the International Commission on Stratigraphy v. 2016/04 (ICS2016/04) time scale (Cohen et al., 2013; updated). This time scale reflects the 2012 Geologic Time Scale (Gradstein et al., 2012) with recent updates from the Lower Pleistocene, Cretaceous, Triassic, and Permian sub-commissions. For data from references that included radiometric ages or direct correlations to stratigraphic sections with radiometric ages, the radiometric age model was maintained. For data from references that included stage-level assignments of the lithostratigraphy, ages were assigned by linearly apportioning stratigraphic height unless the reference included estimates of sedimentation rate. For data from references that assigned ages but did not include stratigraphic data, ages were updated to ICS2016/04 by linearly interpolating between the assigned ages of stage boundaries in each time scale. Some references did not tabulate data; in these cases, the $\delta^{34}S$ and stratigraphic height or age assignment was pulled from a figure in the reference using a MATLAB script available in the Supplemental Information. Many evaporite deposits have benefitted from improved stratigraphic assignments since mid-to-late-twentieth century publication of their sulfur isotope data. The age of evaporite-bearing formations have been updated using the most recent tectono-stratigraphy or oil and gas exploration literature. Data from formations whose age could not be assigned to the stage level were excluded. Appendix A details the method and literature used for each age assignment.

Each proxy material has different, unevenly-spaced temporal distributions. Figure 2A is a bar graph of the number of analyses of each material in 5 Myr bins. Figure 2B is a plot of the standard deviation of data for each proxy material in each of those bins. For each record, a locally weighted regression (LOESS) was fit to the data to estimate the trend of $\delta^{34}S$ through the Phanerozoic. The LOESS curve fits a moving span of 3% of the total data in each dataset. To estimate confidence intervals on the LOESS curve, the residuals between the $\delta^{34}S$ data and the curve were bootstrapped with replacement from the entire dataset 1000 times. Figure 3 plots all of the $\delta^{34}S$ data, as well as the LOESS curves and 1σ confidence intervals on the LOESS curves for each proxy material. The LOESS curves and their confidence intervals were then each linearly interpolated at a 100 kyr resolution. Figure 4 shows the residual between each record's interpolated LOESS curve and that of the evaporite

record. Figure 4 also shows the 2σ confidence interval on the mean residual between each bulk CAS $\delta^{34}S$ analysis and the interpolated evaporite LOESS for each period.

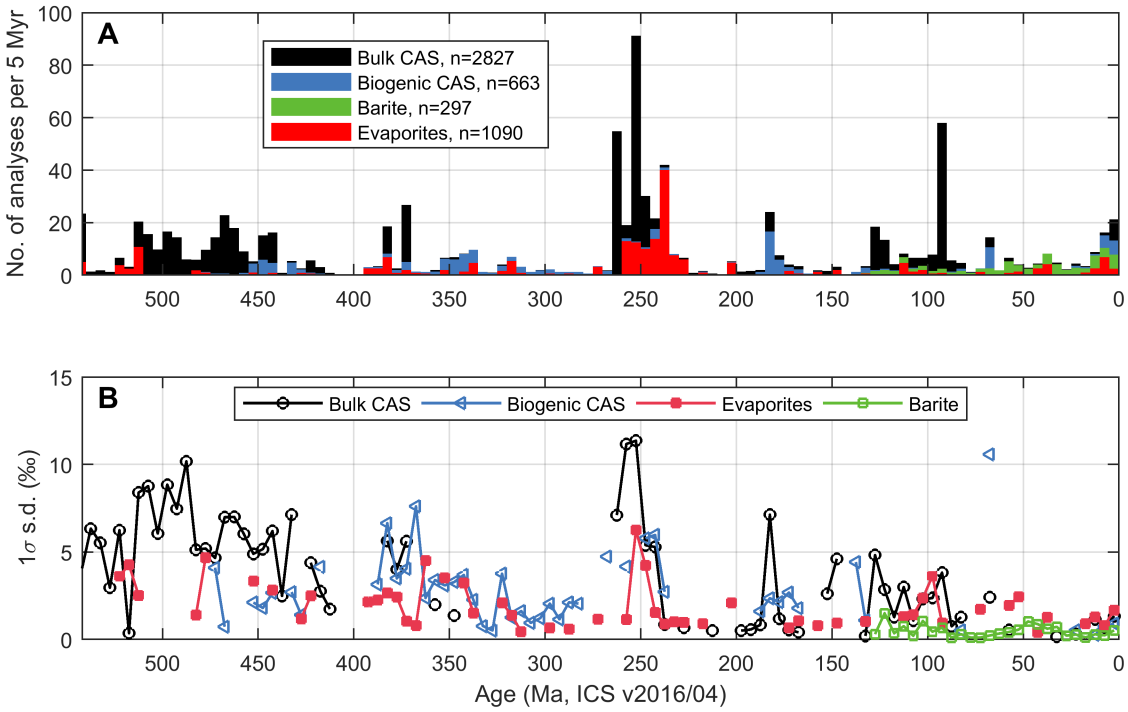

Figure 2: (A) Stacked bar graph of the number of $\delta^{34}S$ analyses of each proxy per 5 Myr bin. (B) Standard deviation of $\delta^{34}S$ analyses of each proxy in each 5 Myr bin.

Figure 3 *[next page]*: Proxy record of the $\delta^{34}S$ composition of sulfate over the Phanerozoic, with LOESS fits of the evaporite data (red curve), bulk CAS data (black curve), biogenic CAS data (blue curve), and barite data (green curve). Shading indicates the 1σ confidence interval on each LOESS fit.

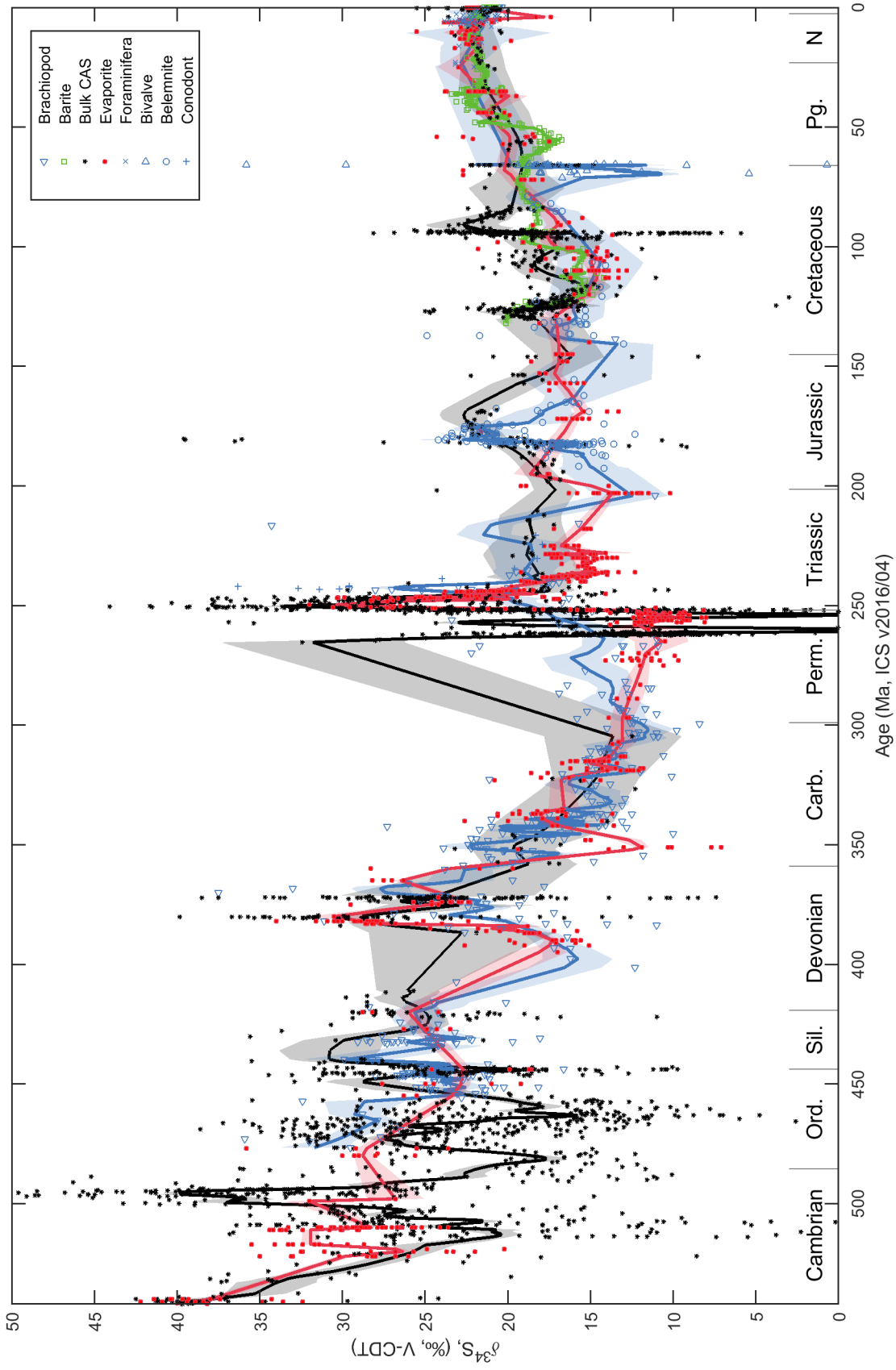
Brachiopod
Barite
Bulk CAS
Evaporite
Foraminifera
Bivalve
Belemnite
Conodont
Cambrian
Ord.
Sil.
Devonian
Carb.
Perm.
Triassic
Jurassic
Cretaceous
Pg.
N
Age (Ma, ICS v2016/04)
δ34S, (‰, V-CDT)

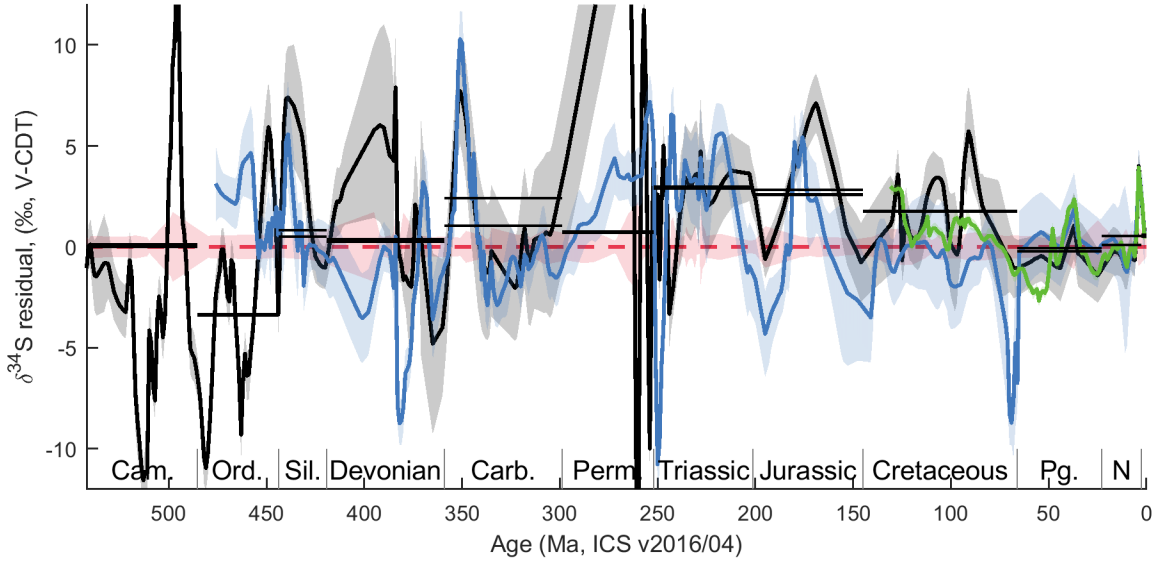

Figure 4: Residuals, interpolated at 100 kyr resolution, between the bulk CAS (black), biogenic CAS (blue), and barite (green) LOESS $\delta^{34}S$ curves and the evaporite record (red). Shading indicates the 1σ confidence interval on each LOESS fit. Each pair of horizontal lines for each period is the 2σ confidence interval on the mean residual between bulk CAS and evaporite data.

Description of the proxy datasets

By attempting to compile a history of Phanerozoic seawater sulfate $\delta^{34}S$ from different geologic materials, it is implicitly assumed that each proxy samples the same primary population (i.e., the population of seawater $\delta^{34}S$ compositions through space and time). Any differences in the sample $\delta^{34}S$ distributions, therefore, reflect temporal or spatial biases inherent to the record, or biogeochemical processes that add variance. For example, the barite record only spans the last 132 Myr, which might bias the average $\delta^{34}S$ and variance compared to records that sample the entire Phanerozoic. Histograms of all Phanerozoic data (Figure 1) show that the sample size, mean, median, and standard deviations of $\delta^{34}S$ compositions are different for each proxy (Table 1). A non-parametric Kruskal-Wallis one-way analysis of variance strongly suggests that the four datasets do not come from the same distribution, ($\chi^2[3,4771] = 178.12$, $p < 0.001$). A post-hoc pairwise analysis of the mean ranks of each proxy dataset indicates that the distribution of bulk CAS $\delta^{34}S$ is significantly different from the distributions of evaporite $\delta^{34}S$ and biogenic CAS $\delta^{34}S$ (Bonferroni-adjusted $p < 0.001$). Evaporite and biogenic CAS $\delta^{34}S$, however, are not significantly

different samples (Bonferroni-adjusted p=0.047). Therefore, evaporites and biogenic CAS $\delta^{34}S$ likely reflect the same temporally or spatially sampling biases and biogeochemical processes that create variance in the time-series of ancient sulfate's $\delta^{34}S$ or in the proxies' records of that time-series.

	n	mean	SD	median (95% CI)	skewness
Evaporite	1090	19.16	6.63	17.00 (16.66 – 17.35)	1.07
Biogenic CAS	663	19.38	5.34	19.50 (19.09 – 19.91)	0.27
Bulk CAS	2827	22.00	9.58	21.16 (20.85 – 21.48)	-0.33
Barite	297	19.91	2.25	20.40 (20.05 – 20.75)	-0.54
All data	*4877*	*20.88*	*8.30*	*20.20 (19.99 – 20.41)*	*0.03*

Table 1: Statistical description of all Phanerozoic $\delta^{34}S$ data. SD = standard deviation. CI = confidence interval.

The standard deviation of data within each 5 Myr interval increases with age for all of the archives (Figure 2B). Bulk CAS has the largest variance overall (Table 1), and generally has more variance in each 5 Myr interval than the other proxies. Barite has the least variance in nearly every 5 Myr interval, although the barite record only extends to the middle Cretaceous and data is sparse for other archives in the late Cretaceous and Paleogene. In the Carboniferous, there is sparse bulk CAS data and the biogenic CAS data is more variable than the evaporite data. A notable increase in variance, with the standard deviation of 5 Myr intervals exceeding 6‰, is apparent in all Lower and Middle Triassic records and in the bulk CAS Cambrian and Lower Ordovician record.

All archives exhibit high $\delta^{34}S$ in the early Paleozoic (>30‰) that falls to a minima in the late Paleozoic (11‰) and increases to modern values (21‰) over Mesozoic and Cenozoic time (Figure 3). This pattern was originally noted in the evaporite record by Ault and Kulp (1959), reaffirmed by more complete evaporite compilations (Claypool et al., 1980; Holser et al., 1989; Holser and Kaplan, 1966; Strauss, 1997), and confirmed in the CAS record by Kampschulte and Strauss (2004). Two higher-order fluctuations in the evaporite record—the Upper Devonian "Souris Event" and the lower Triassic "Röt Event"—were identified by Holser (1977) and are recorded by CAS as well. Additional fluctuations in the bulk CAS,

biogenic CAS, and barite records are apparent due to their higher temporal resolution than the evaporite record for much of the Phanerozoic.

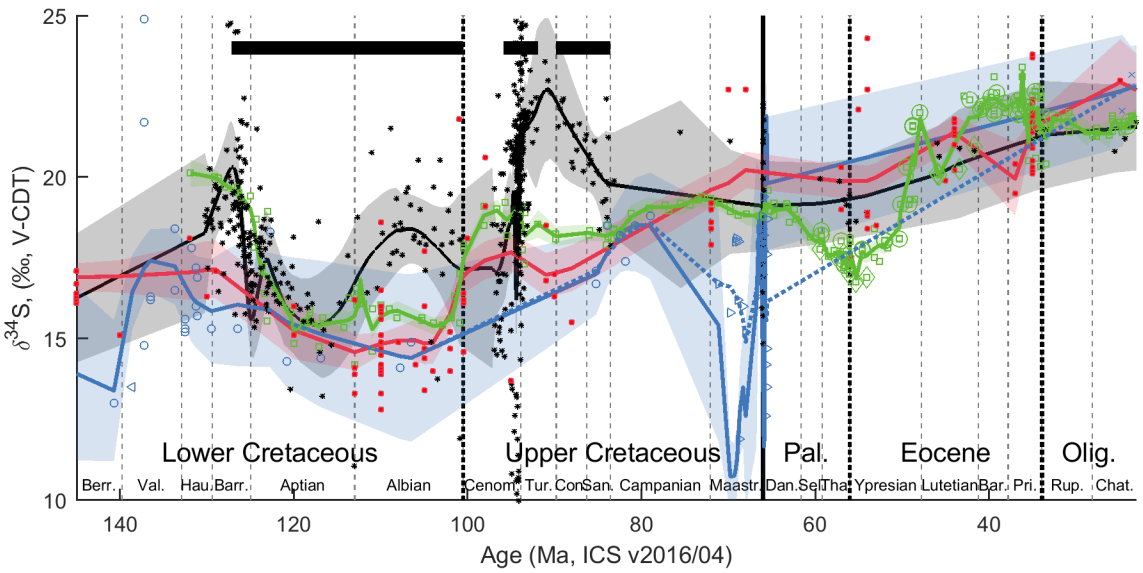

Figure 5: Cretaceous and Paleogene $\delta^{34}S$ records. See Figure 3 for legend for symbols and lines. Horizontal black bars denote OAEs (Jenkyns, 1980). Barite data, shown in green squares, are enclosed by a green circle from core sites that record an early Eocene $\delta^{34}S$ rise, and by a green diamond from core sites that record a later rise. The dotted blue line is the LOESS curve recomputed for biogenic calcite, excluding clearly diagenetically-modified bivalves described by Witts et al. (2018), all of which plot beyond the y-axis scale. Pal. = Paleocene, Olig. = Oligocene, Berr. = Berriasian, Val. = Valanginian, Hau. = Hauterivian, Barr. = Barremian, Cenom. = Cenomanian, Tur. = Turonian, Con. = Coniacian, San. = Santonian, Maastr. = Maastrichtian, Dan. = Danian, Sel. = Selandian, Tha. = Thanetian, Bar. = Bartonian, Pri. = Priabonian, Rup. = Rupelian, Chat. = Chattian.

The most recent major excursions in the $\delta^{34}S$ proxy records occur during the Paleogene and the Cretaceous (Figure 5). Over the gradual Mesozoic to Cenozoic increase in the evaporite $\delta^{34}S$, the barite record exhibits two 4‰ steps to higher and lower values of $\delta^{34}S$ in the Cretaceous, followed by a 5‰ rise in the Eocene (Kurtz et al., 2003; Paytan et al., 2004, 1998; Turchyn et al., 2009; Wu, 2013). The first of these steps begins at the Barremian-Aptian Boundary, at which the barite $\delta^{34}S$ declines 4‰ over 6 Myr. After 20 Myrs of relative stability, the barite record increases 4‰ over 6 Myr through the Cenomanian. The first, declining, step in the barite record begins during a period of widespread organic-rich shale

deposition known as Ocean Anoxic Event 1 (OAE-1) (Jenkyns, 1980). The later, rising, step in the barite record ends at a second OAE (OAE-2). Beginning in the lowest Eocene, the barite record climbs 5‰, reaching approximately the modern seawater $\delta^{34}S$ by the Bartonian. The evaporite and biogenic CAS records lack the sharp variability of the barite record, but exhibit local minima in between the OAEs (Claypool et al., 1980; Kampschulte and Strauss, 2004). The bulk CAS data is much more variable, and additionally records sharp 2-4‰ dips in $\delta^{34}S$ during the OAEs that are not resolved by the other archives (Adams et al., 2010; Gomes et al., 2016; Mills et al., 2017; Ohkouchi et al., 1999; Owens et al., 2013; Poulton et al., 2015; Turchyn et al., 2009). Additionally, the bulk CAS record climbs to its Upper Cretaceous $\delta^{34}S$ values in the early Albian, about 10 Myrs prior to the barite record (Mills et al., 2017), and remains heavier than the barite record until the late Santonian (Owens et al., 2013). The biogenic and bulk CAS data include extreme variability at the Cretaceous-Paleogene Boundary (s.d. = 10.6‰, Figure 2B) that is not resolved by other records (Kaiho et al., 1999; Witts et al., 2018).

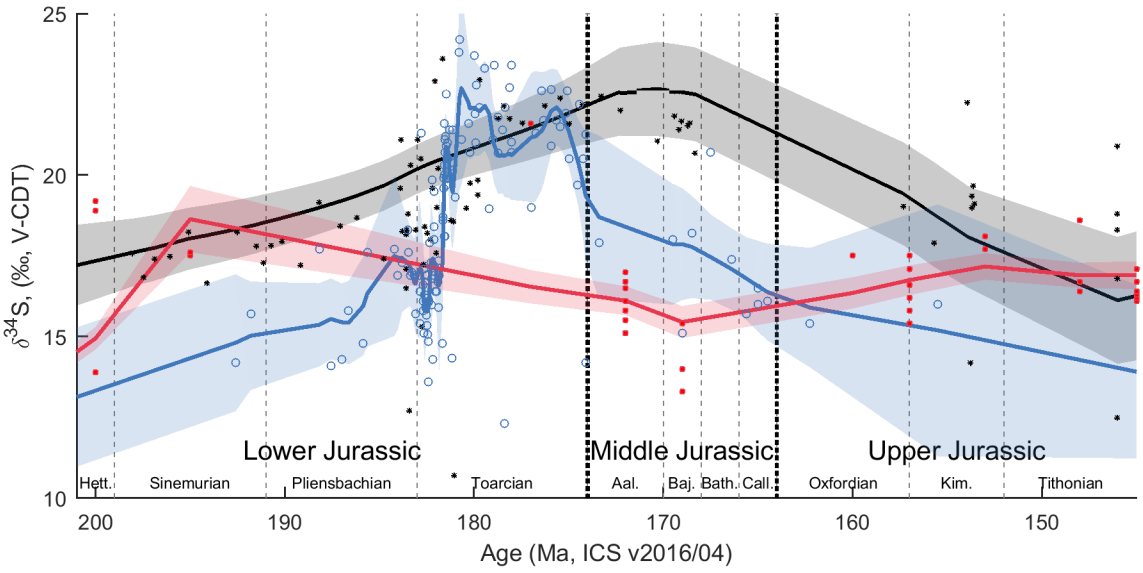

Figure 6: Latest Triassic and Jurassic $\delta^{34}S$ records. See Figure 3 for legend for symbols and lines. Hett. = Hettangian, Aal. = Aalenian, Baj. = Bajocian, Bath. = Bathonian, Call. = Callovian, Kim. = Kimmeridgian.

Beginning at the start of the Toarcian Stage in the Jurassic (Figure 6), biogenic CAS data from belemnite calcite records a 6‰ positive excursion in less than 2 Myr. Like the Cretaceous excursions, the Toarcian step is coincident with an OAE (Gill et al., 2011a; Newton et al., 2011). With the exception of a single analysis of higher $\delta^{34}S$ during the Toarcian, the evaporite data does not resolve an isotope excursion in the Jurassic (Claypool et al., 1980; Thode and Monster, 1970, 1965). Over the Pliensbachian-Toarcian Boundary, bulk CAS data exhibits a step similar to the biogenic CAS to higher $\delta^{34}S$ (Gill et al., 2011a; Newton et al., 2011), with increased variance during the OAE (s.d.=6.9‰, Figure 2B, including $\delta^{34}S$ compositions as high as 39.6‰, Figure 10B). However, the bulk CAS data maintains $\delta^{34}S$ compositions ~5‰ higher than evaporites until the Bajocian stage (Arp et al., 2008; Baldermann et al., 2015; Gill et al., 2011a), while the biogenic CAS data recovers to pre-OAE compositions by the beginning of the Middle Jurassic (Kampschulte and Strauss, 2004).

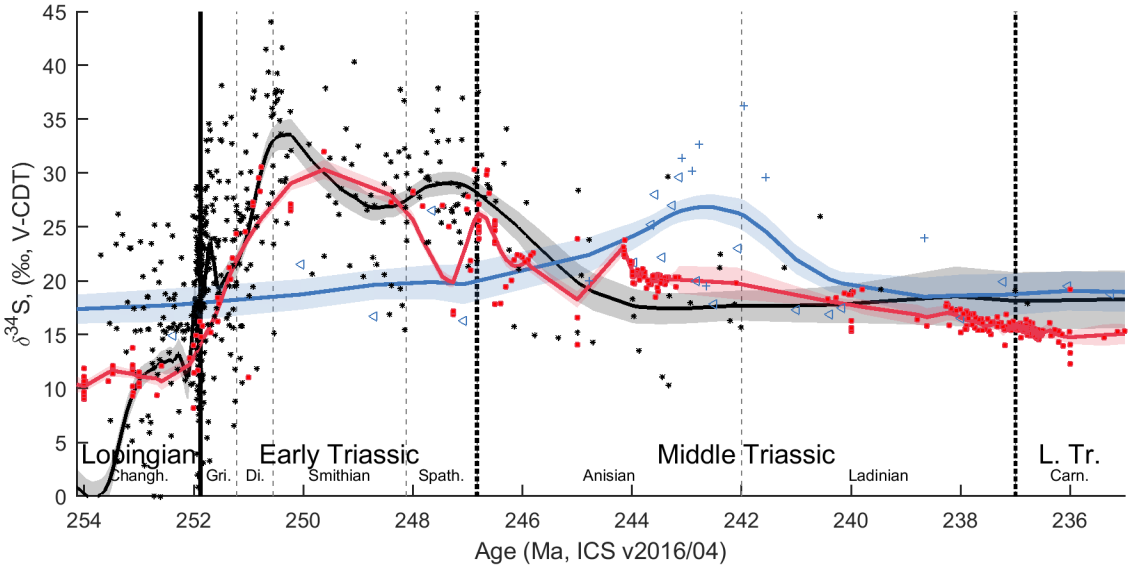

Figure 7: Changhsingian (latest Permian) to Late Triassic $\delta^{34}S$ records. See Figure 3 for legend for symbols and lines. L. Tr. = Lower Triassic, Changh. = Changhsingian, Gri. = Griesbachian, Di. = Dienerian, Spath. = Spathian, Carn. = Carnian.

During the Triassic, a major positive $\delta^{34}S$ excursion is well-resolved in the evaporite data (Figure 7). This was named the "Röt" event by Holser (1977) after the formation that contained the highest $\delta^{34}S$ values during this interval when he compiled the observations. More recent and complete assessment of the Permo-Triassic evaporite record includes compositions as high as 32‰ in the Smithian following an abrupt rise over 2 Myr in the Griesbachian and Dienerian from a latest Permian minimum of 11‰ (Bernasconi et al., 2017). A gradual decline towards Late Triassic compositions of ~15‰ is punctuated by 5-10‰ positive excursions at the Early-Middle Triassic boundary and in the Anisian. Over this interval, the biogenic CAS $\delta^{34}S$ data is sparse, but exhibits a maxima in the Anisian that is 10-15‰ higher than the evaporite data (Kampschulte and Strauss, 2004; Wu et al., 2014). The bulk CAS $\delta^{34}S$ data in the Guadalupian, Lopingian, and Early Triassic includes extreme values ranging from -16‰ to 44‰, and is generally higher than the evaporite data (Kaiho et al., 2006, 2001; Newton et al., 2004; Schobben et al., 2017a, 2015; Song et al., 2014).

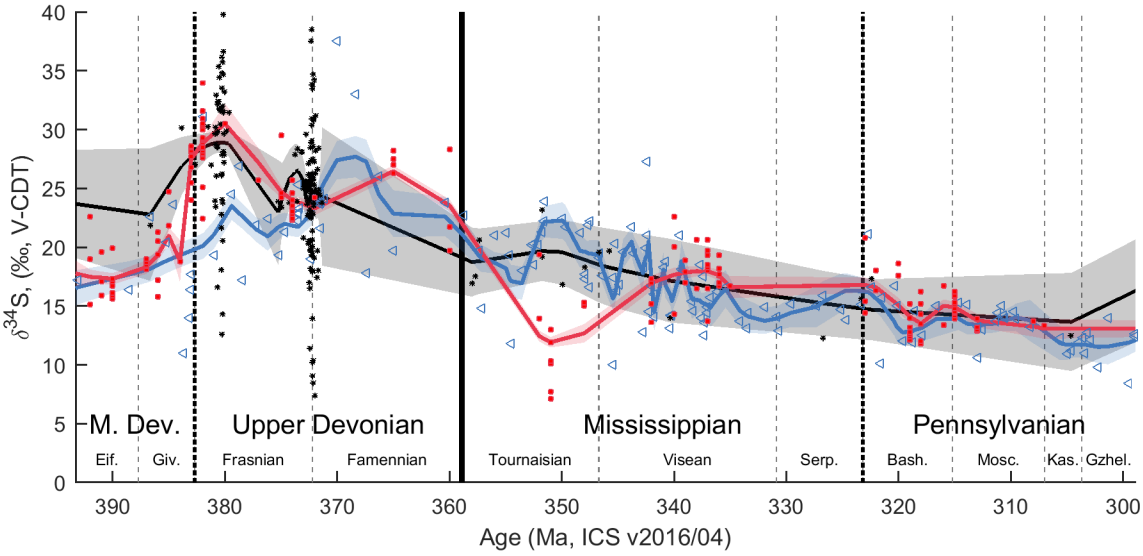

Figure 8: Middle Devonian to Pennsylvanian $\delta^{34}S$ records. See Figure 3 for legend for symbols and lines. M. Dev. = Middle Devonian, Eif. = Eifelian, Giv. = Givetian, Serp. = Serpukhovian, Bash. = Bashkirian, Mosc. = Moscovian, Kas. = Kasimovian, Gzhel. = Gzhelian.

Holser (1977) identified another major positive $\delta^{34}S$ excursion in evaporite data from the Upper Devonian (Figure 8), which he named the "Souris" event. Evaporite $\delta^{34}S$ increases by 15‰ over ~4 Myr in the Giventian, and declines to an early Mississippian minimum over 30 Myr (Claypool et al., 1980; Davies and Krouse, 1975; Holser and Kaplan, 1966; Sakai, 1972; Thode et al., 1958; Thode and Monster, 1965; Vredenburgh and Cheney, 1971; Yeremenko and Pankina, 1972). The Devonian-Carboniferous bulk CAS $\delta^{34}S$ data generally follow this trend, but measurements are extremely variable (s.d.=4.0-5.6‰, Figure 2B) and are concentrated around stratigraphic intervals with positive carbon isotope excursions, including the Late Devonian mass extinction at the Frasnian-Famennian Boundary (Chen et al., 2013; Gill et al., 2007; Kampschulte et al., 2001; Kampschulte and Strauss, 2004; Sim et al., 2015). Biogenic CAS data includes a Late Devonian rise in $\delta^{34}S$ followed by a Carboniferous decrease to the Late Permian minima, but does not record the sharp Giventian rise that appears in the evaporite record (Kampschulte et al., 2001; Kampschulte and Strauss, 2004; Wu et al., 2014). The biogenic CAS record also does not include the Tournaisian minimum observed in the evaporite record.

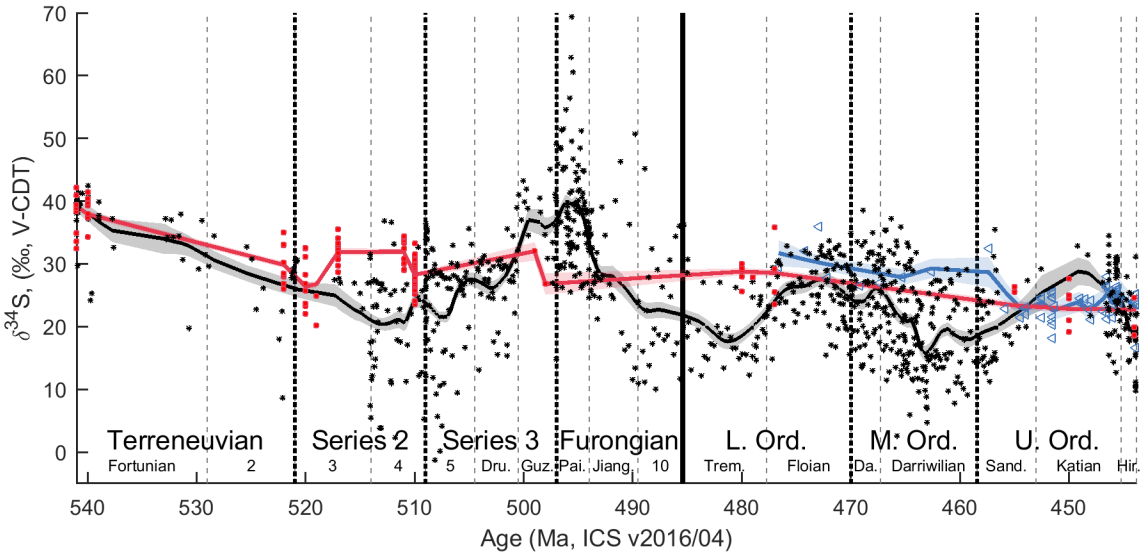

Figure 9: Cambrian and Ordovician $\delta^{34}S$ records. See Figure 3 for legend for symbols and lines. L. Ord. = Lower Ordovician, M. Ord. = Middle Ordovician, U. Ord. = Upper Ordovician, Dru. = Drumian, Guz. = Guzhangian, Pai. = Paibian, Jiang. = Jiangshanian, Trem. = Tremadocian, Da. = Dapingian, Sand. = Sandbian, Hir. = Hirnantian.

In all proxies, Cambrian and Ordovician $\delta^{34}S$ data have higher variance than younger time intervals except for the Souris and Röt events (Figure 2B). Evaporite $\delta^{34}S$ data is highest at the Precambrian-Cambrian boundary, where it has a mean composition of 39‰ (Schröder et al., 2004). Bulk CAS and evaporite $\delta^{34}S$ data are sparse in the earliest part of the Cambrian, but record a decline over the Terreneuvian Epoch (Figure 9) (Fike and Grotzinger, 2008; Kampschulte and Strauss, 2004; Loyd et al., 2012b; Wotte et al., 2012b, 2011). Cambrian and Ordovician evaporite data, while constrained well-enough to assign to a stage if included in this compilation, is compiled from literature that often did not record detailed stratigraphic information (Claypool et al., 1980; Davies and Krouse, 1975; Pisarchik et al., 1977; Pisarchik and Golubchina, 1975; Sakai, 1972; Yeremenko and Pankina, 1972). The bulk CAS record, which is comparatively abundant and better-constrained between Cambrian Series 2 and the earliest Silurian, includes a major positive $\delta^{34}S$ during the Paibian Stage that is not resolved in the evaporite record. This excursion, which is coincident with SPICE, a major positive carbon isotope excursion recorded in Steptoean-age strata on Laurentia, includes CAS $\delta^{34}S$ data as high as 69‰ (Gill et al., 2011b). Otherwise, bulk CAS data have generally lower $\delta^{34}S$ than evaporites of similar age, and records 10-20‰ oscillations with a period of 10-20 Myr (Gill et al., 2007; Hurtgen et al., 2009; Jones and Fike, 2013; Kah et al., 2016; Kampschulte and Strauss, 2004; Loyd et al., 2012b; Marenco et al., 2016, 2013; Present et al., 2015; Thompson and Kah, 2012; Wotte et al., 2012b, 2011; Young et al., 2016). No biogenic CAS data is available in the Cambrian, but Ordovician brachiopods have a $\delta^{34}S$ trend and variance similar to the evaporite data (Kampschulte and Strauss, 2004; Present et al., 2015; this volume, Ch. 2; this volume, Ch. 3; Wu et al., 2014).

Discussion

Despite the difficulties in resolving their age and depositional environment (Strauss, 1997), the mass of sulfate represented by evaporite deposits makes them the most robust proxy to estimate the $\delta^{34}S$ of ancient oceans. However, to generate a high-resolution record of changes in the Earth's Phanerozoic sulfur cycle, CAS and barite archives must be used. In general, the LOESS fits of CAS and barite $\delta^{34}S$ data are within ~10‰ of that of the evaporite record (Figure 4), suggesting that the other proxy materials record the first order features of

the Phanerozoic sulfur cycle. Which higher-frequency sources of variance reflect real spatial or temporal changes in the $\delta^{34}S$ of ancient oceans, and which reflect local or diagenetic controls on the formation of the archive?

Evaporites

The major features of the evaporite record produced by Ault and Kulp (1959)—high $\delta^{34}S$ in the early Paleozoic, a minimum in the late Paleozoic, and a gradual rise to present marine values—have been reaffirmed and refined over the past 60 years (Claypool et al., 1980; Holser et al., 1989; Holser and Kaplan, 1966; Strauss, 1997). The modern evaporite record presented in red in Figure 3 adequately resolves biogeochemical changes occurring on tectonic timescales (1-100 Myr). Bernasconi et al. (2017) recently produced a high-resolution evaporite record that appears to cleanly resolve the major features and excursions of the early Triassic $\delta^{34}S$ volatility (Figure 7), thereby demonstrating that, with careful correlation and assignment of geologic ages it is indeed possible to track changes in the Phanerozoic sulfur cycle with evaporites. Many prior compilations binned evaporite data at the stage scale or coarser, and often only reported maximum, minimum, or mean $\delta^{34}S$ values for entire lithostratigraphic groups. The compilation produced here attempts to use the stratigraphic information contained in the literature to constrain evaporites data to the stage scale or finer, but the record can clearly benefit from improved, stratigraphically-controlled resampling during intervals where $\delta^{34}S$ changes appear in other records.

Such effort may be particularly worthwhile to better resolve the Paleozoic sulfur isotope record. Almost certainly, there is potential biogeochemical insight to be gained from a revived concerted effort to produce a high-resolution evaporite $\delta^{34}S$ record. For example, much of data compiled from the Middle and Late Devonian Souris event (Figure 8) is reported from western Canada, where the lithostratigraphic formations or groups—including the namesake Souris River Formation—have benefitted from improved sequence stratigraphic and chemostratigraphic work since the data was originally tabulated (e.g., Grobe, 2000; Holmden et al., 2006; Whalen et al., 2000). Similarly, sparse evaporite $\delta^{34}S$ data and poor stratigraphic control characterize much of the Lower Ordovician record (Figure 9), but recent improvement of the stratigraphy of Arctic Canada (e.g., Dewing and Nowlan,

2012) increase the potential for a robust record during this period. Evaporites that formed in marginal marine environments throughout the Phanerozoic often interfinger with well-constrained carbonate successions, where modern stratigraphic concepts may aid age assignment (Tucker, 1991; Warren, 2010).

Intra-basinal $\delta^{34}S$ variation remains an outstanding problem in extracting the most accurate estimate of ancient seawater from evaporite deposits. Evaporites often form in restricted basins with salinity-stratified water columns (Warren, 2010). If part of the water column is anoxic, MSR may produce low-$\delta^{34}S$ sulfide and distill the residual sulfate to higher $\delta^{34}S$. This mechanism motivated some early sulfur isotope geochemists to report only the lowest $\delta^{34}S$ composition as the best estimate of ancient seawater sulfate's $\delta^{34}S$ (Davies and Krouse, 1975; Thode and Monster, 1970, 1965). In the Cenozoic and Cretaceous (except during the early Paleogene), open-marine barite $\delta^{34}S$ is generally within the evaporite $\delta^{34}S$ confidence interval or heavier (Figure 4). This suggests that local controls on the $\delta^{34}S$ of evaporites may additionally lower $\delta^{34}S$. Continentally-derived input of isotopically-distinct sulfur or reoxidation of aqueous sulfide may be such sources of low-$\delta^{34}S$ sulfate. However, large and even volumetrically-dominant fractions of non-marine fluids, which are typically sulfate-poor, are required to significantly alter marine $\delta^{34}S$ compositions (Lu and Meyers, 2003). Therefore, mixing of reoxidized sulfide during water-column mixing or early diagenesis appears to be an important source of variance in the evaporite $\delta^{34}S$ record. Consequently, best fits to the evaporite data, rather than the minimum $\delta^{34}S$ composition, are most likely to accurately reflect the evolution of seawater's $\delta^{34}S$.

Barite

Barite is likely a robust proxy for ancient seawater $\delta^{34}S$ because it precipitates in the open-ocean water column and is texturally distinguishable from diagenetically-altered barite that forms in anoxic sediments at redox fronts (Paytan et al., 1993). In the Mesozoic and Cenozoic, the residual between the barite and evaporite records is never greater than 3‰ (Figure 4), despite rapid (~5 Myr) $\delta^{34}S$ steps in the Eocene and Cretaceous of a greater magnitude (Figure 5). The $\delta^{34}S$ variability within evaporite deposits and CAS exceeds this

difference, suggesting that marine barite is the most accurate proxy for the $\delta^{34}S$ of seawater at this time.

The age of barite from marine sediments is constrained by biostratigraphy and strontium isotope stratigraphy (Kurtz et al., 2003; Paytan et al., 2004, 1998, 1993), but at least one major sulfur cycle perturbation recorded by barite lacks sufficient age control. Age models used for sediment cores taken at DSDP Sites 305 and 366 (Kurtz et al., 2003) suggest that the Eocene increase in $\delta^{34}S$ reached its maximum value by the end of the Ypresian (data enclosed by circles in Figure 5), but age models for cores taken at ODP Sites 865 and 1219 (Turchyn et al., 2009) indicate the rise occurred later, in the late Lutetian (data enclosed by diamonds in Figure 5). If the Ypresian age of the $\delta^{34}S$ rise is correct, then the early Eocene sulfur cycle experienced an extremely rapid change in marine sulfate concentrations, pyrite burial fluxes (Kurtz et al., 2003; Wortmann and Chernyavsky, 2007; Wortmann and Paytan, 2012), or $\delta^{34}S$ of buried pyrite (Rennie et al., 2018).

The marine barite record is limited by the availability of open-marine sediments that deposited in high-productivity regions where authigenic enrichment of barite occurs and where pore fluid sulfate concentrations remain above zero (Paytan et al., 1993). Consequently, the barite $\delta^{34}S$ record is unlikely to be extended much further back in time than the current dataset. Paleozoic bedded barite deposits are associated with economically-important metal sulfide deposits (Johnson et al., 2009), but contain large $\delta^{34}S$ variability (>10‰) and do not resolve the ancient seawater record better than other proxy materials. Additionally, the temporal resolution of the marine barite $\delta^{34}S$ record is unlikely to dramatically improve, especially during biogeochemical events characterized by low marine productivity (such as the Cretaceous-Paleogene boundary) or bottom-water anoxia (such as OAEs) that would limit authigenic barite enrichment or preservation.

Biogenic CAS

Biogenic carbonate is likely to produce a robust $\delta^{34}S$ record because it can often be readily separated from limestone components that obviously recrystallized. Burdett et al. (1989) produced the first continuous biogenic CAS dataset for the Neogene, and demonstrated that

it agrees with the evaporite $\delta^{34}S$ record. Kampschulte et al. (2001) and Kampschulte and Strauss (2004) then demonstrated that biogenic CAS reaffirms the first-order features of the Phanerozoic evaporite record, and can be correlated with higher resolution and confidence than evaporites to the carbonate carbon isotope record.

Low-magnesium calcite (LMC), precipitated by many brachiopods, belemnites, and planktonic foraminifera, is thermodynamically-stable at Earth's surface and shallow burial conditions. The LMC biogenic CAS $\delta^{34}S$ record has significantly improved the resolution of the Phanerozoic $\delta^{34}S$ record during three key periods. First, during the Toarcian Ocean Anoxic Event (Figure 6), belemnite CAS resolves a large (6‰) $\delta^{34}S$ excursion that is not apparent in the evaporite record (Gill et al., 2011a; Newton et al., 2011). Second, during the Carboniferous (Figure 8), brachiopod CAS records a prolonged recovery from the $\delta^{34}S$ maxima of the Souris event to the late-Permian $\delta^{34}S$ minimum (Kampschulte et al., 2001; Wu et al., 2014). Finally, brachiopod CAS from the Late Ordovician and early-middle Silurian, including new data presented in Chapters 2 and 3 of this thesis, indicates a stable marine sulfate $\delta^{34}S$ spanning the Late Ordovician mass extinction (Kampschulte and Strauss, 2004; Present et al., 2015; this volume, Ch. 2; this volume, Ch. 3; Wu et al., 2014). Each of these trends are reproduced in samples from multiple localities, and are likely to describe primary changes in the $\delta^{34}S$ of ancient seawater.

Even well-preserved biogenic calcite, however, has been subject to diagenetic alteration that must be considered when interpreting the proxy archive. In each period with dense LMC CAS records from multiple locations (the Ordovician-Silurian, the Upper-Middle Devonian, the Carboniferous, and the Toarcian), the variability of $\delta^{34}S$ in biogenic CAS is different (Figure 2B). During the Toarcian, the standard deviation of belemnite data following the 6‰ positive $\delta^{34}S$ excursion is 2.1‰. During the Carboniferous, the standard deviation of brachiopod data over any 5 Myr varies between 0.5‰ and 4‰. Brachiopods from the Middle and Upper Devonian exhibit substantial variability (s.d. 4-7‰) that does not display the clear temporal trend associated with the Souris event in the evaporite record (Figure 8). Finally, brachiopod $\delta^{34}S$ from the late Ordovician and early Silurian have a standard deviation over

any 5 Myr period between 1.8‰ and 4.2‰. Chapters 2 and 3 include multiple Ordovician-Silurian brachiopod samples from the same bed, indicating that even extremely well-preserved LMC may vary by 3 – 5‰ due to diagenetic processes. This makes it difficult, therefore, to demonstrate the existence of isotope excursions that have a small magnitude. For example, worldwide stratigraphic successions contain a major positive carbon and pyrite-sulfur isotope excursions during the Hirnantian Stage that coincide with the Late Ordovician Mass Extinction and glaciation (Finnegan et al., 2011, 2012; Gorjan et al., 2012; Hammarlund et al., 2012; Jones and Fike, 2013; Saltzman and Young, 2005; Yan et al., 2009; Zhang et al., 2009). However, the $\delta^{34}S$ of brachiopod CAS after the extinction (the Hirnantian and Rhuddanian stages, n=16 over 4.4 Myr, M=24.04‰, s.d.=2.31‰) is statistically identical to the preceding Katian Stage (n=42 over 7.8 Myr, M=24.08‰, s.d.=2.05‰); paired-sample t-test t(57)=0.0498, p=0.96. This suggests that, given the variability imposed by diagenesis, relatively large $\delta^{34}S$ excursions would be required to confidently document changes in the sulfur cycle. Absent statistical evidence for sulfur isotope changes, it seems likely that late Paleozoic seawater sulfate was not perturbed by the Late Ordovician Mass Extinction or by possible drivers of extinction such as glaciation or shoaling of euxinic water masses (Finnegan et al., 2012; Hammarlund et al., 2012). This contrasts with the other Paleozoic mass extinctions in the Late Devonian and Late Permian, which exhibit major changes in the mean composition and variability of brachiopod $\delta^{34}S$. At this time, however, there has been no examination of multiple brachiopods from the same stratigraphic horizon preceding and following these mass extinctions to assess the effect of diagenesis on the biogenic CAS archive.

Aragonite and high-magnesium calcite (HMC, >8 mole % Mg/Ca), precipitated by many bivalves, gastropods, corals, trilobites, echinoderms, bryozoans, and marine algae, is not at equilibrium in any diagenetic environment and are prone to rapid recrystallization or dissolution (Brand and Veizer, 1980). Few studies have reported CAS $\delta^{34}S$ from aragonitic and HMC fossils (Mekhtiyeva, 1974; Present et al., 2015; Witts et al., 2018). Bivalve CAS $\delta^{34}S$ data at the Cretaceous-Paleogene Boundary (Figure 5) has the highest variance in biogenic CAS $\delta^{34}S$ in any 5 Myr period during the Phanerozoic (s.d.= 10.6‰, Figure 2B).

Witts et al. (2018) demonstrate that much of this variance can be attributed to diagenetic alteration of the bivalves, which produces CAS with $\delta^{34}S$ as low as -10.7‰ and as high as 57.7‰ (all excluded samples are <10‰ or >25‰, and plot off the scale of Figure 5). They exclude samples based on covariance of $\delta^{34}S$ in CAS with other geochemical parameters, including CAS concentration, $\delta^{18}O$ of the extracted sulfate, $\delta^{13}C$ and $\delta^{18}O$ of the carbonate, and the concentration and $\delta^{34}S$ of non-CAS extracted sulfur.

The standard deviation of Cretaceous-Paleogene bivalve CAS data, after exclusion of the discernably-altered samples, is 1.8‰. This is comparable to the variance in Maastrichtian evaporite $\delta^{34}S$ (s.d. = 1.7‰) but greater than that of Masstrichtian-Danian barite $\delta^{34}S$ (s.d. = 0.11‰). However, a revised LOESS fit through the Phanerozoic biogenic CAS dataset, excluding the obviously-altered bivalves, indicates Maastrichtian-Danian bivalve CAS $\delta^{34}S$ is still ~3‰ lower than the barite record (dotted blue line in Figure 5). It therefore appears difficult to confidently discern high-resolution seawater $\delta^{34}S$ trends from aragonite or HMC CAS at this point. As with LMC, CAS $\delta^{34}S$ analysis of multiple HMC specimens of the same age is required to assess the amount of variability due to diagenesis. In high-resolution studies of short time intervals, it is necessary to assess the reproducibility of $\delta^{34}S$ analyses from specimens from the same bed, or even multiple analyses of individual fossils.

Bulk CAS

CAS may reflect the $\delta^{34}S$ of syndepositional seawater sulfate if the carbonate component did not recrystallize after precipitation, if recrystallization and cementation occurred in a low-sulfate pore fluid, or if the $\delta^{34}S$ of pore fluid sulfate is not fractionated from seawater. Lyons et al. (2004) showed that the cementation and recrystallization of aragonite mud in shallow subtidal Florida Bay sediments retains the $\delta^{34}S$ of syndepositional seawater because pore fluid sulfate concentrations are low compared to the CAS concentration of the carbonate. Similarly, Gill et al. (2008) demonstrated that the recrystallization of a Pleistocene aragonite coral to calcite during supratidal meteoric diagenesis retains the $\delta^{34}S$ of the primary aragonite because the meteoric fluids are sulfur-poor. Rennie and Turchyn (2014), in pelagic nanofossil oozes, demonstrated that recrystallization may incorporate pore fluid sulfate with $\delta^{34}S$ up to 4‰ higher than the syndepositional sulfate. Alteration occurs if the sediments

recrystallize above the depth at which sulfate is completely consumed by MSR but deep enough that some distillation of pore fluid sulfate's $\delta^{34}S$ has occurred (Rennie and Turchyn, 2014; Witts et al., 2018). Therefore, in pelagic settings, where MSR occurs tens to hundreds of meters below the sediment-water interface, both extremely rapid and extremely low sedimentation rates preserve syndepositional sulfate $\delta^{34}S$ in CAS, but moderate sedimentation rates (~50-200 m/Myr) result in recrystallization within a sulfate-rich region of high-$\delta^{34}S$ pore fluids (Rennie and Turchyn, 2014). In coastal environments, MSR occurs in pore fluids that are only millimeters to centimeters below the sediment-water interface (Jørgensen, 1982), so proportionately-higher sedimentation (Berner, 1978) or recrystallization rates could result in a diagenetic increase in the $\delta^{34}S$ of CAS. Additionally, observations of ancient carbonates often contain CAS with anomalously-low $\delta^{34}S$ interpreted to represent the incorporation of sulfide that was reoxidized during early diagenesis (Baldermann et al., 2015; Fichtner et al., 2017; Marenco et al., 2008b; Present et al., 2015; Riccardi et al., 2006; Yan et al., 2013).

Carbonates recrystallizing during burial may also be prone to diagenetic modification of the $\delta^{34}S$ of CAS if the burial fluids were sulfate-rich. Most burial diagenesis produces LMC cements or recrystallized carbonate that contain lower CAS concentrations than primary aragonite or HMC (Fichtner et al., 2017; Present et al., 2015). However, experimental recrystallization of biogenic aragonite at 175°C produced HMC cements that incorporated sulfate from the diagenetic fluid (Fichtner et al., 2018). The $\delta^{34}S$ in burial fluids may be highly variable, and include sulfate from hydrocarbon or organic matter degradation (Fichtner et al., 2018; Thode and Monster, 1970, 1965), dissolved evaporites, or groundwater modified by MSR (Dogramaci et al., 2001).

The relative rates of sedimentation, sulfate reduction, carbonate cementation and recrystallization, and sulfide oxidation vary with depositional environment. Chapter 4 examines how depositional setting controls the $\delta^{34}S$ in CAS, and shows that high-energy peritidal environments in the Guadalupe Mountains in West Texas best preserve primary seawater sulfate's composition. This is likely because diagenetic stabilization of the

carbonate occurs faster than sulfate reduction in such settings, which contain coarse-grained, organic carbon-poor sediments. Carbonate sediments in lower-energy depositional environments are often finer-grained, mud-rich, and organic-rich, and can develop large pore fluid sulfate gradients by MSR. Figure 10A shows the wide range of bulk CAS $\delta^{34}S$ measurements in the Guadalupian Stage of the Permian, which includes data as low as -37‰ and as high as 32‰ (Yan et al., 2013). Samples from the Guadalupe Mountains include a more limited range of $\delta^{34}S$ compositions between 5‰ and 26‰. Of these, samples deposited in the shallowest depositional environments—on the carbonate platform's intertidal shelf crest and shallow subtidal outer shelf— are marked with purple circles, and fall within the confidence interval of the evaporite $\delta^{34}S$ record. Other samples were deposited in low-energy subtidal settings and tend to have higher $\delta^{34}S$ than the evaporites in West Texas. The lowest compositions likely reflect reoxidation of sedimentary sulfides during periods of increased oxygen penetration into the sediments (Yan et al., 2013).

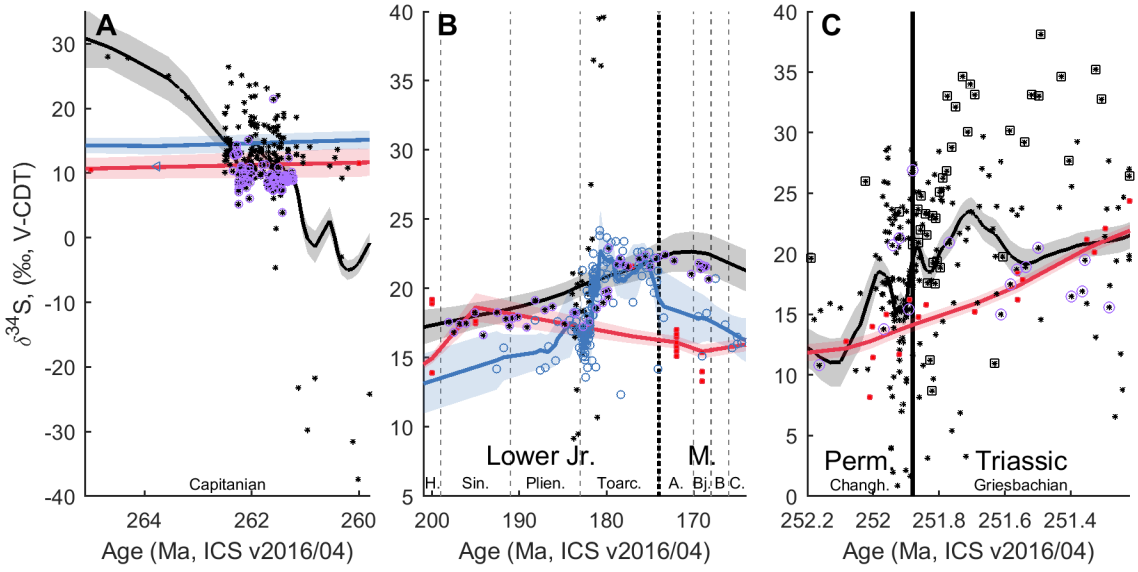

Figure 10: Comparisons of bulk CAS $\delta^{34}S$ from different lithologies with evaporite and biogenic CAS $\delta^{34}S$ records. See Figure 3 for legend for symbols and lines. (A) CAS analyses marked in purple circles from the shelf crest and outer shelf facies tracts of the Capitanian carbonate platform in the Guadalupe Mountains, West Texas. (B) CAS analyses marked in purple circles from the coarse packstone-grainstone facies of the Jurassic Campania-Luciana platform in Monte Sorgenza, Italy. (C) CAS analyses marked in purple circles from the inner ramp depositional setting in Suisi, Italy. CAS analyses marked with black squares from the low-energy platform interior depositional setting in South China. Jr. = Jurassic, H. = Hettangian, Sin. = Sinemurian, Plien. = Pliensbachian, Toarc. = Toarcian, A. = Aalenian, B. = Bathonian, Bj. = Bajocian, C. = Callovian, Changh. = Changhsingian.

Bulk CAS $\delta^{34}S$ is also much more variable than the biogenic CAS in the Jurassic. During the Toarcian OAE, Figure 10B shows that bulk CAS $\delta^{34}S$ ranges from 9‰ to 40‰ (Gill et al., 2011a; Newton et al., 2011). Rocks deposited in shallow, high-energy depositional environments (i.e., ooid-skeletal packstones and grainstones from the Campania-Luciana Platform, Italy, which are marked with purple circles in Figure 10B) better track the Toarcian 6‰ positive $\delta^{34}S$ excursion than heterolithic peloid-ooid packstones and grainstones in the Yungjia Formation, Tibet. In particular, the extreme (>25‰) $\delta^{34}S$ compositions are from shale-rich, laminated, micritic limestones deposited in the deep subtidal part of a carbonate ramp (Newton et al., 2011; Wignall et al., 2006). Newton et al. (2011) suggest that the large magnitude of Toarcian $\delta^{34}S$ excursion in the Tibeten rocks compared to Yorkshire belemnites indicates a seawater sulfate gradient between epeiric seas and the open Tethys Ocean. However, another interpretation is that diagenetic processes that drive $\delta^{34}S$ excursions in seawater sulfate—namely, MSR and pyrite burial—also locally affect bulk CAS $\delta^{34}S$. The OAEs are periods of widespread shale deposition during which increased organic carbon and pyrite burial are thought to drive increases in seawater $\delta^{13}C$ and $\delta^{34}S$ (Gill et al., 2011a; Jenkyns, 1988). Further, most sulfate reduction and pyrite burial occurs in organic-rich inner and outer shelf sediments (Bowles et al., 2014). As global seawater $\delta^{34}S$ increased due to net increases in pyrite burial, the sedimentary environments where pyrite burial was occurring would have greater pore fluid $\delta^{34}S$ gradients and be more prone to diagenetic increases in the $\delta^{34}S$ of CAS.

Extreme $\delta^{34}S$ variability occurs in bulk CAS records from the earliest Triassic during the 15‰ $\delta^{34}S$ rise at the beginning of the Röt event (Figure 10C). Bulk CAS $\delta^{34}S$ is generally 10-15‰ higher than the evaporite data of the same age, and all data shows a more rapid increase in $\delta^{34}S$ at the Permian-Triassic Boundary. Most bulk CAS data has been collected from organic or siliciclastic-rich limestones (Kaiho et al., 2006, 2001; Riccardi et al., 2006; Schobben et al., 2017a, 2015). A large dataset from a carbonate platform in South China includes platform interior data from low-energy peritidal depositional environments (black squares around bulk CAS data in Figure 10C), but these $\delta^{34}S$ data are among the highest relative to the evaporite data (Song et al., 2014). Only carbonates deposited in an inner ramp

depositional setting in Suisi, Italy—including peritidal fenestral dolostone and ooid grainstones highlighted with purple circles in Figure 10C—coincide with the evaporite data both before and after the rapid $\delta^{34}S$ rise at the Permian-Triassic Boundary (Newton et al., 2004). It seems likely that this section was the least likely to experience overprinting of CAS $\delta^{34}S$ during early diagenesis.

Because early diagenesis most effects the $\delta^{34}S$ of CAS, diagenetic overprinting of seawater $\delta^{34}S$ contains paleoenvironmental information about biogeochemical processes and their effect on the sulfur cycle. Over much of the Phanerozoic, bulk CAS $\delta^{34}S$ is higher than evaporite $\delta^{34}S$, likely reflecting pore water sulfate distillation by MSR. Except during the major positive $\delta^{34}S$ excursion during the SPICE, the Cambrian through Silurian periods are the only Phanerozoic time interval during which bulk CAS $\delta^{34}S$ tends to be lower than evaporite or biogenic CAS $\delta^{34}S$ (Figure 4). Additionally, Neoproterozoic bulk CAS has lower $\delta^{34}S$ than evaporites (Fike and Grotzinger, 2008). Fike and Grotzinger (2010) suggest that evaporite $\delta^{34}S$ was driven to higher compositions than bulk CAS by MSR in restricted, salinity-stratified basins. However, evaporite $\delta^{34}S$ is not higher than biogenic CAS $\delta^{34}S$ by the Middle Ordovician (Figure 9), suggesting that another mechanism must bias bulk CAS towards lower $\delta^{34}S$ compositions. Kah et al. (2016) suggest that isolated, euxinic water masses constitute a major sulfur reservoir during the Ordovician that is intermittently mixed with sulfate in ventilated seawater. Perhaps this sulfur reservoir need not be in the oceans' water columns, however, and generally low $\delta^{34}S$ and variable bulk CAS reflects fluctuating oxygen and sulfate penetration into shallow sediments. In such a scenario, widespread sulfide oxidation in pore fluids during this time could create an early diagenetic imprint on the $\delta^{34}S$ of bulk CAS (Riccardi et al., 2006), and evaporites and biogenic CAS would be insulated from the low $\delta^{34}S$ fluids incorporated into bulk CAS. Increased sulfide oxidation also leads to a less negative $\Delta^{34}S$ between sulfate and buried sulfide (Jørgensen, 1979). Wu et al. (2010) compiled pyrite sulfur isotopic compositions through the Phanerozoic, which indicate less negative $\Delta^{34}S$ values in the Paleozoic during the Lower and Middle Ordovician than the Late Ordovician and Silurian. It is therefore reasonable that, after SPICE, increased

sulfide oxidation in shallow sediments created anomalously-low values of Ordovician bulk CAS $\delta^{34}S$.

In summary, bulk CAS can improve the spatial and temporal resolution of seawater sulfate $\delta^{34}S$ proxy record, permitting investigation of sections with sparse to absent biogenic carbonate or evaporites such as the Cambrian, Ordovician, and Precambrian. Lithology, depositional texture, and an interpretation of the depositional environment should be tabulated along with all geochemical data, but this appears particularly important for bulk CAS. Simple lithological descriptions such as limestone, dolostone, or calcareous shale are inadequate to assess diagenetic effects on the $\delta^{34}S$ of CAS. A thorough accounting of the timing of diagenesis and the likely redox conditions during carbonate stabilization are required, but it appears that in many cases, rocks formed in high-energy environments are most likely to preserve global $\delta^{34}S$ compositions of seawater sulfate. However, the $\delta^{34}S$ of bulk CAS may inform changes in biogeochemical processes such as sulfide oxidation even when modified during early diagenesis.

Conclusions

Sulfur isotope data are compiled from Phanerozoic evaporites, barite, biogenic CAS, and bulk rock CAS and updated to a consistent geologic time scale to compare features of each record. The variance of each record increases with age, and increases at important biogeochemical events such as mass extinctions and OAEs. All archives are subject to spatial and temporal biases arising from both syndepositional and diagenetic biogeochemical processes.

The marine barite record has the lowest time-windowed variance and, because it records open-ocean sulfate $\delta^{34}S$, likely most accurately records the $\delta^{34}S$ of ancient oceans. However, its resolution and temporal extent are limited to the availability of marine sediment cores with deep oxygen penetration at sites of high productivity, and the record is unlikely to be significantly extended.

The marine evaporite record represents massive amounts of ancient seawater sulfate, and therefore accurately records ancient seawater $\delta^{34}S$ from periods with favorable climatic and tectonic conditions. A recent effort to constrain the chronostratigraphy of a major $\delta^{34}S$ excursion recorded by early Triassic evaporites (Bernasconi et al., 2017) suggests that the rest of the Phanerozoic evaporite record can be improved by careful application of modern stratigraphic concepts. However, the evaporite record still suffers from uncertainties related to non-marine fluids or modification of seawater $\delta^{34}S$ in restricted basins, limiting the precision to which ancient oceans' $\delta^{34}S$ may be determined from evaporites.

Given the spatial and temporal limitations of the barite and evaporite records, CAS analyses constitute a major portion of the Phanerozoic $\delta^{34}S$ proxy record. Biogenic CAS $\delta^{34}S$ analyses, especially from LMC, reflects similar biogeochemical sources of variance to the evaporite record, but with a higher temporal resolution. This increase in resolution, and the ability to sample multiple specimens of the same age, permits a quantification of the effect of diagenesis on the record. Biogenic CAS successfully resolves marine sulfur cycle features not apparent in other archives during the Late Ordovician and early Silurian, the Carboniferous, and the Toarcian OAE. At other important biogeochemical transitions, including the mass extinctions as the Frasnian-Famennian Boundary, the end Permian, and the Cretaceous-Paleogene Boundary, the effects of diagenesis have not yet been quantified by multiple CAS analyses from the same bed or specimen and the increases in variance are not similar to the barite or evaporite records. Therefore, $\delta^{34}S$ data from even the best-preserved biogenic carbonate material must be interpreted in the context of additional constraints on the diagenetic history of the sample.

Bulk CAS reflects a significantly different distribution of $\delta^{34}S$ compositions than the biogenic CAS, evaporite, or barite records. Early diagenetic overprinting of CAS occurs in organic rich, low-energy depositional environments where carbonate recrystallization and cementation coincides with sulfate-rich pore fluids with modified $\delta^{34}S$. In some cases, such as the Guadalupian, the Toarcian, and the Permian-Triassic Boundary, bulk CAS from high-energy depositional environments agrees best with the evaporite or biogenic CAS records.

Bulk CAS is the only archive able to resolve sulfur cycle changes during short-term biogeochemical events such as OAEs and carbon isotope excursions, and to extend the $\delta^{34}S$ record into the Precambrian. A careful assessment of the timing and style of diagenesis is required to accurately determine seawater sulfate $\delta^{34}S$. However, diagenetic modification of bulk CAS may reflect changes in biogeochemical processes such as sulfide oxidation and pyrite burial. These diagenetic effects impart systematic biases on the bulk CAS $\delta^{34}S$ archive. Possibly, high variability in fine grained carbonates during the Toarcian OAE reflects the locus of increased pyrite burial, and the anomalously-low $\delta^{34}S$ of Ordovician bulk CAS relative to evaporites reflects a mid-Paleozoic increase in the reoxidation of sulfides.

Reconstructing ancient seawater chemistry from sedimentary proxy archives requires assessing primary and diagenetic sources of variance. The critical comparison of different archives of $\delta^{34}S$ in sedimentary sulfates presented here increases confidence in robust features of the record, guides interpretation of data from key biogeochemical transitions in the Phanerozoic, and informs interrogation of Precambrian strata for which fewer archives are available.

Chapter 2

LARGE CARBONATE ASSOCIATED SULFATE ISOTOPIC VARIABILITY BETWEEN BRACHIOPODS, MICRITE, AND OTHER SEDIMENTARY COMPONENTS IN LATE ORDOVICIAN STRATA

Theodore M. Present[1], Guillaume Paris[2], Andrea Burke[3], Woodward W. Fischer[1], Jess F. Adkins[1]

[1]California Institute of Technology, Pasadena, California, USA
[2]Centre de Recherches Pétrographiques et Géochimiques, Nancy, France
[3]University of St. Andrews, St. Andrews, Fife, Scotland, UK

Present, Theodore M., Guillaume Paris, Andrea Burke, Woodward W. Fischer, and Jess F. Adkins. "Large Carbonate Associated Sulfate Isotopic Variability between Brachiopods, Micrite, and Other Sedimentary Components in Late Ordovician Strata." *Earth and Planetary Science Letters* 432 (2015): 187–98. https://doi.org/10.1016/j.epsl.2015.10.005.

Abstract

Carbonate Associated Sulfate (CAS) is trace sulfate incorporated into carbonate minerals during their precipitation. Its sulfur isotopic composition is often assumed to track that of seawater sulfate and inform global carbon and oxygen budgets through Earth's history. However, many CAS sulfur isotope records based on bulk-rock samples are noisy. To determine the source of bulk-rock CAS variability, we extracted CAS from different internal sedimentary components micro-drilled from well-preserved Late Ordovician and early Silurian-age limestones from Anticosti Island, Quebec, Canada. Mixtures of these components, whose sulfur isotopic compositions vary by nearly 25‰, can explain the bulk-rock CAS range. Large isotopic variability of sedimentary micrite CAS (^{34}S-depleted from seawater by up to 15‰) is consistent with pore fluid sulfide oxidation during early diagenesis. Specimens recrystallized during burial diagenesis have CAS ^{34}S-enriched by up to 9‰ from Hirnantian seawater, consistent with microbial sulfate reduction in a confined aquifer. In contrast to the other variable components, brachiopods with well-preserved secondary-layer fibrous calcite—a phase independently known to be the best-preserved

sedimentary component in these strata—have a more homogeneous isotopic composition. These specimens indicate that seawater sulfate remained close to about 25‰ (V-CDT) through Hirnantian (end-Ordovician) events, including glaciation, mass extinction, carbon isotope excursion, and pyrite-sulfur isotope excursion. The textural relationships between our samples and their CAS isotope ratios highlight the role of diagenetic biogeochemical processes in setting the isotopic composition of CAS.

Introduction

The sulfur isotopic composition of Carbonate Associated Sulfate (CAS) is routinely measured as a proxy for the composition of ancient seawater sulfate and informs Earth's surface redox balance (Burdett et al., 1989; Kampschulte and Strauss, 2004). CAS is trace sulfate commonly found in carbonate rocks of all ages (e.g. Burdett et al., 1989; Kah et al., 2004; Kampschulte and Strauss, 2004; Paris et al., 2014a), and generally thought to be incorporated from ambient seawater during precipitation of carbonate phases (Burdett et al., 1989). Because carbonate strata are nearly ubiquitous in the geologic record, and carry abundant geological and geochemical context, CAS has the potential to provide a robust and high-resolution archive of changes in the sulfur cycle (Kampschulte and Strauss, 2004).

Much effort has gone into constructing time-series records of marine sulfate's isotopic composition. Sulfur isotopic compositions are reported in the common $\delta^{34}S$ notation as part-per-thousand (‰) deviations of $^{34}S/^{32}S$ relative to the Vienna Canyon Diablo Troilite (V-CDT) reference standard. Modern oceans constitute a large sulfur reservoir thought to be at steady-state between weathering and volcanic influxes and reduced and oxidized outputs (Bottrell and Newton, 2006; Garrels and Lerman, 1984). Sulfate reduction to sulfide is directly linked to the carbon cycle by microbial metabolisms, and a fraction of this sulfide flux is preserved as pyrite. There can be large kinetic sulfur isotope fractionations associated with microbial sulfate reduction (MSR), so the relative size of the pyrite sink can affect the isotopic composition of seawater (Garrels and Lerman, 1984). Today, this conceptual model leads to an estimated 20 Myr residence time of sulfate in the ocean (Bottrell and Newton, 2006), so longer-term changes in seawater $\delta^{34}S$ reflect the distribution of oxidized and

reduced chemical species on Earth's surface. However, there is a high degree of stratigraphic variability in many CAS $\delta^{34}S$ records, especially those obtained from bulk-rock samples from early Paleozoic strata (Figure 1).

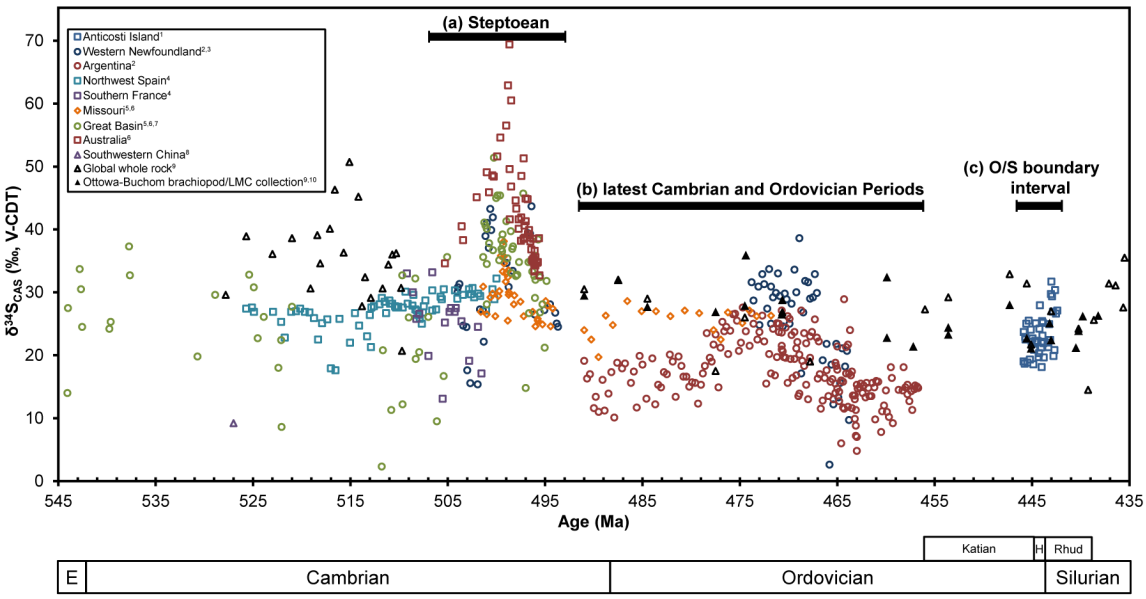

Figure 1: Compilation of previously reported CAS $\delta^{34}S$ values from early Paleozoic successions, plotted by sample collection location. Open symbols represent CAS extracted from bulk-rock (commonly micritic) samples, and closed symbols represent CAS extracted from biogenic calcite. See the text for discussion regarding the Steptoean Stage (a), the latest Cambrian and Ordovician periods (b), and the Ordovician-Silurian (O/S) boundary interval (c). E = Ediacaran, H = Hirnantian. LMC = low-magnesium calcite. Data references: [1]Jones and Fike (2013), [2]Thompson and Kah (2012), [3]Hurtgen et al. (2009), [4]Wotte et al. (2012b), [5]Gill et al. (2007), [6]Gill et al. (2011b), [7]Loyd et al. (2012b), [8]Goldberg et al. (2005), [9]Kampschulte and Strauss (2004), [10]Wu et al. (2014).

Large stratigraphic CAS variability around longer-term trends may be primary, or be a result of secondary processes (Kampschulte and Strauss, 2004). Primary CAS variability would reflect temporal changes in seawater sulfate, or spatial patterns between depositional settings or basins. Secondary processes involve incorporation of sulfate from post-depositional sources. These could include burial or dolomitizing fluids, diagenetically-modified pore fluids, or oxidation of other sulfur-bearing phases in the rock (Gill et al., 2008; Lyons et al., 2004; Marenco et al., 2008b; Rennie and Turchyn, 2014). While secondary processes may mask the interpretation of sulfur isotopes in a global mass balance framework, they do contain additional information about the paleoenvironment and basin history. Finally,

sample preparation itself might oxidize sulfur-bearing phases in the rock and result in measurement of a mixture of CAS and newly generated sulfate (Marenco et al., 2008a; Mazumdar et al., 2008; Wotte et al., 2012a).

Previous workers have tried different methods to reduce the contribution of secondary processes. These methods include mathematically smoothing variability (e.g. Kampschulte and Strauss, 2004; Song et al., 2014), selecting the most robust or best-preserved samples (e.g. fossils in Gill et al., 2011a; Kampschulte et al., 2001; Kampschulte and Strauss, 2004; Newton et al., 2011) (filled triangles in Figure), chemically isolating CAS during extraction from other sulfur-bearing phases (Wotte et al., 2012a), and applying independent geochemical indicators of preservation (Gill et al., 2011a; Goldberg et al., 2005).

Other studies have hypothesized that high CAS variability mainly reflects the primary distribution of marine sulfate, especially in Precambrian and early Paleozoic strata (Gill et al., 2011b; Kah et al., 2004; Loyd et al., 2012b; Thompson and Kah, 2012; Wotte et al., 2012b). The implication is that a small marine sulfate reservoir is necessary to explain observations of rapidly changing (< 1 Myr) or spatially heterogeneous isotopic composition. For example, CAS datasets from the late Cambrian Period include a large positive $\delta^{34}S$ excursion that coincides with the Steptoean Positive Isotopes of Carbon Excursion (SPICE) event, but the magnitude of the excursion varies strongly between localities (interval “a” in Figure) (Gill et al., 2007, 2011b; Hurtgen et al., 2009). Similarly, latest Cambrian through Ordovician CAS records from Argentinian strata show a large range of more than 10‰ over both short and long intervals, and display different trends from North American CAS records of the same age (interval “b” in Figure 1) (Gill et al., 2007; Thompson and Kah, 2012).

To a certain extent, the ability to choose ideal samples for sulfur isotope analysis has been limited by the amount of sulfate required by traditional gas-source mass spectrometric methods. Typically, millimoles of sulfate, corresponding to tens of grams of Phanerozoic carbonates, are precipitated as barite and combusted (as summarized by Wotte et al., 2012a). Because many geologic successions do not offer texturally homogenous samples, traditional CAS analysis of such samples may thus integrate many different phases (primary grains,

micrite, and cements of different age). A recent multi-collector inductively coupled plasma-source mass spectrometric (MC-ICP-MS) method for sulfur isotopic analysis of aqueous sulfate (Paris et al., 2013) facilitates the analysis of nanomole-level sulfur samples from <10 mg of typical Phanerozoic carbonates.

Interval "c" (Ordovician-Silurian boundary interval) in Figure 1 shows a CAS record from texturally heterogeneous limestones collected on Anticosti Island, Canada (Jones and Fike, 2013). This record has variability that is nearly half of the magnitude of secular changes over the entire Phanerozoic interval (Kampschulte and Strauss, 2004; Wu et al., 2014) but is interpreted to reflect a constant seawater $\delta^{34}S$ composition during Late Ordovician time (Jones and Fike, 2013). Near the end of Late Ordovician time there was a major climate change into a glaciated world, which coincides with the Late Ordovician Mass Extinction (LOME)—the second-largest Phanerozoic biotic crisis in terms of raw taxonomic losses (Finnegan et al., 2012, 2011). Globally correlated positive carbon isotope excursions and pyrite-sulfur isotope excursions coincide with peak glaciation and extinction during the end-Ordovician Hirnantian Age (Gorjan et al., 2012; Hammarlund et al., 2012; Saltzman and Young, 2005; Yan et al., 2009; Zhang et al., 2009).

To understand the respective influences of primary and secondary processes in Anticosti Island carbonates, we measured the CAS sulfur isotopes associated with the different petrographic textures and sedimentary components in limestones from the same Anticosti Island stratigraphic sections as Jones and Fike (2013). By exploring and understanding the variability of CAS in such samples, we can point to a phase best recording primary variability. Therefore, we can construct a more precise and accurate record of seawater sulfate, and begin to exploit the information content of CAS measurements that relate to early diagenetic or burial processes.

Geologic setting and samples

Anticosti Island consists of nearly flat-lying exposures of Late Ordovician through lower Silurian strata deposited on a Laurentian tropical carbonate ramp in the Taconic foreland (Desrochers et al., 2010; Jones et al., 2011). During Late Ordovician time, growth of large

ice sheets on the southern hemisphere continent of Gondwana drove a marine regression (Desrochers et al., 2010; Finnegan et al., 2011). This began in the Katian Age (453.0-445.2 Ma), and peaked near the end of the Hirnantian Age (445.2-443.8 Ma), wherein clumped isotope paleothermometry and extinction patterns suggest sharp marine cooling at tropical latitudes (Finnegan et al., 2012, 2011). During this period, mixed carbonate-siliciclastic facies representing near-shore environments were deposited on the eastern sector of the island, and carbonate-dominated facies representing more offshore environments were deposited further west (Copper et al., 2013; Desrochers et al., 2010; Jones et al., 2011). These strata are in the Vauréal, Ellis Bay, and Becsie formations (Figure 2) that, due to subsidence associated with Taconic Orogeny flexure, contain no major unconformities (Desrochers et al., 2010). On the basis of biostratigraphy and chemostratigraphy, the Ordovician-Silurian boundary is thought to lie near the top of the Ellis Bay Formation, which mainly consists of bioturbated and nodular thinly bedded limestones and calcareous shales; higher-order cycles in the eastern sector grade up to sandstones (Copper et al., 2013; Desrochers et al., 2010). The uppermost member of the Ellis Bay Formation, the Laframboise Member, consists of oncolitic grainstones overlain in the more distal western sector by calcimicrobial-coral bioherms and hummocky cross-stratified amalgamated sands and grainstones (Copper et al., 2013; Desrochers et al., 2010).

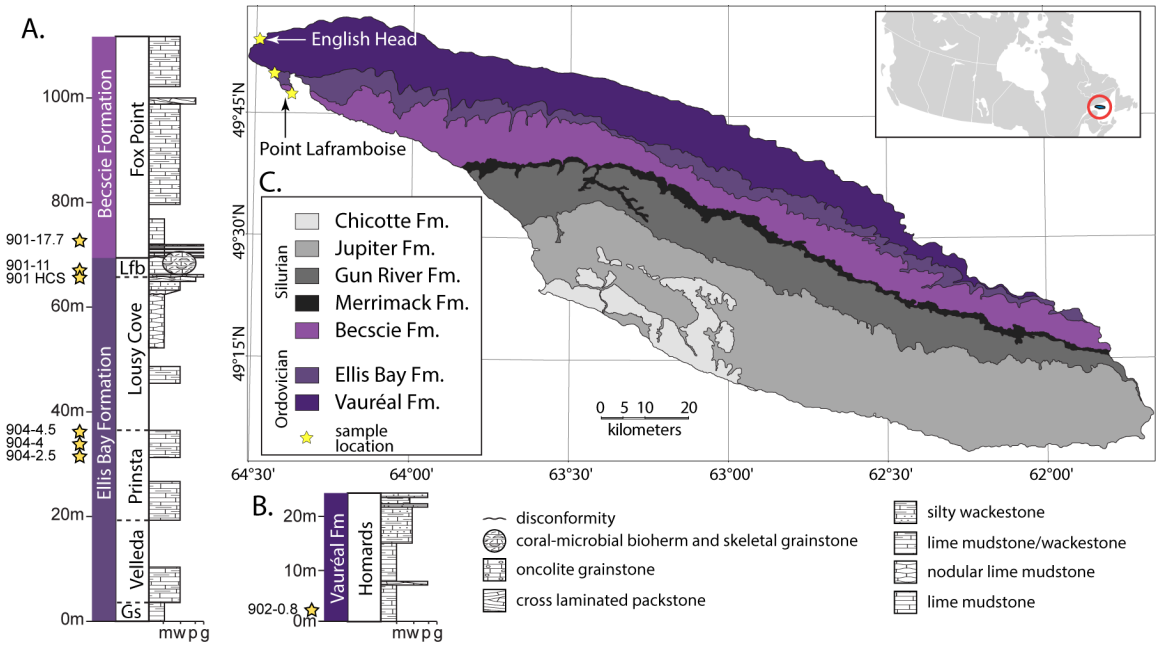

Figure 2: Stratigraphic logs and map of Ordovician and Silurian-age strata on Anticosti Island modified from Jones et al. (2011) after Desrochers and Gauthier (2009). Stars mark locations of stratigraphic sections on the western sector in this study. (A) Composite stratigraphic column of measured sections from Point Laframboise. Gs = Grindstone Member, Lfb = Laframboise Member, m = mudstone, w = wackestone, p = packstone, g = grainstone. (B) Stratigraphic column from English Head. There is approximately 150 m of strata from the top of the English Head section to the bottom of the Point Laframboise section (Jones et al., 2011). Fm. = formation. (C) Map of geologic formations exposed on Anticosti Island, which is in northeastern Quebec, Canada (inset).

Limestones on Anticosti Island are exceptionally well-preserved: dolomitization is rare, primary sedimentary textures are retained, and the rocks experienced little burial alteration (Al-Aasm and Veizer, 1982; Jones et al., 2011; Rohrssen et al., 2013). Trace element and clumped isotope proxies for diagenetic alteration of carbonates indicate that sections on the western side of the island are better preserved than on coeval sections in the east; this sector has the lowest clumped isotope equilibration temperatures, and the least evidence for significant burial or meteoric diagenesis overprint (Finnegan et al., 2011). Low-magnesium calcite (LMC) brachiopods—especially the secondary-fibrous layer of their shells—are exceptionally well-preserved (Al-Aasm and Veizer, 1982; Came et al., 2007; Finnegan et al., 2011).

Limestone samples used in this study come from stratigraphic sections outlined in Finnegan et al. (2011). From this collection, we sampled seven stratigraphic horizons in the Vauréal, Ellis Bay, and Becsie Formations from the well-preserved western sector of Anticosti Island between English Head and Point Laframboise (stars on Figure 2). We intentionally selected heterogeneous limestone hand-samples (classified in Table 1) in order to examine CAS variability on a small spatial scale that may be integrated by traditional CAS extraction techniques. We targeted specific sedimentary components from the bulk-rock samples, including micrite, brachiopods, bryozoans, rugose corals, tabulate corals, trilobites, crinoids, and cements (Figure 3 and Supplemental Figure 1). Specifically, micritic samples came from calcimudstones or wackestones; these lithologies include variable amounts of skeletal fragment allochems, disseminated anhedral pyrite, minor framboidal pyrite, and minor quartz (Figure 4A,C,D). Micrite samples from sample 901-HCS are dolomitic wackestones, and are some of the only dolomitized rocks on Anticosti Island (Jones et al., 2011). Brachiopod shells retain much of their primary textures (Finnegan et al., 2011), although some regions are recrystallized (Figure 4B) or have minor pyrite ingrowth (Figure 4D). Because many of our analyses targeted fossil brachiopods, to explore potential vital effects (Burdett et al., 1989; Kampschulte et al., 2001; Paris et al., 2014b) we also analyzed the CAS isotopic composition of a modern punctate brachiopod valve (*Terebratalia transversa* Sowerby) collected at the San Pedro jetty, Los Angeles County, California and obtained from the Tremper-Long Beach State Collection.

Table 1: Description of samples

Sample name	Formation	Member	Age	Description
901-17.7m	Becscie	Fox Point	Rhuddanian	Brachiopod packstone
901-HCS (9.5m)	Ellis Bay	Lousy Cove	Hirnantian	Very fine dolomitic wackestone and brachiopod wackestone
901-11m	Ellis Bay	Laframboise	Hirnantian	Single rugose coral from a packstone
904-4.5m	Ellis Bay	Prinsta	Katian	Bioclast packstone
904-4m	Ellis Bay	Prinsta	Katian	Brachiopod-coral packstone with fine-medium skeletal wackestone matrix
904-2.5m	Ellis Bay	Prinsta	Katian	Brachiopod floatstone with calcimudstone matrix
904-0.8m	Vaureal	Homards	Katian	Tabulate coral framestone with coarse skeletal grainstone

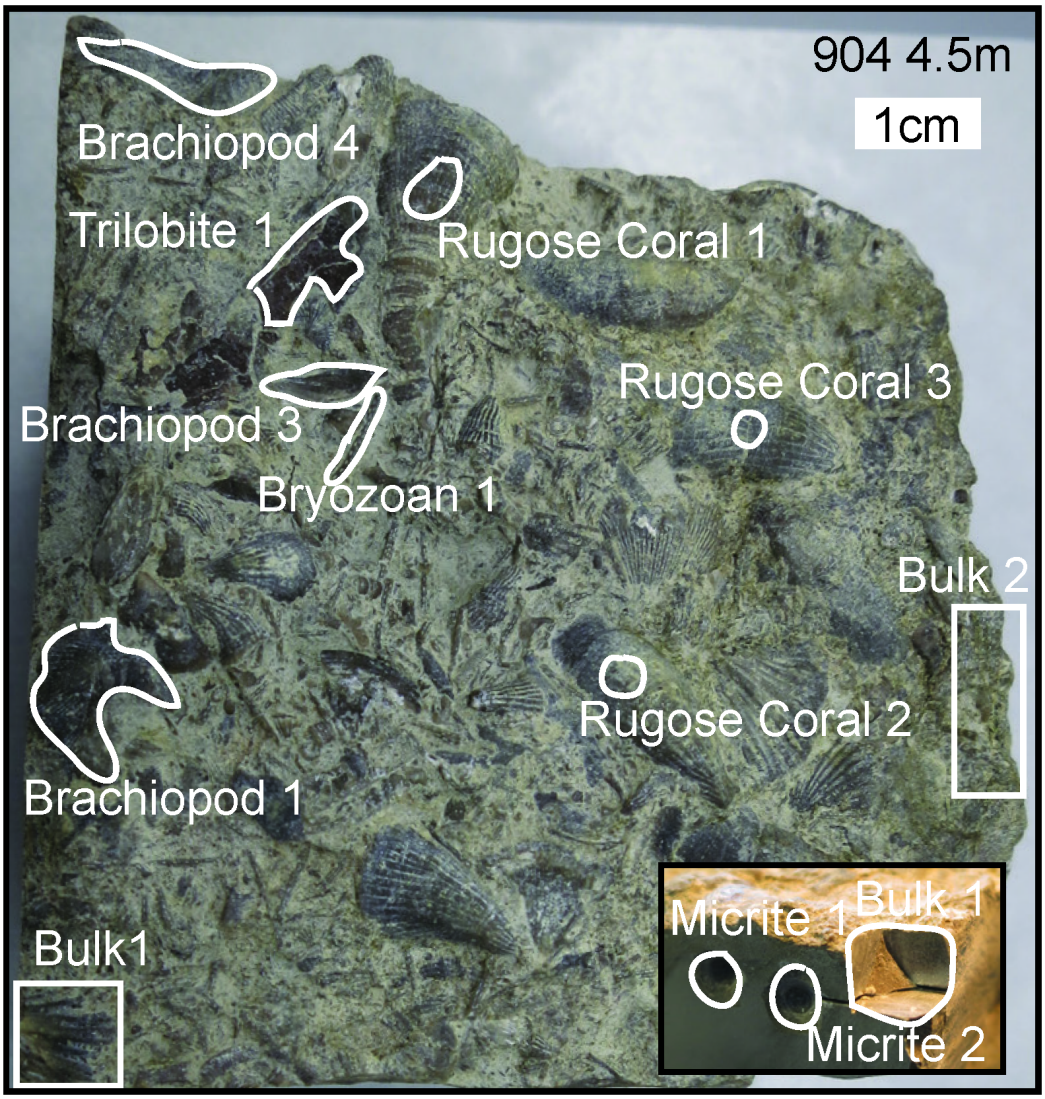

Figure 3: Sample 904-4.5m with the location of analyzed CAS specimens drilled, cut, or picked from a skeletal packstone horizon. Analyzed specimens from the other six hand-samples are shown in Supplemental Figure 1.

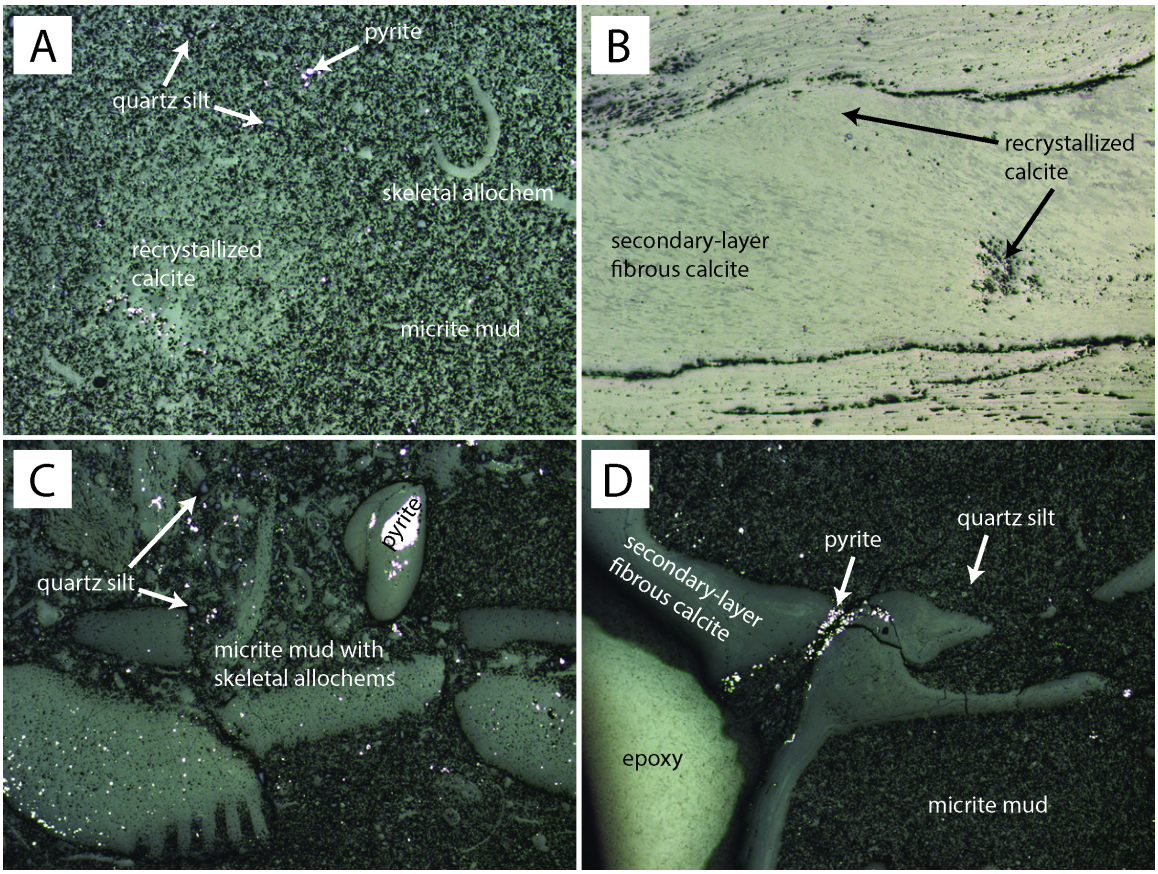

Figure 4: Plane polarized reflected light images of polished thick sections. Width of field of view is about 2.4 mm. (A) Sample 904-2.5 m, calcimudstone with minor quartz silt (purple-gray), disseminated pyrite (bright yellow/white) and a skeletal fragment. (B) Fibrous calcite from the secondary layer of specimen Brachiopod 1 from Sample 904-2.5 m. The beige and gray banding is bireflectance of ~50 μm-long calcite fibers, indicative of well-preserved biogenic low-magnesium calcite. Note that some regions can still be recrystallized. (C) A particularly allochem-rich horizon in Sample 904-4 m with minor quartz silt and disseminated pyrite. Some skeletal grains are partially pyritized. (D) The cardinal process (the junction of the two valves) of specimen Brachiopod 3 from Sample 904-4 m with well-preserved fibrous calcite. Disseminated pyrite, possibly framboidal, is localized between the brachiopod valves.

Methods

Hand-samples were ultrasonicated in tap water followed by deionized water for 4 hours each, and dried in a ~75°C oven. We prepared bulk-rock powders by homogenizing ~1 cm^3 of limestone with a mortar and pestle. Micrite, rugose coral, and tabulate coral specimens were milled with a 1 mm drill bit. Using a dental pick beneath a dissecting microscope, we picked 5-10 mg specimens of all other sedimentary components. Flakes of these components (but not the milled components) were inspected under higher magnification to avoid matrix

material, pyrite, or oxide inclusions (Cummins et al., 2014). Brachiopod specimens were inspected to include only optically transparent secondary-layer fibrous calcite (with the exception of one recrystallized small specimen in sample 901-HCS, which we analyzed nonetheless). For some brachiopod specimens, scanning electron microscope images were obtained at the Caltech Geological and Planetary Sciences Division Analytical Facility (ZEISS 1550VP Field Emission SEM using a 15kV accelerating voltage and 8 mm working distance) to examine the extent of recrystallization and ensure there were no microscopic sulfide or oxide inclusions (Figure 5 and Supplemental Figure 2). Such inclusions were never observed in any specimen under the dissecting microscope or in the electron micrographs.

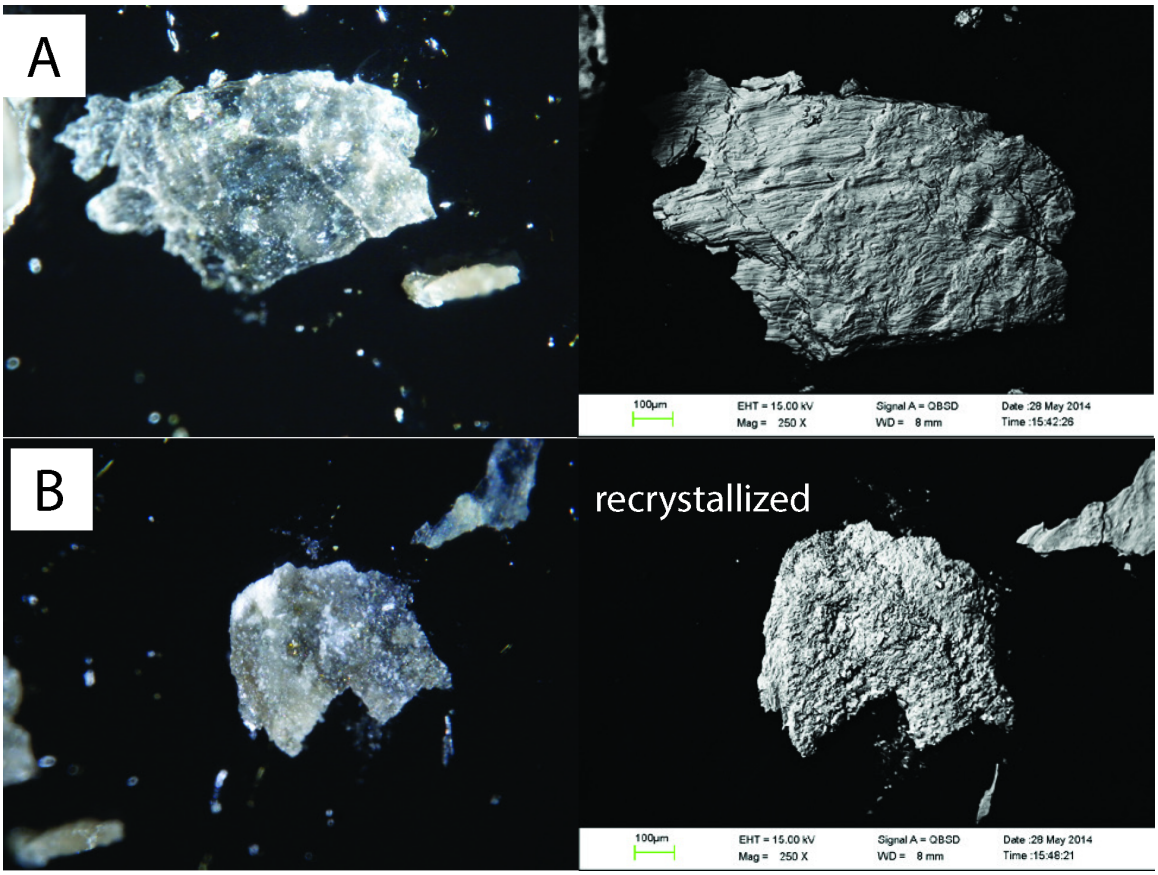

Figure 5: Binocular microscope (left) and electron microscope backscatter intensity (right) images of two representative flakes picked from Brachiopod 1 from Sample 904-2.5m. Metal oxides or sulfides would show up as extremely bright spots in the electron microscope images. (A) A well preserved flake. The lineations are fibers of well-preserved secondary layer calcite; the best-preserved secondary layer fibrous calcite is optically clear. (B) A poorly-preserved flake excluded from analysis. When diagenetically altered, the fibrous calcite recrystallizes to fine equant grains and often turns yellow-brown. More examples of representative flakes that were included in specimens for CAS analyses are shown in Supplemental Figure 2.

To accurately measure trace sulfate in such small specimens (less than 255 nmol, typically 30-50 nmol sulfate), we minimized and tracked procedural blanks (i.e., contamination by sulfate from the laboratory, on the order of 0.3 nmol). After picking, specimens were handled in laminar flow benches in acid-cleaned vials and introduced only to 18.2 MΩ-cm water (Millipore Milli-Q) or trace-metal pure reagents (Seastar Baseline).

Specimens were pre-cleaned prior to dissolution by ultrasonicating for >4 hr in 1 mL 10% (w/w) NaCl solution and rinsing three times in 1 mL water, centrifuging and removing the

supernatant between each rinse. In a clean vial, specimens were dissolved in 500 μL 0.5 N HCl for 4-12 hours while agitated on a shaker table, and then centrifuged. The supernatant was aliquoted for sulfate concentration analysis and sulfur isotopic composition analysis. Sulfate concentrations are reported in parts-per-million (ppm) by mass and exclude the weight of insoluble residue. This is equivalent to micrograms of sulfate per gram of acid-soluble rock, which we assume is calcite.

To ensure that our pre-cleaning or dissolution protocol does not influence the sulfur-bearing phases extracted from the specimen, we tested different protocols on multiple powder aliquots from bulk-rock samples. For some aliquots, we neglected the NaCl leach steps. For others, we added an oxidative leach step after the NaCl rinse step. Oxidative leaching involved ultrasonicating in 1 mL of a 1:1 solution of 2 M NaOH and 30% H_2O_2 for 10 min and then in methanol for 10 min, and centrifuging and removing supernatant between steps. This was done three times before completing pre-cleaning with three water rinses as with other powders. To extract total sulfur as sulfate, some of these powder aliquots were dissolved for 4 hours in *aqua regia* (3:1 concentrated HCl and HNO_3).

A specific concern is potential oxidation, by oxygen or ferrous iron, of reduced sulfur during dissolution. We tested our CAS extraction protocol on 10 mg mixtures of powdered deep-sea coral (*Desmophyllum dianthus* SS0108-STA011 collected in January 2008 off Tasmania) and pyrite "CIT-12021" (Huanazala Mine, Caltech Mineralogy Collection). The coral samples came from two halves of one skeleton initially covered with an iron-manganese-oxide crust. The first half was ground with a mortar and pestle and sieved to 63-250 μm, with the crust, to mimic the presence of iron oxides in ancient limestones. The crust was abraded from the second half, which was then ground, treated for 11 hours in a 1:1 mixture of 2 M NaOH and 30% H_2O_2, rinsed four times with water, dried, and sieved. The $\delta^{34}S$ composition of the pyrite is 1.08±0.35‰ (1 s.e., n=8), determined by combustion in a Costech elemental analyzer with a Thermo Delta-S isotope ratio mass spectrometer (IRMS). The coral and coral/pyrite mixtures were then pre-cleaned following the NaCl and water rinse

protocol and dissolved for 4 hours in 0.5N HCl. Another chunk from the abraded coral half was rinsed four times in water, dried, sieved, and dissolved in 10% $HClO_4$ without any pyrite.

To investigate vital effects in the modern brachiopod, we cut the sample into four subsamples with a razor. The specimens were pre-cleaned with the NaCl and water rinse protocol. We released CAS with 0.5N HCl from two specimens, and released total sulfur with *aqua regia* from the others. We expect the *aqua regia* digestion to release organically coordinated sulfur and inform any difference between CAS and organic sulfur.

We are able to analyze such small amounts of sample powder (5-10 mg of limestone) with a new analytical technique that requires ~5 nmol of sulfate (Paris et al., 2013), which is about three orders of magnitude less sample than traditional IRMS techniques. We determined sulfate concentrations by ion chromatography (Dionex ICS-2000, using an AS-19 column and 20 mM KOH eluent at the Caltech Environmental Analysis Center). We used anion exchange chromatography to purify sulfate from the remaining dissolved carbonate (Paris et al., 2014a) to analyze in duplicate as aqueous sodium sulfate by MC-ICP-MS on a Thermo Scientific Neptune Plus at Caltech (described previously by Paris et al., 2013). Specimens were prepared and analyzed in sets of 12-16, and always along with 2-4 procedural blanks, 2 replicates of an in-house dissolved deep-sea coral consistency standard, and 2 replicates of seawater.

The long-term $\delta^{34}S$ reproducibility of ~18 nmol sulfate replicates from the coral consistency standard is 0.35‰ (1s.d., excluding one >5s.d. outlier) and is 0.13‰ (1 s.d., excluding one >8 s.d. outlier) for ~280 nmol sulfate replicates of seawater. The precision of isotope measurements reported here is a combination of instrument stability, short-term reproducibility of the same sulfate solution, and variability of the procedural blank composition and amount. Procedural blanks were 0.32±0.24 nmol (1 s.d.) sulfate with an isotopic composition of $\delta^{34}S$=2.6±0.49‰ V-CDT. Blank correcting specimens typically increased their isotopic composition by 0.1 to 0.3‰. Reproducibility of sulfate concentration

measurements is typically 3-5% (1 relative s.d.), based on reproducibility of diluted seawater and dissolved coral triplicates run alongside specimens in each analytical session.

We determined the carbonate carbon and oxygen isotopic composition of samples that had remaining flakes or powder after CAS extraction. Approximately 100-250 μg of the sample were accurately weighed into 10 mL glass vials, flushed with helium, dissolved for 1 hour at 75°C in ~200 μL concentrated H_3PO_4, and analyzed with a Thermo Gasbench autosampler and Thermo Delta V IRMS. Reproducibility of two in-house carbonate reference standards is better than 0.06‰ (1σ s.e.) for $\delta^{13}C$ and 0.23‰ (1σ s.e.) for $\delta^{18}O$. Carbon and oxygen isotopic compositions are reported relative to the Vienna Pee Dee Belemnite (V-PDB) carbonate reference.

Results

The modern brachiopod we analyzed has an average CAS concentration of 4214±453 ppm (1s.d.), and isotopic composition of 20.57±0.05‰ (1s.d.) (Figure 6, Supplemental Table 1). There is no isotopic difference between the extracted CAS and the total sulfur extracted with *aqua regia*.

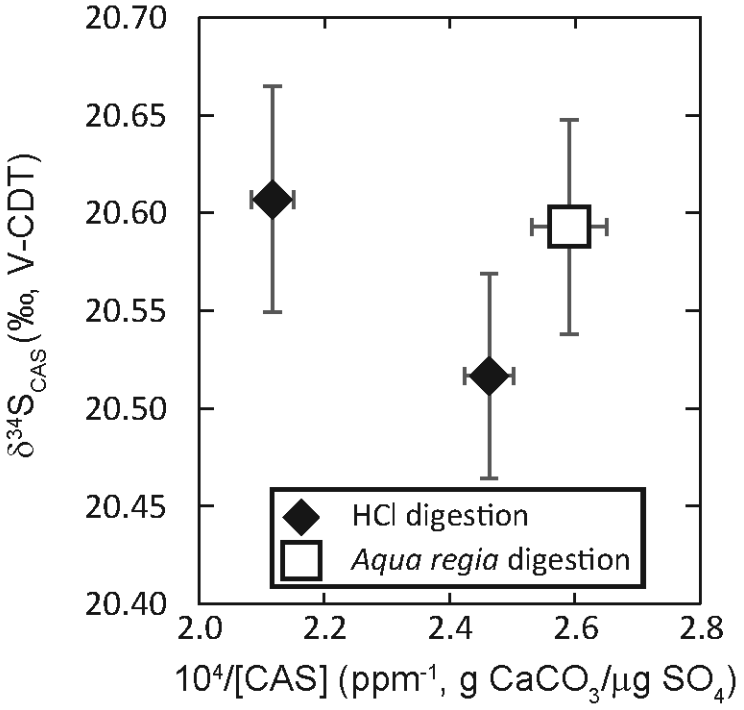

Figure 6: Composition of sulfate extracted by 0.5N HCl and aqua regia from a single valve of the modern brachiopod T. transversa collected in southern California. For reference, modern seawater sulfate is 21.15±0.15‰ (Johnston et al., 2014).

Results of pre-cleaning protocol tests are presented in Figure 7 and tabulated in Supplemental Table 1. Aliquots from a bulk-rock powder from sample 901-HCS, with any pre-cleaning protocol, vary between 11‰ and 21‰ (Figure 7A). Generally, sulfate extracted from aliquots exposed to the oxidative leach is isotopically lighter than specimens exposed to only the NaCl leach or only the water rinsing, and is less concentrated. This would be consistent with pre-cleaning removing a ^{34}S-enriched phase. However, we had poorly homogenized the bulk-rock powder by mortar and pestle (Figure 7B), so we repeated the pre-cleaning experiment with sample 904-4. In this case, the bulk-rock specimen was carefully homogenized (Figure 7D). Aliquots of sample 904-4, with any pre-cleaning protocol, showed less isotopic variability (between 28‰ and 31‰, Figure 7C) than aliquots of sample 901-HCS. In both samples, the total variability among bulk-rock aliquots with any pre-

cleaning protocol is less than the variability between sedimentary components treated with the same (NaCl leach and water rinses only) pre-cleaning protocol.

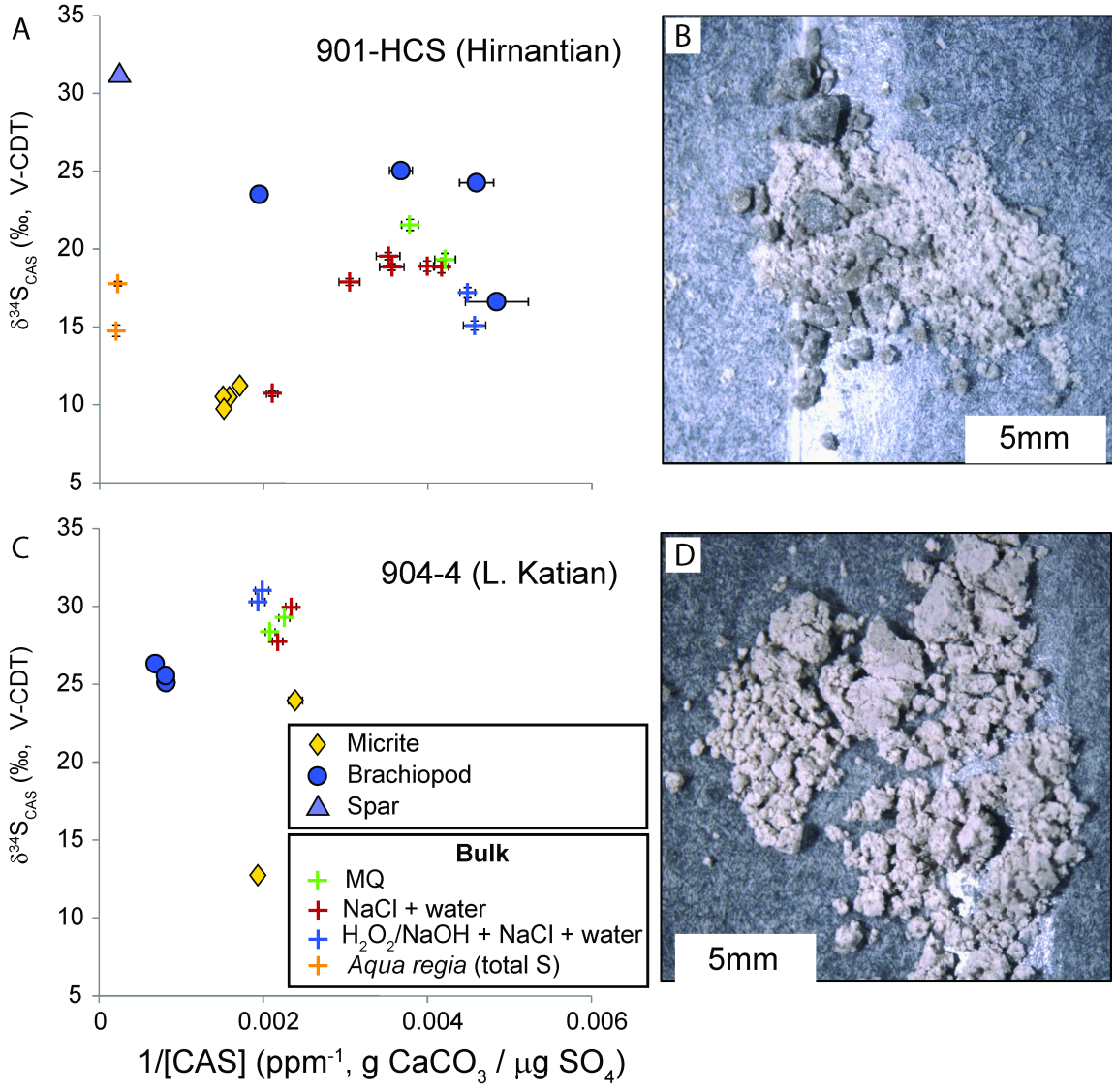

Figure 7: Plots of isotopic composition against inverse concentration for cleaning tests performed on two bulk-rock samples (plusses) and the associated texture-specific specimens (filled symbols). Colors of the bulk-rock data correspond to the extraction pre-cleaning and digestion protocol. (A) Isotopic composition and concentration of extracted sulfate from hand-sample 901-HCS. (B) Poorly homogenized sample powder from hand-sample 901-HCS. (C) Isotopic composition and concentration of extracted sulfate from hand-sample 904-4m. (D) Well homogenized sample powder from hand-sample 904-4m lacks the large dark gray chunks visible in panel B.

Results of the coral and pyrite dissolution experiments, using the NaCl and water pre-cleaning protocol, are presented in Figure 8 and tabulated in Supplemental Table 2. The coral without any iron-manganese oxide crust has a CAS concentration of 4923±456 ppm (1 s.d.) and a $\delta^{34}S$ of 22.38±0.56‰ (1 s.d.). The coral with the iron-manganese oxide crust has a CAS concentration of 3950±554 ppm (1 s.d.) and a $\delta^{34}S$ of 22.39±0.11‰ (1 s.d.). These values are consistent with the range of deep-sea coral measurements analyzed with other cleaning and dissolution protocols (gray box in Figure 8, data in Supplemental Table 3). All coral/pyrite mixtures (i.e., both with and without ferrous iron) except one had indistinguishable sulfate concentrations and compositions from this range.

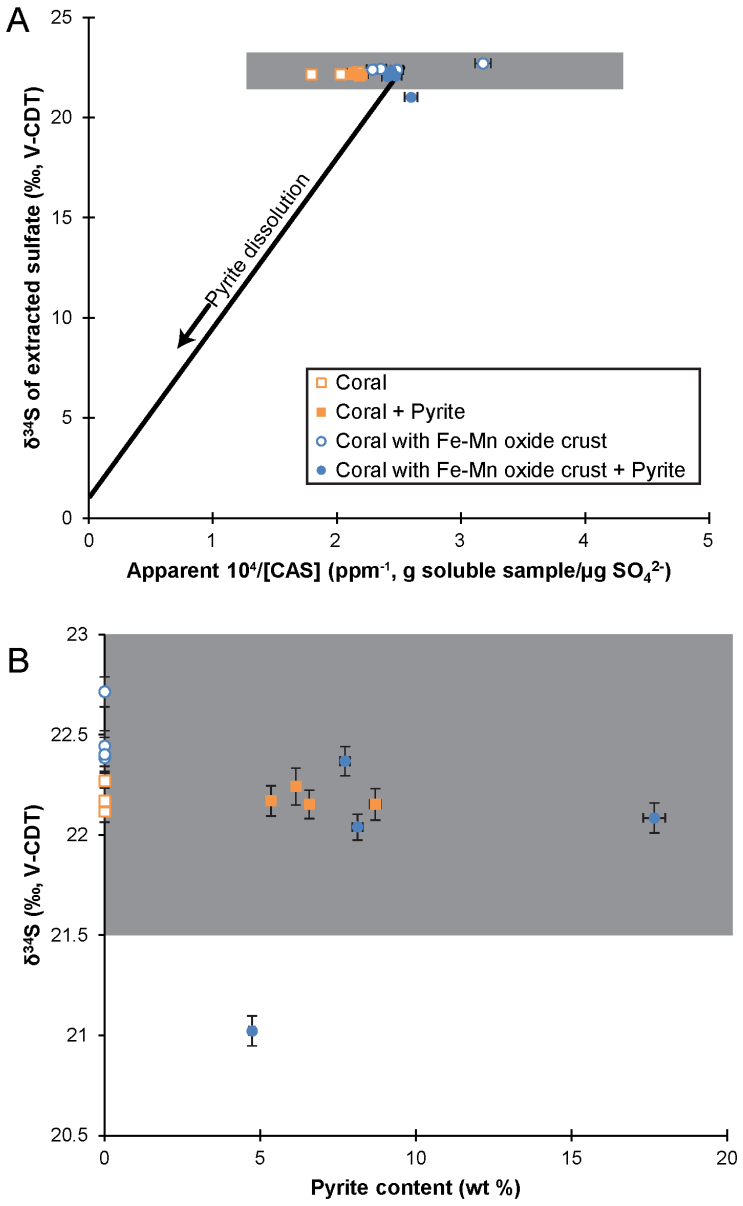

Figure 8: Apparent CAS compositions from deep-sea coral specimens intentionally mixed with pyrite, plotted with 1σ standard error bars. (A) Apparent CAS isotopic composition plotted against inverse apparent CAS concentration. The gray field is the total range of CAS concentrations and isotopic compositions determined from the same coral polyp, but with different cleaning and dissolution protocols (see Supplemental Table 3). The black vector represents the expected trend from mixing pure pyrite with the average coral composition. (B) Apparent CAS isotopic composition plotted as a function of the amount of pyrite added to the samples. The gray field is the total range of coral CAS isotopic compositions as in panel A.

The CAS $\delta^{34}S$ and concentration for all Ordovician-Silurian specimens is extremely heterogeneous, spanning 9 to 34‰ and 79 to 3331 ppm. Values are plotted in Figure 9, and tabulated in Supplemental Table 1. Plots of isotopic composition against inverse concentration provide a natural space to examine possible mixing relationships between different textures. In this plot, binary mixtures would fall on a straight line.

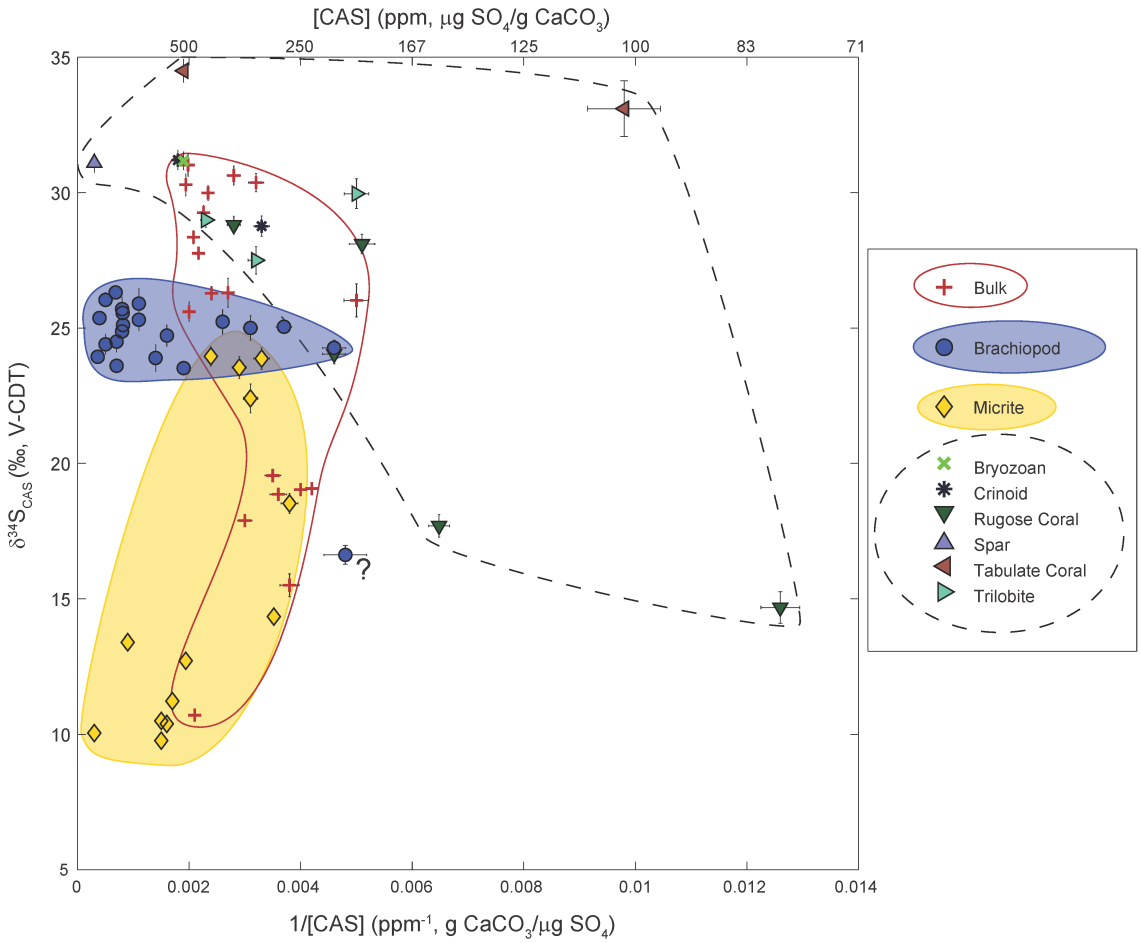

Figure 9: Cross-plot of CAS isotopic composition and inverse concentration with 1σ standard errors for all Anticosti Island specimens analyzed in this study and pre-cleaned by the NaCl + water rinsing method. The question mark notes the outlying, poorly preserved brachiopod specimen from sample 901-HCS.

Discussion

The total sulfur isotopic range of CAS we analyzed from different petrographic textures in Anticosti Island limestones is 25‰. This is nearly as large as the observed range in all Phanerozoic CAS data, which typically varies between about 10‰ and 40‰ (Kampschulte and Strauss, 2004; Wu et al., 2014). We first assess if artifacts during CAS extraction can explain this variability, and then discuss the geological implications of this data.

Extraction of CAS

Significant effort has gone into optimizing CAS extraction procedures and this is summarized in detail by Wotte et al. (2012a). They concluded that oxidative leaching steps tend to contaminate CAS by partially oxidizing reduced sulfur phases. Pyrite oxidation would add sulfate to the CAS liberated during dissolution, and cause an increase in sulfate concentration and corresponding change in sulfate isotopic composition (Marenco et al., 2008a; Mazumdar et al., 2008). Point Laframboise has pyrite with sulfur isotopic compositions between -21 and 6‰ (Jones and Fike, 2013), so if pyrite oxidation occurred, we would expect it to add ^{34}S-depleted sulfate to the analyte solution.

Micrite and bulk-rock specimens contain disseminated pyrite that could not be physically segregated from carbonate components. The results of our pre-cleaning protocol tests (Figure 7) imply the high variability of bulk-rock extractable sulfate cannot be fully explained by procedural contamination of CAS with different sulfur-bearing phases. Pyrite-bearing micrite and bulk-rock samples treated with an oxidative leaching step should be vulnerable to CAS contamination (Wotte et al., 2012a), but the isotopic variation of these samples is still smaller than that observed between picked carbonate components. Therefore, the Anticosti Island CAS variability is best explained by variation in the relative abundance of carbonate components of the rocks with different CAS compositions.

Further, the results of our pyrite dissolution tests (Figure 8) indicate that negligible amounts of pyrite oxidation contributed to the sulfur isolated by our pre-cleaning and CAS extraction protocol. With the exception of one sample, all of the CAS variability in the pyrite/coral mixtures can be explained by the primary range of CAS in the coral without any pyrite (gray field in Figure 8A). This remains true for the coral samples with iron-manganese oxide crusts, which liberate abundant ferric iron and high valent manganese as potential pyrite oxidants during dissolution. The δ^{34}S of the single outlying point (a coral with its iron-manganese crust and 4.7 wt. % pyrite) is about 1‰ lighter than the average sulfur isotopic composition of the coral. However, this point does not fall on the expected vector of increasing CAS concentration and decreasing isotopic composition for pyrite dissolution (black line in Figure 8A). Additionally, samples with higher pyrite content would be

expected to experience more pyrite contamination, but there is no relationship between apparent extracted sulfate isotopic composition and pyrite content (Figure 8B). Thus, we conclude that our CAS pre-cleaning and extraction protocol does not contribute measurable amounts of pyrite-derived sulfate to the primary CAS.

In summary, sample pre-cleaning tests (Figure 7) indicate that the CAS variability in our Ordovician-Silurian samples cannot be explained by contamination by non-CAS sulfur bearing phases, and our pyrite dissolution tests (Figure 8) confirm that our extraction protocol leads to negligible oxidation of pyrite. Regardless of the pre-cleaning technique employed, a key strength of this method is the ability to microscopically screen samples for the presence of possible contaminating phases such as pyrite before dissolution (Figure 5 and Supplemental Figure 2).

Brachiopod fibrous calcite CAS preserves seawater composition

We confirmed that modern brachiopod CAS is close to the isotopic composition of modern seawater sulfate (Figure 6), which is 21.15±0.15‰ (Johnston et al., 2014). The slight ^{34}S-depletion of modern biogenic CAS relative to seawater is comparable to other calcifying organisms that can vary from seawater by up to 2‰ (Burdett et al., 1989; Kampschulte et al., 2001; Paris et al., 2013, 2014b).

Brachiopod calcite likely preserves primary geochemical signatures over geologic time scales because it is composed of relatively large and thermodynamically-stable LMC crystals (Popp, 1986). In addition, recrystallization, when it occurs, is petrographically obvious (Popp, 1986). Carefully screened brachiopods offer demonstrably the best proxy archives for many geochemical records, such as seawater carbon, oxygen, and strontium isotopic compositions (Al-Aasm and Veizer, 1982; Cummins et al., 2014; Finnegan et al., 2011; Grossman et al., 1993). Popp (1986) reported the first sulfate-sulfur isotope measurements from 3-5 g of Permo-Carboniferous brachiopods. Kampschulte et al. (2001) extended this Carboniferous brachiopod CAS record, and also compared CAS data from biogenic calcite to that obtained from bulk-rock samples; they observed only about 2‰ difference between brachiopods and bulk-rock data. This record of biogenic calcite was expanded to the

Phanerozoic-scale by Kampschulte and Strauss (2004) and Wu et al. (2014), but its resolution was limited by the availability of large (>1 g), well-preserved brachiopods or samples comprised of multiple brachiopods.

Indeed, brachiopod calcite from Anticosti Island appears to provide a robust archive for the sulfur isotopic composition of Ordovician-Silurian seawater sulfate. For this study, we microscopically isolated flakes of brachiopod fibrous calcite to avoid small sulfide or iron-bearing inclusions (Figure 5 and Supplemental Figure 2) (i.e., phases that might contaminate CAS). The brachiopod specimens where we isolated enough calcite to also determine the carbonate carbon and oxygen isotopic composition were consistent with chemostratigraphic data published by Jones et al. (2011). The brachiopod calcite specimens show the least CAS sulfur isotopic variability of all observed phases (24‰ to 26‰, except for the outlier in sample 901-HCS, Figure 9). One outlier specimen (marked by a question mark in Figure 9) was the smallest analyzed (with the least amount of sulfate recovered, less than 10 nmol), and had poor textural preservation. We analyzed two additional brachiopod specimens from the same hand-sample to confirm that their CAS isotopic compositions fell within the same range as all other brachiopods specimens. From the brachiopod suite, we estimate end-Ordovician and early Silurian seawater sulfate had a sulfur isotopic composition of 24.86±0.40‰ (2 s.e. n=18, excluding the outlier). The stability of the brachiopods' CAS isotopic composition (Figure 10) implies that seawater sulfate did not significantly vary across the Hirnantian glaciation or Ordovician/Silurian boundary, consistent with the conclusions of Jones and Fike (2013).

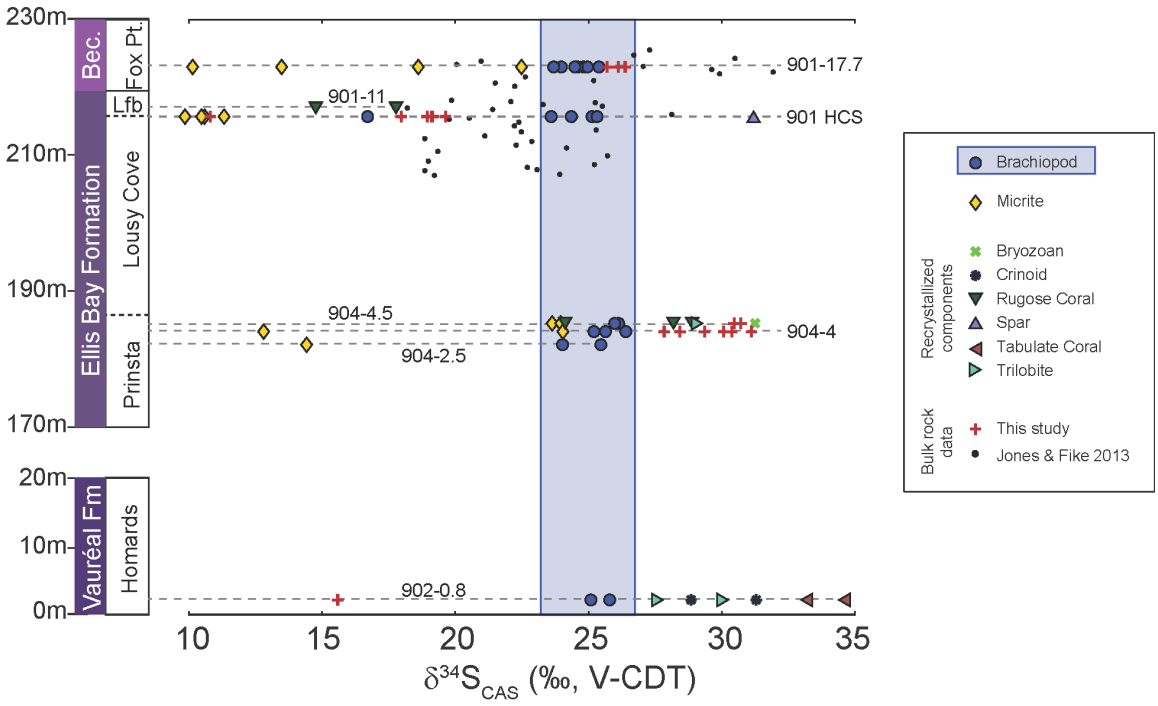

Figure 10: Sulfur isotopic compositions of CAS specimens arranged by stratigraphic height. Colored symbols are data from this study, and small black dots are bulk-rock data from Jones and Fike (2013). The blue field demarcates the range of brachiopod CAS (excluding the small, recrystallized outlier discussed in the text), which does not vary through the succession. Gray dashed lines connect specimens from the same hand-sample. Bec. = Becscie Formation, Lfb. = Laframboise, Pt. = Point.

Patterns of CAS isotopic variability in other phases

There is large $\delta^{34}S$ variability in phases other than the well-preserved brachiopods. CAS composition is different between the various components of our samples and is related to petrographic texture. Micrite powders are extremely variable (10‰ to 25‰) and are consistently isotopically lighter than co-occurring brachiopods (Figure 9, Figure 10). All other components are generally isotopically heavier than brachiopods, and have variable and visible amounts of recrystallization. In aggregate, our texture-specific data can explain the variable composition of homogenized bulk-rock samples (red plusses in Figure 9) as a physical mixture of different sedimentary components.

Even within each of our analyzed hand-samples there is large heterogeneity in the CAS isotopic composition (Figure 10). For example, we observed a range of as much as 21‰

within Sample 901-HCS (Figure 10). In addition, all of the hand-samples are collected from the same distal carbonate ramp facies from the western sector of Anticosti Island, so the variability is not explained by spatial heterogeneity or temporal changes of seawater sulfate. Our observed variability among all measured specimens is larger than the 13‰ range of bulk-rock CAS analyzed from the same stratigraphic sections by Jones and Fike (2013) (black dots in Figure 10). Those authors suggested that the bulk-rock CAS variability did not reflect rapid change in the isotopic composition of Ordovician/Silurian seawater sulfate, which they argued remained nearly constant (as confirmed by our brachiopod data) over the duration of the record (less than 1.5 Myr as allowed by biostratigraphic constraints).

These observations are consistent with the hypothesis that CAS variability on Anticosti Island reflects post-depositional processes. Micrite is commonly targeted for CAS studies and often interpreted to represent lime mud (e.g. Gill et al., 2011b; Wotte et al., 2012b). We deliberately selected hand-samples with heterogeneous sedimentary components, but high variability is also observed among micrite subsamples within a hand-sample. Micrite can be formed by multiple processes that are not easily distinguishable by rock texture (Flugel and Munnecke, 2010). It can be allochthonous (allomicrite) or authigenic (automicrite), precipitate from biological or inorganic processes, form in either seawater or evolved pore fluids, or be the result of physical erosion or biologic boring of larger allochems (Flugel and Munnecke, 2010). Micrite must then lithify by addition of carbonate cements and/or recrystallization, processes that can closely associate carbonate components precipitated from different solutions (Lyons et al., 2004; Rennie and Turchyn, 2014). Our micrite samples are fine-grained carbonate matrix material with variable amounts of skeletal fragment allochems (Figure 4). We observed up to 15‰ variation between micrite powders milled only a few centimeters apart (yellow diamonds in Figure 10). Like the bulk-rock data, the CAS variability of Anticosti Island micrites is likely a consequence of secondary processes.

Diagenetic insights from CAS variability

By accepting well-preserved brachiopod secondary-layer fibrous calcite CAS as a reliable proxy for seawater sulfate, we can explore the information content of CAS in the other

components. Our dataset has two populations around the brachiopods: micrite specimens that are ^{34}S-depleted, and recrystallized specimens that are highly variable and generally ^{34}S-enriched (Figure 9). Processes likely to diagenetically alter sulfate isotopic composition from seawater are sulfide oxidation and MSR.

Previous workers have examined the potential for non-seawater sulfate sources in CAS. Two important studies suggested that the isotopic composition of CAS can be resistant to diagenetic alteration. Lyons et al. (2004) showed that the isotopic composition of bulk-sediment CAS remained unchanged in a carbonate mud sediment core with both carbonate precipitation and sulfate reduction. Secondly, Gill et al. (2008) showed that CAS δ^{34}S in a recent aragonitic head coral remains unchanged by aragonite neomorphism during meteoric diagenesis. However, those authors noted that these settings lack the leverage to substantially alter CAS. In the first case, diagenetically-precipitated carbonate represented a small portion of the total sediment mass relative to primary carbonate. In the second case, meteoric fluids have very little sulfate. Contrastingly, other researchers have identified diagenetic alteration of CAS. Rennie and Turchyn (2014) demonstrated that CAS in late Cenozoic nanofossil ooze bulk sediment may be ^{34}S-enriched relative to seawater if carbonate cementation is slower than enrichment of pore fluid sulfate by MSR, but only by up to about 4‰ under those relative sedimentary fluxes. On longer timescales, Marenco et al. (2008b) argued that dolomitization incorporates ^{34}S-depleted sulfate—by up to about 10‰— into CAS. Loyd et al. (2012a) looked specifically at diagenetic carbonate concretions forming from pore fluids where sulfate reduction was prominent, and observed large enrichment (up to 15‰) relative to seawater. However, these studies have not observed the range of values (24.7‰) measured in the limestones preserved on Anticosti Island, which includes both large ^{34}S-enrichments and depletions relative to the inferred isotopic composition of seawater.

Micrite powders from Anticosti Island lie on an array of increasing CAS concentration and decreasing isotopic composition (yellow ellipse in Figure 9). Such a trend is predicted by oxidation of pyrite during CAS extraction (Marenco et al., 2008a; Mazumdar et al., 2008), but as discussed above from experimental results, we think this type of contamination was

negligible in our procedure. Instead, natural sulfide oxidation sometime in the rocks' histories, followed by precipitation of more carbonate to incorporate the CAS, may explain the diagenetic array. This could have occurred before lithification, and pore fluid aqueous sulfide oxidation could have been microbially mediated. Later stabilization, cementation, and lithification of the micrite could have incorporated variable amounts of this recycled sulfur.

Alternatively, fluids carrying ^{34}S-depleted sulfate could have migrated from a separate locus of pyrite oxidation to the lithifying or recrystallizing micrites, and effected other geochemical changes (e.g. dolomitizing fluids in Marenco et al., 2008b). Of all of the micrite samples we analyzed, the lightest CAS sulfur isotopic composition came from Sample 901-HCS, which is the only dolomite-containing wackestone in our sample suite (Figure 10). Previously-collected clumped isotope data from Anticosti Island provide further evidence that micrite diagenesis proceeded in an open system with respect to fluid-rock interactions (Finnegan et al., 2011).

A third option is that sulfide oxidation could have occurred during modern surficial weathering or sea level lows younger than the rock, when corrosive meteoric fluids could mobilize sulfur derived from pyrite. Weathering of pyrite would produce insoluble iron oxides (such as goethite or hematite) and aqueous sulfate, and the latter could be incorporated into recrystallizing carbonate minerals. Some micrite samples showed petrographic evidence for iron oxides. Also, rock magnetic data shows evidence for a low-temperature (<100°C) thermally-decomposed component oriented parallel to the modern magnetic field (Seguin and Petryk, 1986). Seguin and Petryk (1986)report demagnetizing about 200 mA/m of this component, which is probably goethite. Assuming it is all goethite (density of ~4.3 g/cm^3 and saturation magnetism of ~2 emu/cm^3), then the rocks (~2.7 g/cm^3) have about 200ppmv goethite. For our 10 mg rock specimens, this corresponds to about 35 nmol of iron. If all of the iron is from weathered pyrite in a closed system, then potentially 70 nmol of weathered and oxidized sulfide could have contaminated the CAS. Most micrite specimens were about 70% carbonate, corresponding to potentially ~1000 ppm "weathered" sulfate contamination.

Thus, micrites from hand-sample 901-HCS, for example, could include up to about 65% weathered sulfide incorporated as CAS. However, meteoric dissolution of pyrite would also be corrosive to carbonate, and not conducive to incorporation into micrite CAS. Thus, we hypothesize that Anticosti Island micrite CAS records active microbial sulfide oxidization in the Ordovician-Silurian-age shelf sediments.

The CAS composition of calcite spar and recrystallized coral, trilobite, crinoid, and bryozoan fossils varies widely (field enclosed by dashed line in Figure 9). Most are ^{34}S-enriched with respect to the brachiopods, and likely incorporated ^{34}S-enriched sulfate that was the residual of MSR. The most recrystallized fossil was a tabulate coral (Sample 902-0.8, Supplemental Table 1), which also had the heaviest CAS composition (33 to 34‰). These recrystallized fossils were likely precipitated as high-magnesium calcite and susceptible to stabilization to LMC (Wilkinson, 1979). Specimens from Anticosti Island recrystallized late in the burial diagenesis process at clumped-isotope temperatures over 50°C, coinciding with enrichments of iron and manganese and depletion of strontium indicative of meteoric groundwater (Finnegan et al., 2011). Explaining the ^{34}S-enriched CAS in recrystallized phases requires an aquifer where water is significantly ^{34}S-enriched by MSR and sulfate-rich enough for this modified groundwater sulfate to be incorporated into CAS. Dogramaci et al. (2001) describe a potential modern analog in the western Murray Basin, Australia where sulfate in a deep, confined aquifer has an isotopic composition between 20‰ and 60‰ and is from a mixture of marine and freshwater. The highly heterogeneous CAS in recrystallized specimens from Anticosti Island may record calcite stabilization in a similar heterogeneous and sulfate-bearing aquifer.

Conclusions

With a new MC-ICP-MS analytical technique for sulfate, we demonstrated that the CAS of common petrographic textures can be highly heterogeneous on small spatial scales in well-preserved marine limestones from late Ordovician and early Silurian-age strata on Anticosti Island. This heterogeneity does not reflect spatial or temporal variability in aqueous marine sulfate. Instead, it records part of the diagenetic history of the samples. Because our

analytical technique can be applied to small samples, it allows for the careful selection of samples well-suited as archives of seawater sulfate. Well-preserved brachiopod fibrous calcite could be successfully isolated from other CAS-bearing phases and pyrite, and provides a reliable archive.

Our Anticosti Island brachiopod data provide a record of marine sulfate maintaining a $\delta^{34}S$ composition of 24.86±0.40‰ (2 s.e.) through the Ordovician-Silurian boundary interval. This confirms that despite substantial changes in biogeochemical cycling and climate through the Hirnantian, no excursion occurred in the isotopic composition of seawater sulfate, consistent with the conclusions of Jones and Fike (2013). Given the constancy of marine sulfate's isotopic composition, CAS sulfur isotopes from micrite and other components demonstrate the importance of secondary processes and vary by nearly the total range of secular variation observed over the Phanerozoic Eon. On Anticosti Island, the CAS in micrite is ^{34}S-depleted relative to contemporaneous seawater, and may be explained by sulfide oxidation in pore fluids during early diagenesis, or incorporation of ^{34}S-depleted sulfate-rich dolomitizing fluids. The CAS in components recrystallized during burial diagenesis is characterized by $\delta^{34}S$ values higher than contemporaneous seawater, and requires active sulfate reduction in Anticosti Island groundwater.

More generally, our data suggest that scatter in Phanerozoic bulk-rock CAS records (e.g. those shown in Figure) does not unambiguously record primary seawater sulfate chemistry, and could reflect later incorporation of sulfate modified by early diagenetic and recrystallization processes. Analyzing well-preserved specimens allows for a more precise and accurate record of seawater sulfate than numerically smoothing noisy datasets— there is no guarantee that variation in a dataset is symmetrical about the value of seawater during the time of deposition. In addition, once primary changes in seawater sulfate composition are better constrained, the remaining variation in CAS records can provide additional information about secondary local biogeochemical processes during lithification and burial. Large $\delta^{34}S$ variability in coexisting carbonate components— including in calcimudstone and wackestone samples commonly called micrite and analyzed in CAS records of all ages—

may be indicative of unique diagenetic regimes. Fluxes associated with pore fluid sulfide oxidation and groundwater sulfate reduction are poorly constrained in modern sediments and aquifers, but may be important biogeochemical processes in Earth's history. Overall, new approaches analyzing CAS in smaller, carefully characterized samples will improve the accuracy and precision of the marine sulfate record.

Acknowledgements

Funding for this work was provided by the American Chemical Society Petroleum Research Fund New Directions grant #53994-ND2, NSF Division of Earth Sciences award EAR-1349858, and the Agouron Institute. We thank David Jones and Benjamin Gill for thoughtful reviews. We thank David Fike and Seth Finnegan for helpful input and field context for the Anticosti Island specimens. We thank Renata Cummins for instruction on how to prepare brachiopod secondary-layer fibrous calcite, and Lindsey Hedges, Fenfang Wu, and Nathan Dalleska for analytical support. We thank Joe Kirschvink for help interpreting rock magnetic data. Thank you to Kristin Bergmann for providing the *T. transversa* specimen, and Nivedita Thiagarajan for help preparing deep-sea coral samples. Ion chromatography was done at the Caltech Environmental Analysis Center.

Supplemental figures

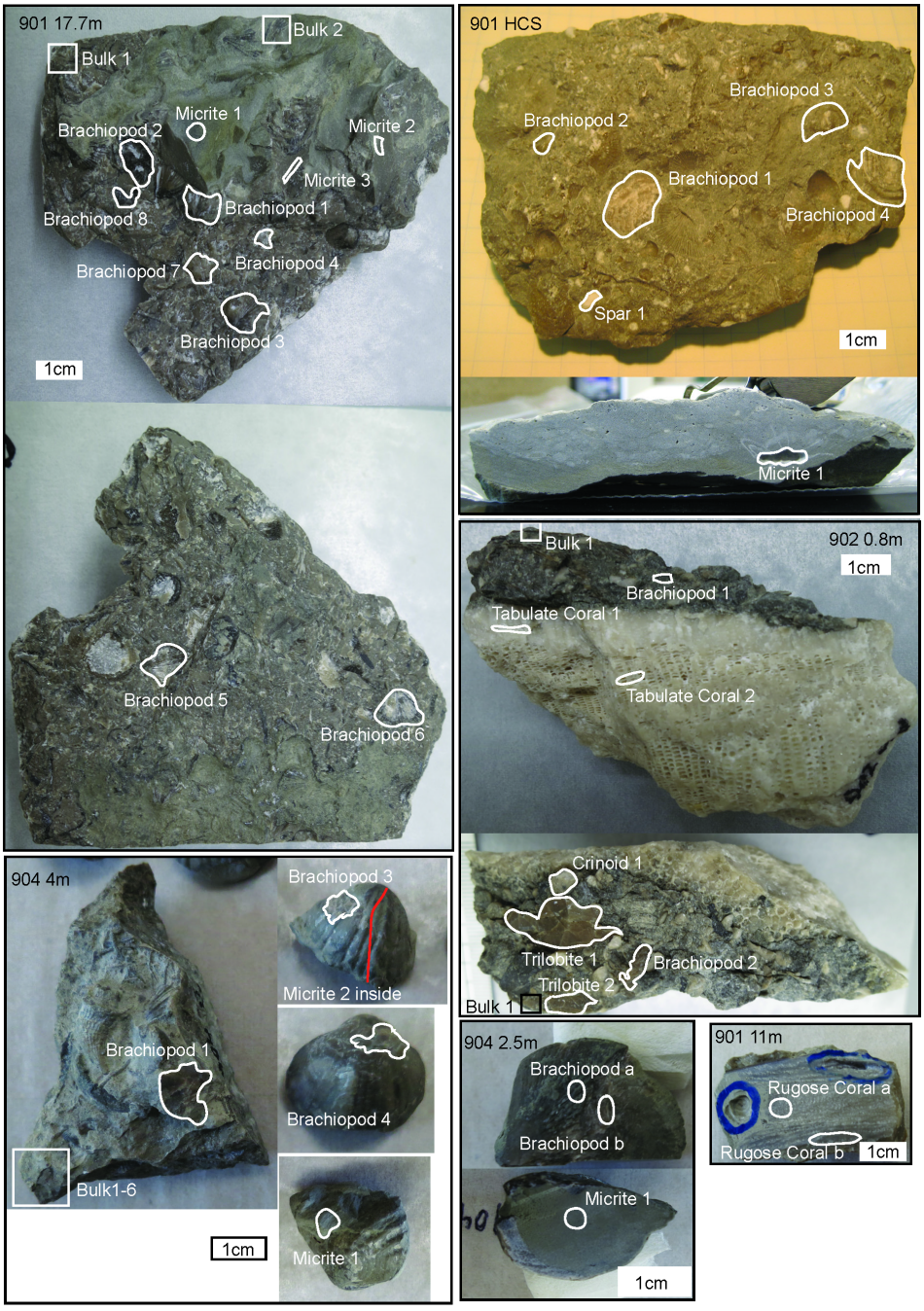

Supplemental Figure 1: Analyzed specimens from the six remaining hand-samples not shown in the main text.

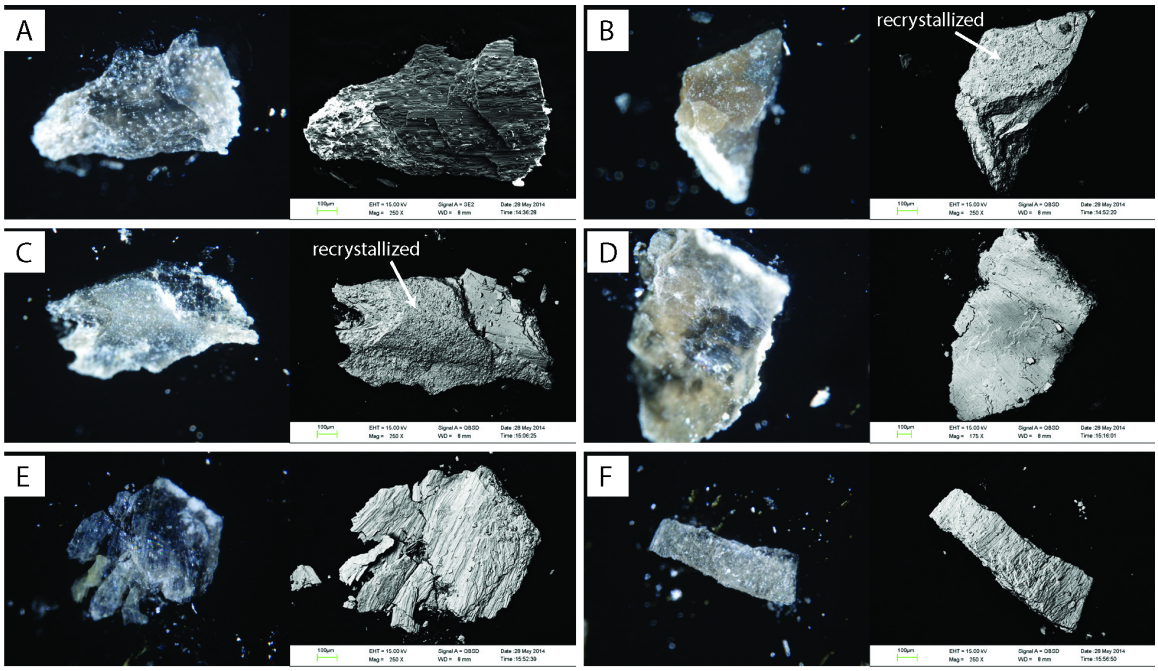

Supplemental Figure 2: Binocular microscope (left) and electron microscope backscatter intensity (right) images of more representative flakes picked from brachiopod specimens to illustrate how flakes were included or excluded in CAS analyses. (A) Sample 904-4.5m, Brachiopod 1 still shows fibrous calcite lineation and is optically transparent; flakes like this would have been dissolved for analysis. (B) A poorly-preserved flake from Sample 904-4.5m, Brachiopod 2 has lost its fibrous calcite texture and incorporated contaminants that caused yellowing during recrystallization. Flakes like this would normally be removed from specimens before dissolution. However, this specimen was prohibitively small and included recrystallized flakes. (C) A flake from Sample 904-4.5m, Brachiopod 3 with both well-preserved and recrystallized fibrous calcite. A flake like this would have been further broken with the point of a dental pick so that only the optically transparent portions would be kept for analysis. (D) A flake from Sample 904-4.5m, Brachiopod 4 still maintains the fibrous calcite lineations and is generally transparent, but has some discoloration associated with recrystallization. Flakes like this were kept and analyzed in this specimen. (E) A well-preserved flake from Sample 904-4m, Brachiopod 3. (F) A well-preserved flake from Sample 904-4m, Brachiopod 4.

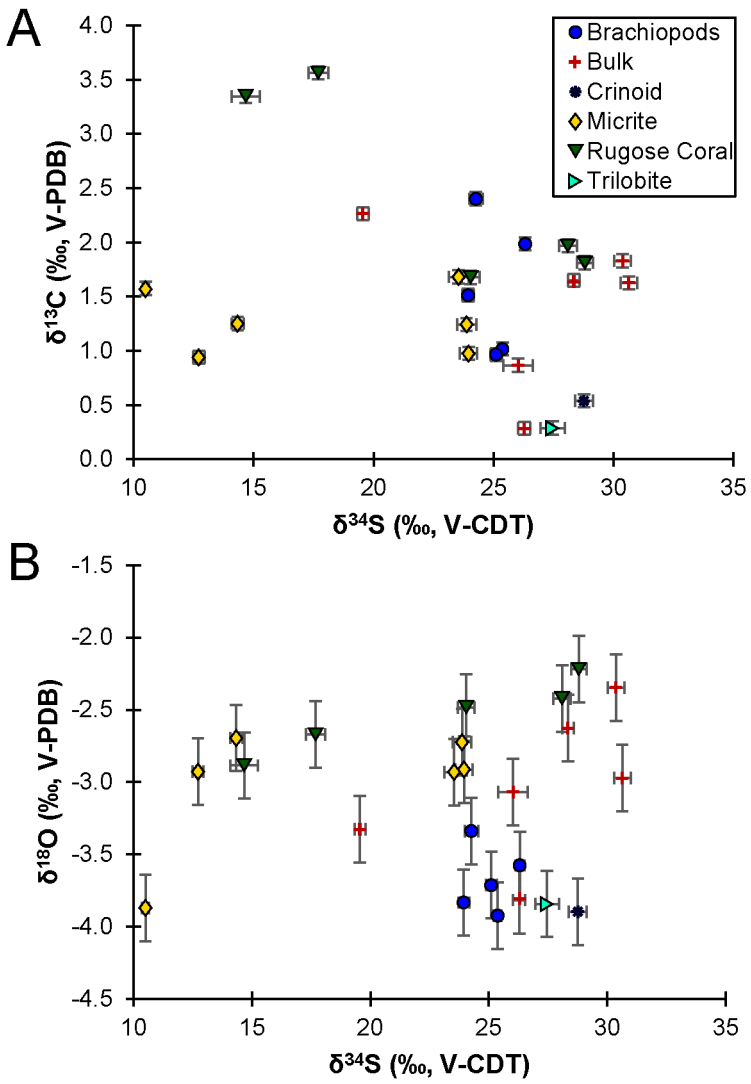

Supplemental Figure 3: Carbonate (A) carbon and (B) oxygen isotopic compositions of remaining powders and flakes after CAS analysis.

Supplemental data tables

Supplemental Table 1: Geochemical data from modern brachiopod and Anticosti Island samples. Protocol A = NaCl + water pre-cleaning, and dissolved in 0.5N HCl. Protocol B = NaCl + water pre-cleaning, and dissolved in *aqua regia*. Protocol C = pre-cleaning in only water and dissolving in 0.5N HCl. Protocol D = pre-cleaning in NaCl, H2O2, methanol, and water, and dissolving in 0.5N HCl.

	$[SO_4^{2-}]$ (ppm)	**1σ s.d. (ppm)**	**SO_4^{2-} (nmol)**	**1σ s.d. (nmol)**	**$\delta^{34}S$ (‰)**	**1σ s.e. (‰)**	**$\delta^{33}S$ (‰)**	**1σ s.e. (‰)**	**Cleaning/ dissolution**	**$\delta^{13}C$ (‰)**	**1σ s.e. (‰)**	**$\delta^{18}O$ (‰)**	**1σ s.e. (‰)**
Terebratalia transvera (Sowerby) brachiopod, San Pedro jetty, Los Angeles County													
M1A-1	4060	65	471	7.5	20.52	0.05	10.53	0.12	A				
M1B-1	4725	75	494	7.9	20.61	0.06	10.58	0.10	A				
M1B-2	3859	89	364	5.9	20.59	0.05	10.74	0.11	B				
901-17.7m, Becsie Fm., Fox Point Mbr.													
Brach 1	644	25	71	2.7	24.72	0.40	12.66	0.46	A				
Brach 2	1264	47	125	4.7	24.87	0.18	12.68	0.34	A				
Brach 3	699	27	64	2.4	23.89	0.50	12.28	0.48	A				
Brach 5	1465	55	111	4.2	24.50	0.39	12.43	0.48	A				
Brach 6	1349	51	123	4.6	23.60	0.27	12.21	0.39	A				
Brach 7	916	36	49	2.0	25.32	0.41	13.08	0.94	A				
Brach 8	2063	78	116	4.4	24.37	0.36	12.61	1.02	A				
Bulk 1a	200	9	20	0.9	26.02	0.61	13.43	0.63	A	0.87	0.06	-3.07	0.23
Bulk 1b	370	15	36	1.5	26.28	0.53	13.19	0.86	A				
Bulk 2a	416	17	38	1.5	26.28	0.25	13.45	0.46	A	0.29	0.06	-3.82	0.23
Bulk 2b	489	19	45	1.8	25.60	0.36	13.20	0.82	A				

	$[SO_4^{2-}]$ (ppm)	1σ s.d. (ppm)	SO_4^{2-} (nmol)	1σ s.d. (nmol)	$\delta^{34}S$ (‰)	1σ s.e. (‰)	$\delta^{33}S$ (‰)	1σ s.e. (‰)	Cleaning/ dissolution	$\delta^{13}C$ (‰)	1σ s.e. (‰)	$\delta^{18}O$ (‰)	1σ s.e. (‰)
Micrite 1a	3331	125	207	7.9	10.05	0.30	5.04	0.39	A				
Micrite 1b	1167	44	108	4.1	13.40	0.28	6.89	0.45	A				
Micrite 2	265	11	32	1.3	18.52	0.37	9.31	0.38	A				
Micrite 3	323	13	31	1.3	22.38	0.53	11.38	1.19	A				
901-HCS (9.5m), Ellis Bay Fm., Lousy Cove Mbr., Hirnantian Age													
Brach 1a	218	10	19	0.9	24.26	0.29	12.47	0.28	A	2.40	0.06	-3.34	0.23
Brach 1b	272	10	25	0.9	25.04	0.25	12.65	0.33	A				
Brach 2	207	16	10	0.8	16.62	0.35	8.32	0.47	A				
Brach 3	514	15	42	1.3	23.51	0.18	12.20	0.29	A				
Brach 4	390	15	46	1.8	25.23	0.45	12.87	0.48	A				
Bulk 1	264	7	29	0.8	21.82	0.09	10.99	0.16	C				
Bulk 2	238	7	22	0.7	19.73	0.11	9.97	0.21	C				
Bulk 3	240	5	25	0.5	19.07	0.10	9.67	0.18	A				
Bulk 4	250	5	27	0.5	19.03	0.09	9.71	0.18	A				
Bulk 5	223	5	25	0.5	17.69	0.09	9.00	0.19	D				
Bulk 6	219	7	23	0.7	15.30	0.08	7.98	0.19	D				
Bulk 7	4475	70	476	7.4	18.36	0.05	9.24	0.09	B				
Bulk 8	4927	77	528	8.2	15.66	0.05	8.19	0.09	B				
Bulk 9	281	12	21	0.9	18.85	0.21	9.72	0.26	A				
Bulk 10	476	16	33	1.1	10.71	0.15	5.52	0.25	A				
Bulk 11	329	14	22	0.9	17.89	0.21	9.37	0.30	A				

	$[SO_4^{2-}]$ (ppm)	1σ s.d. (ppm)	SO_4^{2-} (nmol)	1σ s.d. (nmol)	$\delta^{34}S$ (‰)	1σ s.e. (‰)	$\delta^{33}S$ (‰)	1σ s.e. (‰)	Cleaning/ dissolution	$\delta^{13}C$ (‰)	1σ s.e. (‰)	$\delta^{18}O$ (‰)	1σ s.e. (‰)
Bulk 12	284	12	22	0.9	19.55	0.23	9.94	0.34	A	2.27	0.06	-3.33	0.23
Micrite 1a	657	20	37	1.2	10.50	0.14	5.38	0.20	A	1.58	0.06	-3.87	0.23
Micrite 1b	640	20	37	1.2	10.39	0.13	5.26	0.18	A				
Micrite 1c	656	20	40	1.2	9.77	0.14	4.89	0.23	A				
Micrite 1d	586	18	37	1.2	11.23	0.14	5.52	0.25	A				
Spar 1	3968	174	97	4.5	31.10	0.36	15.86	0.76	A				
901-11m, Ellis Bay Fm., Laframboise Mbr., Hirnantian Age													
Rugose Coral 1a	79	2	8	0.2	14.67	0.59	7.81	0.80	A	3.35	0.06	-2.89	0.23
Rugose Coral 1b	154	4	14	0.5	17.69	0.41	8.94	0.30	A	3.56	0.06	-2.67	0.23
904-4.5m, Ellis Bay Fm., Prinsta Mbr., Katian Age													
Brach 1	2194	92	214	9.0	26.04	0.27	13.63	0.66	A				
Brach 4	879	37	71	3.0	25.90	0.56	13.24	0.71	A				
Bryozoan 1	521	22	59	2.5	31.17	0.33	16.02	0.62	A				
Bulk 1	314	14	31	1.4	30.37	0.34	15.80	0.78	A	1.83	0.06	-2.35	0.23
Bulk 2	357	15	38	1.6	30.63	0.35	15.87	1.01	A	1.63	0.06	-2.97	0.23
Micrite 1	344	15	29	1.3	23.54	0.41	12.17	0.92	A	1.68	0.06	-2.93	0.23
Micrite 2	305	13	27	1.2	23.87	0.40	12.10	0.94	A	1.24	0.06	-2.72	0.23

	$[SO_4^{2-}]$ (ppm)	1σ s.d. (ppm)	SO_4^{2-} (nmol)	1σ s.d. (nmol)	$\delta^{34}S$ (‰)	1σ s.e. (‰)	$\delta^{33}S$ (‰)	1σ s.e. (‰)	Cleaning/ dissolution	$\delta^{13}C$ (‰)	1σ s.e. (‰)	$\delta^{18}O$ (‰)	1σ s.e. (‰)
Rugose Coral 1	216	10	20	0.9	24.04	0.36	12.49	0.68	A	1.68	0.06	-2.48	0.23
Rugose Coral 2	196	9	21	0.9	28.10	0.36	14.21	1.18	A	1.97	0.06	-2.42	0.23
Rugose Coral 3	356	15	39	1.6	28.80	0.33	14.67	0.82	A	1.81	0.06	-2.22	0.23
Trilobite 1	444	19	44	0.9	28.99	0.28	14.84	0.67	A				
904-4m, Ellis Bay Fm., Prinsta Mbr., Katian Age													
Brach 1	1464	41	143	4.5	26.31	0.19	13.61	0.20	A	1.99	0.06	-3.58	0.23
Brach 2										1.25	0.06	-4.29	0.23
Brach 3	1235	39	86	3.3	25.55	0.21	13.22	0.16	A				
Brach 4	1225	35	112	3.7	25.11	0.23	12.87	0.17	A	0.97	0.06	-3.71	0.23
Bulk 1	480	14	43	1.4	28.35	0.24	14.62	0.18	C	1.65	0.06	-2.63	0.23
Bulk 2	443	13	38	1.3	29.26	0.26	14.94	0.19	C				
Bulk 3	460	13	43	1.4	27.76	0.22	14.23	0.19	A				
Bulk 4	427	12	37	1.3	29.98	0.28	15.21	0.22	A				
Bulk 5	515	21	23	1.2	30.29	0.40	15.63	0.26	D				
Bulk 6	504	21	22	1.2	31.02	0.43	15.98	0.26	D				
Micrite 1	418	15	22	1.0	23.95	0.36	12.29	0.25	A	0.98	0.06	-2.91	0.23
Micrite 2	516	17	32	1.3	12.72	0.24	6.74	0.19	A	0.94	0.06	-2.93	0.23

	$[SO_4^{2-}]$ (ppm)	1σ s.d. (ppm)	SO_4^{2-} (nmol)	1σ s.d. (nmol)	$\delta^{34}S$ (‰)	1σ s.e. (‰)	$\delta^{33}S$ (‰)	1σ s.e. (‰)	Cleaning/ dissolution	$\delta^{13}C$ (‰)	1σ s.e. (‰)	$\delta^{18}O$ (‰)	1σ s.e. (‰)
904-2.5m, Ellis Bay Fm., Prinsta Mbr., Katian Age													
Brach 1a	2529	70	256	8.0	25.37	0.17	13.03	0.19	A	1.02	0.06	-3.92	0.23
Brach 1b	2771	86	206	7.5	23.94	0.23	12.47	0.20	A	1.51	0.06	-3.83	0.23
Micrite 1	284	9	21	0.8	14.34	0.26	7.59	0.23	A	1.25	0.06	-2.69	0.23
904-0.8m, Vauréal Fm., Homards Mbr., Katian Age													
Brach 1	326	13	34	1.4	24.96	0.46	12.40	0.99	A				
Brach 2	1206	45	180	6.7	25.71	0.44	13.22	0.87	A				
Bulk 1	261	12	23	1.0	15.47	0.42	7.81	1.02	A				
Crinoid 1a	299	12	27	1.1	28.76	0.38	14.68	0.44	A	0.54	0.06	-3.90	0.23
Crinoid 1b	549	21	54	2.1	31.19	0.37	15.92	0.80	A				
Tabulate Coral 1	518	20	48	1.9	34.48	0.43	17.74	0.95	A				
Tabulate Coral 2	102	7	9	0.6	33.08	1.03	17.23	1.62	A				
Trilobite 1	200	9	21	0.9	29.96	0.55	15.37	0.68	A				
Trilobite 2	309	14	25	1.1	27.45	0.50	13.71	1.14	A	0.29	0.06	-3.84	0.23

Supplemental Table 2: Results of CAS extractions of coral-pyrite mixtures.

	$[SO_4^{2-}]$ (ppm)	**1σ s.d. (ppm)**	**SO_4^{2-} (nmol)**	**1σ s.d. (nmol)**	**$\delta^{34}S$ (‰)**	**1σ s.e. (‰)**	**$\delta^{33}S$ (‰)**	**1σ s.e. (‰)**	**Pyrite content (wt. %)**
Coral 1	4617	92	346	6.9	22.27	0.07	11.45	0.26	
Coral 2	4584	92	460	9.2	22.12	0.05	11.40	0.19	
Coral 3	4924	98	342	6.8	22.17	0.07	11.58	0.20	
Coral 4	5567	111	556	11	22.17	0.07	11.36	0.27	
Coral + Pyrite 1	4739	95	385	7.7	22.15	0.08	11.07	0.22	8.7
Coral + Pyrite 2	4693	94	310	6.2	22.15	0.07	11.66	0.19	6.6
Coral + Pyrite 3	4535	91	410	8.2	22.17	0.08	11.17	0.22	5.3
Coral + Pyrite 4	4697	94	364	7.3	22.24	0.09	11.38	0.26	6.1
Coral with Fe-Mn oxide crust 1	3148	63	262	5.2	22.72	0.07	11.29	0.20	
Coral with Fe-Mn oxide crust 2	4253	85	283	5.7	22.44	0.08	11.28	0.22	
Coral with Fe-Mn oxide crust 3	4027	81	369	7.4	22.38	0.08	11.75	0.20	
Coral with Fe-Mn oxide crust 4	4374	87	300	6.0	22.40	0.09	11.47	0.29	
Coral with Fe-Mn oxide crust + Pyrite 1	3850	77	414	8.3	21.02	0.07	11.05	0.22	4.7
Coral with Fe-Mn oxide crust + Pyrite 2	4149	83	303	6.1	22.04	0.06	11.37	0.19	8.1
Coral with Fe-Mn oxide crust + Pyrite 3	4047	81	328	6.6	22.09	0.07	11.47	0.22	17.7
Coral with Fe-Mn oxide crust + Pyrite 4	4101	82	343	6.9	22.37	0.07	11.35	0.24	7.7

Supplemental Table 3: CAS concentration and composition of *Desmophyllum dianthus* SS0108-STA011 collected in January 2008 off Tasmania. Fe-Mn crust was removed from coral with Dremel rotary tool, and then crushed and sieved. Protocol A = pre-cleaning for 11 hr at 75°C in 1:1 mixture of 2M NaOH and 30% H_2O_2, then rinsing with methanol and 4x with water before dissolution in 3N HCl. Protocol B = pre-cleaning by only rinsing 4x in water and dissolution in 10% $HClO_4$.

Sieve fraction	$[SO_4^{2-}]$ (ppm)	1σ s.d. (ppm)	SO_4^{2-} (nmol)	1σ s.d. (nmol)	$\delta^{34}S$ (‰)	1σ s.e. (‰)	$\delta^{33}S$ (‰)	1σ s.e. (‰)	Proto-col
<63 µm	4649	177	199	9.7	22.24	0.11	11.44	0.38	A
<63 µm	4032	155	179	8.8	22.23	0.11	11.47	0.38	A
<63 µm	5092	525	23	2.5	n/a	n/a	n/a	n/a	A
<63 µm	2348	225	12	1.2	n/a	n/a	n/a	n/a	A
<63 µm	4794	238	99	5.7	22.24	0.11	11.45	0.38	A
63-250 µm	4441	164	468	22.3	22.31	0.11	11.49	0.38	A
63-250 µm	4382	213	157	9.0	22.03	0.11	11.35	0.38	A
63-250 µm	5162	242	136	7.6	22.29	0.11	11.52	0.38	A
63-250 µm	4307	162	186	9.0	22.27	0.11	11.44	0.38	A
63-250 µm	n/a	n/a	n/a	n/a	22.19	0.11	11.47	0.38	A
250 µm -1 mm	4639	174	230	11.0	22.23	0.11	11.42	0.38	A
250 µm -1 mm	4593	217	159	8.9	21.50	0.11	11.19	0.38	A
250 µm -1 mm	4701	221	226	12.6	21.98	0.11	11.35	0.38	A
250 µm -1 mm	4769	220	566	31.2	22.13	0.11	11.35	0.38	A
250 µm -1 mm	4638	220	299	16.8	22.25	0.11	11.54	0.38	A
250 µm -1 mm	n/a	n/a	n/a	n/a	22.36	0.11	11.47	0.38	A
251 µm -1 mm	n/a	n/a	n/a	n/a	21.91	0.11	11.22	0.38	A
>1 mm	5054	190	248	11.9	22.13	0.11	11.48	0.38	A
>1 mm	4768	178	278	13.3	22.28	0.11	11.45	0.38	A
>1 mm	4703	218	354	19.6	22.49	0.11	11.52	0.38	A
>1 mm	5022	231	424	23.3	22.50	0.11	11.53	0.38	A
>1 mm	n/a	n/a	n/a	n/a	22.60	0.11	11.68	0.38	A
>1 mm	7037	231	487	21.7	21.89	0.10	11.32	0.38	B
>1 mm	7336	241	520	23.1	21.97	0.09	11.38	0.38	B
>1 mm	7527	248	342	15.2	21.82	0.10	11.15	0.38	B
>1 mm	6365	213	265	11.9	22.21	0.09	11.42	0.38	B
251 µm -1 mm	6544	216	385	17.1	22.71	0.09	11.69	0.38	B

Sieve fraction	$[SO_4^{2-}]$ (ppm)	1σ s.d. (ppm)	SO_4^{2-} (nmol)	1σ s.d. (nmol)	$\delta^{34}S$ (‰)	1σ s.e. (‰)	$\delta^{33}S$ (‰)	1σ s.e. (‰)	Proto-col
252 μm -1 mm	6402	213	400	17.9	22.14	0.09	11.43	0.38	B
253 μm -1 mm	6631	220	423	18.9	22.29	0.09	11.53	0.38	B
254 μm -1 mm	6675	220	366	16.3	22.62	0.09	11.79	0.38	B
63-250 μm	5529	185	339	15.3	23.01	0.09	11.91	0.38	B
63-250 μm	6607	218	369	16.5	23.14	0.09	11.87	0.38	B
63-250 μm	6534	216	348	15.5	22.63	0.09	11.51	0.38	B
63-250 μm	6561	218	411	18.4	22.13	0.09	11.41	0.38	B
<63 μm	4703	176	222	10.6	21.89	0.10	11.44	0.38	B
<63 μm	7025	231	417	18.6	23.13	0.09	11.84	0.38	B
<63 μm	7250	238	417	18.6	21.89	0.09	11.32	0.38	B
<63 μm	6744	223	473	21.1	22.81	0.10	11.63	0.38	B

Chapter 3

PRELIMINARY UPPER ORDOVICIAN TO MIDDLE SILURIAN SULFUR ISOTOPE RECORD FROM BRACHIOPOD CARBONATE-ASSOCIATED SULFATE

Theodore M. Present[1], Woodward F. Fischer[1], Jess F. Adkins[1]

[1]California Institute of Technology, Pasadena, California, USA

Abstract

Glaciations, mass extinctions, and orogenies during the Late Ordovician and Silurian periods possibly affected the ventilation and composition of Earth's oceans. Major carbon isotope excursions coincident with climatic and biologic changes may have been caused by the development of euxinic conditions or changes in the composition of rocks undergoing weathering. If widespread or long-lasting, marine euxinia could produce spatially variable sulfur isotopic compositions of marine sulfate and weathering changes could produce temporally variable compositions. To examine marine sulfur isotopic variability, we measured the sulfur isotopic composition of carbonate-associated sulfate incorporated into well-preserved brachiopods from the Cincinnati Arch, Indiana, Kentucky, and Ohio, USA, and from Gotland, Sweden. The quality of this proxy archive for ancient seawater sulfate is variable, and, therefore requires careful consideration of primary and diagenetic sources of isotopic variability. We used a recently-developed aqueous sulfate analytical technique to make replicate measurements of the same brachiopod for the first time, and observe up to a 4‰ range among replicates. This diagenetic variability of even the best-preserved brachiopods can account for all of the sulfur isotope change over the Late Ordovician and Silurian, suggesting that seawater sulfate was globally well-mixed and temporally invariant. Therefore, changes in the ventilation of the ocean or the composition of weathering rock were likely not severe or long-lasting enough to affect the global sulfur budget.

Introduction

During the Late Ordovician and Silurian periods, major ecologic, climatic, and tectonic reorganizations may have affected the composition of the oceans. These included the Taconic Orogeny, glaciation of Gondwana, the Late Ordovician Mass Extinction (LOME), and Silurian alteration between upwelling and downwelling coastal ocean circulation patterns (e.g. Holland and Patzkowsky, 1996; Jeppsson, 1990; Rodgers, 1971). These are reflected by organic carbon, carbonate carbon, and pyrite sulfur isotope excursions likely linked to changes in the net amount or mechanism of organic carbon burial, weathering, and pyrite burial (Brenchley et al., 1994; Hammarlund et al., 2012; Jones and Fike, 2013; Kump et al., 1999; Patzkowsky et al., 1997). A primary question is whether the ocean remained well-mixed and oxygenated during these events. Today, carbon isotopes reflect gradients in the productivity and ventilation of water masses but sulfate sulfur isotopes are well-mixed. In a well-mixed ocean at steady-state, temporal changes in the sulfur isotopic composition ($\delta^{34}S$) of marine sulfate therefore reflect changes of pyrite burial or weathering fluxes (Kump, 1989; Kump and Garrels, 1986). Alternatively, spatial heterogeneity in $\delta^{34}S$ would reflect a stratified ocean with major euxinic water masses.

Biogenic carbonate incorporates minor amounts of sulfate called carbonate-associated sulfate (CAS), which likely preserves the $\delta^{34}S$ of the seawater in which the organism grew (Burdett et al., 1989; Kampschulte et al., 2001; Mekhtiyeva, 1974). To investigate spatial and temporal variability in the $\delta^{34}S$ of seawater, we report 53 new CAS measurements from 40 brachiopods from Upper Ordovician strata in the Cincinnati Arch, Kentucky, Indiana, and Ohio and lower Wenlock-age (Silurian) strata in Gotland, Sweden. These samples, and previously published data, span 30 Myr of deposition in multiple Laurentian and Baltica environments.

Descriptions of samples

Late Ordovician (late Sandbian – Katian), Cincinnati Arch, USA

Late Ordovician brachiopods of uppermost Sandbian to upper Katian age were previously collected from the Cincinnati Arch in the Cincinnati region in Indiana, Kentucky, and Ohio,

USA by Finnegan et al. (2011). The Cincinnati Arch was a shallow epicontinental sea in the foreland basin of the Taconic Orogeny, which contained a mixed carbonate-siliciclastic ramp dipping northeast from the peripheral bulge (Table 1) (Holland, 1993; Pope and Read, 1997). The oldest unit, the Mohawkian-age Lexington Limestone, deposited as a high-energy ramp and is composed predominately of subtidal skeletal wackestone-packstones and shale with minor grainstone shoals and fenestral mudstone tidal flats (Pope and Read, 1997). It is overlain by the Cincinnatian Series, which is predominately low-energy supratidal to shallow subtidal carbonate mudstones and subtidal shales, with minor transgressive lagoonal wackestones and high-energy packstone-grainstones (Holland, 1993). The Cincinnatian Series is comprised of six shallowing-upward sequences (Holland, 1993; Holland and Patzkowsky, 1996).

The Cincinnati Series experienced burial temperatures inferred from conodont alteration of less than 100°C (Ellwood et al., 2007; Epstein et al., 1977). The Cincinnati Series exhumed as the Cincinnati Arch as the peripheral bulge of the Carboniferous-Permian Alleghenian Orogeny (Root and Onasch, 1999). Connate fluids with elevated temperatures (100-300°C) associated with Mississippi Valley-type mineralization may have migrated through permeable units and along sequence boundaries on the western limb of the arch and into the Illinois Basin, but no evidence suggests that such fluids affected the Indiana-Kentucky-Ohio region (Elliott and Aronson, 1993; Stearns and Reesman, 1986). Finnegan et al. (2011) measured elevated carbonate clumped isotope temperatures on two brachiopods from the Cincinnati Series, which equilibrated at 38.3°C (Waynesville Formation) and 40.9°C (Kope Formation) that are likely similar to depositional seawater temperatures in the shallow carbonate ramp environment. More recrystallized components, such as a crinoid from the Waynesville Formation, also equilibrated at a similar temperature and with seawater-like oxygen isotopic compositions of the diagenetic fluid (Finnegan et al., 2011).

<table>
<tr><th>Age (Ma)</th><th>Series</th><th>Stage</th><th>Regional Series</th><th>Regional Stage</th><th>Formation</th><th>Sequence</th></tr>
<tr><td rowspan="2">445.2-</td><td rowspan="11">Upper Ordovician</td><td>Hirnantian</td><td colspan="4">[unconformity]</td></tr>
<tr><td rowspan="10">Katian</td><td rowspan="8">Cincinnatian</td><td rowspan="5">Richmondian</td><td>Elkhorn</td><td>C6</td></tr>
<tr><td>Whitewater*</td><td rowspan="3">C5</td></tr>
<tr><td>Liberty</td></tr>
<tr><td>Waynesville*</td></tr>
<tr><td>Arnheim*</td><td>C4</td></tr>
<tr><td rowspan="2">Maysvillian</td><td>Grant Lake*</td><td>C3</td></tr>
<tr><td>Fairview*</td><td>C2</td></tr>
<tr><td>Edenian</td><td>Kope*</td><td>C1</td></tr>
<tr><td rowspan="2">453.7-</td><td rowspan="2">Mohawkain</td><td>Chatfieldian</td><td>Lexington*</td><td>M6</td></tr>
<tr><td>Sand.</td><td></td><td></td><td></td></tr>
</table>

Table 1: Ages of Upper Ordovician formations, regional stages, and sequences in the Cincinnati Region (Bergström et al., 2009, 2010b; Holland, 1993; Holland and Patzkowsky, 1996). Asterisks mark formations from which brachiopod CAS data are reported here. Sand. = Sandbian.

Early Wenlockian (Sheinwoodian), Gotland, Sweden

Latest Llandovery through Ludlow-age strata deposited on a carbonate ramp in the tectonically-stable Baltic Basin, which formed on a stable, slowly subsiding craton between two foreland basins during the Scandian Orogeny (Calner et al., 2004; Samtleben et al., 1996). Sheinwoodian-age (430.5-433.4 Ma) brachiopods from Gotland, Sweden were obtained from the collection used for carbonate clumped isotope analysis by Cummins et al. (2014).

The Lower Visby, Upper Visby, and Högklint formations (Table 2) represent a depositional sequence that transitions from sub-storm wave base marls and fine-grained limestones, to decimeter-relief rugose and tabulate coral reefs and skeletal packstone-grainstones, and to stromatoporid sponge bioherms and biostromes with coarse skeletal grainstones (Munnecke et al., 2003; Samtleben et al., 1996). An abrupt graptolite extinction called the Ireviken Event occurs at the contact between the Lower Visby and the Upper Visby formations, which is pyritized and may represent a hardground and depositional hiatus; this surface is colonized

by *Phaulactis* solitary rugose corals and serves as a regional datum (Munnecke et al., 2003). This surface also is the base of a positive carbon isotope anomaly that continues through the Högklint Formation (Cramer et al., 2010; Munnecke et al., 2003). Brachiopod samples analyzed here are from the Lower Visby and Upper Visby formations (Cummins et al., 2014).

The Högklint is unconformably overlain by the Tofta Formation, which comprises lagoonal oncoid rudstones and stromatolitic bioherms (Calner et al., 2004; Munnecke et al., 2003; Samtleben et al., 1996). Marl and reef deposition returns in the overlying Hangvar Formation and Slite Group (Calner et al., 2004; Samtleben et al., 1996). Brachiopod samples analyzed here are from the Slite group above the end of the Ireviken Event carbon isotope excursion (Cummins et al., 2014), indicating that they are mid-Sheinwood in age (Cramer et al., 2010).

Gotland Island has been minimally-buried and lithified, with negligible conodont color alteration and thermal annealing (Epstein et al., 1977; Jeppsson, 1983). Brachiopod calcite is extremely well preserved and retains its primary growth microstructure (Cummins et al., 2014). However, Cummins et al. (2014) measured carbonate clumped isotope equilibration temperatures of 30°C to 60°C. The elevated clumped isotope temperatures represent isotope exchange during recrystallization with a warm diagenetic fluid; this fluid alteration is weakly correlated with iron and manganese concentrations and negatively correlated with strontium concentrations in the carbonate (Cummins et al., 2014).

Age (Ma)	Series	Stage	Formation
433.4-	Wenlock	Sheinwoodian	Slite*
			Hangvar
			Tofta
			Hogklint
			Upper Visby*
			Lower Visby*
	Llandovery	Telychian	

Table 2: Lowest strata of Silurian-age on Gotland, Sweden (Cramer et al., 2010). Asterisks mark formations from which brachiopod CAS data are reported here.

Methods

Sampling targeted the best-preserved fibrous calcite of the brachiopods' secondary fibrous layer because it is composed of thermodynamically-stable low-magnesium calcite with microstructure that is obviously destroyed when recrystallized (Al-Aasm and Veizer, 1982; Grossman et al., 1993). Following Present et al. (2015) and Cummins et al. (2014), brachiopods were broken away from matrix material and ultrasonicated overnight. Flakes of brachiopod calcite were then separated from recrystallized calcite, cements, pyrite, iron oxides, and matrix material geochemical analysis with a dental pick and tweezers under a binocular microscope (Cummins et al., 2014; Present et al., 2015). Two to 80 mg of material was obtained from each brachiopod. As 5 – 10 mg are required for CAS analysis (Present et al., 2015), this permitted, for the first time, replicate analyses of single brachiopods.

Brachiopods, especially those from the Cincinnati Arch, were variably well-preserved. Samples were therefore assigned a visual preservation score from 0 (best) to 5 (worst) that is the number of diagenetic features observed at 50x magnification, including recrystallized (non-fibrous) calcite, residual matrix or cement, discoloration, opaque flakes, and mineral (likely pyrite or iron oxide) inclusions. A representative flake from each brachiopod was also fixed to carbon tape to assess finer-scale preservation with electron microscopy, and

duplicate or triplicate 3 – 5 mg aliquots were preserved from each brachiopod for carbonate clumped isotope analysis; these analyses have not yet been performed.

Additional specimens were obtained from leftover samples analyzed for carbonate clumped isotopes by Cummins et al. (2014). Cummins et al. (2014) powdered the sample flakes, and they are not assigned a visual preservation score.

In a clean laboratory with ultrapure water and reagents, specimens were pre-cleaned of soluble sulfate and dissolved following the methods in Present et al. (2015). Samples were ultrasonicated overnight in 2 mL 10 wt. % NaCl and centrifuged to discard supernatant with a pipette. Samples were then rinsed four times in 1 mL water, centrifuging and discarding each supernatant, and transferred to acid-clean 2 mL centrifuge tubes before dissolution for 4 hr in 500 μL 0.5N HCl. The dissolved sample was centrifuged and the supernatant was transferred to a Savillex beaker. A 25 μL aliquot was diluted to 125 μL for later trace metal content determination; this analysis has not yet been performed.

Carbonate content was determined from the dry mass of initial sample and dry mass of any insoluble residue. The dissolved sample separated from the insoluble residue was dried in a laminar flow hood overnight on a 125°C hotplate and re-suspended in 3.3 mN HCl. Sulfate was purified from the matrix by anion exchange chromatography following Paris et al. (2014a) and the column eluent was again dried in a laminar flow hood overnight on a 125°C hotplate. Sulfate was re-suspended in water to determine amount by ion chromatography with a Dionex ICS-3000 system. Precision and accuracy, which were better than 0.5%, were determined with three in-house sulfate concentration standards. CAS concentrations are reported as parts-per-million by mass, which corresponds to micrograms of sulfate per gram of soluble carbonate.

Sulfate $\delta^{34}S$ compositions were determined by sample-standard-bracketing using Thermo Fisher Scientific Neptune (“George”) and Neptune Plus (“Louis”) multi-collector inductively-coupled plasma mass spectrometers with a Cetac Aridus II desolvating spray chamber (Paris et al., 2013, 2014a). Purified sulfate samples were matrix matched to an in-

house Na_2SO_4 bracketing standard by addition of the appropriate amount of NaOH. However, many samples had poorly matched intensity to the bracketing standard (relative intensities less than 0.7), indicating sample loss, likely while drying down, between sulfate concentration determination and sample preparation. Samples with relative intensities of 0.4 to 0.7 have $\delta^{34}S$ compositions biased by less than -0.3‰ (Paris et al., 2013), but these solutions should be reanalyzed.

Reported precisions, between 0.08‰ and 0.37‰, are the propagated 1σ standard error of the internal uncertainty of ion counting and machine blank subtraction, the intermediate reproducibility of the same sulfate solution analyzed twice in a measurement session (John and Adkins, 2010), and the arithmetic subtraction of procedural blank amount and composition. This precision is comparable to the external reproducibility of in-house dissolved coral and seawater consistency standards (coral 1σ s.e = 0.13‰, n = 6; seawater 1σ s.e. = 0.37‰, n = 6). Total procedural blanks and 1σ s.e. are 0.52±0.09 nmol with a $\delta^{34}S$ of 8.79±1.29‰ (n=31).

Results

Table 1 indicates the total preservation score for each brachiopod, and Supplemental Table 1 indicates which visible diagenetic features were apparent in each specimen. Silurian brachiopods from Gotland generally had better textural preservation than Ordovician samples from the Cincinnati Arch (Figure 1); no Ordovician brachiopod was visually perfectly preserved.

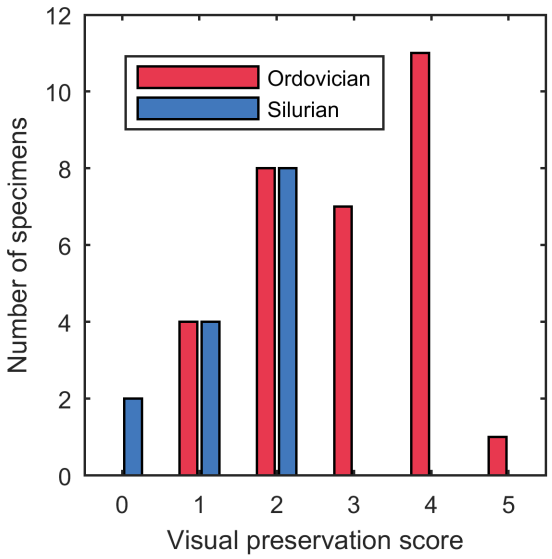

Figure 1: Histograms of preservation scores of Ordovician and Silurian brachiopod flakes picked for CAS analysis. 0 = best (no visible diagenetic features), 5 = worst (recrystallization, residual matrix, discoloration, opaque flakes, and mineral inclusions all present).

Table 3 includes the CAS concentrations and $\delta^{34}S$ compositions of the brachiopods, which are plotted in Figure 2. CAS concentrations are highly variable, ranging from 315 to 8645 ppm. CAS $\delta^{34}S$ ranges from 18‰ to 29‰, and there is no difference between the mean composition of Ordovician brachiopods (M = 23.8‰, SD = 2.19‰, n = 30) and Silurian brachiopods (M = 24.9‰, SD = 2.76‰, n = 23); paired-samples t-test, t(51) = -1.70, p = 0.094. There is also no difference in $\delta^{34}S$ between samples of different visual preservation scores (one-way analysis of variance, F[4,38] = 0.74, p = 0.57). However, samples with the lowest CAS concentrations are amongst the least-well preserved (Figure 3).

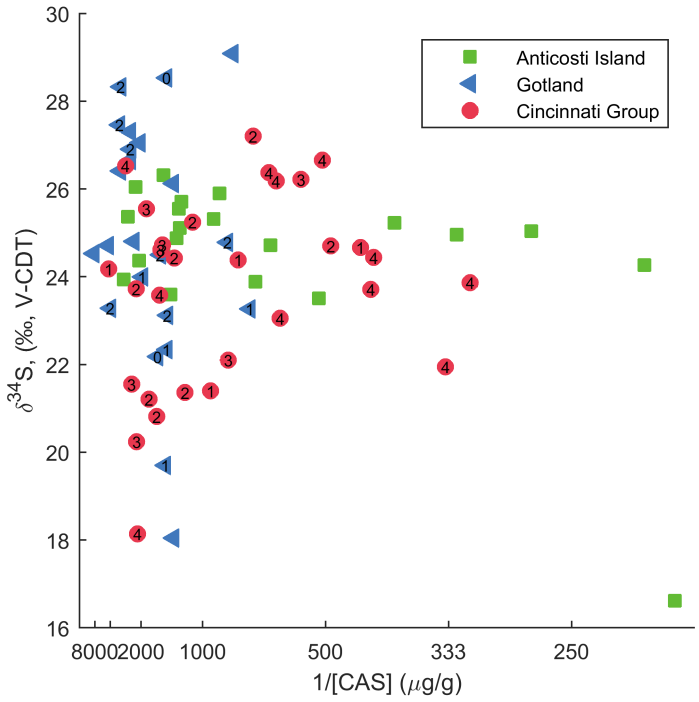

Figure 2: Plot of inverse CAS concentration versus $\delta^{34}S$ (i.e., concentration increases to the left). Small numbers on each symbol are the preservation score of the sample. Also plotted in green squares are brachiopod CAS data reported in Chapter 2 from Anticosti Island (Present et al., 2015).

Table 3: Geochemical results for Late Ordovician and Sheinwoodian brachiopods. PS = preservation score, RI = relative intensity. Shein. = Sheinwoodian, Eden. = Edenian, Frank. = Franklinian, Mays. = Maysvillian, Rich. = Richmondian, Sand. = Sandbian.

No.	Lab Code	Formation	Stage	Age (Ma)	PS	% Carb.	[CAS] (ppm)	1σ	$\delta^{34}S$ (‰)	1σ	RI
Br-001	001A	Slite	Shein.	431.5	1	99.0	722	23	23.27	0.24	0.88
Br-002	002A	Kope	Eden.	451.5	3	95.9	2145	68	20.24	0.29	0.87
Br-003	003A	Lexington	Frank.	452.5	2	96.7	1165	37	21.36	0.23	0.69
Br-003	003C	Lexington	Frank.	452.5	2	97.7	489	16	24.70	0.25	0.83
Br-004	004A	Waynesville	Rich.	446	1	99.6	937	30	21.40	0.24	0.81
Br-005	005A	Fairview	Mays.	449	2	98.5	2166	69	23.72	0.27	0.25
Br-006	006A	Upper Visby	Shein.	432.5	2	89.8	3076	98	27.46	0.33	0.34

No.	Lab Code	Formation	Stage	Age (Ma)	PS	% Carb.	[CAS] (ppm)	1σ	$\delta^{34}S$ (‰)	1σ	RI
Br-007	007A	Arnheim	Rich.	447	5	94.5	869	28			
Br-008	008A	Kope	Eden.	451.5	3	95.9	2355	75	21.55	0.26	0.64
Br-008	008B	Kope	Eden.	451.5	3	88.4	1836	58	25.55	0.31	0.41
Br-008	008C	Kope	Eden.	451.5	3	96.2	1511	48	24.61	0.24	0.55
Br-009	009A	Slite	Shein.	431	2	96.1	3999	127	23.28	0.27	0.40
Br-009	009B	Slite	Shein.	431	2	96.4	831	26	24.78	0.25	0.77
Br-009	009C	Slite	Shein.	431	2	92.7	1523	49	24.50	0.19	0.57
Br-010	010A	Waynesville	Rich.	446.5	4	96.3	2663	85	26.53	0.27	0.39
Br-010	010B	Waynesville	Rich.	446.5	4	99.2	649	21	26.37	0.15	0.92
Br-011	011A	Waynesville	Rich.	446.5	4	96.3	625	20	26.18	0.22	0.70
Br-011	011B	Waynesville	Rich.	446.5	4	85.2	506	16	26.66	0.17	0.79
Br-012	012A	Upper Visby	Shein.	432.5	2	95.2	2410	77	26.91	0.13	0.48
Br-012	012B	Upper Visby	Shein.	432.5	2	89.8	2979	95	28.33	0.37	0.31
Br-013	013A	Slite	Shein.	431	2	94.4	2135	68			
Br-014	014A	Grant Lake	Mays.	448.5	2	98.1	1296	41	24.43	0.26	0.76
Br-015	015A	Slite	Shein.	431.5	0	84.0	1574	50	22.18	0.26	0.53
Br-016	016A	Grant Lake (?)		448	1	98.0	4175	133	24.18	0.19	0.30
Br-017	017A	Platteville Group (?)	Sand. (?)	454	4	89.7	613	20	23.05	0.09	1.20
Br-017	017B	Platteville Group (?)	Sand. (?)	454	4	96.6	336	11	21.95	0.24	0.84
Br-018	018A	Fairview	Mays.	449	4	92.8	418	13	24.44	0.24	0.92
Br-018	018B	Fairview	Mays.	449	4	76.8	422	13	23.71	0.19	0.88
Br-018	018C	Fairview	Mays.	449	4	93.2	315	10	23.87	0.15	0.95
Br-019	019A	Kope	Eden.	451.5	2	99.5	1592	51	20.82	0.15	0.46
Br-020	020A	Kope	Eden.	451.5	4	93.7	2112	67	18.14	0.09	0.94
Br-021	021A	Lower Visby	Shein.	433	1	93.4	1957	62	24.00	0.13	0.46
Br-022	022A	Lower Visby	Shein.	433	2	93.2	1399	45	23.12	0.09	0.94
Br-023	023A	Upper Visby	Shein.	432.5	1	100.5	1433	46	19.70	0.10	0.94
Br-024	024A	Slite	Shein.	431.5	0	98.7	1412	45	28.53	0.31	0.19
Br-025	025A	Waynesville	Rich.	446.5	2	100.9	1768	56	21.21	0.09	0.85
Br-026	026A	Lexington	Frank.	452.5	1	96.1	774	25	24.38	0.13	0.61
Br-026	026B	Lexington	Frank.	452.5	1	99.3	438	14	24.67	0.14	0.91

No.	Lab Code	Formation	Stage	Age (Ma)	PS	% Carb.	[CAS] (ppm)	1σ	$\delta^{34}S$ (‰)	1σ	RI
Br-027	027A	Kope (?)		451.5	2	99.4	1088	35	25.24	0.11	0.72
Br-028	028A	Waynesville	Rich.	446.5	3	99.9	827	26	22.10	0.11	0.92
Br-028	028B	Waynesville	Rich.	446.5	3	96.7	555	18	26.22	0.20	0.98
Br-029	029A	Kope	Eden.	451.5	3	100.2	1481	47	24.72	0.11	0.61
Br-030	030A	(?)			2	90.4	708	23	27.20	0.13	0.84
Br-031	031A	Slite	Shein.	431	1	99.2	1410	45	22.34	0.09	0.83
Br-032	032A	Upper Visby	Shein.	432.5	C	93.7	379	12			
Br-033	033A	Lower Visby	Shein.	433	C	93.5	2419	77	27.31	0.16	0.38
Br-034	034A	Upper Visby	Shein.	432.5	C	99.5	803	26	29.08	0.13	0.61
Br-035	035A	Upper Visby	Shein.	432.5	C	94.2	1311	42	26.12	0.10	0.71
Br-036	036A	Slite	Shein.	431	C	97.5	1310	42	18.04	0.08	0.79
Br-037	037A	Whitewater	Rich.	446	4	87.5	1532	49	23.58	0.10	0.89
Br-038	038A	Slite	Shein.	431.5	C	100.6	3005	96	26.41	0.15	0.46
Br-039	039A	Upper Visby	Shein.	432.5	C	92.6	2034	65	27.05	0.21	0.75
Br-040	040A	Upper Visby	Shein.	432.5	C	111.5	2423	77	26.65	0.14	0.52
Br-041	041A	Slite	Shein.	431.5	C	96.4	4293	137	24.71	0.11	0.60
Br-042	042A	Upper Visby	Shein.	432.5	C	98.3	615	20			
Br-043	043A	Upper Visby	Shein.	432.5	C	101.8	2269	72	24.81	0.08	0.92
Br-044	044A	Slite	Shein.	431	C	101.6	1205	38			
Br-045	045A	Upper Visby	Shein.	432.5	1	100.8	8646	275	24.53	0.10	0.70

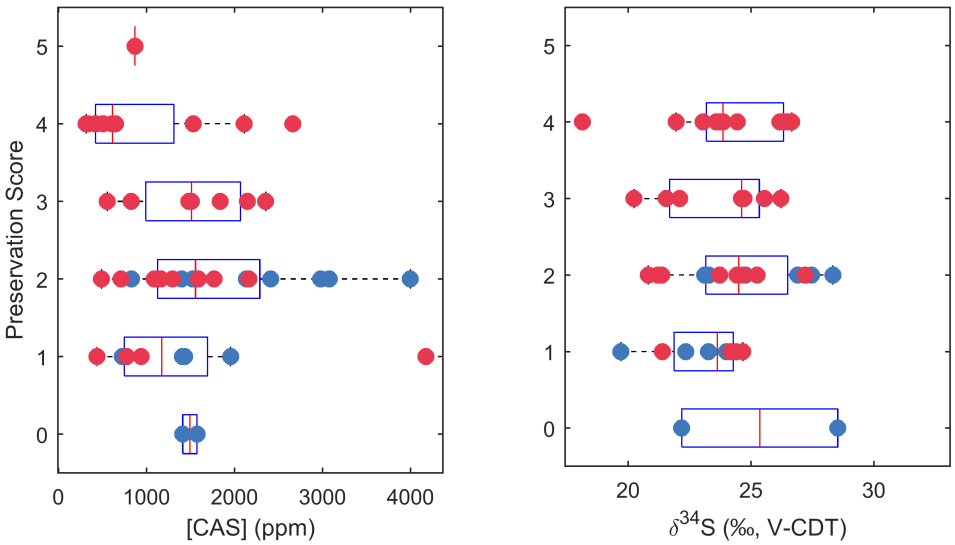

Figure 3: Concentration and $\delta^{34}S$ of Ordovician (red) and Silurian (blue) brachiopod CAS by preservation score from worst (5) to best (0). Box and whisker plots are also shown for all data of each preservation score.

By analyzing $\delta^{34}S$ by MC-ICP-MS, we can measure 1000 times less sulfate than traditional gas source isotope ratio mass spectrometry methods, and can therefore analyze less than 5 mg of brachiopod calcite. Reported here are the first replicate measurements of individual fossil brachiopods (Figure 4). One brachiopod measured in duplicate varied by as much as 4.1‰ (Br-028), and another measured in triplicate only varied by 0.7‰ (Br-018). The best-preserved brachiopod measured in duplicate (Br-026) had a preservation score of 1 due to visible recrystallization of the fibrous calcite. It had a small range in $\delta^{34}S$ (0.29‰) between duplicates, but remaining brachiopods measured in replicate with scores of 2 – 4 have no relationship between score and observed range (Figure 4).

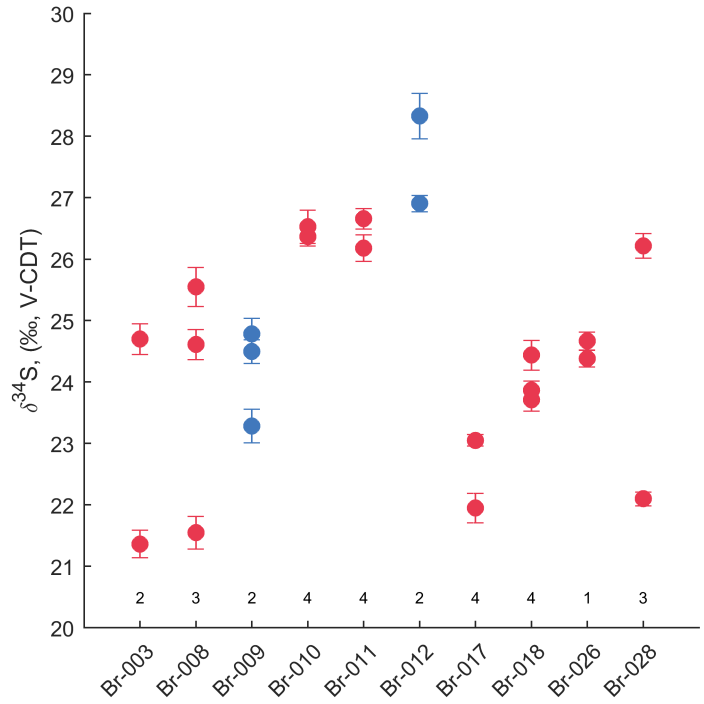

Figure 4: Comparison of CAS $\delta^{34}S$ of replicates from individual brachiopods. Numbers above the x-axis are the preservation score. Blue points are Silurian brachiopods, and red points are Ordovician brachiopods. Error bars are 1σ s.e. including internal and intermediate reproducibility and propagated uncertainty of procedural blank correction, which cannot explain the difference between brachiopod recplicates.

Three brachiopods were split into two specimens with different visual preservations. Br-010 and Br-011 are samples from two valves of the same individual with a preservation score of 4, but different discoloration (black and beige, respectively). Each was measured in duplicate, and the total range was only 0.5‰. Br-021 and Br-022 both contained mineral inclusions, but residual matrix could not be separated from Br-022; these specimens vary by 0.9‰. Br-019 and Br-020 were both recrystallized and discolored, but Br-020 was opaque and contained residual matrix material; Br-020 is 2.7‰ lighter than Br-019.

We observe larger variability between different brachiopods from the same bed. Brachiopods Br-015 and Br-024 were both composed of visually perfectly-preserved flakes

(score of 0) from the same bed in the Slite Formation. However, Br-015 (22.2‰) is 6.3‰ permil lighter than Br-024 (28.5‰). Br-031, which has a preservation score of 1, is 4.3‰ heavier than Br-036 from the same bed, which was a powder obtained from Cummins et al. (2014).

Discussion

Modern brachiopods have CAS with $\delta^{34}S$ within 2‰ of that of seawater sulfate (Kampschulte et al., 2001; Present et al., 2015), and fossil brachiopods of various ages are close to the isotopic composition of contemporaneous evaporite deposits (Kampschulte et al., 2001; Kampschulte and Strauss, 2004). It is therefore reasonable that the CAS $\delta^{34}S$ measurements of brachiopods well represent the $\delta^{34}S$ of ancient seawater sulfate. However, Present et al. (2015) observed up to a 3‰ range in brachiopod CAS from latest Ordovician and earliest Silurian strata on Anticosti Island, Quebec, Canada (Figure 2). Here, specimens from the same brachiopod exhibit comparable variability (Figure 4), and up to a 6.3‰ difference between brachiopods from the same bed. This clearly reflects diagenetic alteration of the brachiopod CAS.

Diagenetic alteration may either increase or decrease the $\delta^{34}S$ of CAS by incorporating non-seawater sources of sulfate into the carbonate during recrystallization or cementation (Kampschulte et al., 2001). Microbial sulfate reduction (MSR), which occurs in anoxic sediments, preferentially consumes low- $\delta^{34}S$ sulfate, producing low- $\delta^{34}S$ sulfide and leading to an increase in the $\delta^{34}S$ of the residual sulfate (Kaplan and Rittenberg, 1964). Rennie & Turchyn (2014) demonstrated that CAS in pelagic nanofossil ooze may be enriched relative to the seawater it precipitated from if it recrystallized slowly enough that MSR had distilled pore fluid sulfate to higher $\delta^{34}S$, but rapidly enough that recrystallization occurred before MSR consumed all of the sulfate. Alternatively, reoxidation of sedimentary sulfide minerals may produce sulfate with low $\delta^{34}S$. Oxidation primarily occurs by oxygen, or microbially by nitrate, iron oxides, or manganese oxides (Schippers and Jørgensen, 2002).

Unfortunately, visual assessment of brachiopod preservation does not predict which samples are diagenetically altered (statistical test results above). While many of the worst preserved-

brachiopods (score of 4) have lower CAS concentrations than the other samples, many well-preserved brachiopods have the same range of $\delta^{34}S$ without a loss of CAS concentration (Figure 3). Cummins et al. (2014) observed ultra-fine-scale diagenetic alteration resulting in increased carbonate clumped isotope temperatures and low oxygen isotope compositions from the Gotland brachiopod collection, despite only subtle to negligible textural alteration that was invisible without electron backscatter diffractometry. They also noted within-bed variability of geochemical preservation. Bergmann et al. (2018) observed similar increased and variable clumped isotope and oxygen compositions from Late Ordovician brachiopods from the Decorah Formation in Wisconsin, USA, which correlates to the lower Lexington Limestone. Therefore, other geochemical data, including carbonate carbon and oxygen isotope composition, clumped isotope composition, and trace metal content, may correlate with CAS alteration and refine estimates of the best-preserved $\delta^{34}S$. However, Chapter 4 of this thesis demonstrates that much diagenetic alteration of CAS $\delta^{34}S$ occurs during the earliest marine diagenesis, which often does not impart large carbon or oxygen isotope gradients that might create covariation with CAS.

Brachiopod CAS $\delta^{34}S$ compositions reported here match the compositions (24.86‰ ± 0.40‰ 2σ s.e.) of Katian, Hirnantian, and Rhuddanian brachiopods spanning the Late Ordovician Mass Extinction on Anticosti Island (Present et al., 2015). Kampschulte and Strauss (2004) and Wu et al. (2014) additionally report similar $\delta^{34}S$ compositions from brachiopods of Sandbian to Pridoli age (Figure 5). There is a data gap in the Telychian Stage that could be filled with analyses of brachiopods from the Jupiter Formation on Anticosti Island, which Came et al. (2007) demonstrated are well-preserved and retain Silurian-age seawater oxygen isotopic compositions. Therefore, given the inability to distinguish trends in the isotopic composition of Late Ordovician through Silurian seawater sulfate, it is most parsimonious to assume that it remained constant for at least 30 Myr.

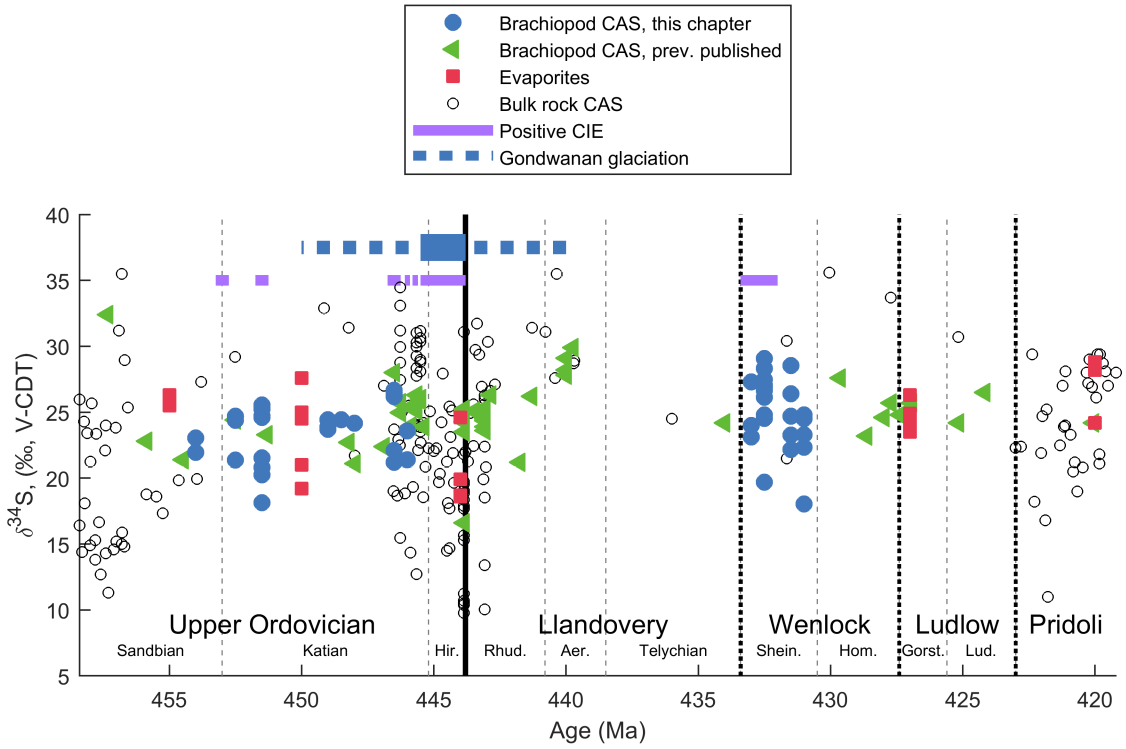

Figure 5: CAS and evaporite $\delta^{34}S$ record of the Upper Ordovician and Silurian. Purple bars mark the duration of positive carbon isotope excursions (CIE) (Bergström et al., 2010a; Cramer et al., 2010; Jones et al., 2011). Blue bar marks the duration of glaciation of Gondwana (Finnegan et al., 2011). Previously published brachiopod data from Present et al. (2015), Kampschulte and Strauss (2004), and Wu et al. (2014). Evaporite data from Thode and Monster (1965), Claypool et al. (1980), Holser and Kaplan (1966), Ault and Kulp (1959), Sakai (1972), and Yeremenko and Pankina (1972). Bulk rock CAS data from Kampschulte and Strauss (2004), Gill et al. (2007), Present et al. (2015), Jones and Fike (2013), Thompson and Kah (2012), and Young et al. (2016).

Additionally, the indistinguishable CAS $\delta^{34}S$ compositions come from globally-dispersed brachiopods in different depositional environments. Lexington Limestone brachiopods are from a high-energy, subtidal ramp in an epicontinental foreland basin on Laurentia (Pope and Read, 1997). Cincinnati Series brachiopods are from a lower-energy but shallower, peritidal environment in the same foreland basin (Holland, 1993; Holland and Patzkowsky, 1996). Anticosti Island brachiopods are from a high-energy ramp in a different Laurentian foreland basin during the Taconic Orogeny, which became increasingly restricted but remained subtidal throughout the Hirnantian glaciation (Copper et al., 2013; Copper and Jin, 2014; Desrochers et al., 2010; Jones et al., 2011). Finally, Gotland brachiopods are from a stable cratonic margin on Baltica (Calner et al., 2004; Samtleben et al., 1996).

A constant, globally-homogenous seawater $\delta^{34}S$ during the Late Ordovician and Silurian is striking due to the assortment of climatic, ecologic, and tectonic changes that affected the isotopic compositions of pyrite, carbonate, and organic carbon buried over this interval(e.g. Bergström et al., 2010a; Jones and Fike, 2013; Kump et al., 1999; Pancost et al., 1999; Patzkowsky et al., 1997; Young et al., 2005). A positive carbon isotope excursion in the early Katian coincided with regional extinction events and may have increased organic carbon burial, contributing to Late Ordovician global cooling and glaciation of Gondwana (Bergström et al., 2010a; Pancost et al., 1999; Patzkowsky et al., 1997; Young et al., 2005). In the Hirnantian, increased glacial severity, loss of shelf area, and global cooling drove the LOME (Finnegan et al., 2012, 2011), which may have been exacerbated by shoaling of euxinic waters onto remaining shelf environments after glacial termination (Hammarlund et al., 2012; Zou et al., 2018), coincided with synchronous positive isotope excursions in carbonate carbon, organic carbon, and pyrite sulfur (Brenchley et al., 1994; Hammarlund et al., 2012; Jones and Fike, 2013). Finally, additional regional faunal changes coincided with a series of global positive carbonate carbon isotope excursion and ocean circulation changes in the Sheinwoodian Stage (Bickert et al., 1997; Jeppsson, 1990; Munnecke et al., 2003).

Many of these events have been attributed to marine stratification and development of euxinic water masses, either regionally or globally. Euxinia could enhance burial and preservation of organic carbon and pyrite. However, our data indicates that the $\delta^{34}S$ of seawater sulfate remained globally mixed in the ocean. Jones and Fike (2013) suggested that Hirnantian positive pyrite sulfur isotope excursion was driven by decreasing sulfur isotope fractionation during the glaciation because more—and more labile—organic carbon was buried coincident with the positive carbon isotope excursion. They note that even if widespread increases in euxinia increased pyrite burial, the mass balance of sulfate in the ocean was not sufficiently perturbed to drive synchronous sulfur isotope excursions in pyrite and sulfate. Our data similarly suggests that, even if euxinia episodically expanded in deepwater environments and shoaled to exacerbate the LOME (Hammarlund et al., 2012), integrated pyrite burial did not change over multiple seawater sulfate residence times. Increased weathering of carbonate rocks exposed at the Hirnantian glacial maximum may

also have contributed to the carbon isotope excursion (Kump et al., 1999), but changes in weathering apparently did not affect the $\delta^{34}S$ of seawater sulfate.

Conclusions

We report CAS $\delta^{34}S$ compositions from well-preserved brachiopod calcite from the Upper Ordovician Cincinnati Arch, USA and from the Sheinwoodian Gotland, Sweden. Diagenetic alteration of the $\delta^{34}S$ of brachiopod CAS creates 3-5‰ of variability between brachiopods in the same bed or specimens of the same brachiopod. That these $\delta^{34}S$ data are indistinguishable from each other, and from other globally-distributed brachiopod CAS $\delta^{34}S$ data, suggests that seawater sulfate composition was constant and globally well-mixed for at least 30 Myr, despite major biogeochemical reorganizations. As Earth's climate transitioned from a Late Ordovician glacial climate to a Silurian greenhouse, significant carbon isotope excursions reflect changes in weathering or carbon burial, and pyrite sulfur isotope excursions reflect changes in ventilation or organic carbon respiration. However, flux changes in sulfate weathering or pyrite burial were either too short-lived or minor to resolve in the CAS $\delta^{34}S$ record. Additional sampling from the lower Silurian on Anticosti Island and further geochemical and petrographic characterization of the brachiopods may improve the quality of the $\delta^{34}S$ record.

Acknowledgements

Thank you to Kristin Bergmann and Seth Finnegan for sample collection and guidance, Renata Cummins for giving us laboriously-picked brachiopods, Jared Marske for patient help with the mass spectrometry, and James Rae and Andrea Burke for stimulating discussion and motivation.

Supplemental Data Table

Supplemental Table 1: Sample names, stratigraphic assignment, and preservation of picked brachiopod flakes. X indicates a diagenetic texture was observed. R = recrystallized, M = residual matrix or cement, D = discolored, O = opaque, I = mineral inclusions, PS = preservation score (0 = best, 5 = worst).

No.	Sample	Formation	Member	Period	Stage	R	M	D	O	I	PS	Mass (mg)
Br-001	G13 1.0 to 2.0	Slite		Silurian	Sheinwoodian		X				1	11.58
Br-002	HC-K 18m-19.5m	Kope	Economy	Ordovician	Edenian		X	X		X	3	4.22
Br-003	SGH-L 48.5m	Lexington		Ordovician	Franklinian		X	X			2	40.26
Br-004	SGH-W 42.5 ~1.5m below min Flexycalymere bed	Waynesville	Blanchester	Ordovician	Richmondian			X			1	31.94
Br-005	TFP-M 2.4-2.7	Fairview	Miamitown	Ordovician	Maysvillian		X	X			2	22.09
Br-006	G2 0.4 to 0.6	Upper Visby		Silurian	Sheinwoodian			X		X	2	12.49
Br-007	SGH-A 4.8m Top Oregonia	Arnheim		Ordovician	Richmondian	X	X	X	X	X	5	14.47
Br-008	MCb-K constrained float	Kope		Ordovician	Edenian	X	X	X			3	42.73
Br-009	G13 31.4 to 32.4	Slite		Silurian	Sheinwoodian	X		X			2	42.25
Br-010	SGH float above 13m below 3rd bench Waynesville: black flakes	Waynesville		Ordovician	Richmondian	X	X	X	X		4	42.43
Br-011	SGH float above 13m below 3rd bench Waynesville: beige flakes	Waynesville		Ordovician	Richmondian	X	X	X	X		4	58.49
Br-012	G11 0.0 to 0.2 B1	Upper Visby		Silurian	Sheinwoodian			X	X		2	57.49
Br-013	G13 33.4 B1	Slite		Silurian	Sheinwoodian	X		X			2	24.12
Br-014	TFP-B Bellevue Float	Grant Lake	Bellevue	Ordovician	Maysvillian	X		X			2	13.98

No.	Sample	Formation	Member	Period	Stage	R	M	D	O	I	PS	Mass (mg)
Br-015	G13 6.5 to 7.5 B4	Slite		Silurian	Sheinwoodian						0	10.23
Br-016	TFP-CV Float	Grant Lake (?)	Corryville (?)	Ordovician			X				1	7.37
Br-017	Dickeyville Roadcut Platteville	Platteville Group (?)		Ordovician	Sandbian (?)	X	X	X	X		4	39.11
Br-018	MCc-F 4.8-5.0	Fairview	Mount Hope	Ordovician	Maysvillian	X	X	X	X		4	81.59
Br-019	MCc-K 0.2(1)	Kope		Ordovician	Edenian	X		X			2	10.39
Br-020	MCc-K 0.2(2) (seconds)	Kope		Ordovician	Edenian	X	X	X	X		4	6.16
Br-021	G1 -0.6 to -0.4 B1(1)	Lower Visby		Silurian	Sheinwoodian					X	1	26.78
Br-022	G1 -0.6 to -0.4 B1(2) (seconds)	Lower Visby		Silurian	Sheinwoodian		X			X	2	9.24
Br-023	G2 0.2 to 0.4 B3	Upper Visby		Silurian	Sheinwoodian	X					1	6.38
Br-024	G13 6.5 to 7.5 B2	Slite		Silurian	Sheinwoodian						0	4.88
Br-025	SGH-W 9.3 B1	Waynesville		Ordovician	Richmondian	X		X			2	5.01
Br-026	SGH-L 49.8m	Lexington		Ordovician	Franklinian	X					1	46.57
Br-027	MCb-6.4	Kope (?)		Ordovician		X		X			2	13.72
Br-028	SGH-W 13.0m	Waynesville		Ordovician	Richmondian	X		X	X		3	24.99
Br-029	SCE-K 2.0-3.0m	Kope		Ordovician	Edenian	X		X		X	3	9.74
Br-030	FN-1 4.4m	(?)		Ordovician		X	X				2	5.34
Br-031	G13 31.4 to 32.4 B3	Slite		Silurian	Sheinwoodian			X			1	15.28
Br-032	G11 0.4 to 0.6 B2 (Cummins et al., 2014)	Upper Visby		Silurian	Sheinwoodian						0	2.28
Br-033	G1 -1.2 to -0.8 B1 (Cummins et al., 2014)	Lower Visby		Silurian	Sheinwoodian					X	1	7.10

No.	Sample	Formation	Member	Period	Stage	R	M	D	O	I	PS	Mass (mg)
Br-034	G4 2.0 to 3.0 B1 (Cummins et al., 2014)	Upper Visby		Silurian	Sheinwoodian						0	13.72
Br-035	G2 0.5 to 0.6 B1 (Cummins et al., 2014)	Upper Visby		Silurian	Sheinwoodian						0	13.44
Br-036	G13 31.4 to 32.4 B1 (Cummins et al., 2014)	Slite		Silurian	Sheinwoodian			X		X	2	9.24
Br-037	SGH-WW Float excavated from Trackway B1	Whitewater		Ordovician	Richmondian	X		X	X	X	4	11.33
Br-038	G13 5.0 to 6.0 B1 (Cummins et al., 2014)	Slite		Silurian	Sheinwoodian						0	2.27
Br-039	G11 0.4 to 0.6 B1 (Cummins et al., 2014)	Upper Visby		Silurian	Sheinwoodian						0	2.15
Br-040	G11 0.2 to 0.4 B1 (Cummins et al., 2014)	Upper Visby		Silurian	Sheinwoodian						0	2.38
Br-041	G8 1.2 to 2.0 B1 (Cummins et al., 2014)	Slite		Silurian	Sheinwoodian						0	3.72
Br-042	G11 0.6 B1 (Cummins et al., 2014)	Upper Visby		Silurian	Sheinwoodian						0	4.56
Br-043	G3 0.0 B1 (Cummins et al., 2014)	Upper Visby		Silurian	Sheinwoodian						0	2.59
Br-044	G13 35.6 to 36.0 B1 (Cummins et al., 2014)	Slite		Silurian	Sheinwoodian						0	2.52
Br-045	G2 0.0 to 0.2 B1 (Cummins et al., 2014)	Upper Visby		Silurian	Sheinwoodian						0	2.60

Chapter 4

DIAGENETIC CONTROLS ON THE ISOTOPIC COMPOSITION OF CARBONATE-ASSOCIATED SULFATE IN THE PERMIAN CAPITAN REEF COMPLEX, WEST TEXAS

Theodore M. Present[1], Melissa Gutierrez[1], Guillaume Paris[2], Charles Kerans[3], John P. Grotzinger[1], Jess F. Adkins[1]

[1]California Institute of Technology, Pasadena, California, USA
[2]Centre de Recherches Pétrographiques et Géochimiques, Nancy, France
[3]University of Texas at Austin, Austin, Texas, USA

Abstract

Late Paleozoic-age strata from the Capitan Reef in west Texas show facies-dependent heterogeneity in the sulfur isotopic composition of carbonate-associated sulfate, which is trace sulfate incorporated into carbonate minerals that is often used to reconstruct the sulfur isotopic composition of ancient seawater. The sulfur isotopic composition of carbonate-associated sulfate may have been influenced by diagenetic pore fluid processes. These processes variously modify the sulfur isotopic composition of incorporated sulfate from syndepositional seawater in shelf crest, outer shelf, shelf margin, and slope depositional settings. Carbonates representing peritidal facies in the Yates and Tansill formations preserve the sulfur isotopic composition of Guadalupian seawater sulfate despite alteration of the carbon and oxygen isotopic compositions by meteoric and dolomitizing diagenetic processes. However, limestones deposited in reef and slope facies in the Capitan and Bell Canyon Formations largely incorporate sulfate from anoxic marine-phreatic pore fluids that is isotopically modified from seawater by microbial sulfate reduction, despite generally preserving the carbon and oxygen isotopic compositions of Permian seawater. Both early and late meteoric calcite cements have carbonate-associated sulfate with sulfur isotopic compositions distinct from that of Permian seawater. Detailed petrographic and sedimentary context for carbonate-associated sulfate analyses will allow for improved reconstructions of ancient seawater composition and diagenetic conditions in ancient carbonate platforms. The

results of this study indicate that carbonates that diagenetically stabilize in high energy environments without pore fluid sulfate gradients can provide a robust archive of ancient seawater's sulfur isotopic composition.

Introduction

Sulfate—a metabolically-available, major ion in seawater—links the cycles of carbon, oxygen, and iron through Earth's ocean (Bottrell and Newton, 2006; Garrels and Lerman, 1984). Small amounts are incorporated into the lattice of carbonate minerals (called Carbonate Associated Sulfate [CAS]; Burdett et al., 1989; Kampschulte and Strauss, 2004) and its sulfur isotopic composition (reported in $\delta^{34}S$ notation as part-per-thousand changes in $^{34}S/^{32}S$ from the Vienna-Canyon Diablo Troilite [V-CDT] reference standard) may track that of the ancient seawater from which the minerals precipitated. A history of seawater sulfate's $\delta^{34}S$ composition constrains ancient biogeochemical budgets because secular enrichment in the $\delta^{34}S$ of seawater sulfate represents increased burial of sulfide with lower $\delta^{34}S$ produced by anoxic microbial sulfate reduction (MSR) (Garrels and Lerman, 1984).

In Precambrian through early Mesozoic successions, CAS data with different isotopic compositions imply a low, heterogeneous, and rapidly changing marine sulfate reservoir, especially during biotic crises (Algeo et al., 2015; Bernasconi et al., 2017; Gill et al., 2007, 2011b; John et al., 2010; Kah et al., 2004; Li et al., 2009; Loyd et al., 2012b; Marenco et al., 2008b; Newton et al., 2004; Schobben et al., 2017b; Sim et al., 2015; Song et al., 2014; Thompson and Kah, 2012; Witts et al., 2018; Wotte et al., 2012b; Yan et al., 2013; L. Zhang et al., 2015). However, few studies have systematically examined the role of depositional setting, including overprinting diagenetic regimes, on the isotopic composition of CAS (e.g. Marenco et al., 2008b; Wotte et al., 2012b), despite chemostratigraphic records being constructed from various paleoenvironments. Was Paleozoic seawater sulfate indeed heterogeneous?

Well-preserved biogenic calcite appears to preserve primary seawater sulfur isotopic compositions (Gill et al., 2011a; John et al., 2010; Kampschulte et al., 2001; Kampschulte and Strauss, 2004; Newton et al., 2011; Present et al., 2015; Witts et al., 2018; Wu et al.,

2014), but such material is limited in the geologic record. Other studies of CAS in bulk carbonate material conclude that early diagenetic processes such as neomorphism, dolomitization, and authigenic cementation may incorporate sulfate from diagenetically-modified or non-seawater fluids (Baldermann et al., 2015; Feng et al., 2016; Fichtner et al., 2017; Gill et al., 2008; Goldberg et al., 2005; Loyd et al., 2012a; Present et al., 2015; Rennie and Turchyn, 2014; Riccardi et al., 2006). Screening for the effect of such processes typically entails textural, trace metal, and carbon and oxygen isotope analyses associated with meteoric or burial diagenesis that may not correlate with sulfur isotope alteration (Fichtner et al., 2017; Gill et al., 2011a, 2011b; Goldberg et al., 2005; Yan et al., 2013). Because the early diagenetic history of a rock varies with its depositional setting, a thorough accounting of early diagenetic effects on CAS $\delta^{34}S$ requires detailed sedimentological context.

To discern the sulfur isotope composition of ancient seawater when biogenic calcite is unavailable or poorly preserved, CAS analyses are here considered in the context of a regional depositional facies model and diagenetic framework. CAS and carbonate carbon and oxygen isotope results are reported from the late Guadalupian-age platform and slope carbonates of the Capitan Reef in the Permian Basin, West Texas. In outcrop, detailed biostratigraphic and sequence stratigraphic models tightly constrain shelf-to-basin correlations (Borer and Harris, 1991; Kerans and Tinker, 1999; Lambert et al., 2002; Osleger, 1998; Rush and Kerans, 2010; Silver and Todd, 1969; Tyrrell Jr, 1969; Wilde et al., 1999). This allows comparison of the $\delta^{34}S$ of CAS in carbonates deposited in the same body of water, but in different depositional settings. Further, well-documented petrographic and geochemical features in these carbonates record diverse diagenetic processes during deposition, burial, and uplift (Frost et al., 2012; Garber et al., 1989; Given and Lohmann, 1986; Mazzullo, 1999; Mazzullo and Cys, 1977; Melim and Scholle, 1999; Mruk, 1989; Mutti and Simo, 1994, 1993; Newell et al., 1953; Schmidt, 1977; Scholle et al., 1992; Yurewicz, 1977). Understanding the depositional environments and diagenetic regimes that affect CAS allows further exploration of the expression of sedimentary biogeochemical processes in the rock record.

Geologic and geochemical setting

The Capitan Reef rims a mixed carbonate and siliciclastic shelf that surrounded the restricted, epeiric seawater of the Delaware Basin during the late Guadalupian Epoch (Figure A) (King, 1942; Lang, 1937; Ward et al., 1986). Following burial, Cenozoic extension exhumed part of the Capitan Reef in the Northwest Shelf province of the Delaware Basin; it is exposed as largely structurally-intact outcrop in western Texas and southern New Mexico in the Guadalupe Mountains (King, 1948, 1942; Lang, 1937). Detailed biostratigraphic and sequence stratigraphic work allows precise correlation of lithostratigraphic units and timelines from shelf to basin (Figure 2) (Borer and Harris, 1991; Kerans and Tinker, 1999; Lambert et al., 2002; Osleger, 1998; Rush and Kerans, 2010; Silver and Todd, 1969; Tyrrell Jr, 1969; Wilde et al., 1999). Samples for this study were collected from the Yates, Tansill, Capitan, and Bell Canyon formations, whose stratigraphy and diagenesis are described below.

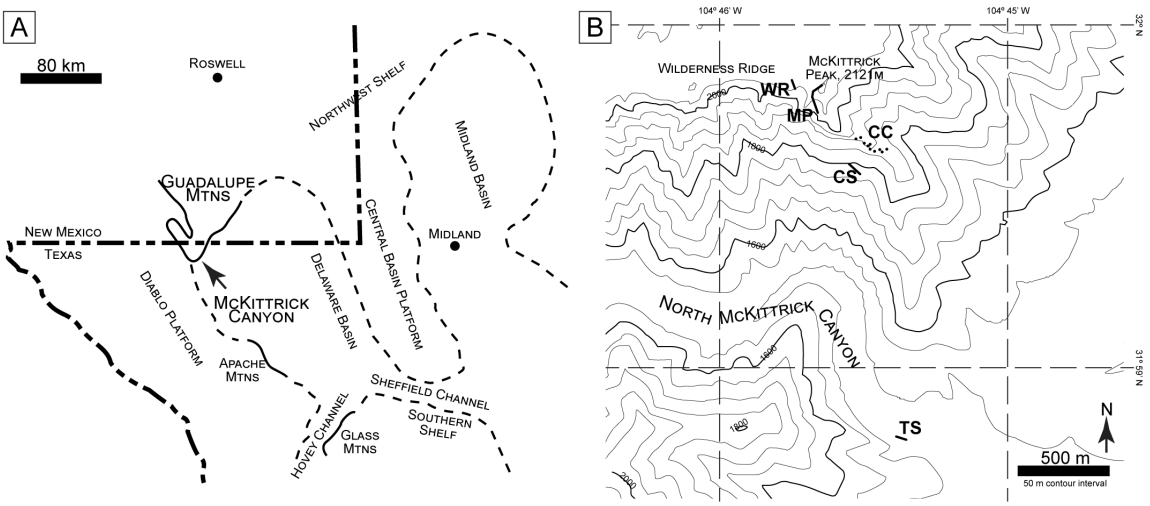

Figure 1: A) Paleogeography of the Delaware Basin during deposition of the upper Capitan Formation reef modified from Ward et al. (1986) showing the location of the Permian Reef shelf margin in outcrop (solid line) and the subsurface (dashed line). The arrow shows the location of McKittrick Canyon in the Guadalupe Mountains, west Texas. B) Topographic map of North McKittrick Canyon in the Guadalupe Mountains National Park showing the locations of measured stratigraphic sections on Wilderness Ridge (WR), McKittrick Peak (MP), Capitan Formation Slope (CS), and Bell Canyon Formation Toe-of-Slope (TS). Dots on the cliff (CC) indicate sample positions from the massive facies of Capitan Formation that were collected without a measured stratigraphic section. Map assembled with GeoMapApp v3.6.6 (www.geomapapp.org) using topographic data from Ryan et al. (2009).

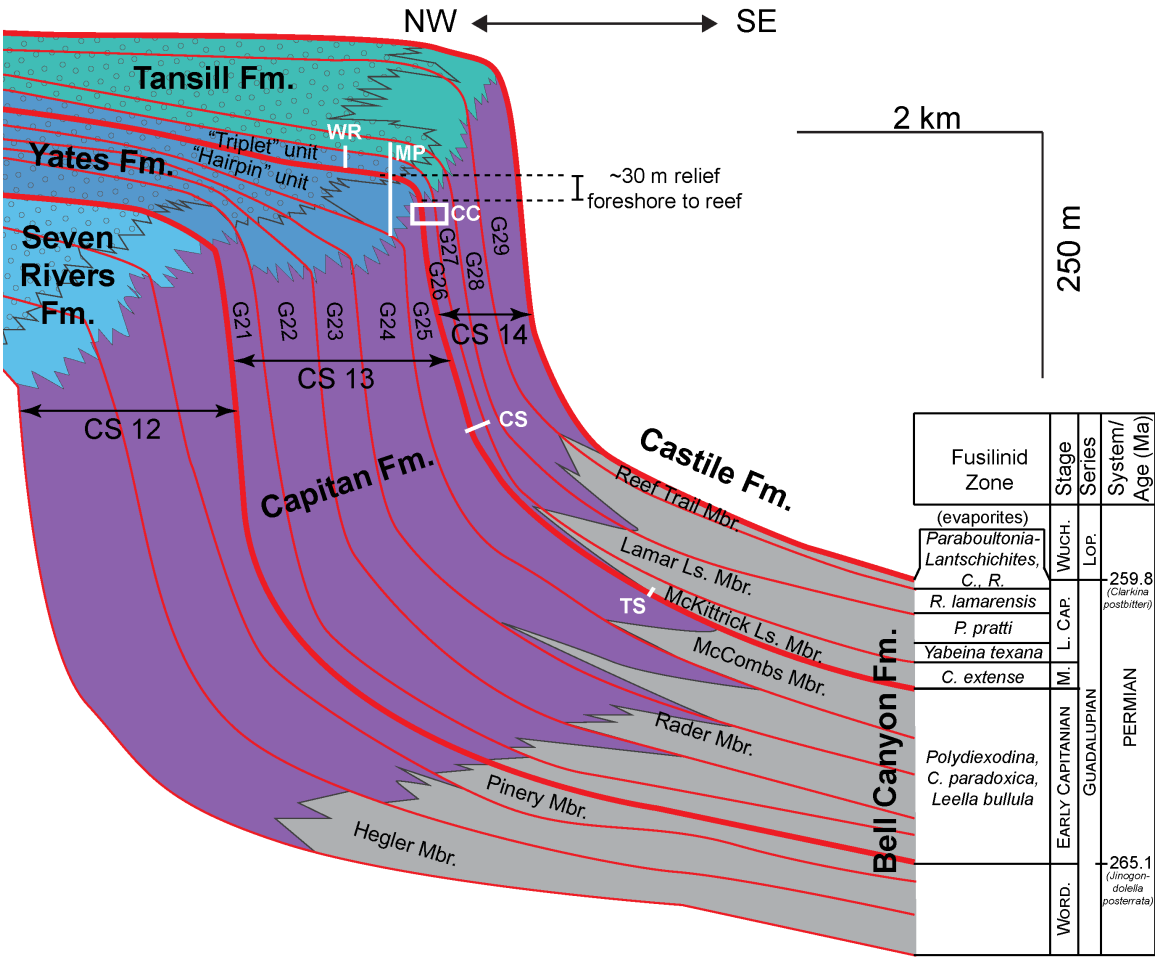

Figure 2: Correlation of lithostratigraphy, biostratigraphy, and sequence stratigraphy of the Guadalupian-age strata modified from Tinker (1998), Kerans & Tinker (1999), and Rush & Kerans (2010). Bold red lines delineate Composite Sequence boundaries, and thin red lines delineate High Frequency Sequence boundaries. White lines show the locations of measured stratigraphic sections on Wilderness Ridge (WR), McKittrick Peak (MP), Capitan Formation Slope (CS), and Bell Canyon Formation Toe-of-Slope (TS). White box indicate where on the Capitan Formation cliffs (CC) samples from the massive reef facies were collected without a measured stratigraphic section. Dotted pattern delineates the shelf crest facies tract extent. Fusilinid zones from Wilde et al. (1999). Absolute ages based on conodont biostratigraphy by Lambert et al. (2002) and updated to the ICS v2016/04 timescale (Cohen et al., 2013; updated). Fm. = Formation, Ls. = Limestone, Mbr. = Member, *C.* = *Codonofusiella*, *R.* = *Reichelina*, *P.* = *Paradoxiella*, Word. = Wordian, M. = Middle Capitanian, L. Cap. = Late Capitanian, Wuch. = Wuchiapingian, Lop. = Lopingian.

The northern wall of North McKittrick Canyon, in Guadalupe Mountains National Park, hosts a well-exposed shelf-to-basin transect made accessible by the Permian Reef Geology Trail (Bebout and Kerans, 1993; King, 1942; Newell et al., 1953). Well-bedded shelf dolomites and sandstones of the Yates Formation interfinger with massive and poorly-

bedded reef and slope dolomitic limestones of the middle Capitan Formation, which in turn pass laterally into well-bedded basinal limestones and sandstones of the Bell Canyon Formation (Babcock and Yurewicz, 1989; King, 1942) (Figure 2). Dolomites of the Yates Formation interfinger up-dip to the northwest with well-bedded evaporite-rich lagoonal facies (Borer and Harris, 1991; King, 1942). The Capitan and Bell Canyon Formations are overlain by thick, basin-filling evaporites of the Castile Formation, and the Yates Formation is overlain by more shelf deposits of the Tansill Formation, which interfingers with the upper Capitan Formation (Babcock and Yurewicz, 1989; DeFord and Riggs, 1941; King, 1942). The Yates Formation overlies older shelf deposits of the Seven Rivers Formation (King, 1942).

Two informal lithostratigraphic units— the "Hairpin" and the "Triplet"— in the upper Yates Formation record sea level changes on the shelf (Neese and Schwartz, 1977). The Hairpin dolomite is correlated through the Capitan Formation and into the McCombs Limestone Member of the Bell Canyon Formation (Kerans and Kempter, 2002; Kerans and Tinker, 1999; King and Newell, 1956; Newell et al., 1953; Osleger, 1998; Osleger and Tinker, 1999; Rush and Kerans, 2010; Tinker, 1998). The unconformably-overlying "Triplet" consists of a lower sandstone unit, a middle dolomite unit, and an upper sandstone unit (Neese and Schwartz, 1977). The lower and middle units of the Triplet correlate to a limestone tongue in the Bell Canyon Formation known as the McKittrick Canyon Limestone (Brown, 1996; Rush and Kerans, 2010; Wilde et al., 1999). The upper sandstone unit of the Triplet and the overlying basal dolomite unit of the Tansill Formation correlate to the Lamar Limestone Member of the Bell Canyon Formation (Tyrrell Jr, 1969).

Each set of genetically-related strata (i.e., the Hairpin with the McCombs Limestone, the lower and middle Triplet with the McKittrick Limestone, and the upper Triplet and basal Tansill with the Lamar Limestone) is a locally unconformity-bounded package called a High Frequency Sequence (HFS) composed of higher-order cycle sets; they are the Guadalupian 25 (G25), Guadalupian 26 (G26), and Guadalupian 27 (G27) HFSs, respectively (Kerans and Kempter, 2002; Osleger and Tinker, 1999; Rush and Kerans, 2010; Tinker, 1998). HFSs

represent fourth-order cyclic accommodation fluctuations and record deposition over ~100-650 kyr (Borer and Harris, 1991; Goldhammer et al., 1990; Rush and Kerans, 2010). Third-order cycles— comprised of multiple HFSs and called Composite Sequences (CSs)—represent 1-3 Myr of deposition (Goldhammer et al., 1990; Tinker, 1998). The G25 HFS is the last sequence of the Permian CS 13, with a major unconformity at the top of the Hairpin unit separating it from the overlying G26 and G27 HFSs of the Permian CS 14 (Kerans and Kempter, 2002; Kerans and Tinker, 1999; Osleger and Tinker, 1999; Rush and Kerans, 2010; Tinker, 1998).

Tinker (1998) classified McKittrick Canyon facies by their lithology, texture, grain composition, and sedimentary structures. Some of these include barrier island tepee-pisolite complexes and foreshore grainstones and rudstones (Figure 3A); shelf algal and coated grain grainstones, rudstones, and packstones (Figure 3B); shelf margin skeletal-peloid wackestones and reef boundstones and framestones (Figure 3C); and slope conglomerates, rudstones, and lithoclast packstones (Figure 3D) (Borer and Harris, 1991; Dunham, 1972; Esteban and Pray, 1983; Garber et al., 1989; Mutti and Simo, 1993; Tinker, 1998). Early diagenetic and shallow burial processes varied with stratigraphic position and included neomorphism and dissolution of aragonite or high-Mg calcite grains; precipitation of aragonite, calcite, dolomite, and anhydrite cements; silicification; mimetic dolomitization; and compaction and fracturing (Frost et al., 2012; Garber et al., 1989; Given and Lohmann, 1986; Mazzullo, 1999; Mazzullo and Cys, 1977; Melim and Scholle, 1999; Mruk, 1989; Mutti and Simo, 1993; Newell et al., 1953; Schmidt, 1977; Yurewicz, 1977). Deeper burial diagenetic processes included further fabric destructive dolomite recrystallization and anhydrite and carbonate dissolution (Garber et al., 1989; Melim and Scholle, 1999; Mutti and Simo, 1994, 1993; Schmidt, 1977). During uplift of the Guadalupe Mountains, further calcite spar precipitation replaced evaporite cements (Mazzullo, 1999; Mruk, 1989; Schmidt, 1977; Scholle et al., 1992).

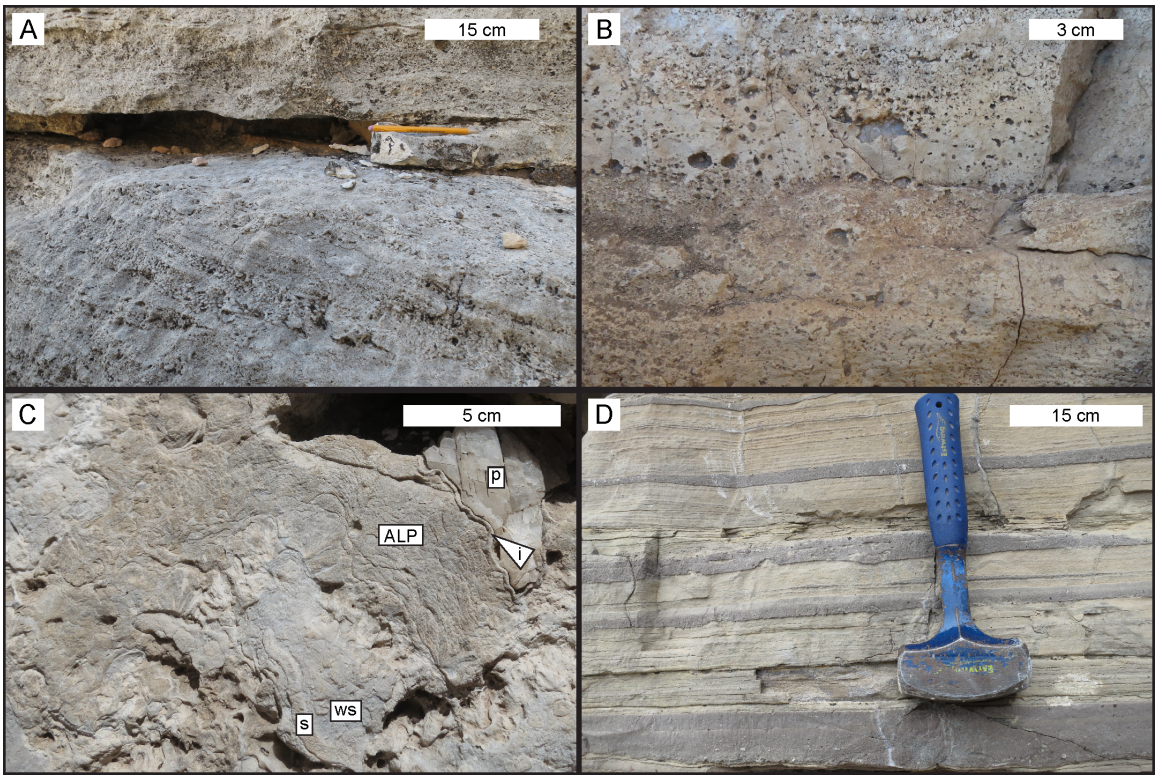

Figure 3: Outcrop photographs of typical lithologies in each facies tract. A) Dolomite cross-bedded oncoid-Polydiexodina rudstone in the shelf crest facies tract. B) Dolomite fenestral coated grain-mollusk packstone/grainstone capping a cycle set in the outer shelf facies tract. Many fenestrae are solution-enlarged and filled by sparry calcite. C) Limestone cement-sponge boundstone in the reef facies of the shelf margin facies tract. A sponge (s) is encrusted by *Archaeolithoporella* and botryoidal cements (*Archaelithoporella*). Internal cavities in the reef are filled by wackestone (ws), isopachous cement (i), and late poikilitic calcite spar (p). D) Limestone lithoclast-skeletal packstone/grainstone gravity flow beds (gray) interbedded with dolomitic laminated mudstone-wackestone (beige) from the toe-of-slope in the slope facies tract.

The $\delta^{34}S$ of sulfate in Delaware Basin seawater can be constrained to about 10‰ V-CDT by the composition of bedded evaporites in the inner shelf facies of the Seven Rivers Formation (Sarg, 1981) and varved evaporites in the Castile Formation (Hill, 1990; Holser and Kaplan, 1966; Kirkland et al., 2000; Leslie et al., 1997; Thode et al., 1961). The reef facies contains abundant early marine cements and evidence for syndepositional brittle fracture and failure of the shelf margin that suggest unusually high carbonate saturation states for Phanerozoic basins (Babcock and Yurewicz, 1989; Grotzinger and Knoll, 1995; Mruk, 1989; Rush and Kerans, 2010; Stanton and Pray, 2004). Given and Lohmann (1985) measured the isotopic compositions of early marine cements in the Capitan Formation; the carbon and oxygen

isotopic compositions are reported in $\delta^{13}C$ and $\delta^{18}O$ notation as part-per-thousand changes in $^{13}C/^{12}C$ and $^{18}O/^{16}O$ from the Pee Dee Belemnite (PDB) reference standard. They argue that the $\delta^{18}O$ of primary aragonite marine cements was approximately -3‰ PDB, in agreement with data from well-preserved and globally distributed Capitanian brachiopods (Korte et al., 2005). Therefore, normal Capitanian marine conditions included warmer seawater and/or a lower $\delta^{18}O$ of seawater than the modern ocean (Given and Lohmann, 1985; Korte et al., 2005). The $\delta^{13}C$ of Delaware Basin primary marine cements and brachiopods are 5-7‰ PDB, which are among the heaviest of the Phanerozoic (Given and Lohmann, 1985; Korte et al., 2005; Mutti and Simo, 1993). These $\delta^{13}C$ values are heavier than contemporaneous Tethyan samples and may represent effects of restriction in the Delaware Basin or a difference between the Tethyan and Panthalassic seawater compositions (Korte et al., 2005).

Methods

One hundred and twenty samples were collected from four measured stratigraphic sections in the Yates, Tansill, Capitan, and Bell Canyon Formations spanning strata from the Hairpin unit to the lower Tansill Formation (i.e., the G25 through G27 HFSs) and their correlative down-dip strata, and assorted samples from G26 and G27-equivalent massive facies of the Capitan Formation (Figure B). We sampled to survey the range of facies identified by Tinker (1998) (Figure 4) and grouped samples by facies tracts, which are associated facies and successions of facies that characterize an energy, accommodation, and sediment supply regime (Rush and Kerans, 2010; Tinker, 1998). Polished slabs were prepared and a handheld rotary micro-drill was used to collect 265 sub-samples of 5-20 mg of various diagenetic and sedimentary textures. We analyzed the sub-samples for carbonate carbon and oxygen isotopic composition, CAS concentration, and CAS sulfur isotopic composition.

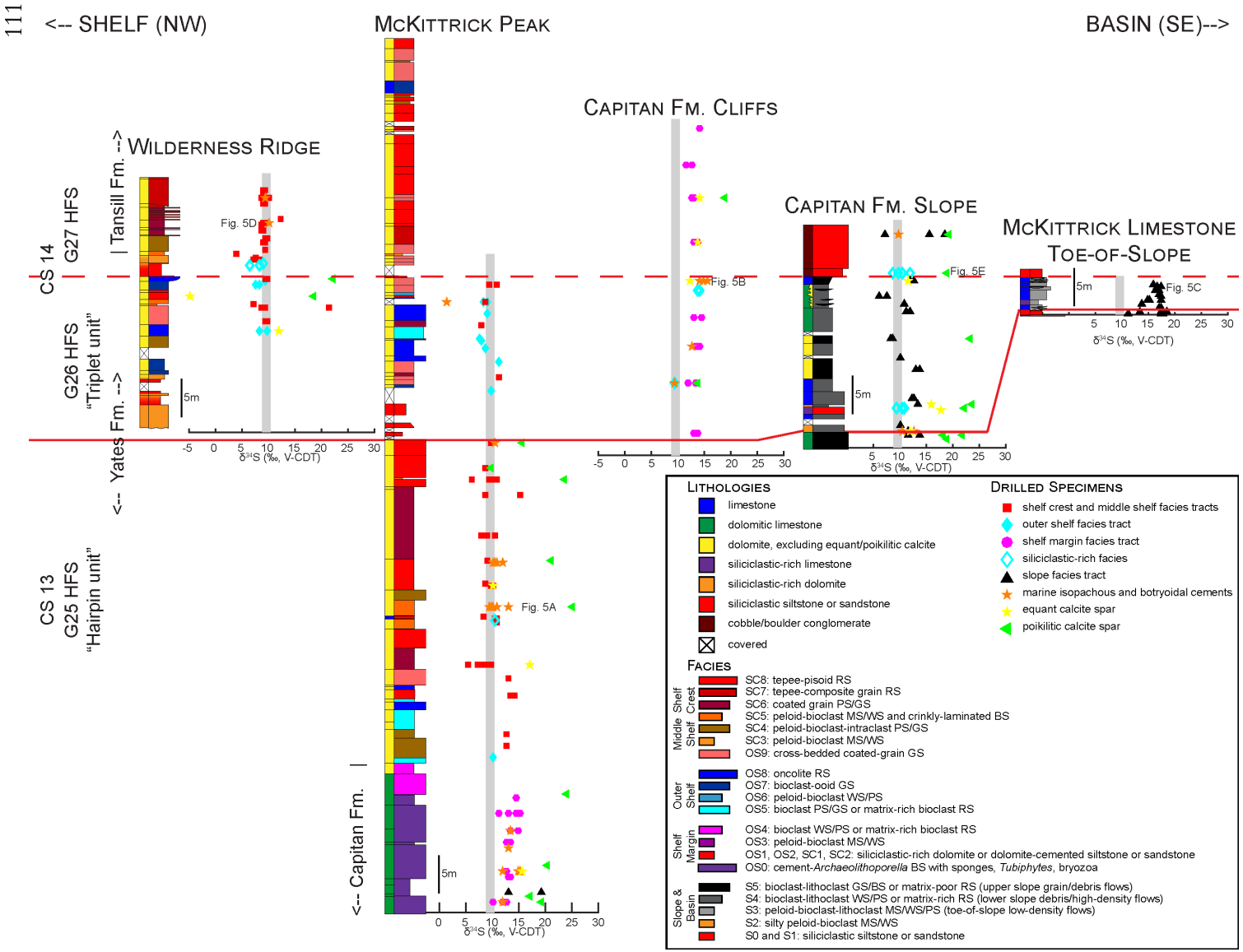
<-- SHELF (NW)
McKittrick Peak
BASIN (SE)-->
Wilderness Ridge
Capitan Fm. Cliffs
Capitan Fm. Slope
McKittrick Limestone Toe-of-Slope
CS 14
G27 HFS
| Tansill Fm. -->
G26 HFS
"Triplet unit"
<-- Yates Fm. -->
CS 13
G25 HFS
"Hairpin unit"
<-- Capitan Fm. |
Fig. 5A
Fig. 5B
Fig. 5C
Fig. 5D
Fig. 5E
5m
δ34S (‰, V-CDT)
Lithologies
limestone
dolomitic limestone
dolomite, excluding equant/poikilitic calcite
siliciclastic-rich limestone
siliciclastic-rich dolomite
siliciclastic siltstone or sandstone
cobble/boulder conglomerate
covered
Drilled Specimens
shelf crest and middle shelf facies tracts
outer shelf facies tract
shelf margin facies tract
siliciclastic-rich facies
slope facies tract
marine isopachous and botryoidal cements
equant calcite spar
poikilitic calcite spar
Facies
Middle Shelf Crest
SC8: tepee-pisoid RS
SC7: tepee-composite grain RS
SC6: coated grain PS/GS
SC5: peloid-bioclast MS/WS and crinkly-laminated BS
SC4: peloid-bioclast-intraclast PS/GS
SC3: peloid-bioclast MS/WS
OS9: cross-bedded coated-grain GS
Outer Shelf
OS8: oncolite RS
OS7: bioclast-ooid GS
OS6: peloid-bioclast WS/PS
OS5: bioclast PS/GS or matrix-rich bioclast RS
Shelf Margin
OS4: bioclast WS/PS or matrix-rich bioclast RS
OS3: peloid-bioclast MS/WS
OS1, OS2, SC1, SC2: siliciclastic-rich dolomite or dolomite-cemented siltstone or sandstone
OS0: cement-Archaeolithoporella BS with sponges, Tubiphytes, bryozoa
Slope & Basin
S5: bioclast-lithoclast GS/BS or matrix-poor RS (upper slope grain/debris flows)
S4: bioclast-lithoclast WS/PS or matrix-rich RS (lower slope debris/high-density flows)
S3: peloid-bioclast-lithoclast MS/WS/PS (toe-of-slope low-density flows)
S2: silty peloid-bioclast MS/WS
S0 and S1: siliciclastic siltstone or sandstone

Figure 4 *[prev. page]*: Measured stratigraphic sections and geochemical data from McKittrick Canyon. Facies are codified corresponding to Tinker (1998). Gray bars denote the $\delta^{34}S$ range of Delaware Basin evaporites in the Seven Rivers and Castile Formations (Hill, 1990; Holser and Kaplan, 1966; Kirkland et al., 2000; Sarg, 1981; Thode et al., 1961). The solid red line represents a timeline at the top of Composite Sequence 13, and the dashed red line represents a timeline at the top of High Frequency Sequence G26. Samples shown in Figure 5 are annotated. Samples from the massive shelf margin facies of the Capitan Formation were collected from the top and base of cliffy outcrops without measured sections, but timelines were biostratigraphically determined to be sub-vertical so longitude was used a proxy for age instead of stratigraphic height. MS = mudstone, WS = wackestone, PS = packstone, GS = grainstone, RS = rudstone, BS = boundstone

For carbonate carbon and oxygen isotope analysis, 50-200 μg of each sub-sample were weighed into 12 mL Labco Exetainer vials, which were then sealed with septum caps and flushed for 5 min with helium. The carbonate was digested for >2 hr at 72°C by adding 50-100 μL of 85% phosphoric acid through the septum cap with a syringe and needle. The evolved CO_2 was analyzed with a Thermo Fisher Scientific GasBench II maintained at 72°C coupled to a Thermo Fisher Scientific Delta V Plus isotope ratio mass spectrometer. The carbon and oxygen isotopic compositions of the evolved CO_2 were determined relative to the Vienna-Pee Dee Belemnite (V-PDB) reference standard by normalization to a laboratory CO_2 tank that was calibrated against the NBS-19 international calcite reference material. The oxygen isotopic composition of the dissolved carbonate was calculated from the acid fractionation factor of calcite dissolution at 72°C. Some samples were a mixture of calcite and dolomite, so reported $\delta^{18}O$ values may be as much as 1.3‰ too high if they were pure dolomite (Kim et al., 2015). Accuracy was monitored by running two in-house calcite standards in triplicate at the beginning and end of each analytical session. Precision was monitored by running a third in-house dolomite standard between every five samples, and was typically better than 0.2‰ for $\delta^{13}C$ and 0.3‰ for $\delta^{18}O$ (1σ standard deviations [s.d.]).

The remaining carbonate powder was then pre-cleaned of soluble sulfates by ultra-sonicating in 10% NaCl and rinsing three times with ultra-pure water (18.2 Ω-cm resistivity), centrifuging and discarding the supernatant with a pipette between each rinse. Samples were then transferred to acid-clean micro-centrifuge vials, dissolved in trace metal-clean 0.5 N hydrochloric acid, centrifuged, and pipetted away from any insoluble residue (Present et al., 2015). Sulfate was purified from its cation matrix by anion exchange chromatography (Paris et al., 2014a), after which its concentration was determined by ion chromatography using a

Dionex ICS-3000 system using three in-house concentration standards to assess accuracy and precision, which were better than 0.5% (1σ relative s.d.) (Paris et al., 2013; Present et al., 2015). CAS concentrations were calculated from the measured sulfate amount, and from the dry weights of the cleaned powder and the insoluble residue. Measuring sulfate concentrations after column purification permits improved intensity matching of samples to a bracketing standard for mass spectrometry, but may bias CAS concentration measurements towards lower values because a small amount of dissolved carbonate liquid remained with the insoluble residue (<10 μL of the 1 mL used to dissolve samples remained in the vials, i.e., <1% of the sample). CAS $\delta^{34}S$ was determined using a Thermo Fisher Scientific Neptune Plus multi-collector inductively-coupled plasma mass spectrometer with a Cetac Aridus II desolvating spray chamber by matrix matching and sample-standard bracketing with an in-house Na_2SO_4 standard (Paris et al., 2013, 2014a). Samples contained 3-550 nmol sulfate (typically ~50 nmol) and full procedural blanks were 0.33 ± 0.23 nmol (1σ s.d.). The long-term $\delta^{34}S$ reproducibility of ~18 nmol sulfate replicates from a dissolved deep sea coral consistency standard was 0.31‰ (1σ s.d.) and was 0.28‰ (1σ s.d.) for ~280 nmol sulfate replicates of a diluted seawater consistency standard. Reported precisions of isotope measurements (Appendix B) combine instrument stability, reproducibility of the same sulfate solution within an analytical session, and propagated uncertainty of the procedural blank composition and amount.

Results

A full list of petrographic descriptions and geochemical results is given in Appendix B. The CAS $\delta^{34}S$ data from McKittrick Canyon are highly variable, ranging from -4.7‰ to 25.2‰. Most data from a given hand sample are isotopically similar, and vary by only a few permil. Early diagenetic cements, such as isopachous and botryoidal cements, are of similar $\delta^{34}S$ to the allochems in the same hand sample (Figure 5). However, late, poikilitic calcite spar in vuggy, fracture, and breccia porosity is as much as 15‰ more enriched in ^{34}S than earlier depositional textures from the same hand sample (Figure 5A). Facies tract—and therefore depositional environment—better predicts a sample's CAS $\delta^{34}S$ than age or stratigraphic height; the full range of CAS $\delta^{34}S$ is expressed within the G26 HFS. Similarly, sponge-

cement boundstones or peritidal grainstones/rudstones are each of similar isotopic composition, regardless of the HFS in which they deposited (Figure 4). Barring the latest calcite spars, the CAS data cluster into distinct populations governed by their depositional facies tract (Figure 6). Samples from the shelf crest and outer shelf facies tracts have a mean $\delta^{34}S$ of 9.6‰. Samples from the shelf margin (reef) facies tract have a mean of 13.2‰, and samples from the slope facies tract are highly variable, ranging from 6.1‰ to 19.3‰.

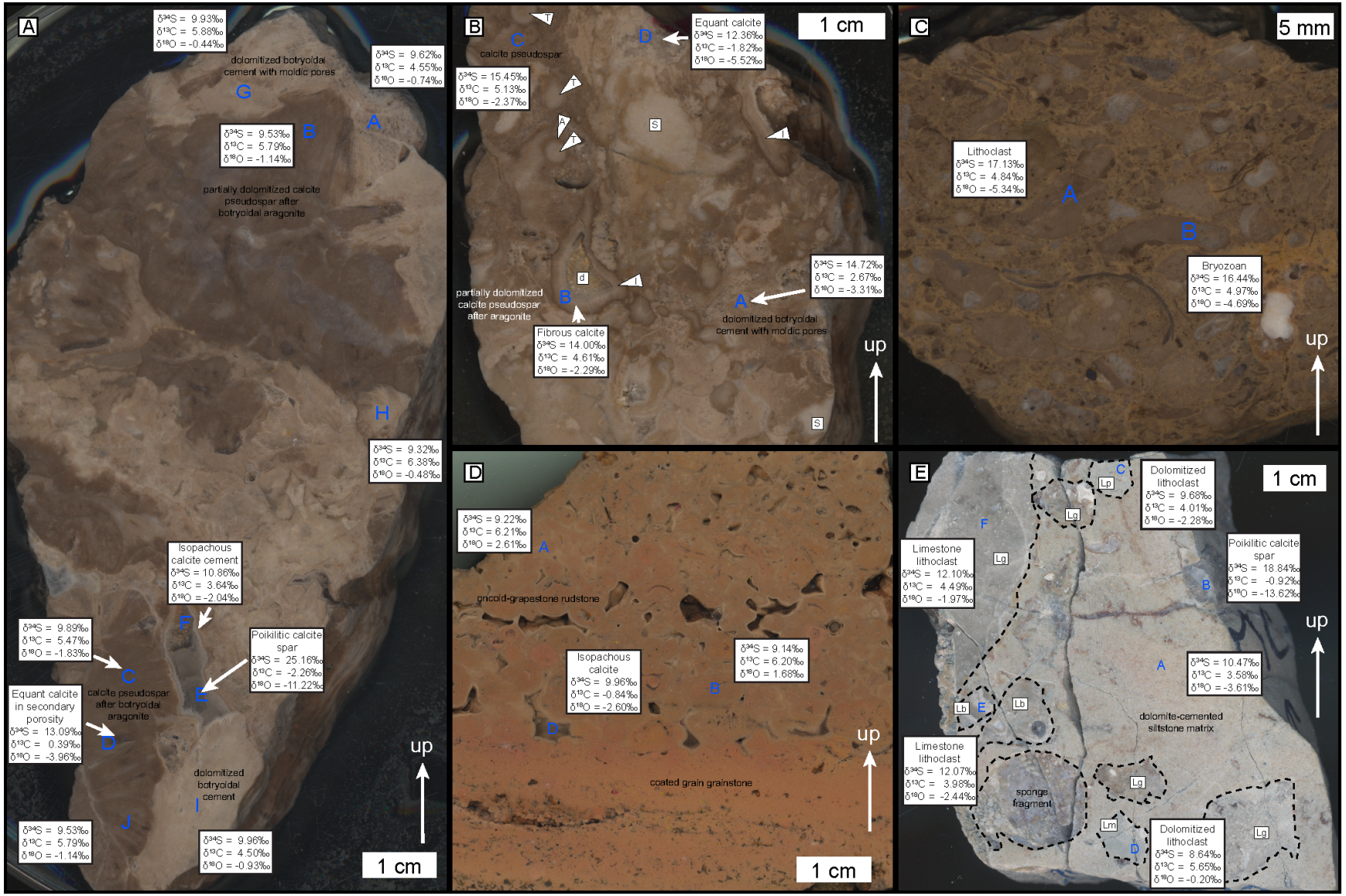
A
δ34S = 9.93‰
δ13C = 5.88‰
δ18O = -0.44‰
dolomitized botryoidal cement with moldic pores
δ34S = 9.62‰
δ13C = 4.55‰
δ18O = -0.74‰
G
A
δ34S = 9.53‰
δ13C = 5.79‰
δ18O = -1.14‰
B
partially dolomitized calcite pseudospar after botryoidal aragonite
H
δ34S = 9.32‰
δ13C = 6.38‰
δ18O = -0.48‰
Isopachous calcite cement
δ34S = 10.86‰
δ13C = 3.64‰
δ18O = -2.04‰
F
δ34S = 9.89‰
δ13C = 5.47‰
δ18O = -1.83‰
C
Poikilitic calcite spar
δ34S = 25.16‰
δ13C = -2.26‰
δ18O = -11.22‰
E
Equant calcite in secondary porosity
δ34S = 13.09‰
δ13C = 0.39‰
δ18O = -3.96‰
calcite pseudospar after botryoidal aragonite
D
dolomitized botryoidal cement
I
J
δ34S = 9.53‰
δ13C = 5.79‰
δ18O = -1.14‰
δ34S = 9.96‰
δ13C = 4.50‰
δ18O = -0.93‰
up
1 cm
B
1 cm
C
calcite pseudospar
δ34S = 15.45‰
δ13C = 5.13‰
δ18O = -2.37‰
D
Equant calcite
δ34S = 12.36‰
δ13C = -1.82‰
δ18O = -5.52‰
S
δ34S = 14.72‰
δ13C = 2.67‰
δ18O = -3.31‰
partially dolomitized calcite pseudospar after aragonite
B
Fibrous calcite
δ34S = 14.00‰
δ13C = 4.61‰
δ18O = -2.29‰
A
dolomitized botryoidal cement with moldic pores
up
C
5 mm
Lithoclast
δ34S = 17.13‰
δ13C = 4.84‰
δ18O = -5.34‰
A
B
Bryozoan
δ34S = 16.44‰
δ13C = 4.97‰
δ18O = -4.69‰
up
D
δ34S = 9.22‰
δ13C = 6.21‰
δ18O = 2.61‰
A
oncoid-grapestone rudstone
Isopachous calcite
δ34S = 9.96‰
δ13C = -0.84‰
δ18O = -2.60‰
δ34S = 9.14‰
δ13C = 6.20‰
δ18O = 1.68‰
B
D
coated grain grainstone
up
1 cm
E
1 cm
C
Lp
Lg
Dolomitized lithoclast
δ34S = 9.68‰
δ13C = 4.01‰
δ18O = -2.28‰
F
Limestone lithoclast
δ34S = 12.10‰
δ13C = 4.49‰
δ18O = -1.97‰
Lg
Poikilitic calcite spar
δ34S = 18.84‰
δ13C = -0.92‰
δ18O = -13.62‰
B
up
A
δ34S = 10.47‰
δ13C = 3.58‰
δ18O = -3.61‰
Lb
E
Lb
dolomite-cemented siltstone matrix
Limestone lithoclast
δ34S = 12.07‰
δ13C = 3.98‰
δ18O = -2.44‰
sponge fragment
Lg
Lm
D
Dolomitized lithoclast
δ34S = 8.64‰
δ13C = 5.65‰
δ18O = -0.20‰
Lg

Figure 5 *[previous page]*: Polished slabs annotated with isotopic data. **A)** Cement boundstone from a vertical syndepositional fracture in a tepee structure in the Hairpin unit (sample MC-187, 39.4 m in the McKittrick Peak section). Botryoidal aragonite neomorphosed to brown calcite pseudospar, and appears beige where dolomitized. Isopachous calcite marine cement, neomorphosed aragonite marine cement, and dolomitized aragonite marine cements all preserve the $\delta^{34}S$ and $\delta^{13}C$ of the Delaware Basin seawater ($\delta^{34}S \approx 10‰$, $\delta^{13}C \approx 6‰$), but the $\delta^{18}O$ of the dolomite is enriched by evaporation. Molds of aragonite needles in dolomitized botryoids at the top of the slab indicate that some dolomitization preceded neomorphism, but most calcite pseudospar and dolomite retain the aragonite botryoidal fabric. Equant calcite fills secondary porosity created during dissolution after dolomitization, and has a higher $\delta^{34}S$ and lower $\delta^{13}C$ and $\delta^{18}O$ created by MSR in a meteoric-phreatic groundwater lens. Poikilitic calcite spar has dramatically higher $\delta^{34}S$ and lower $\delta^{18}O$ reflecting hotter telogenetic meteoric fluids. **B)** Cement-*Tubiphytes* boundstone from the G26-age reef facies of the Capitan Formation (sample MC-099 collected at 31.99394°N, 104.75804°W). Sponges (S) and *Tubiphytes* (T) are encrusted by brown calcitic *Archaeolithoporella* (A), partially-dolomitized calcite pseudospar after botryoidal aragonite, and isopachous fibrous calcite marine cements (I). Unlike on the shelf, the neomorphosed and dolomitized cements in the reef have higher $\delta^{34}S$ than Delaware Basin seawater. The equant calcite has lower $\delta^{34}S$ than the marine cements, but is also higher than the composition of seawater, suggesting less efficient MSR in the meteoric-phreatic fluids than in the marine-phreatic pore fluids. **C)** Lithoclast-bioclast rudstone from the G26-age toe-of-slope facies in the Bell Canyon Formation (sample MC-017, 3.1 m in the Toe-of-Slope section). Bioclasts include reef-derived bryozoan, brachiopod, crinoid, and *Tubiphytes* fragments. Lithoclasts are bioclast wackestones that include the same assemblage. The $\delta^{34}S$ of the bioclasts and lithoclasts match other matrix and grain analyses from the toe-of-slope and are the highest non-sparry calcite compositions measured, indicating that CAS is incorporated from pore fluids into the re-deposited grains during early marine diagenesis. **D)** Oncoid rudstone from the shelf crest foreshore facies in the Tansill Formation (sample MC-052, 27 m in the Wilderness Ridge section). Isopachous calcite marine cement (gray) lines interparticle porosity between pink dolomitized oncoids and aggregate grains. Both components preserve the $\delta^{34}S$ of Delaware Basin seawater, despite alteration of $\delta^{18}O$ and enrichment in transition metals as evidenced by the pink coloration during dolomitization. The isotopic composition of poikilitic calcite spar that fills remaining interparticle porosity was not analyzed in this sample. **E)** Lithoclast rudstone at the top of the G26-age slope (sample MC-213, 22.5 m in the Capitan Formation Slope section). Lithoclasts (dashed outlining) are reef-derived *Archaeolithoporella* boundstone (Lb), spicule-bryozoan-ostracod grainstone (Lg), peloid packstone (Lp), and laminated mudstone (Lm). The finer-grained mudstone and packstone lithoclasts are selectively dolomitized, and the siltstone matrix is dolomite-cemented. These components largely preserve the $\delta^{34}S$ of Delaware Basin seawater, although some are slightly isotopically-depleted and may have incorporated re-oxidized sulfide during early diagenesis. The $\delta^{34}S$ compositions of lime boundstone and grainstone lithoclasts are higher than that of seawater. Late poikilitic calcite spar has the highest $\delta^{34}S$.

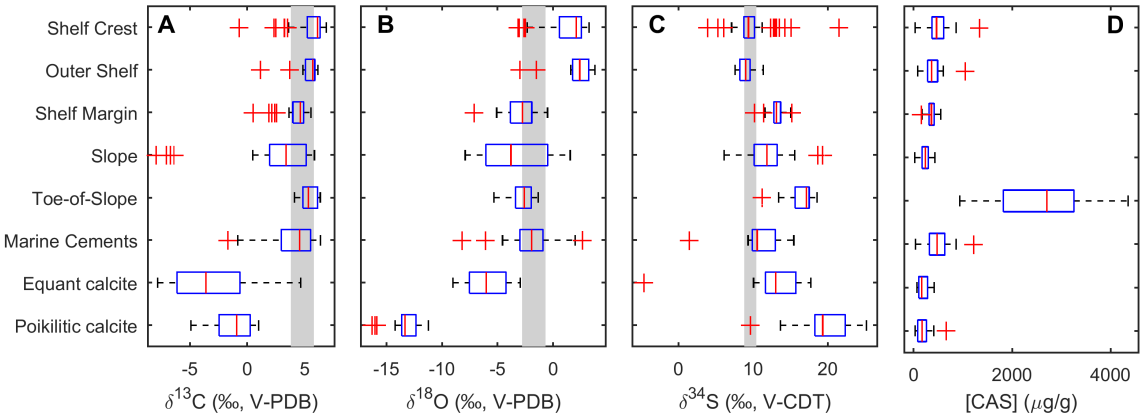

Figure 6: Box plots of geochemical data from each facies tract and stage of diagenesis. Whiskers span the range of adjacent data, which excludes data plotted as outliers that are more than 50% of the interquartile range above third the quartile or below the first quartile. Gray bars denote estimates of the isotopic composition of carbonates precipitated from normal late Permian seawater: $\delta^{13}C$ and $\delta^{18}O$ ranges are of brachiopod calcite and well-preserved marine cements (Given and Lohmann, 1986; Korte et al., 2005), and $\delta^{34}S$ range is of Delaware Basin evaporites in the Seven Rivers and Castile Formations (Hill, 1990; Holser and Kaplan, 1966; Kirkland et al., 2000; Sarg, 1981; Thode et al., 1961). **A)** $\delta^{13}C$. **B)** $\delta^{18}O$. **C)** $\delta^{34}S$ of CAS. **D)** CAS concentration.

Sulfate concentrations in the samples also vary. Most samples average about 400 ppm (i.e., μg SO_4^{2-} per g soluble carbonate), but the late poikilitic calcite spar averages 200 ppm sulfate and well-bedded toe-of-slope limestones contain an average of 2600 ppm sulfate (Figure 6).

The carbonate $\delta^{13}C$ and $\delta^{18}O$ compositions of the samples reflect trends in previously published data: peritidal dolomites in the Yates and Tansill Formations have the highest compositions ($\delta^{13}C$ is between 2‰ and 7‰, and $\delta^{18}O$ is between 0‰ and 4‰), and subtidal limestones in the Capitan and Bell Canyon Formations are generally lower (Figure 7) (Budd et al., 2013; Frost et al., 2012; Given and Lohmann, 1986, 1985; Loyd et al., 2013; Mazzullo, 1999; Melim and Scholle, 2002; Mutti and Simo, 1994). Trends towards $\delta^{13}C$ compositions as low as -8‰ and $\delta^{18}O$ compositions as low as -16‰ reflect the influence of meteoric and burial fluids (Budd et al., 2013; Given and Lohmann, 1986; Loyd et al., 2013; Mazzullo, 1999; Mruk, 1989; Mutti and Simo, 1994; Scholle et al., 1992).

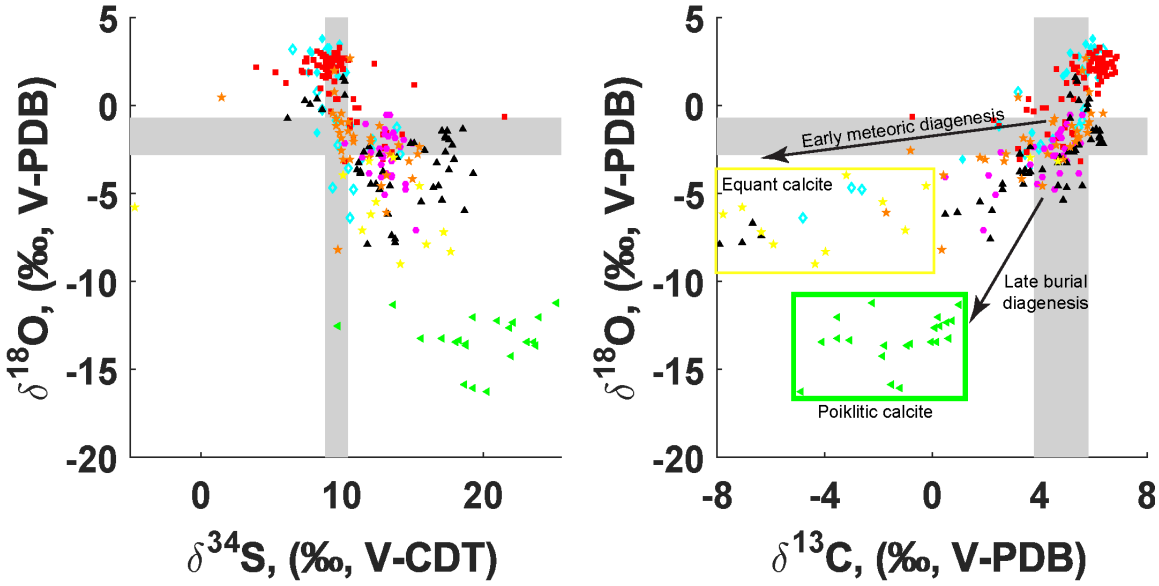

Figure 7: Carbon, oxygen, and sulfur isotope cross-plots. Symbols correspond to legend in Figure 4. Gray bars denote estimates of the isotopic composition of carbonates precipitated from normal late Permian seawater: $\delta^{13}C$ and $\delta^{18}O$ ranges are of brachiopod calcite and well-preserved marine cements (Given and Lohmann, 1986; Korte et al., 2005), and $\delta^{34}S$ range is of Delaware Basin evaporites in the Seven Rivers and Castile Formations (Hill, 1990; Holser and Kaplan, 1966; Kirkland et al., 2000; Leslie et al., 1997; Sarg, 1981; Thode et al., 1961). **A)** $\delta^{18}O$ vs $\delta^{34}S$. **B)** $\delta^{18}O$ vs $\delta^{13}C$. Steeper slopes correspond to mixing of marine components with a meteoric calcite end-member that has lower $\delta^{18}O$ formed at higher temperatures and higher $\delta^{13}C$ produced by more rock-buffering of the fluid.

Discussion

Incorporation of CAS during Diagenesis

The $\delta^{34}S$ of CAS in the shelf crest and outer shelf facies tracts are the only samples that record the sulfur isotopic composition of Delaware Basin seawater (Figure 6C), inferred to have been 8‰ to 10‰ from published analyses of sulfate evaporites in the Seven Rivers Formation and the Castile Formation (Hill, 1990; Holser and Kaplan, 1966; Kirkland et al., 2000; Leslie et al., 1997; Sarg, 1981; Thode et al., 1961). In allochems and early diagenetic cement textures deposited contemporaneously during the G26 HFS, the $\delta^{34}S$ of CAS increases from ~10‰ in peritidal carbonates in the Yates Formation to ~13‰ in sub-wave base limestones in the Capitan Formation, and to as high as 19‰ in deep, basinal limestones in the Bell Canyon Formation (Figure 4). During the deposition of the G26 HFS, there was ~20 m of relief between the foreshore facies in the Yates Formation and the shelf margin massive reef facies (Figure 2) (Rush and Kerans, 2010), and ~600 m of relief between the

foreshore facies and the toe-of-slope facies (Newell et al., 1953). The shelf-to-basin gradient in the $\delta^{34}S$ of CAS may represent a depth gradient of the $\delta^{34}S$ of Delaware Basin seawater, or facies-dependent diagenetic control on the $\delta^{34}S$ of sulfate incorporated as CAS. Higher $\delta^{34}S$ of sulfate may be developed by MSR, which preferentially leads to the fixation of low-$\delta^{34}S$ sulfate in sulfide minerals and leaves the residual sulfate enriched in ^{34}S (Thode et al., 1961). MSR can only occur in anoxic conditions, thereby implying a chemocline in the water column above the shelf margin reef facies. However, this condition is precluded by abundant reef-dwelling benthic heterotrophic animals. Therefore, the observed shelf-to-basin gradient in the $\delta^{34}S$ of CAS cannot represent a syndepositional depth gradient in the $\delta^{34}S$ of Delaware Basin seawater. Although a water-column chemocline may have developed below the shelf margin (because the slope and toe-of-slope facies lack fossils in their life position), CAS in many samples must incorporate an isotopically-distinct, diagenetic source of sulfate.

To unpack the controls on the $\delta^{34}S$ of CAS, the following discussion is organized by stage of diagenesis, in which each diagenetic process is examined from shelf to basin. Figure 8 is a simplified paragenetic sequence for the Guadalupe Mountains. Samples analyzed for CAS experienced the integrated effect of multiple diagenetic processes during different but overlapping periods of time in different locations from shelf to basin. Figure 9 organizes the CAS $\delta^{34}S$ data by texture and facies tract to visualize where and when each diagenetic process preserves the $\delta^{34}S$ of seawater.

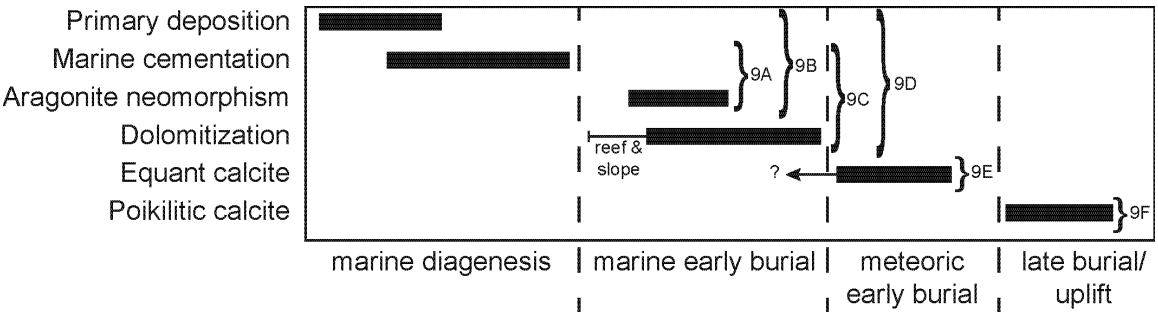

Figure 8: Paragenetic sequence of processes influencing the texture and chemical composition of the Capitan Reef, from deposition in the marine environment to progressively more recent diagenetic events. Brackets indicate the integrated set of diagenetic processes represented by the textures in each panel in Figure 9.

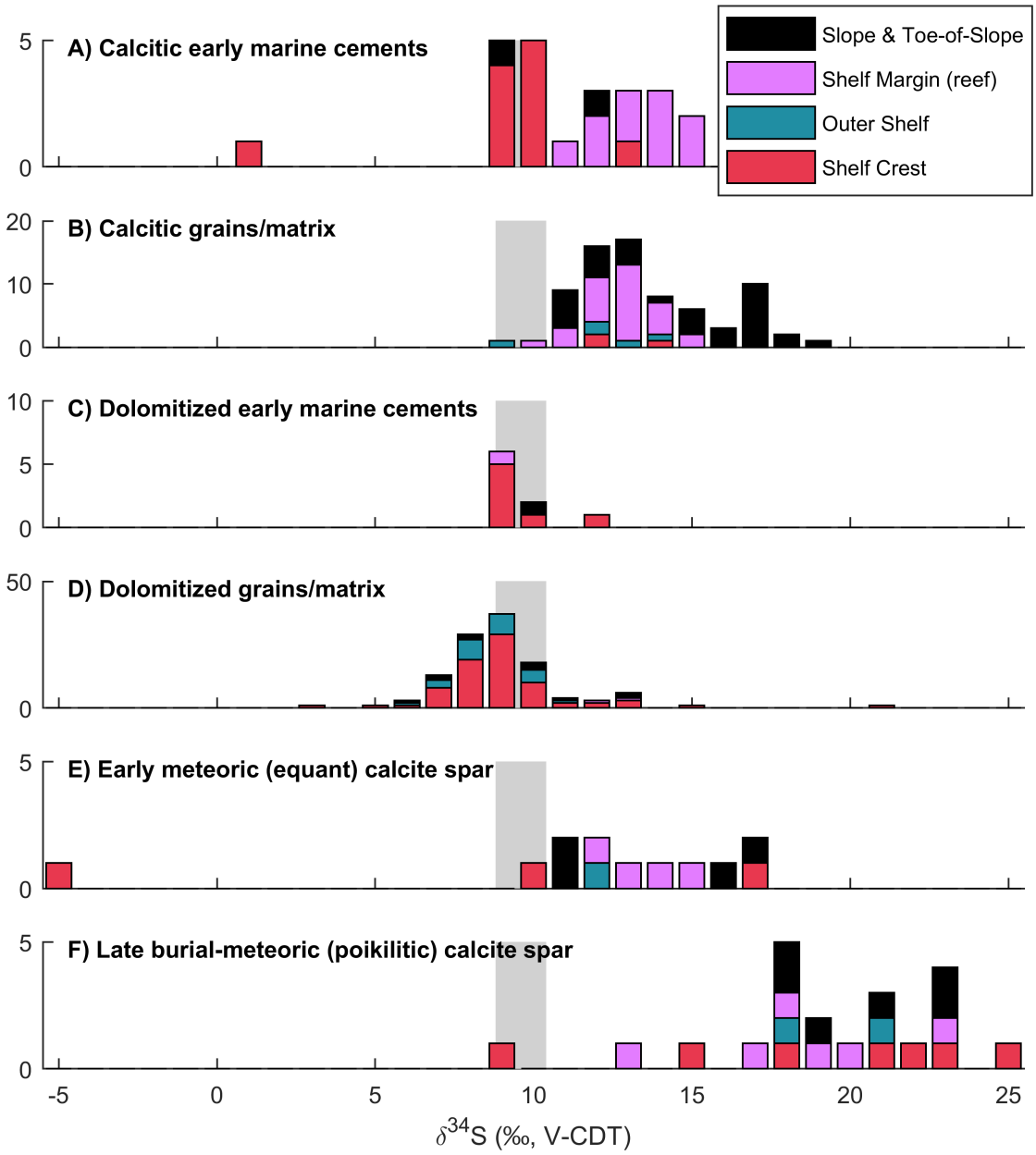

Figure 9: Histograms of the $\delta^{34}S$ of CAS in depositional and diagenetic textures, with the color of the bar corresponding to the facies tract from which the sample was collected. Gray bars denote the estimated $\delta^{34}S$ composition of Delaware Basin seawater from evaporites in the Seven Rivers and Castile Formations (Hill, 1990; Holser and Kaplan, 1966; Kirkland et al., 2000; Leslie et al., 1997; Sarg, 1981; Thode et al., 1961). **A)** Calcitic early marine cements incorporate CAS from the seawater in which the aragonite botryoids precipitated, and pore fluids in which the aragonite neomorphically inverted to brown calcite pseudospar. The pore fluid $\delta^{34}S$ was distilled towards higher compositions in the shelf margin by MSR, but was advectively connected to seawater in the shelf crest. **B)** Calcitic grains and micrite matrix incorporate CAS from the seawater in which the grains or mud precipitated, the pore fluids in which they were cemented, and the pore fluids in which any aragonite neomorphically inverted to calcite. These pore fluids were distilled towards higher compositions by MSR. **C)** Dolomitized early marine cements incorporate CAS from the dolomitizing fluids, in addition to the fluids responsible for

the calcitic cements in (A). In the shelf crest, the cements were dolomitized by many pore volumes of a reducing fluid, but it was sulfate-poor or its $\delta^{34}S$ was not modified from that of seawater. Dolomitization in the reef and slope was fabric-destructive, and possibly preceded aragonite neomorphism. **D)** Dolomitized grains and micrite matrix similarly incorporates CAS from seawater and the suite of earlier diagenetic regimes. $\delta^{34}S$ of CAS lighter than seawater is generally associated with the finest-grained or most siliclastic-rich facies, and may reflect the addition of low-$\delta^{34}S$ sulfate from reoxidized sulfides. **E)** Equant calcite spar incorporated CAS from reducing meteoric groundwater. **F)** Poikilitic calcite spar incorporated CAS from a much younger, extrabasinal, possibly Neogene meteoric groundwater.

Early marine diagenesis – Excluding calcite spars, the relative homogeneity of the $\delta^{34}S$ of CAS in texturally-diverse samples within each facies tract—including the samples whose $\delta^{34}S$ is distinct from that of seawater— suggests that CAS includes sulfate incorporated during early diagenesis. The interquartile $\delta^{34}S$ of CAS in the shelf crest samples is similar to that in outer shelf samples, and distinct from the interquartile in the shelf margin, slope, and toe-of slope samples (Figure 6).

The early marine diagenetic processes operating during CAS incorporation include marine isopachous fibrous calcite cementation, botryoidal aragonite cementation, and the neomorphic inversion of aragonite to calcite. Neomorphosed components include bioclasts and coated grains, which are now pervasively dolomitized in the shelf facies tracts and are predominately calcite elsewhere. Brown calcite pseudospar represents the neomorphic inversion of botryoidal aragonite (Mazzullo, 1980). In tepee structures in the shelf crest facies tract (Figure 5A), the CAS in brown calcite records the $\delta^{34}S$ of seawater (red bars in Figure 9A). In cavities in the shelf margin facies tract (Figure 5B), the CAS in brown calcite has a higher $\delta^{34}S$ than seawater (purple bars in Figure 9A). In both cases, the $\delta^{34}S$ of CAS in these calcitic early marine cements matches that of neomorphosed allochems and cements in the same hand samples, as well as that of micritic and peloidal matrix whose original mineralogy is unknown (Figure 9B and C). Therefore, the $\delta^{34}S$ of CAS records the pore fluid sulfate during early cementation and neomorphism. The $\delta^{34}S$ of pore fluid sulfate matched that of seawater in the shelf crest and outer shelf facies tracts, but preferential consumption of low $\delta^{34}S$ pore fluid sulfate by MSR distilled the residual sulfate towards higher compositions in the shelf margin and slope facies tracts.

Clasts and grains precipitated on the shelf and transported to deeper environments during deposition provide further evidence of CAS incorporation post-dating primary carbonate precipitation. For example, bryozoan fragments and lime wackestone lithoclasts derived from the shelf margin and redeposited in the toe-of-slope have $\delta^{34}S$ of CAS of 16-17‰ (Figure 5C), which is comparable to other CAS analyses from the toe-of-slope but higher than those in the shelf margin (Figure 6).

Dolomitization – Allochems, micrite, and cements in the shelf crest and outer shelf facies tracts are now mimetically dolomitized (Figure 5D), likely by reflux dolomitization following marine cementation (Adams and Rhodes, 1960; Melim and Scholle, 2002). The $\delta^{34}S$ of CAS in partially dolomitized botryoidal cements (Figure 5A) matches that of the brown calcite pseudospar (the range of red bars in Figure 9A overlaps that in Figure 9C and D). Therefore, dolomitization on the shelf does not appear to have changed the $\delta^{34}S$ of CAS incorporated during earlier stages of marine diagenesis, which preserved the $\delta^{34}S$ of seawater (Figure 9D). This may be because the dolomitizing fluids were sulfate-poor, or because their $\delta^{34}S$ of sulfate was not modified from that of seawater.

Some packstone-grainstone beds in the slope facies tract and high-permeability regions of the shelf margin facies tract are discordantly dolomitized, as well. Slope mimetic dolomite and dolomite-cemented siltstones have CAS with $\delta^{34}S$ that is ~10‰ (Figure 5E), matching the isotopic composition of seawater despite diagenetic enrichment of $\delta^{34}S$ in calcitic specimens, including limestone lithoclasts, from the same facies. Therefore, in the shelf margin and slope facies tracts, dolomitization likely began before most neomorphism and marine cementation. This early dolomitization of the slope occurred with fluids with a $\delta^{34}S$ composition similar to that of seawater sulfate (black bars in Figure 9D). Aragonite neomorphism and early marine cementation in the shelf margin and slope facies tracts likely followed dolomitization, after enrichment of pore fluid sulfate $\delta^{34}S$ could occur (black bars in Figure 9B). Cementation of the shelf crest and outer shelf preceded cementation of the shelf margin and slope, with reflux dolomitization occurring in the interim.

The limestones from the shelf margin and slope facies tracts represent well the carbon and oxygen isotopic compositions of the Delaware Basin (Given and Lohmann, 1985; Korte et al., 2005) but are not useful for chemostratigraphic reconstructions of seawater sulfate (Figure 7). Samples with $\delta^{34}S$ of CAS most distinct from syndepositional seawater deposited in the toe-of-slope. Within each facies tract, there is weak correlation between $\delta^{34}S$ and $\delta^{18}O$ or $\delta^{13}C$, which is often used to geochemically screen samples for diagenetic alteration. However, the diagenetic processes that influence the $\delta^{18}O$ and $\delta^{13}C$ of carbonate are different than those that influence the $\delta^{34}S$ of CAS. CAS in samples from the coarse-grained, high-porosity shelf facies best preserve the $\delta^{34}S$ of seawater sulfate, despite a complicated diagenetic history that includes early marine cementation and dolomitization. Dolomitization enriched the $\delta^{18}O$ of the carbonate (Mutti and Simo, 1994), likely by the flushing of many pore volumes with evaporated mesosaline brines (Melim and Scholle, 2002), but evaporation to mesosaline concentrations modifies the $\delta^{34}S$ of sulfate in the brine by less than 0.5‰ (Raab and Spiro, 1991). Carbonate sediments deposited in lower-energy, deeper reef and slope environments generally preserve primary $\delta^{18}O$ and $\delta^{13}C$ compositions that match late Permian brachiopod calcite and marine cements (Given and Lohmann, 1985; Korte et al., 2005). Neomorphism and marine phreatic (botryoidal and isopachous) cementation in these environments was coincident with MSR that led to enrichment in the $\delta^{34}S$ of pore fluids and CAS, but these processes do not fractionate carbon or oxygen isotopes.

Early burial-meteoric diagenesis – In the shelf, shelf margin, and slope facies tracts, a generation of equant calcite spar post-dates a dissolution event following early marine cementation. This equant calcite fills secondary porosity in neomorphosed botryoidal cements, moldic porosity replacing aragonitic allochems and evaporite casts, and fenestrae (Given and Lohmann, 1986; Mruk, 1989; Mutti and Simo, 1993). It has a $\delta^{34}S$ of CAS between 10 and 18‰, except for a single analysis of an early generation of calcite filling a solution-enlarged vug that is -4.6‰ (Figure 9E). Based on its equant, inclusion-rich texture, $\delta^{18}O$ near 8‰, and variable $\delta^{13}C$, it likely corresponds to calcite “Spar I” in the Capitan Formation as defined by Mruk (1989) and Given and Lohmann (1986) and identified as

sparry calcite cathodoluminescence zone CLI in the Yates Formation by Mutti and Simo (1993). It crystallized from meteoric-phreatic fluids, probably during lowstands between HFSs (Budd et al., 2013; Given and Lohmann, 1986; Mazzullo, 1999; Mruk, 1989), so its $\delta^{34}S$ compositions heavier than Guadalupian seawater $\delta^{34}S$ may represent active MSR in this groundwater lens.

Some samples from the shelf crest, outer shelf, and slope facies tracts incorporate CAS with lower $\delta^{34}S$ than contemporaneous seawater, which probably reflect incorporation of reoxidized sulfide. Many of these samples are largely indistinguishable from the other samples in each facies tract with $\delta^{18}O$ and $\delta^{13}C$ (Figure 7). This may be because sulfide oxidation locally produces high acidity that would dissolve nearby carbonate, strongly rock-buffering the carbon and oxygen isotopic composition. These samples are also among the finest-grained supratidal evaporitic mudstones, fenestral algal-coated grain packstones, and siliciclastic-rich packstones that cap depositional cycles. The lowest $\delta^{34}S$ composition, -4.6‰, is in a cloudy calcite cement similar to Spar 1 that rims a solution-enlarged vug in a fenestral packstone. Meteoric vadose pendant cements in some samples are likely related to recent outcrop weathering, but other samples lack such cements. Therefore, there may have also been Permian-age oxidizing meteoric diagenesis, which would have reoxidized low $\delta^{34}S$ sedimentary sulfides. Telogenetic gypsum with both low and high $\delta^{34}S$ has been observed and similarly interpreted in Seven Rivers Formation lagoonal evaporites (Sarg, 1981). Additionally, in the slope, some dolomitized peloidal grainstones and fine-grained packstones have low $\delta^{34}S$ of CAS (Figure 5E and black bars in Figure 9D), consistent with incorporation of sulfate with anomalously-low $\delta^{34}S$ into CAS during dolomitization (Fichtner et al., 2017; Marenco et al., 2008b; Present et al., 2015).

Late burial-meteoric diagenesis – CAS with the highest $\delta^{34}S$ compositions is in late-stage poikilitic calcite spar that fills interparticle and fracture porosity (Figure 5A and E). The $\delta^{34}S$ of CAS is as high as 25‰ (Figure 9F), which is as much as 15‰ heavier than early diagenetic textures in the same hand sample (Figure 5A). This calcite cement is only observed in the uplifted outcrops of the Guadalupe mountains, and replaces anhydrite cements that are only

observed in subsurface drill core (Budd et al., 2013; Garber et al., 1989; Mazzullo, 1999; Mruk, 1989; Scholle et al., 1992). It corresponds to calcite "Spar II" as defined by Given and Lohmann (1986), "Spars II and III" as defined by Mruk (1989), and sparry calcite cathodoluminescence zones CLII and CLIII defined by Mutti and Simo (1993). The poikilitic spars with the highest $\delta^{34}S$ have end-member $\delta^{18}O$ and $\delta^{13}C$ compositions that are lighter in $\delta^{18}O$ and heavier in $\delta^{13}C$ than early diagenetic equant calcite spars, representing more rock-buffering and warmer meteoric basinal fluids (Budd et al., 2013; Loyd et al., 2013). Despite replacing Capitanian or Ochoan-age anhydrite cement, the distinct $\delta^{34}S$ of CAS in these spars suggests a non-Permian source for the sulfate associated with meteoric groundwater advection during burial and uplift. The lack of Permian $\delta^{34}S$ compositions is particularly surprising because the poikilitic spar includes anhydrite inclusions indicative of a direct replacement (Scholle et al., 1992).

Implications for CAS Chemostratigraphy

CAS in recent biogenic carbonate accurately preserves the $\delta^{34}S$ of modern seawater (Burdett et al., 1989; Kampschulte et al., 2001; Paris et al., 2014b), and well-preserved biogenic carbonate, especially low-magnesium calcite in brachiopods and belemnites, may robustly preserve the composition of ancient seawater (Gill et al., 2011a; Kampschulte and Strauss, 2004; Newton et al., 2011; Present et al., 2015; Wu et al., 2014). Unfortunately, such well-preserved fossiliferous material is rare in the geologic record and absent in Precambrian strata. Therefore, CAS in bulk carbonate rock is an attractive proxy for reconstructing the isotopic composition of ancient seawater because carbonates are widely-deposited in space and time in the rock record.

Fine-grained limestones and micritic textures are frequently sampled in CAS chemostratigraphy studies because, in some depositional environments, the CAS in primary aragonite mud represents a dominant mass fraction of the total CAS in recrystallized and cemented carbonate (Lyons et al., 2004; Rennie and Turchyn, 2014). However, in environments with high sedimentation rates or high organic carbon fluxes, CAS measurably incorporates diagenetically-enriched pore fluid sulfate during recrystallization and cementation (Loyd et al., 2012a; Rennie and Turchyn, 2014). Fine-grained slope or basinal

limestones are therefore likely to be poor archives of ancient seawater sulfate. Peritidal fine-grained limestones, on the other hand, may incorporate isotopically-light sulfate that is the product of re-oxidized sulfide and pyrite during early meteoric or dolomitizing diagenesis (Fichtner et al., 2017; Marenco et al., 2008b; Present et al., 2015). Meteoric replacement of biogenic aragonite leaches sulfate without fractionating its isotopes if the meteoric fluids are sulfate-poor (Gill et al., 2008), but organic-rich, fine-grained carbonate sediments are pyrite-rich (e.g. Crémière et al., 2017), providing a source of isotopically-light sulfur that would be mobile during early diagenesis.

Covariation between trace or minor element concentrations and stable isotope data is often used to geochemically screen samples for diagenetic alteration of primary seawater compositions because many diagenetic processes re-equilibrate a sample towards a diagenetic end-member composition with a distinct thermodynamic equilibrium composition (Brand and Veizer, 1981, 1980). However, the early marine diagenetic processes that incorporate high-$\delta^{34}S$ sulfate into a carbonate (MSR coincident with marine-phreatic cementation or recrystallization) occur in a pore fluid environment without $\delta^{18}O$ or $\delta^{13}C$ gradients from seawater. Meteoric and burial diagenetic end-member compositions indeed create covariation with $\delta^{34}S$ (Figure 7), but the "primary" carbon and oxygen end-member in the reef and slope facies tracts still incorporated diagenetic sulfate.

Additionally, in a low-energy depositional environment without pore fluid advection, the pore fluid minor and trace elements will equilibrate with the carbonate sediment. Constituents that are abundant in the pore fluid but not in the solid—such as sulfate— will dominate the carbonate phase's composition without measurable covariation with common diagenetic proxy elements such as strontium (which is abundant in the carbonate but not the fluid). Covariation with redox-sensitive trace elements such as manganese and iron (which are abundant in reduced fluids compared to the primary carbonate) will depend on the unknowable primary ratio of sulfur, oxygen, carbon, and metals in the ancient depositional environment. Further study of the trace element distribution of the Permian Reef may help identify depositional environments and diagenetic regimes where such elements predict CAS

diagenetic alteration, but their enrichment is not a clear indication of CAS alteration. For example, metal enrichment evidenced by pink-orange coloration in many carbonates in the Yates and Tansill Formations (e.g. Figure 5D) indicates that reducing conditions during dolomitization led to incorporation of ferrous iron, which was later oxidized, but the fluids were evidently not carrying sulfate fractionated from seawater.

Previously published CAS data from Guadalupian successions have a large $\delta^{34}S$ variability. Sparse biogenic carbonate data includes one analysis of brachiopod calcite that is 11.0‰ and another that is 14.9‰ (Kampschulte and Strauss, 2004; Wu et al., 2014). Bulk carbonate analyses from limestones deposited in the Tethyan Ocean in South China include $\delta^{34}S$ excursions from -40‰ to 40‰ (Li et al., 2009; Yan et al., 2013) that are well beyond the range of all other Paleozoic CAS and evaporite data, and imply periods of heavily stratified oceans with heterogeneous sulfate concentrations. Our data, although temporally-restricted to the time represented by 2-3 HFSs (~10^6 yrs), suggests that variable diagenetic regimes can contribute to observed CAS variability. Extremely high $\delta^{34}S$ of CAS measurements may reflect periods of intense pore fluid sulfate reduction driven by high organic carbon burial fluxes and exacerbated by low bottom-water oxygen concentrations (Yan et al., 2013). Extremely negative $\delta^{34}S$ of CAS measurements may reflect re-oxidation of sulfide in shallowly buried sediments as the chemocline in the sediments or water column episodically shoaled and deepened (Li et al., 2009; Riccardi et al., 2006; Yan et al., 2013; G. Zhang et al., 2015).

For future CAS chemostratigraphy studies where well-preserved biogenic calcite is unavailable, coarse-grained carbonates deposited in high-energy peritidal depositional environments should provide the best record of seawater sulfate. Such depositional environments have high fluid advection within pore networks of seawater-like fluids that inhibit development of pore fluid sulfate gradients during diagenesis, and do not have large aqueous sulfide or pyrite reservoirs that may be easily re-oxidized during dolomitization or meteoric diagenesis. However, sediments in such environments form porous and permeable

grainstones and matrix-poor rudstones whose $\delta^{18}O$ may be fluid-buffered and dramatically different from that precipitated from syndepositional seawater.

Conclusions

By comparing the $\delta^{34}S$ of CAS along a shelf-to-basin transect of carbonates synchronously deposited in peritidal to deep environments, we demonstrated that CAS may incorporate diagenetic sources of sulfate that are isotopically distinct from synsedimentary seawater. Fine-grained limestones deposited in low-energy environments, which are often targeted in isotope chemostratigraphy studies because they are more rock-buffered during early and burial diagenesis, are most likely to incorporate $\delta^{34}S$ reflecting residual pore fluid sulfate. Fabric-retentive dolomitization during early diagenesis of grainy sediments deposited in high-energy depositional settings appears to incorporate sulfate with seawater-like $\delta^{34}S$ into CAS.

While CAS in peritidal, high-energy grainstones and rudstones in the shelf crest and outer shelf accurately record the $\delta^{34}S$ of Delaware Basin seawater sulfate, $\delta^{34}S$ of CAS in the deeper facies constrains the timing and conditions of diagenesis in the Capitan Reef. Limestones in the shelf margin and slope facies tracts have heavier $\delta^{34}S$ compositions reflecting neomorphism and cementation in a regime of active MSR. However, because many dolomites associated with high-permeability regions in the shelf margin and slope facies tract incorporate CAS with $\delta^{34}S$ similar to or even lighter than seawater, dolomitization in these environment must have at least partially preceded neomorphism and cementation. Sparry calcite cements formed during meteoric diagenesis range between seawater-like compositions up to 8‰ heavier, indicating active MSR in the groundwater present during cementation. Burial meteoric fluids that replaced evaporite cements during uplift incorporate high $\delta^{34}S$ sulfate from an isotopically-distinct fluid.

Physical admixture of the sparry calcite cements into neomorphic components creates covariation between $\delta^{34}S$ and $\delta^{18}O$, but such vectors are not produced during early marine diagenesis. This indicates that the absence of covariation between $\delta^{34}S$ and $\delta^{18}O$ is not an adequate geochemical screening method for determining primary seawater $\delta^{34}S$. Sulfur

isotope chemostratigraphy intended to reconstruct ancient seawater composition and biogeochemical fluxes must consider early diagenetic processes in the sedimentary environment.

Acknowledgements

This research was funded by the American Chemical Society Petroleum Research Fund New Directions grant #53994-ND2, and by a Society for Sedimentary Geology (SEPM) Student Research Grant to TMP. We thank Jonena Hearst and the National Park Service for invaluable assistance and for research permits GUMO-2012-SCI-0014, GUMO-2013-SCI-0016, and GUMO-2016-SCI-0010; Kathryn Snell, Dan Johnson, and Kristin Bergmann for field assistance; Paul M. Harris and Benjamin Smith for helpful discussion; Nathan Dalleska, Jared Marske, Kat Dawson, Fenfang Wu, and Lindsey Hedges for analytical support; and Katelyn Masiuk for help drafting figures. CAS concentration was determined in the Caltech Environmental Analysis Center.

Chapter 5

PYRITE-WALLED TUBE STRUCTURES IN A MESOPROTEROZOIC SEDIMENT-HOSTED METAL SULFIDE DEPOSIT

Theodore M. Present[1], Kristin D. Bergmann[2], Corinne Myers[3], Sarah P. Slotznick[4], Jessica R. Creveling[5], Jerry Zieg[6], Woodward W. Fischer[1], Andrew H. Knoll[7], John P. Grotzinger[1]

[1]California Institute of Technology, Pasadena, California, USA
[2]Massachusetts Institute of Technology, Cambridge, Massachusetts, USA
[3]The University of New Mexico, Albuquerque, New Mexico, USA
[4]University of California, Berkeley, Berkeley, California, USA
[5]Oregon State University, Corvallis, Oregon, USA
[6]Sandfire Resources America, Inc., White Sulphur Springs, Montana, USA
[7]Harvard University, Cambridge, Massachusetts, USA

Present, Theodore M., Kristin D. Bergmann, Corinne Myers, Sarah P. Slotznick, Jessica R. Creveling, Jerry Zieg, Woodward W. Fischer, Andrew H. Knoll, and John P. Grotzinger. "Pyrite-Walled Tube Structures in a Mesoproterozoic Sediment-Hosted Metal Sulfide Deposit." *Geological Society of America Bulletin* 130, no. 3–4 (2017): 598–616. https://doi.org/10.1130/B31504.1.

Abstract

Unusual decimeter-scale structures occur in the sediment-hosted Black Butte Copper deposit within lower Mesoproterozoic strata of the Belt Supergroup, Montana. These low domal and stratiform lenses are made up of millimeter-scale, hollow or mineral-filled tubes bounded by pyrite walls. X-ray micro-computed tomography (micro-CT) shows that the tube structures are similar to the porous fabric of modern diffuse hydrothermal vents, and do not resemble textures associated with the mineralization of known microbial communities. We determined the sulfur isotopic composition of sulfide minerals with *in situ* secondary ion mass spectrometry (SIMS) and of texture-specific sulfate phases with multi-collector inductively coupled plasma mass spectrometry (MC-ICP-MS). The sedimentological setting, ore paragenesis, sulfur isotope systematics, and porosity structure of these porous precipitates constrain the site of their formation to above the sediment-water interface where metalliferous hydrothermal fluids vented into the overlying water column. These data

constrain the geochemistry of the Mesoproterozoic sediment-water interface and the site of deposition for copper-cobalt-silver mineralization. Metals in the hydrothermal fluids titrated sulfide in seawater to create tortuous fluid flow conduits. Pyrite precipitated at the vent sites exhibits large sulfur isotope fractionation (>50‰), which indicates a close association between the vents and sulfate-reducing microbiota. In the subsurface, base metal sulfides precipitated from sulfide formed during the reduction of early diagenetic barite, also ultimately derived from seawater. This model suggests dynamic bottom water redox conditions at the vent site driven by the interplay between sulfate-reducing organisms and metalliferous fluid effluence.

Introduction

Stratabound iron sulfides containing economically significant concentrations of base metals, commonly lead and zinc**,** constitute an important type of Mesoproterozoic metal deposit in sedimentary rocks. Models for their formation invoke metalliferous hydrothermal fluids venting into seawater or debouching into shallow sedimentary pore fluids and precipitating iron sulfides along stratiform horizons (Goodfellow et al., 1993; Large et al., 2005; Leach et al., 2010; Lydon, 1996; Russell et al., 1981). The preponderance of such deposits in Mesoproterozoic strata has been linked to increasing marine sulfate concentrations following the rise of atmospheric oxygen (Farquhar et al., 2010; Leach et al., 2010; Lydon, 1996; Lyons et al., 2006). Stratabound copper deposits are also tied to the Proterozoic oxygenation of Earth's surface (Hitzman et al., 2010). Curiously, despite their apparent synsedimentary or early diagenetic origins, many of these deposits lack obvious geological evidence for exhalative vents, such as a stockwork feeder zone or hydrothermal edifices (Large et al., 2005; Leach et al., 2005; Sangster, 2002), which could inform the chemistry of the hydrothermal fluids and seawater.

In this paper, we describe unusual structures composed of millimeter-scale tube-like features in the lower Mesoproterozoic Belt Supergroup at the site of the sediment-hosted Black Butte Copper deposit, Helena Embayment, Montana (Figure 1). Graham et al. (2012) first described the tube-shaped features, which they termed "net-textured pyrite," as decimeter-

scale lenses and beds characterized by millimeter-scale ovoid pores bound by a network of fine-grained pyrite. These features represent three-dimensional connected networks, and here we refer to them as pyrite-walled tube structures. Amalgamations of the pyrite walls are overgrown by crystalline and euhedral pyrite, and enclose tube-shaped spaces often filled by quartz, barite, or dolomite (Figure 2).

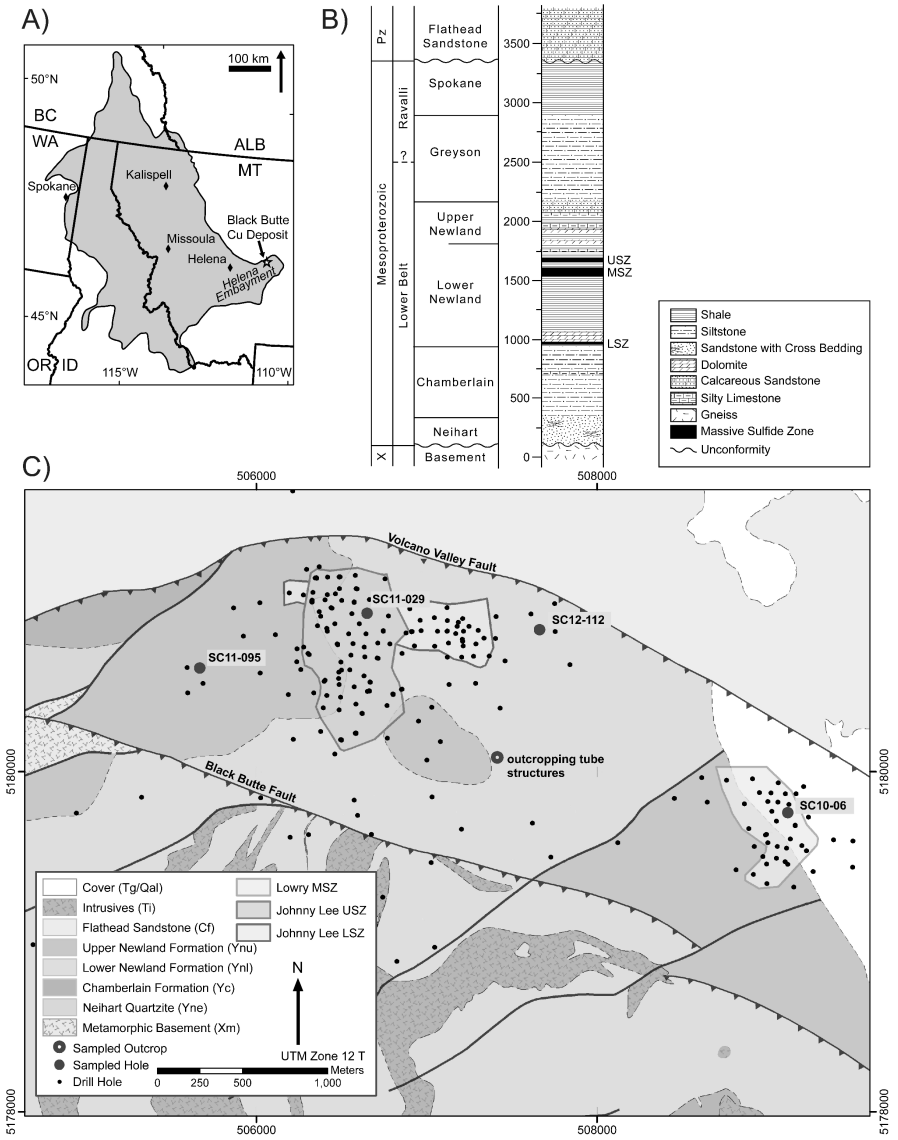

Figure 1: Geologic setting of the Black Butte Copper deposit, modified from Slotznick et al. (2015) with detailed map prepared by Tintina Resources, Inc. (A) Map of the Belt Supergroup outcrop limit. Star marks the location of the Black Butte Copper deposit within the Helena Embayment. (B) Lithostratigraphy of the Helena Embayment near Black Butte, with height in meters. USZ = Upper Sulfide Zone, MSZ = Middle Sulfide Zone, LSZ = Lower Sulfide Zone, X = Paleoproterozoic Era, Pz = Paleozoic Era. (C) Geologic map of the Black Butte region (WGS84 datum). Dots mark all locations drilled by Tintina Resources Inc. or Cominco American Inc. Drill cores and outcrop sampled for this study are labeled.

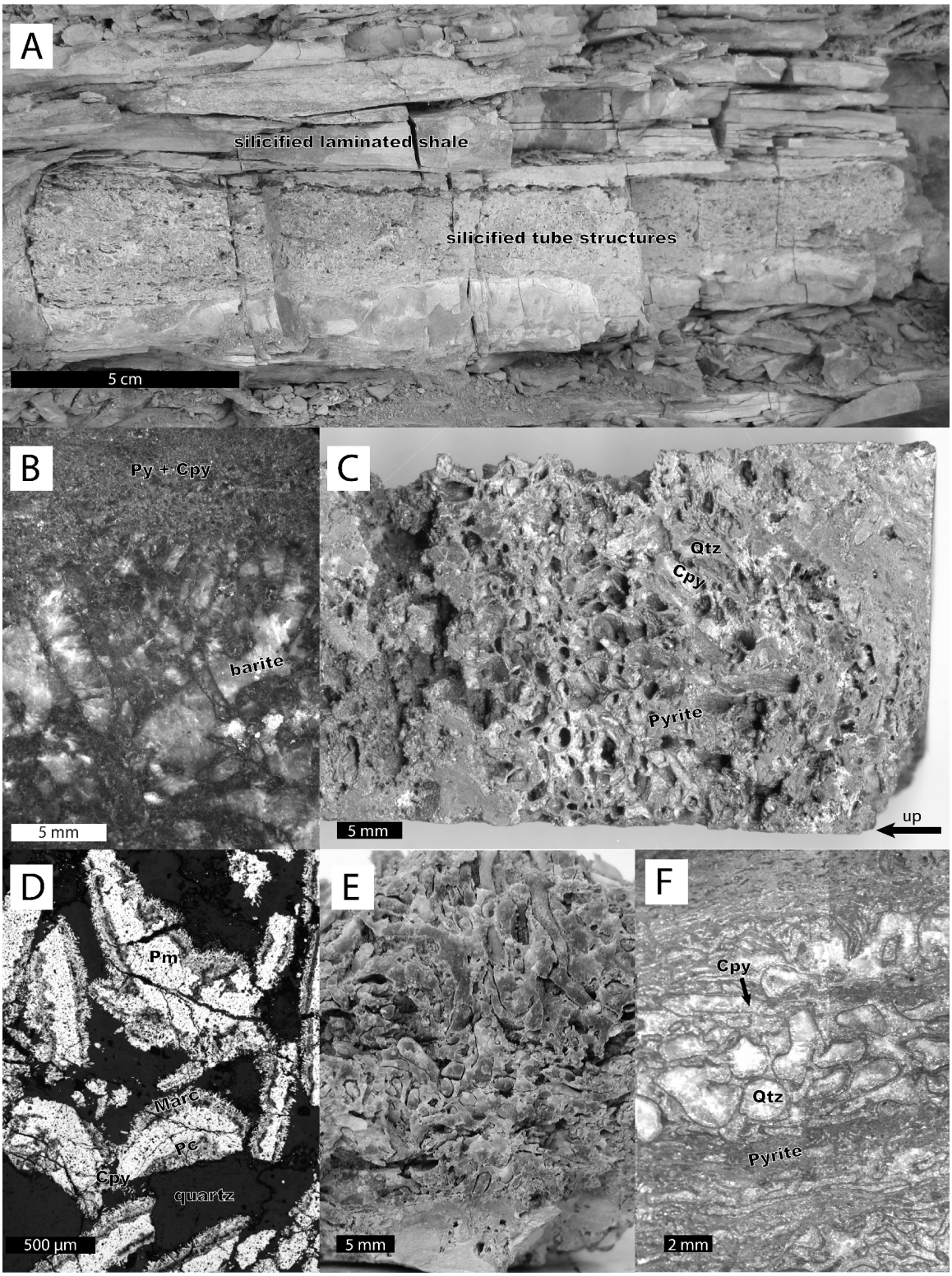
A
silicified laminated shale
silicified tube structures
5 cm
B
Py + Cpy
barite
5 mm
C
Qtz
Cpy
Pyrite
5 mm
up
D
Pm
Marc
Pc
Cpy
quartz
500 µm
E
5 mm
F
Cpy
Qtz
Pyrite
2 mm

Figure 2 *[prev. page]*: Pyrite-walled tube structures. (A) Outcrop photograph of decimeter-scale lens of tube structures in silicified gossan. (B) Core photo of sub-vertical pyrite-walled tube structures cemented by barite from drill core SC11-095 410.11-410.09 m. (C) Core photo of SC11-029 56.50-56.44 m (micro-CT sample B1) with primary porosity partly occluded by chalcopyrite and euhedral quartz. (D) Fragments of tube structures with marcasite coating, SC11-029-76.35 m. (E) Tube structures that lack pyrite walls collected from the silicified gossan outcrop. (F) Photomosaic of tube structures showing spatial zonation of diameter, with the largest tubes clustered in the center of a region of narrower tubes. Tubes are filled with quartz that is rimmed by chalcopyrite. Py = pyrite, Cpy = chalcopyrite, Qtz = quartz, Pm = mottled pyrite, Marc = marcasite.

Laminated pyrite around the Black Butte Copper deposit is often crinkly, and was therefore interpreted to represent mineralized microbial mats (Lyons et al., 2006; Schieber, 1989a, 1990). Pyrite interpreted to preserve microbial textures is also found associated with other sediment-hosted base metal deposits (Dunster, 1997; Ireland et al., 2004; McGoldrick, 1998, 1999; Oehler and Logan, 1977; Rohrlach et al., 1998; Schieber, 1989a). Tube structures at Black Butte are closely associated with crinkly pyrite and therefore might represent a novel morphology of a permineralized microbial community (McGoldrick and Zieg, 2004). However, close spatial association with microbial communities does not by itself provide evidence that the tube structures were built biologically (e.g. Grotzinger and Knoll, 1999).

While intermittently present near the Black Butte Copper deposit, porous pyrite structures have, to the best of our knowledge, only rarely been described in other sediment-hosted deposits. The Paleoproterozoic Walford Creek deposit includes millimeter-scale "open-framework" pyrite interpreted as microbialites (Rohrlach et al., 1998), the Mesoproterozoic Gaobanhe deposit contains centimeter- to decimeter-scale pyrite chimneys (Li and Kusky, 2007), and the Carboniferous Ballynoe deposit contains millimeter-scale "curtains and sheaves" associated with hydrothermal vent chimneys (Boyce et al., 1983; Larter et al., 1981; Russell et al., 1989). More frequently, at least in Phanerozoic deposits, recognition of hydrothermal vent structures hinges on the occurrence of fossilized worm (animal) tubes (Banks, 1985; Boyce et al., 2003; Campbell et al., 2002; Moore et al., 1986), and these are often found in deposits hosted in volcanic rather than sedimentary rocks (Haymon et al., 1984; Little et al., 1997, 1998, 1999a, 1999b). However, if formed biologically, millimeter-scale structures in Mesoproterozoic rocks would necessarily indicate a novel mode of bioconstruction and therefore assumptions about their genesis should be examined.

Based on physical, mineralogical, and isotopic analyses at the outcrop, drill core, and microscopic scale, we argue that the Black Butte tube structures represent local sites of hydrothermal fluid effluence to the seafloor in the Helena Embayment. This, in turn, suggests that the tube structures reflect syngenetic mineralization at the site of hydrothermal fluid venting and, thus, record paleoenvironmental information about the Belt Basin seawater and hydrothermal system. While isotopic data indicate that microbial sulfate reduction was an important source of sulfide for early pyrite deposition at Black Butte, this does not require that the tubes were accreted biologically; they could, as well, indicate abiotic precipitates colonized by bacterial communities.

Geologic setting

The Black Butte zinc-poor, copper-cobalt-rich sediment-hosted deposit occurs in the lower Newland Formation within the northern Helena Embayment, a syndepositional graben extending eastward from the center of the Mesoproterozoic lower Belt-Purcell Basin (Figure 1A). The Newland Formation overlies the Neihart and Chamberlain formations (Figure 1B); the latter represent a fluvial/eolian sand blanket and supra-wave base silty carbonaceous shale, respectively (Godlewski and Zieg, 1984; Schieber, 1989b; Winston and Link, 1993; Zieg, 1986; Zieg et al., 2013). The Neihart Formation is a coarse to very coarse, mature, hematitic quartz arenite with increasing very fine micaceous sand and silty shale as it grades into the overlying Chamberlain Formation (Schieber, 1989b). Correlation of the Newland Formation to the Prichard Formation to the northwest indicate a depositional age of about 1470 Ma (Aleinikoff et al., 2015; Graham et al., 2012; Sears et al., 1998). The lower Newland Formation marks rapid deepening associated with graben formation and comprises sub-wave base laminated calcareous to dolomitic shale with intercalated conglomeratic debris flows and turbiditic sandstones. The upper Newland Formation and overlying lowermost Greyson Formation comprise two sub-wave base carbonate-to-siliciclastic cycles. The Greyson Formation features relatively shallower, sub- and supra-storm wave base siltstones (Zieg, 1986).

In Late Cretaceous time, the south-dipping reverse Volcano Valley Fault truncated pre-mid-Cambrian south-dipping (possibly Mesoproterozoic and/or synsedimentary) normal faults (Figure 1C). Reverse faulting duplicated the lower Newland Formation in the Black Butte area and thrust lower Newland rocks over unconformable overlying mid-Cambrian rocks (Graham et al., 2012; Zieg et al., 2013). The Black Butte Copper deposit includes multiple stratabound sulfide zones in the Newland Formation, five of which are Cu-Co-Ag-enriched. Three are economically important (Figure 1C). Two, the Upper Sulfide Zone (USZ) and Middle Sulfide Zone (MSZ), occur in the hanging wall of the Volcano Valley Fault. The third, the Lower Sulfide Zone (LSZ), is found in both the footwall and hanging wall of the Volcano Valley Fault, is resource quality in the footwall, and is bounded on the north by one of the south-dipping normal faults called the Buttress Fault (Graham et al., 2012).

Materials and methods

Samples were collected from both outcrop and 4 subsurface cores previously drilled and stored in the Black Butte area by Tintina Resources, Inc. (Figure 1C). Mineralogical and textural characterization of pyrite-walled tube structures was accomplished by reflected light petrography of 15 thin sections, binocular microscopy of 27 drill core segments, and centimeter-scale logging of a 6 m-long core segment. Qualitative elemental compositions and compositional contrasts were validated with electron dispersion spectroscopy and backscatter electron microscopy using a ZEISS 1550VP Field Emission Scanning Electron Microscope (SEM) at the Caltech Geological and Planetary Sciences Division Analytical Facility, and with synchrotron-based X-ray fluorescence and absorption near-edge spectroscopy (Slotznick et al., 2015).

Three-dimensional morphology, porosity, density and connectivity of the tube structures were determined using micro-computed tomography (micro-CT)—a non-destructive, micron-scale, three-dimensional imaging method. Scanning was completed using an X-ray tube tomography system with a tungsten X-ray source (X-TEK HMX-ST 225, Nikon Metrology) at the Center for Nanoscale Systems at Harvard University. The scans were

completed at 115-190 kV source voltage, 42-135 μA source current, 0.1-2.0 mm copper filter, 1-2 s integration time, ~2,100-3,200 frames acquired over 360°, and ~ 2 hr scan time per sample. Three-dimensional reconstructions were generated using CTPro (Metris) and VGStudio Max 2.0 (Volume Graphics). Using density differences with the surrounding material (Supplemental Figure 1), internal volumes (hypothesized pores) were identified from the reconstructions. Potential pore networks were filtered using an edge-preserving, curvature-driven algorithm in Avizo Fire 8.1 (FEI). An interactive thresholding process characterized potential pores by size and orientation; these were separated and given unique labels. Length, width, aspect ratio, volume, and orientation data were then extracted for all pores using Avizo Fire. Pore orientation data was analyzed with the RFOC Spherical Statistics and R Stats packages (Lees, 2014; R Core Team, 2015).

Two Black Butte samples were scanned: (1) sample B1, an USZ sample with pyrite walls and open pores from drill core SC11-029-56.5 m (Figure 2C); and (2) sample B3, a silica-replaced outcrop sample from 46° 46.368'N, 110° 52.843'W above USZ gossan (Figure 2A).

In addition, three samples from potential modern analogs were analyzed: (1) sample M1, an anhydrite-walled chimney from a 300-311°C vent called “Hot Harold” in the Mothra vent field on the Juan de Fuca Ridge (collected during *HOV Alvin* cruise AT-15-23 on September 9, 2007 at 47°55.42566’N, 129°6.49176’W, 2278 m depth); (2) sample LCL, an inactive carbonate-walled chimney (sample 3871-1442 collected during *HOV Alvin* cruise AT-7-41) in the Lost City Hydrothermal Field; and (3) sample LCM, a carbonate-walled flange called “IMAX” on a 53-60°C vent on the Poseidon structure in the Lost City Hydrothermal Field (sample 3869-1404 collected at Marker 2 during *HOV Alvin* cruise AT-7-41) (Bradley, 2008; Bradley et al., 2009; Kelley et al., 2005). The Mothra vent field is a high-temperature hydrothermal complex of steep-spired pyrite and sulfate chimneys in the axial trench of the Juan de Fuga Ridge, and the Hot Harold sample (M1) comes from an active, fault-controlled vent that is younger than the last eruptive basaltic dike emplacement on the ridge ($10^2 – 10^3$ years) (Glickson et al., 2007; Kelley et al., 2001a; Lin et al., 2016). The Lost City Hydrothermal Field (samples LCL and LCM) is a long-lived (10^5 years), lower temperature

hydrothermal system driven by exothermic serpentinization reactions of peridotite exposed by detachment faulting in the Atlantis Fracture Zone, off-axis of the slow-spreading Mid-Atlantic Ridge (Früh-Green et al., 2003; Kelley et al., 2001b, 2005; Ludwig et al., 2006).

Sulfide-sulfur isotopic compositions of pyrite and chalcopyrite were determined on two thin sections (SC11-029-56.42 m and SC11-095-389.22 m) by Secondary Ion Mass Spectrometry (SIMS) on a Cameca 7f-Geo at the Caltech Microanalysis Center. One-inch round polished thin sections (25 μm-thick) were prepared from sections of drill core (Supplemental Figure 2) and examined with a polarizing reflected light microscope, backscatter electron microscopy, and energy dispersive electron spectroscopy to understand the micro-texture of the pyrite-walled tube structures and to select analysis sites for *in situ* sulfide-sulfur isotope measurements. The sections were then coated with 30 nm of gold using a Cressington Sputter Coater. A 19kV $^{133}Cs^{+}$ primary beam was used to pre-sputter a ~100 μm^2 surface with a ~3 nA current. The same primary beam with a 1-3 nA current was used to acquire 10 cycles of ^{32}S for 0.96 s and ^{34}S for 2 s on a ~25 μm^2 spot; typical count rates were ~10^9 counts per second (cps) for ^{32}S and ~10^8 cps for ^{34}S. Mass resolution was between 3,000 and 4,500 to ensure measured ^{34}S intensities were at least 10^5 times the intensity of the ^{33}SH isobaric interference. For each analysis, 2-standard deviation outliers were culled from the 10 cycles. Measured ratios were converted to the Vienna-Canyon Diablo Troilite (V-CDT) isotopic reference scale by bracketing blocks of ~16 analyses with sets of 4 analyses of an in-house pyrite standard mounted and polished in the thick section (Fischer et al., 2014; Johnson et al., 2013). Ablation pits in pyrite and chalcopyrite are accurately determined relative to the pyrite standard. Reproducibility of $^{34}S/^{32}S$ of the in-house pyrite standard was typically 0.3 to 0.7‰ (2σ s.e.) for each block. Galena was analyzed precisely, but we did not embed an in-house galena standard in the thick sections so the accuracy of the measurements is subject to matrix effect biases (Kozdon et al., 2010).

Texture-specific sulfate-sulfur isotopic compositions of barite and carbonate associated sulfate (CAS, e.g., Burdett et al., 1989) in dolomite were determined on micro-drilled powders from polished drill core slabs from all three sulfide zones. Ten milligrams of silty

dolomite or 50-300 μg of barite were pre-cleaned by sonicating for 4 hr in a 10% (w/w) NaCl solution and then rinsing three times in Milli-Q water (Millipore), centrifuging and removing the supernatant between each step (Present et al., 2015). Carbonates were dissolved in 0.5N trace-metal pure HCl (Seastar Baseline), and barites were dissolved by exchange with a concentrated $NaCO_3$ solution (Breit et al., 1985). Sulfate was purified from other ions with a Biorad AG-1-X8 anionic exchange resin before analysis in duplicate as aqueous sulfate by Multi Collector Inductively Coupled Plasma Mass Spectrometry (MC-ICP-MS) on a Thermo Finnegan Neptune Plus at Caltech (Paris et al., 2013, 2014a). Analysis by this method requires matrix-matching samples to an in-house Na_2SO_4 bracketing standard. To do this, an appropriate amount of NaOH solution was added to samples; their sizes were determined to be 5-300 nmol of sulfate by ion chromatography with a Dionex ICS-2000 on an AS-19 column using 20 mM KOH eluent at the Caltech Environmental Analysis Center. Due to instrument instability when these analyses were performed, precision of $\delta^{34}S$ measurements of sulfate was generally between 0.2 and 1.4‰ (1σ s.e.). Analytical procedural blanks are 0.4±0.28 nmol S (1σ s.d.).

Tube lithology, morphology, and texture

Lithofacies

Pyrite-walled tube structures and associated sediments in the USZ were logged at centimeter-scale in core SC11-095 between 412.07 m and 406.07 m where tube structures are abundant (Figure 3). Tube structures occur within the pyrite lithofacies, which are closely associated with laminated striped shale and breccia lithofacies (Graham et al., 2012).

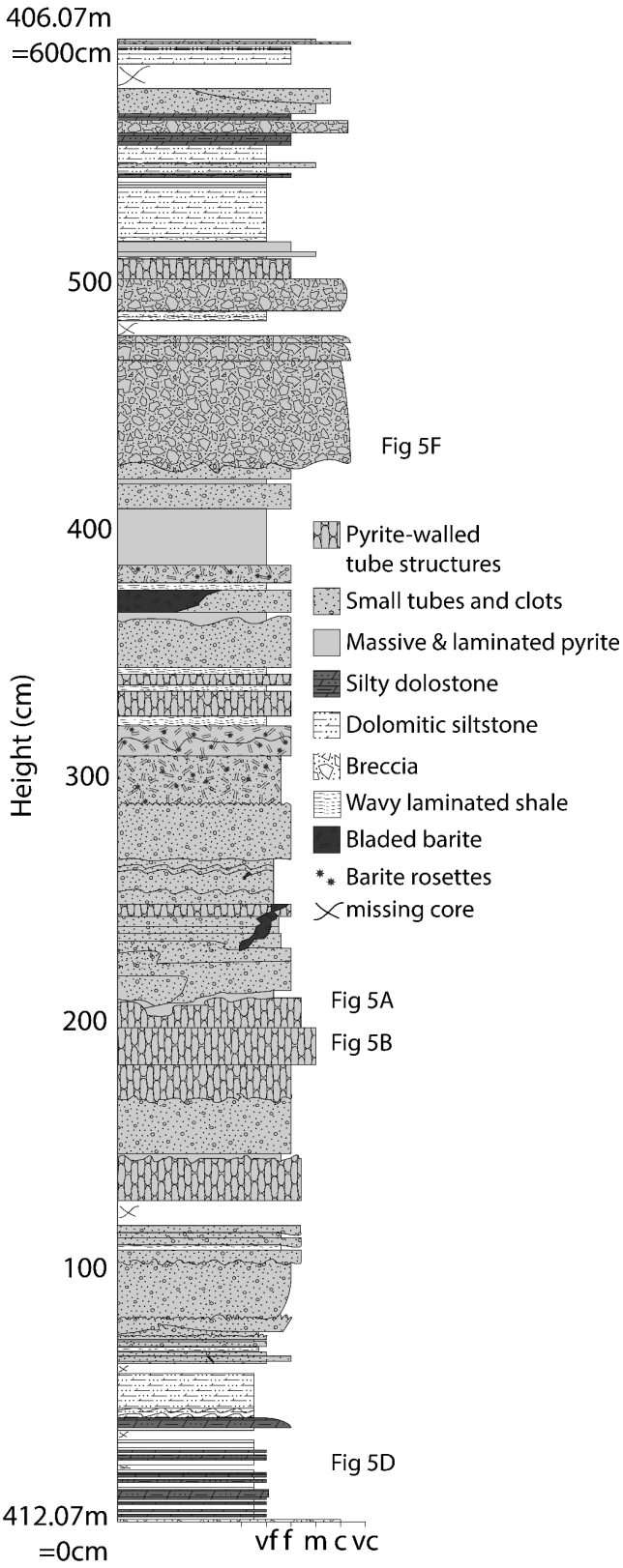

Figure 3: Lithostratigraphic log of core SC11-095 between 412.07 m (base of section) and 406.07 m (top of section, at 600 cm). Where indicated, photographs of the core are shown in Figure 4

Pyrite Lithofacies – Tube structures occur within decimeter-thick intervals of mottled and porous fine-grained pyrite (Figure 4A,B,C). The fine-grained pyrite occurs as polyframboid aggregates (cf. Love, 1971), or as clotted pyrite in a barite or silt matrix. Aggregates consist of sub-millimeter spheroidal clusters of coalesced 5-25 μm pyrite grains (cf. Type PD, Himes and Peterson, 1990). Clots are larger clusters of pyrite aggregates, up to 1 mm in size, with irregular spheroidal or ovoid form, and dark color. These textures are often mingled with small irregular incipient tubes that grade up into well-developed tube structures (arrow in Figure 4A). In some cases, layers of fine-grained, crinkly-laminated sulfide minerals enclose or are interbedded with tube-bearing build-ups (Figure 4A,C). The crinkly-laminated fabric is defined by pyrite/chalcopyrite aggregates and clots, barite-filled irregular voids, and rare, millimeter-sized incipient tubes.

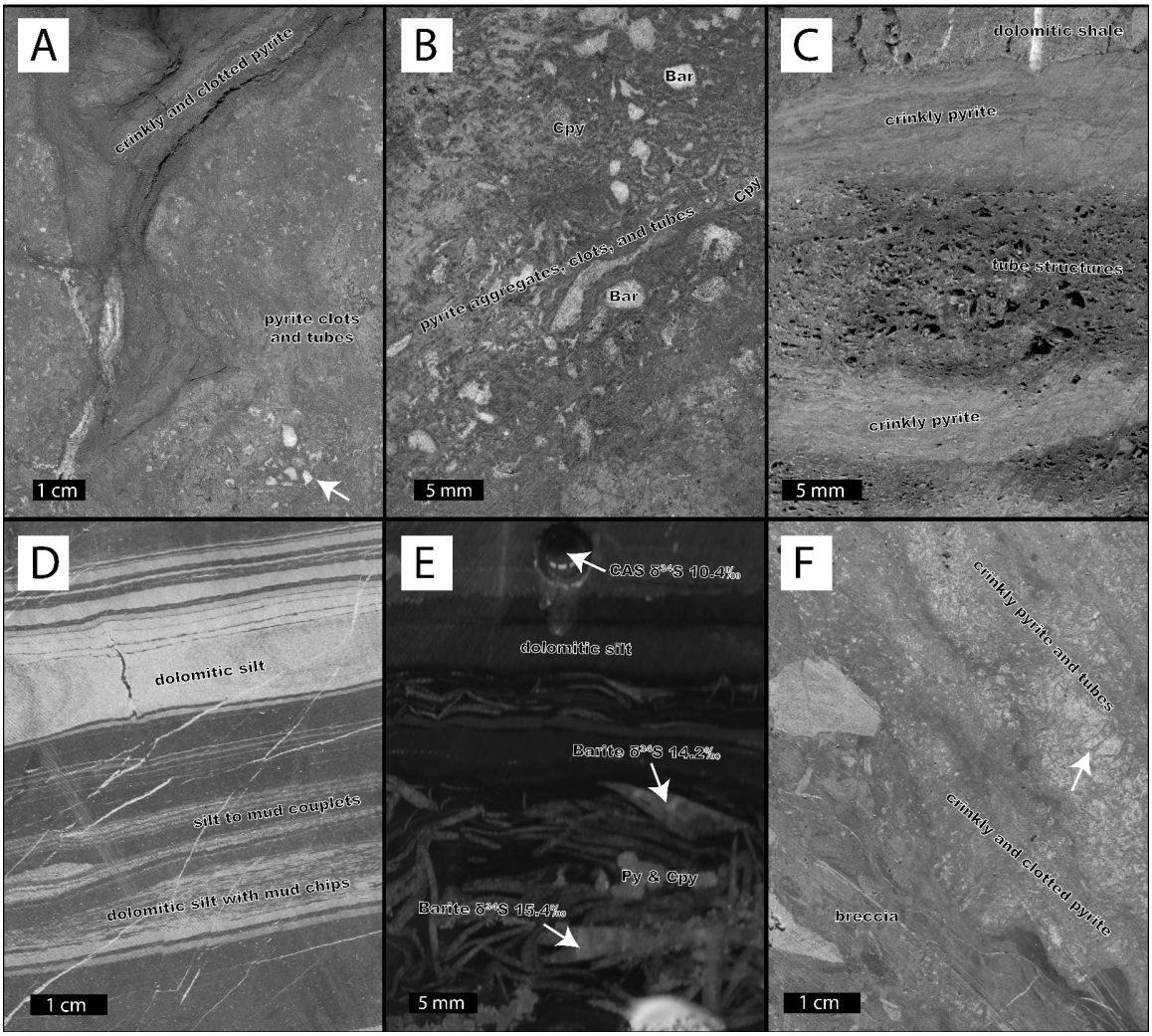

Figure 4: Representative examples of the lithofacies associated with pyrite-walled tube structures from vertical cuts through drill core. (A) SC11-095 drill core intercept of the USZ at 410.02 m, showing the pyrite lithofacies with barite-filled irregular pyrite-walled tube structures that are overgrown by coarse pyrite. Note the three-dimensional structure defined by crinkly pyrite with larger pyrite-walled tube structures near its core (arrow) and finer poorly-laminated pyrite along its edges. (B) SC11-095 drill core at 410.17 m, showing clotted and porous pyrite lithofacies with barite-filled pores and tube structures, and some replacement by chalcopyrite. (C) SC11-029 drill core at 76.20 m, showing tube structures intercalated with crinkly-laminated pyrite in the pyrite lithofacies. (D) SC11-095 drill core at 411.97 m. Laminated striped shale lithofacies, showing graded lamina, recrystallization of dolomite into proto-nodules with fracture prior to compaction, dolomitic siltstone with small mud-chips, and barite-filled high-angle fractures with reverse offset. (E) Dolomitic cap of graded laminations and synsedimentary barite rosettes being replaced by pyrite in the USZ from core SC11-029, 61.185 m. The sulfur isotopic composition of silty dolomite CAS samples is lighter than that of barite samples. (F) SC11-095 drill core at 407.77 m showing pyrite-walled tube structures (arrow) and barite lathes underlain by clast-supported breccia lithofacies with a pyrite-rich matrix.

The best-expressed tube structures are up to 3 mm in diameter with irregular shape and finely crystalline sulfide walls about 100 μm thick (Figure 2). Sulfide walls often are discontinuous and have a preferential sub-vertical orientation (Figure 2B,C,E). The largest tubes cluster to form concentrations normal to bedding (Figure 2F). Coarser sulfides overgrow the walls. Chalcopyrite, dolomite, barite and/or quartz often fill the tube structures and polygonal spaces between them; uncommonly residual porosity is preserved (Figure 2C, 4C). In outcrop, silica completely filled the tubes and pyrite is no longer present (sample B3 and Figure 2A,E).

Centimeter-sized lathes and veins of a late-stage barite may pervasively overgrow pyrite lithofacies, especially where early diagenetic barite lathes dominate interstratified shales (Graham et al., 2012).

Laminated Striped Shale Lithofacies – Carbonaceous, thinly laminated quartz/dolomite siltstone and very thinly bedded quartz silt to dolomite mud graded couplets (Figure 4D) characterize this facies (Graham et al., 2012; Schieber, 1989c; Zieg, 1986). Disseminated pyrite — including nodules similar to the clots and aggregates in the crinkly laminated pyrite — and irregular-shaped lenses of fine-grained pyrite are ubiquitous. Light gray silty intervals containing 1-2 mm black mud chips form wavy beds up to 3 cm thick. Dolomite is finely crystalline and some beds show recrystallization into nodules associated with minor fractures that are filled with siliciclastic mud. Laminae are planar to slightly wavy where compacted around nodules (Figure 4D); their bases are either sharp or scoured. Wavy-bedded mudstone forms partings up to 3 cm thick.

Early diagenetic barite lathes up to 1 cm long displace the laminated striped shale facies and tend to be concentrated within particular intervals. Compaction around lathes and pyrite nodules deformed silt beds and disrupted fine-grained pyrite lenses (Figure 4E).

Breccia Lithofacies – Both matrix- and clast-supported sedimentary breccias contain poorly-sorted angular granule to cobble-sized clasts of the laminated striped shale and pyrite lithofacies (Figure 4F, Supplemental Figure 4B,D,F). The latter include pyrite-walled tube

structures, indicating that they formed prior to resedimentation. The matrix is variably composed of dolomite, silty shale, and fine-grained pyrite. The breccia lithofacies is often overlain by pyrite-walled tube structures (arrow in Figure 4F) in the pyrite lithofacies.

Three Dimensional Morphology

The two Black Butte micro-CT reconstructions show broadly similar three-dimensional tube morphology featuring arcuate pores with rounded ends and a tendency to form centimeter-scale clusters. This is best illustrated by the subsurface sample that has minimal occlusion of tube porosity (sample B1, Figure 2C, Figure 5A,D,G, Supplemental Movie B1) due to the strong density contrast between open pores and the pyrite walls. Tubes sampled from the gossan outcrop (sample B3, Supplemental Movie B3) are completely silicified and original wall material— presumably pyrite— is absent (Figure 2A,E).

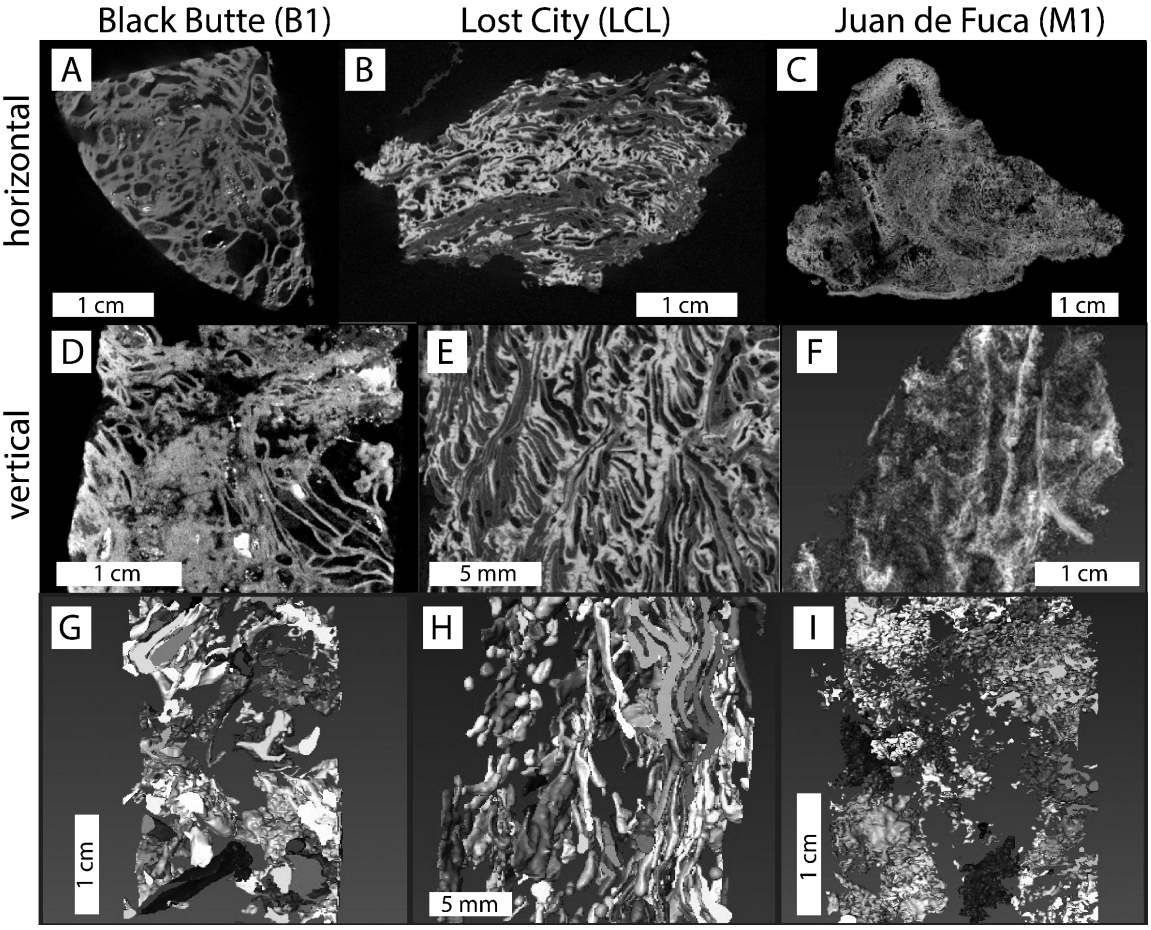

Figure 5: Micro-CT reconstructions of the 3D porosity structure. (A) Grayscale density image of the Mesoproterozoic Black Butte subsurface sample B1 in the horizontal plane, with the brightest white indicating the densest sulfide phases. (B) Grayscale density image of the modern carbonate-brucite-walled sample LCL from Lost City in the horizontal plane, with the brightest white indicating the densest carbonate. (C) Grayscale density image of the modern anhydrite-walled structure M1 from the Juan de Fuca Ridge in the horizontal plane, with the brightest white indicating the densest anhydrite. (D-F) Vertical cross sections of the three samples described above. (G-I) Subset of pores reconstructed from each of the above samples by hiding material denser than a threshold, with volume ≥0.05 mm3, and that highlight characteristic features of the sample. Grayscale differentiates nearby pores, and does not indicate connectivity between pores of the same tone. (G) Subset of reconstructed pores from Black Butte sample B1 that have any trend, and a long-axis plunge of 45-65°. Bedding in this section of drill core dips 55°C relative to the core axis that defines the vertical axis of reconstruction, so these pores had a sub-vertical paleo-orientation. (H) Subset of reconstructed pores from Lost City sample LCL that have any plunge, and a long-axis trend in the same 100°-wide arc. (I) Subset of reconstructed pores from Juan de Fuca Ridge sample M1 that have any trend, and a long-axis plunge of 34-75°. The largest sub-vertical fluid conduits are not enclosed by the sample.

The Lost City samples (LCL and LCM) show very similar three-dimensional anastomosing pore morphologies, including smooth-walled, arcuate pores with rounded terminations (Figure 5B,E,H, Supplemental Movies LCL and LCM). The Juan de Fuca sample (M1), featuring tubes formed by anhydrite walls, shows numerous laterally-linked small pores that produce an overall porous texture, and fewer larger fluid flow paths (Figure 5C,F,I, Supplemental Movie M1). Reconstructions were challenging because the small pores are difficult to resolve individually, while larger fluid flow paths are generally not fully enclosed within the sample. Although it is not well suited for the micro-CT porosity reconstruction method used here, we included this data.

Quantifiable characteristics of porosity include the length, width, aspect ratio, and orientation of individual pore spaces. We measured these characteristics for hundreds of pores in each sample, and the mean and standard deviation of quantifiable characteristics are reported in Table 1. Visual analysis of reconstructed pore networks show that tube structures have pore volumes equal to or greater than 0.05 mm^3 (e.g., Figure 5G-I). Comparison of pore characteristics indicates a similar range of pore sizes between the Black Butte structures and the modern chimney fluid flow structures (Table 1). All have similar lengths (~2-3 mm) and widths (~1 mm), with mean dimensions indistinguishable within one standard deviation. The orientation of the pores was calculated by measuring the trend (Θ) and plunge (Φ) of the long axes relative to arbitrary horizontal axes and a vertical axis. The samples that we analyzed exhibit predominantly sub-vertical pores that are steeply-plunging with respect to bedding. However, some pyrite-walled tube structures from other Black Butte samples appear oriented more horizontally, and may be crushed or flattened (Graham et al., 2012).

Table 1. Micro-CT quantification results

Sample	n*	Length (mm)	Width (mm)	Aspect Ratio	Volume (mm^3)	Length Φ† (°)	Length Θ§ (°)	Width Φ (°)	Width Θ (°)
B1 (Black Butte core)	470	3.49 ± 2.00#	1.53 ± 0.99	2.46 ± 0.85	2.84 ± 4.78	55 ± 21	182 ± 94	60 ± 22	174 ± 106
B3 (Black Butte outcrop)	308	3.26 ± 2.66	1.57 ± 1.40	2.29 ± 0.62	2.13 ± 4.41	54 ± 22	268 ± 176	64 ± 20	159 ± 102
M1 (Juan de Fuca Ridge)	740	2.18 ± 1.68	1.02 ± 0.88	2.25 ± 0.57	1.38 ± 5.35	55 ± 21	182 ± 102	59 ± 22	174 ± 98
LCL (Lost City, inactive)	904	1.92 ± 1.41	0.68 ± 0.35	2.74 ± 1.04	0.36 ± 0.53	47 ± 22	170 ± 95	66 ± 17	185 ± 99
LCM (Lost City, active)	371	2.46 ± 1.45	0.90 ± 0.53	2.88 ± 1.00	0.53 ± 0.94	49 ± 23	158 ± 85	59 ± 23	206 ± 104

*number of pores with reconstructed volume ≥ 0.05 mm^3

†angle between the pore's axis and the z-axis (i.e., plunge), between 0° and 90°

§angle between the pore's axis and the x-axis (i.e., azimuth), between 0° to 360°

#Uncertainties tabulated as one standard deviation

Paragenesis

Paragenesis of pyrite-walled tube structures in the USZ occurred in three main stages (Figure 6A). In the first, abundant disseminated fine-grained pyrite and pyrite nodules formed within surface sediments, and early diagenetic barite lathes precipitated. Second, tube walls precipitated as constructional edifices at the sediment-water interface, possibly as a metastable sulfide, hydroxide, carbonate, or sulfate. Mottled pyrite and colloform pyrite soon replaced the original mineralogy of the tube structures. In some cases, euhedral marcasite overgrew the tube structures (Figure 2D). Third, these textures were infilled by massive barite. Dolomite and quartz occluded most remaining porosity, and replaced the massive barite (Graham et al., 2012). Barite, dolomite, quartz, and the earlier pyrite textures associated with tube structures were in turn overgrown or replaced by coarse pyrite and base metal minerals (Graham et al., 2012). These textures are described in Table 2 and illustrated in Figure 7.

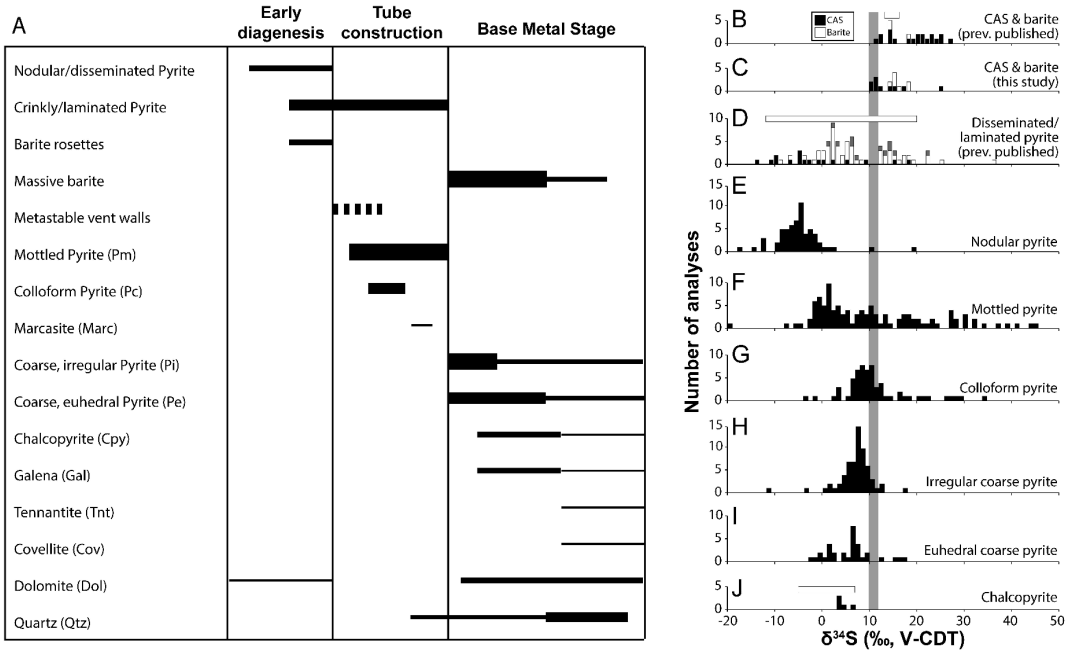

Figure 6**:** (A) Paragenesis of tube structures and associated rocks from the USZ. Phases with thicker bars are qualitatively more abundant. Dashed bar for metastable vent walls indicates that the phase is inferred, but no longer present (see text for details). (B-J) Histograms of sulfur isotope data from the literature and this study. White horizontal bars are data ranges reported by Zieg and Leitch (1998) for barite, laminated pyrite, and chalcopyrite. Data in (B) compiled from Gellatly and Lyons (2005), Strauss (1993), and Strauss and Schieber (1990). Data in (D) compiled from Strauss and Schieber (1990) (black), Lyons et al. (1993) (gray), and Lyons et al. (2000) (white). Gray shaded region highlights the interpreted sulfur isotopic composition of seawater sulfate in the Helena Embayment during deposition of the Newland Formation (see text for details).

Table 2: Sulfide textures in pyrite-walled tube structures and related lithofacies

Sulfide texture	Description
Disseminated pyrite	Anhedral (occasionally framboidal) pyrite crystallites less than 5 μm wide, often with euhedral overgrowths (Graham et al., 2012; Himes and Peterson, 1990; Schieber, 1989c; Strauss and Schieber, 1990; White et al., 2013)
Nodular pyrite (Pn)	Ovoid porous masses, up to 1 mm in diameter, of disseminated pyrite crystallites coalesced and/or encrusted by later euhedral pyrite (Graham et al., 2012; Himes and Peterson, 1990; Strauss and Schieber, 1990)
Colloform pyrite (Pc)	Botryoidal and isopachous fine-grained pyrite layers up to 5 μm thick; accreted both towards the interior of tube structures, and away from the exterior tube wall surfaces into polygonal void spaces; often intergrown with quartz
Mottled pyrite (Pm)	Clusters of anhedral to euhedral pyrite grains up to 25 μm in diameter (cf. Type PB, Himes and Peterson, 1990) that are overgrown by brighter coarsely-crystalline pyrite; abundant small (<2 μm) pores and inclusions of other sulfide minerals; intergrown with colloform pyrite; referred to as "spongy pyrite" by Graham et al. (2012)
Marcasite (Marc)	Coarse euhedral grains, often bladed, up to 40 μm long
Coarse, irregular pyrite (Pi)	Bright, uniform, anhedral pyrite with embayed margins and numerous small (<2 μm) inclusions of galena, chalcopyrite, and tennantite; overgrows earlier pyrite stages by following colloform topography, fills cross-cutting veins up to 10 μm wide, and rims quartz filling tube structures
Coarse, euhedral pyrite (Pe)	Bright, uniform, subhedral to euhedral continuous overgrowth on coarse irregular pyrite; dominant sulfide occluding tube structure porosity; commonly contains exsolved anhedral blebs of chalcopyrite and galena
Chalcopyrite (Cpy) and galena (Gal)	Porosity-occluding anhedral crystals; blebs up to 20 μm in diameter exsolved from coarse euhedral pyrite; smaller (<10 μm) anhedral grains replacing mottled and colloform pyrite
Covellite (Cov)	Porosity-occluding anhedral crystals; chains of anhedral grains replacing chalcopyrite associated with colloform pyrite
Tennantite (Tnt)	Porosity-occluding anhedral crystals

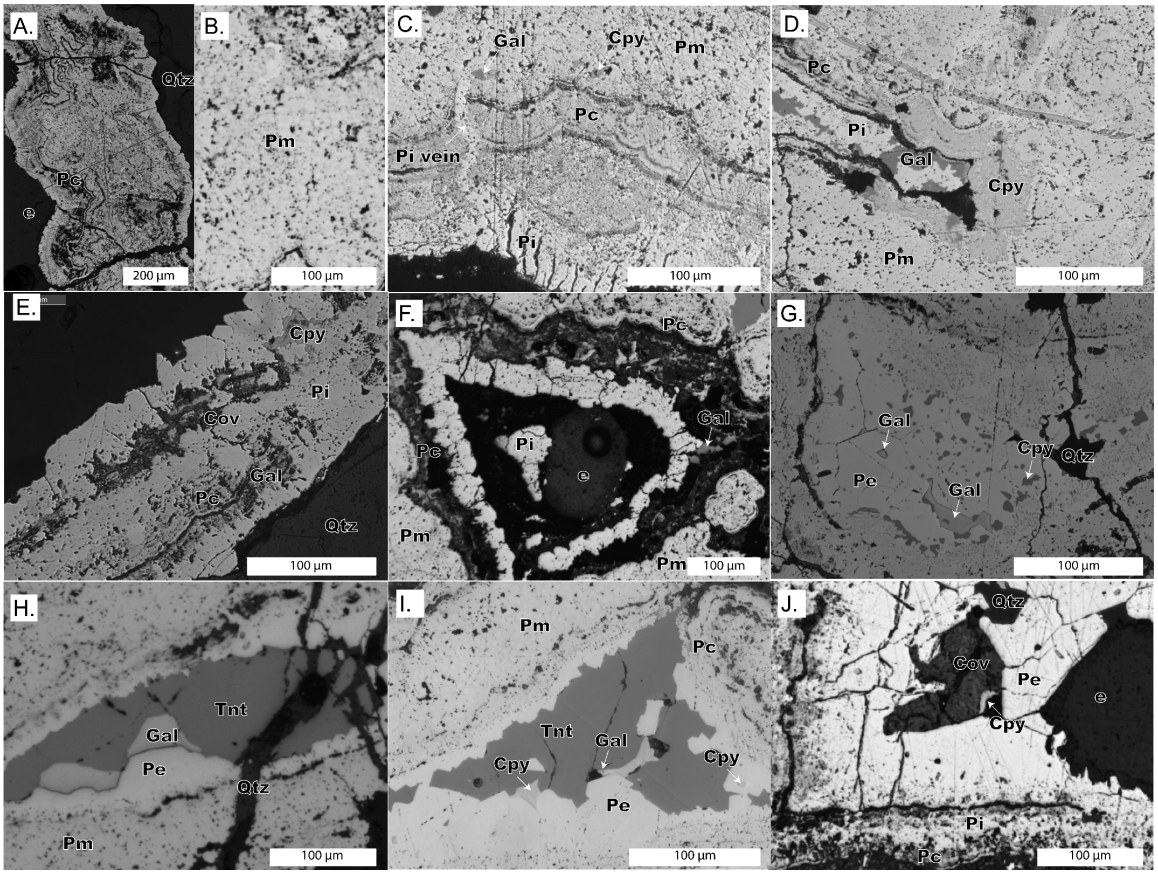

Figure 7: Reflected light photomicrographs from SC11-029-56.42 m showing sulfide minerals and textures associated with tube structures. Mineral texture abbreviations as in Table 2. (A) Colloform pyrite comprises tube structures' walls, with growth direction into both void spaces; quartz fills void space to the right, and epoxy (e) used to mount the slide fills remnant porosity. (B) Mottled pyrite. (C) Intergrown colloform and mottled pyrite overgrown by irregular coarse pyrite with anhedral blebs of galena and chalcopyrite. (D) Bands of colloform pyrite controlling overgrowth and replacement of mottled/colloform pyrite with chalcopyrite, and intergrowth of galena with irregular coarse pyrite. (E) Colloform pyrite overgrown by irregular coarse pyrite, galena, and chalcopyrite; the chalcopyrite is replaced by covellite. Quartz fills the tube structure. (F) Irregular coarse pyrite overgrowing colloform pyrite and filling porosity; galena replaces some colloform pyrite. (G) Euhedral coarse pyrite overgrowing colloform/mottled pyrite, with exsolved chalcopyrite and galena, cut by a quartz-filled fracture. (H) Tennantite, galena, and euhedral coarse pyrite fill porosity in mottled/colloform pyrite, and is cut by a quartz-filled fracture. (I) Chalcopyrite and galena intergrown with tennantite fill porosity remaining after euhedral coarse pyrite with exsolved chalcopyrite and galena overgrows mottled/colloform pyrite. (J) Covellite and chalcopyrite fill porosity remaining after euhedral coarse pyrite and irregular coarse pyrite overgrew colloform pyrite.

Gangue mineralogy differs significantly among sulfide zones (Graham et al., 2012; Zieg et al., 2013). In the USZ, carbonate occurs as fine sediment in the laminated striped shale lithofacies (Figure 4D, Supplemental Figure 3A,E), as dolostone clasts in the breccia lithofacies (Figure 4F, Supplemental Figure 3B,D,F,G), as dolomite rims and overgrowths

on quartz, and as coarse dolomite cement filling porosity (Figure 8A). Barite forms early-diagenetic lathes that precipitated in the laminated striped shale lithofacies prior to sediment compaction (Figure 4E, Supplemental Figure 3C,D), and as later veins and lathes that occlude porosity (Supplemental Figure 3F,G). Quartz occurs as veins cross-cutting all of the pyrite generations (Figure 7G), and as porosity-occluding subhedral crystals that fill the pyrite-walled tube structures (Figure 2B,C,F, 8B,C); it is often rimmed by coarse irregular pyrite (Figure 8B). Quartz is also closely intergrown with the colloform pyrite (Figure 8B,D).

Sulfur isotope results

The sulfur isotopic composition of carbonate associated sulfate (CAS) and early diagenetic barite lathes was determined in samples micro-drilled from 8 polished slabs from all three sulfide zones (Figure 4E, Supplemental Figure 3). Silty dolomite dissolved for CAS sulfur isotopic analyses was collected from the tops of graded silt-to-carbonate couplets from the laminated striped shale facies, and from silty dolomite clasts in the breccia facies. Barite and CAS sulfate isotopic compositions and concentrations (for CAS) are reported in Table 3.

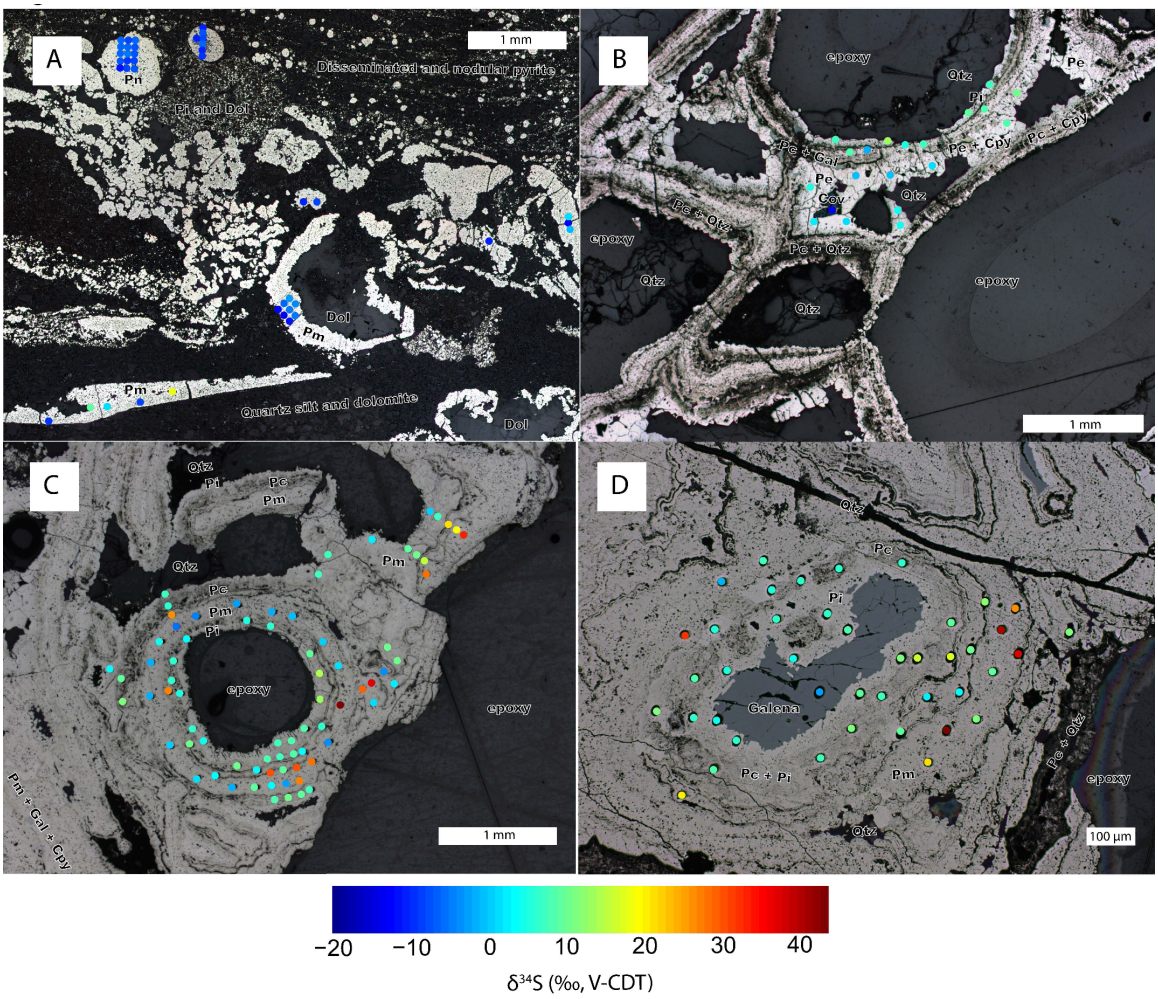

Figure 8: SIMS sulfide-sulfur $\delta^{34}S$ analysis pits colored by isotopic composition overlain on plain-polarized reflected light composite photomicrographs. See Supplemental Figure 2 for location of sites on the thick sections. Further analysis pits are shown in Supplemental Figure 4. Mineral texture abbreviations are as in Table 2. (A) SC11-095-389.22 m, Sites 7, 8, and 9. Pyrite nodules and fragments of tube structures in a thick conglomerate lamina within very thinly laminated striped shale. (B) SC11-029-56.42 m, Site 6. Coarse pyrite overgrowing delicate pyrite-walled tube structures with partial quartz occlusion. (C) SC11-029-56.42 m, Site 3. Pyrite-walled tube structures overgrown by coarse pyrite and largely devoid of porosity-occluding gangue minerals. (D) SC11-029-56.42 m, Site 1. Pyrite-walled tube structure overgrown by coarse irregular pyrite and filled with galena, with a late quartz-filled fracture.

Table 3: Sulfate-sulfur results

Sample	Type	% Carbonate*	[CAS] (ppm†)	$\delta^{34}S_{SO4}$ (‰, V-CDT)
USZ				
SC11-029, 49.09 m (a)	Barite lathe	N.A. §	N.A.	18.32 ± 0.14#
SC11-029, 49.09 m (b)	Barite lathe	N.A.	N.A.	16.22 ± 0.26
SC11-029, 61.185 m (a)	Dolomitic mudstone	88	656 ± 51	10.42 ± 0.61
SC11-029, 61.185 m (b)	Barite lathe	N.A.	N.A.	14.15 ± 0.24
SC11-029, 61.185 m (c)	Barite lathe	N.A.	N.A.	15.44 ± 0.57
SC11-095, 362.51 m (a)	Dolostone clast	79	152 ± 12	13.66 ± 1.00
SC11-095, 362.51 m (b)	Dolostone clast	55	217 ± 21	9.97 ± 1.09
SC11-095, 362.51 m (c)	Dolostone clast	61	129 ± 12	11.27 ± 0.82
SC11-095, 485.83 m (a)	Dolostone clast	91	23 ± 2	11.38 ± 1.50
SC11-095, 485.83 m (b)	Barite cement	N.A.	N.A.	15.40 ± 1.94
SC11-095, 486.29 m (a)	Barite lathe	N.A.	N.A.	15.04 ± 0.21
SC11-095, 486.29 m (b)	Barite lathe	N.A.	N.A.	17.64 ± 0.17
MSZ				
SC10-06, 378.31 m	Dolostone clast	102**	70 ± 5	16.78 ± 0.98
LSZ				
SC12-112, 335.02 m	Dolomitic mudstone	60	102 ± 9	25.45 ± 1.31
SC12-112, 327.83 m (a)	Dolomitic mudstone	51	334 ± 36	11.83 ± 0.64
SC12-112, 327.83 m (b)	Dolomitic mudstone	58	136 ± 13	14.78 ± 1.14
SC12-112, 372.83 m (c)	Dolomitic mudstone	53	388 ± 37	11.27 ± 0.82

*Functionally refers to the acid-soluble portion of the rock.
†ppm = parts per million by mass, equivalent to μg SO_4^{2-}/g carbonate.
§N.A. = not applicable.
#Uncertainties tabulated as 1σ standard error
**Insoluble residue after dissolution too negligible to weigh accurately.

Barite samples have a $\delta^{34}S$ composition of 14 to 18‰ V-CDT (open boxes in Figure 6C). CAS samples have a composition of 10 to 25‰ V-CDT, but most samples are generally ^{34}S-depleted relative to the barite samples and have an isotopic composition of less than 13‰ V-CDT (solid boxes in Figure 6C). A range of CAS $\delta^{34}S$ compositions of up to 4‰ is observed across short stratigraphic thicknesses in the laminated striped shale facies (Supplemental Figure 3A), and amongst co-occurring silty dolomite clasts in the breccia facies (Supplemental Figure 3B).

Sulfur isotopic measurements of the 10 μm-wide ablation pits in sulfide minerals are illustrated in Figure 8 and Supplemental Figure 4. All data are tabulated in Appendix 1 and summarized in Table 4.

Table 4: Statistical description of sulfide $\delta^{34}S$ data

Mineral	**n**	**Mean (‰)**	**1σ s.d.*** **(‰)**	**Median (‰)**	**IQR†** **(‰)**
Pyrite texture					
Nodular pyrite (Pn)	61	-5.3	5.3	-5.5	4.4
Mottled pyrite (Pm)	108	10.3	12.5	7.5	17.2
Colloform pyrite (Pc)	63	10.8	7.1	9.2	4.6
Irregular coarse pyrite (Pi)	64	6.4	3.8	6.9	2.7
Euhedral coarse pyrite (Pe)	33	5.4	4.9	5.7	5.4
Coarse pyrite§	97	6.1	4.2	6.5	3.7
Base-metal sulfides					
Chalcopyrite	5	3.9	1.2	3.4	1.6
Galena	6	-6.7#	1.2	-6.6#	2.2

*s.d. = standard deviation
†IQR = inter-quartile range
§Coarse pyrite is the joint population of Pi and Pe pyrite
#No galena standard was used, so accuracy is unknown (but precision is reliable)

In situ sulfur isotope data from the tube structures and diagenetic pyrite nodules generally coincide with Newland Formation pyrite data reported previously (Figure 6D) (Lyons et al., 2000, 1993; Strauss and Schieber, 1990; Zieg and Leitch, 1998). Pyrite nodules have a mode of ~-5‰ V-CDT, with data right-skewed to values as high as 19‰ V-CDT (Figure 6E). Mottled pyrite has a $\delta^{34}S$ mode of ~1‰ V-CDT, and the data are right-skewed to values as high as 45‰ V-CDT (Figure 6F). Colloform pyrite has a mode of ~10‰, and is right-skewed to a value of 34‰ V-CDT (Figure 6G). Coarse irregular pyrite and coarse euhedral pyrite each have a mode of ~6‰ V-CDT and symmetrically distributed values (Figure 6H,I). Chalcopyrite grains were only large enough to measure in five locations, but have a mean composition of 3.9‰ V-CDT (Figure 6J).

Discussion

Sulfur biogeochemistry during deposition of the Newland Formation

The presence of broken pyrite-walled tube structures as intraclasts in the breccia facies indicates that they formed in shallow sediments or above the sediment-water interface (Figure 2D, 8A). They are also closely associated with crinkly laminated pyrite (Figure 4A,C), which has been previously interpreted as a preserved microbial mat texture at Black Butte (Lyons et al., 2006; Schieber, 1989c, 1990). During deposition of the Newland Formation, deep water in the Black Butte area of the Helena Embayment was anoxic but contained sulfate (Planavsky et al., 2011; Slotznick et al., 2015). Sulfur isotope studies of disseminated and framboidal sedimentary sulfides (Figure 6D, E) suggest that sulfate from the ocean fed microbial sulfate-reducing communities in shallow sediments (Lyons et al., 2000, 1993; Strauss and Schieber, 1990).

The isotopic composition of CAS and early diagenetic barite constrains the isotopic composition of seawater sulfate. In modern carbonates, CAS provides an accurate proxy for the isotopic composition of contemporaneous seawater sulfate (Burdett et al., 1989; Kampschulte et al., 2001; Lyons et al., 2004); however, for older strata the fidelity of this archive is less certain (Present et al., 2015). Our data generally overlaps with a compilation of previously published barite and CAS data for the Helena Embayment rocks (Figure 6B,C) (Gellatly and Lyons, 2005; Strauss, 1993; Strauss and Schieber, 1990; Zieg and Leitch, 1998). It is common in organic-rich marine sediments for sulfate reduction in sediment pore fluids to exceed the rate that sulfate can diffuse from seawater into the sediments; this leads to closed system behavior during the kinetic fractionation of sulfate, and enriches the residual pore fluid sulfate in ^{34}S (Jørgensen, 1979). This behavior appears to be present in our sulfate $\delta^{34}S$ data. This interpretation is reinforced by the observation that the barite is generally higher in $\delta^{34}S$ relative to CAS by ~4‰ in samples where both barite and CAS were measured (Figure 4E, Supplemental Figure 3). Based on petrographic textures (Figure 4E), diagenetic barite precipitated below the sediment-water interface from sulfate more likely to be diagenetically ^{34}S-enriched, while synsedimentary dolomite was more likely to preserve CAS values recording the original composition of seawater. Some CAS measurements are

much heavier in $\delta^{34}S$ (up to 25‰ V-CDT, Supplemental Figure 3E), so it is possible that significant amounts of diagenetically high $\delta^{34}S$ sulfate could be incorporated into the dolomite during recrystallization of a primary carbonate phase (Lyons et al., 2004; Present et al., 2015; Rennie and Turchyn, 2014).

Taking the isotopic data in the context of petrographic fabric, the maximum $\delta^{34}S$ composition of contemporaneous seawater sulfate is approximated by the lowest CAS $\delta^{34}S$ measurements, between 10‰ and 12‰ V-CDT. The lightest CAS measurements are consistently observed within dolomite debris flow clasts transported from outside the area of active sulfide mineralization, where closed-system sulfate reduction would be minimized due to less fixation by iron or less reduction by organic carbon (Jørgensen, 1979). An inferred seawater sulfate composition of 10-12‰ V-CDT is lighter than previously suggested on the basis of Newland Formation barites (Strauss, 1993; Strauss and Schieber, 1990; Zieg and Leitch, 1998), but is comparable to previously reported CAS from the Newland Formation and other Mesoproterozoic successions (Gellatly and Lyons, 2005; Guo et al., 2015; Kah et al., 2004).

What we interpret as the paragenetically earliest pyrite (nodules in SC11-029-389.22 m, Figure 8A, Supplemental Figure 4F) also has the lowest $\delta^{34}S$ composition (Table 4). Values as light as -18‰ V-CDT indicate fractionation from seawater sulfate of nearly 30‰ (Figure 6E), comparable to kinetic fractionations associated with microbial sulfate reduction in an open system (Jørgensen, 1979). These data are generally lighter than *in situ* sulfur isotope data from Archean (i.e., before oxygenation of Earth's surface and therefore lower marine sulfate concentrations) diagenetic pyrite nodules, and lack isotopic zonation from core to rim that may have suggested more sulfate-limiting pore fluid conditions during nodule growth (Fischer et al., 2014; Gregory et al., 2015; Johnson et al., 2013; Kamber and Whitehouse, 2007; Marin-Carbonne et al., 2014).

A broad range of isotopic compositions of early pyrite in the Helena Embayment was observed by Lyons et al. (2000) and Luepke and Lyons (2001) (Figure 6D), who further noted large, systematic stratigraphic trends interpreted as basin-scale reservoir effects on the

composition of pyrite. In contrast, Strauss and Schieber (1990) identified two phases in disseminated pyrite: a low $\delta^{34}S$ early diagenetic pyrite and a higher $\delta^{34}S$ coarsely-crystalline concretionary overgrowth. They attributed the variability in pyrite compositions to changes in the diffusive supply of sulfate to the sediments; heavier isotopic compositions reflect a more closed system (Jørgensen, 1979). With *in situ* measurements, we observed a pattern similar to that reported by Strauss and Schieber (1990), especially in SC11-029-389.22 m Site 5 (Supplemental Figure 4F). Early diagenetic nodules are generally lighter than coarser pyrite overgrowths, consistent with minimal sulfate limitation during early pore fluid sulfate reduction and pyrite nodule growth. It is therefore likely that the pyrite nodules precipitated shallower in the sediments than the barite rosettes and coarse pyrite overgrowths, whose $\delta^{34}S$ enrichment suggest pore fluid sulfur isotope reservoir effects. Barium was likely supplied by the remineralization of organic matter in the sediments, and concentrated along diagenetic fronts at the base of the sulfate reduction zone (Torres et al., 1996).

Estimates for the concentration of sulfate in marine waters during the Mesoproterozoic range from <0.1 mM to 4.5 mM, and may have been globally variable (Canfield et al., 2010; Kah et al., 2004; Luo et al., 2015; Sperling et al., 2014). The lowest estimates are based on observations of small isotopic differences (<10‰) between contemporaneous sulfate and sulfide (Canfield et al., 2010; Luo et al., 2015), and are precluded in the Helena Embayment by our and published data (Figure 6B-E). In modern environments, Algeo et al. (2015) and Canfield et al. (2010) empirically identified a correlation between observed sulfur isotope fractionation and sulfate concentrations. If this relationship holds in the Mesoproterozoic, then the sulfur isotopic depletion we observe in pyrite nodules— about 10-30‰ lighter than the $\delta^{34}S$ of contemporaneous seawater sulfate— correlates to 2-6 mM sulfate concentrations (with a mode of 3 mM) in the Helena Embayment during deposition of the Newland Formation (Algeo et al., 2015). This estimate is a conservative estimate of the minimum sulfate concentration, given the interpretation that seawater is represented by the lowest CAS $\delta^{34}S$ measurement and assuming that the pyrite nodules formed contemporaneously with the CAS.

Precipitation of tube structures

While the pyrite-walled tube structures are interbedded with crinkly laminated pyrite and debris flows, intergrowth of mottled pyrite with colloform pyrite and quartz (Figure 8B,D) suggests that at least in some cases they are closely associated with the early stages of base metal mineralization. We interpret that the tube structures formed at sites of hydrothermal fluid effluence to the seafloor (Figure 9).

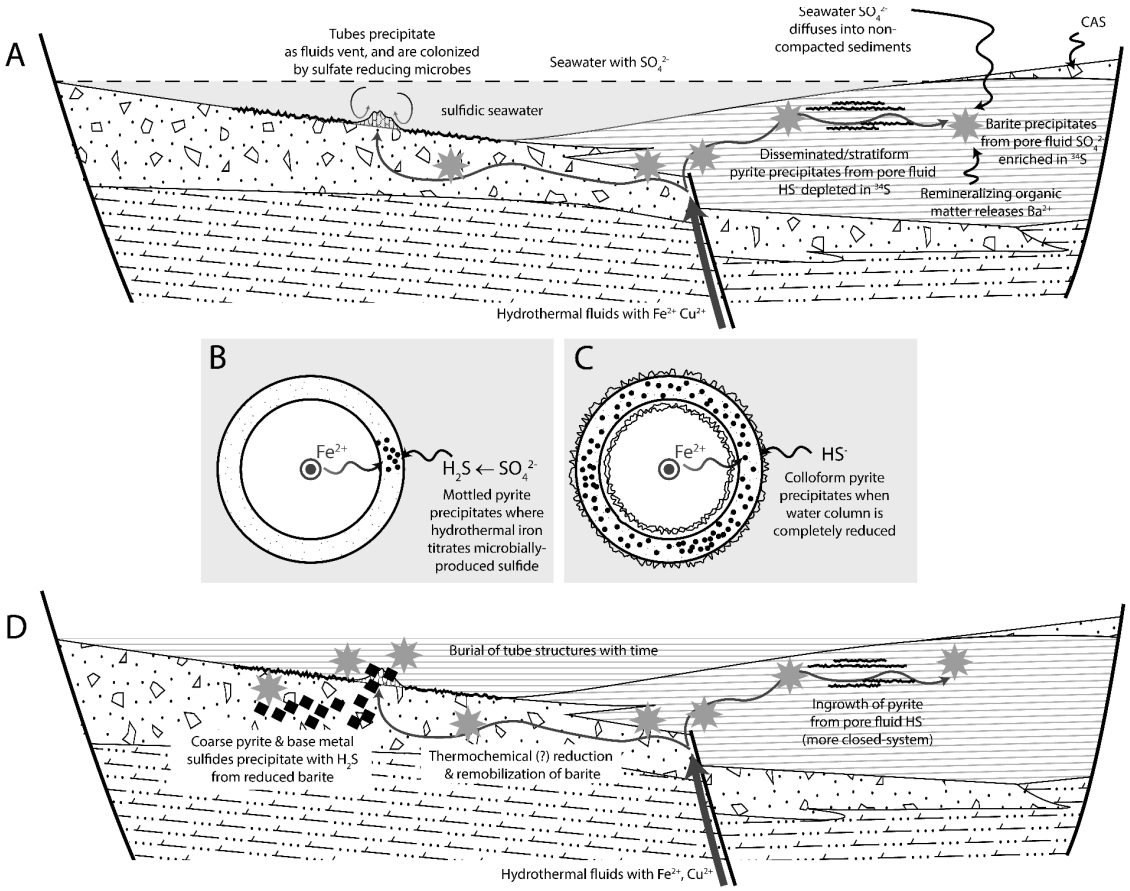

Figure 9: Schematic illustrating how seawater sulfate interacts with hydrothermal fluids to create tube-shaped vent structures of mottled and colloform pyrite. (A) Metalliferous hydrothermal fluids seep up, possibly along faults, and interact with seawater or diagenetically modified pore fluids. Disseminated and nodular pyrite forms from sulfide microbially produced in the sediments under open-system conditions with respect to seawater sulfate supply. Diagenetic barite precipitates deeper in the uncompacted sediments from residual pore fluid sulfate isotopically distilled by microbial sulfate reduction and barium released by remineralizing organic matter. Tube-shaped conduits precipitate as the metalliferous fluids vent to the seafloor in the restricted basin, where euxinic or suboxic seawater contains temporally-variable amounts of sulfate and sulfide. Possibly, microbial mats colonize the tube structures and seafloor near vent sites. (B-C) Cross section of a single tube-shaped fluid conduit. (B) Sulfide in the water column produced by microbial communities growing on or around the vent structures reacts with iron to precipitate mottled pyrite within the metastable precursor of the tube walls. (C) During intervals of nearly complete sulfate reduction in the basin, colloform pyrite precipitates on tube walls as iron is slowly supplied by continued venting. (D) After burial of the tube structures, continued supply of metals reacts with sulfate reduced from barite to form coarse pyrite and base metal sulfides. Fractionation of sulfur isotopes by thermochemical sulfate reduction of barite can explain the coarse pyrite and chalcopyrite isotopic compositions. Later coarse pyrite overgrowth of nodular and disseminated pyrite is also isotopically heavier than earlier pyrite, reflecting sulfur isotope distillation in the deeper pore fluids.

Fluid inclusion data indicate a moderate salinity (1.1-3.5 mol/kg) and a homogenization temperature of less than 250°C for Black Butte hydrothermal fluids (Himes and Peterson, 1990); under these conditions, expelled fluids, upon mixing with cold seawater, would have acted as a brine denser than seawater (Himes and Peterson, 1990; Sangster, 2002) (Himes and Peterson, 1990; Sangster, 2002). This would diminish the buoyancy of the expelled fluid relative to seawater, so precipitation and accretion patterns would resemble those at low-velocity modern diffuse vents (Hannington et al., 1995).

At diffuse hydrothermal vents, both biologic and inorganic processes contribute to the formation of tube-shaped structures. One possible biologic process would involve preservation of macroscopic organisms as a cast or mold. Preservation of macroscopic organisms (such as worm tubes) with broadly comparable size and porosity may create similar structures in Phanerozoic deposits (e.g. Banks, 1985; Campbell et al., 2002; Haymon et al., 1984; Little et al., 1999a, 1999b; Moore et al., 1986), but there are few definitive examples of macroscopic organisms in Proterozoic strata and no known organisms that provide unambiguous analogs for tube formation. Although problematic macrofossils (*Grypania* and *Horodyskia*) have been described in shallower paleoenvironments in the Helena Embayment and other contemporaneous successions (Fedonkin and Yochelson, 2002; Kumar, 1995; Walter et al., 1990), these do not resemble known tube structures and neither these nor any other Mesoproterozoic macrofossils have been described from the deep-slope, below wave-base setting characteristic of Black Butte sedimentary rocks (Horodyski, 1993).

Alternatively, the tube structures' close association with crinkly-laminated pyrite might suggest that they are unique Mesoproterozoic microbialites formed by the sulfide-permineralization of microbial communities (McGoldrick and Zieg, 2004). Mineralization could have encrusted locally abundant mats or streamers of colonial or filamentous microorganisms, as is observed in cold seeps and alkaline springs (e.g. Arp et al., 1998; Barbieri and Cavalazzi, 2005; Cady et al., 2003; Fouke et al., 2000; Hofmann and Farmer, 2000; Reitner et al., 2005). Biological accretion in this manner predicts a consistent 3-D

form controlled by the morphology of microbial communities. Streamer fabrics are encapsulated in tube-shaped structures that have a near constant diameter with a high aspect ratio controlled by the average colony size; aspect ratio and diameter have low variances. The strands are oriented roughly parallel to fluid flow or, in still water, under the influence of gravity (Cady et al., 2003; Hofmann and Farmer, 2000). Most sedimentary environments show fluid flow parallel to the sediment-water interface, which predicts that tube structures would have a strong preferential pore orientation in the horizontal plane.

The Black Butte tube structures have irregular shapes (Figure 2, 5G), not the consistent dimensions or repeating organization predicted by mineralization of macroscopic organisms. They do not have the high aspect ratio with low variance, low variance of tube width, and strong horizontal preferred orientation (Table 1) predicted by mineralization of filamentous microbial communities by analogy to modern microbial hydrothermal communities. Thus, the 3-D form of the millimeter-scale tube structures does not match known biologic hydrothermal morphologies.

Encrustation of microbial material also predicts specific sulfide petrographic textures that are not observed in the Black Butte tube structures. Preservation of the microbial outline as a mold generally results from crystal precipitation towards a free aqueous surface (Jones et al., 2008; Li and Kusky, 2007; Shapiro and Fricke, 2002). However, colloform pyrite in the ~100 μm walls of the tube structures propagates away from both sides of the tube structures' walls (Figure 8B,C), indicating a free surface on either side of the mottled pyrite. Perhaps organic material defining a millimeter-scale community structure was removed prior to colloform pyrite mineralization, but intergrowth of mottled and colloform pyrite (Figure 8C) suggests that this is not the simplest option.

Abiotic mineralization at diffuse hydrothermal vents creates textures and structures similar to those found at Black Butte. Precipitation of early hydrothermal minerals governs fluid flow and controls redox and temperature gradients between hydrothermal fluids and seawater (Hannington et al., 1995; Tivey, 2007). The fluid conduits in these buildups have an internal architecture characterized by networks of millimeter-scale tortuous conduits similar to the

Black Butte tube structures (Gamo et al., 1991; Kelley et al., 2001b; Koski et al., 1994; Ludwig et al., 2006). Tubes are highly variable in size and aspect ratio with tube orientation generally in the direction of fluid flow, and often elongate normal to the sediment water interface. Black Butte tube dimensions are similar to those in Lost City and Juan de Fuca networks, with mean dimensions for all samples within one standard deviation (Table 1) (Haymon and Kastner, 1981; Kelley et al., 2001b). Further, the sub-vertical fabric, variably ovoid aspect ratio, millimeter-scale tortuous porosity, and extensive cementation in tube structures is consistent with morphologies found at modern diffuse vent sites (Delaney et al., 1992; Koski et al., 1994; Ludwig et al., 2006; Okumura et al., 2016).

By analogy to modern diffuse vent structures, mottled and colloform pyrite in the Black Butte tube structures probably replaced or precipitated on an unobserved earlier phase that defined the walls of tube structures (Figure 9A). As iron-rich hydrothermal fluid diffused through these walls and met sulfide in seawater, granular sulfides would have precipitated within the precursor (Figure 9B) (Haymon, 1983; Tivey, 1995). The replaced initial tube walls were likely iron-sulfide colloids or poorly ordered minerals (Russell et al., 1989; Russell and Hall, 1997), but a variety of metastable phases (e.g., anhydrite, brucite, aragonite) commonly precipitate at deep vent sites and do not remain in the geologic record (Breier et al., 2010; Haymon and Kastner, 1981; Kelley et al., 2001b; Ludwig et al., 2006; Okumura et al., 2016).

Overall, the texture and 3D structure are difficult to explain as bioconstructions without hypothesizing a complicated and entirely new model for microbial communities. Nonetheless, the low and variable $\delta^{34}S$ composition of the mottled pyrite suggests microbial sulfate reduction sourced much of the sulfide. Mottled pyrite has an extremely variable sulfur isotopic composition (IQR=17.2‰, Table 4) over millimeter scales, with compositions as light as -20‰ V-CDT and as heavy at 45‰ V-CDT (Figure 6F). We suggest, then, that the three-dimensional features of the tube structures primarily reflect fluid flow, whereas sulfur geochemistry indicates that sulfate-reducing bacteria provided sulfide for the accreting structures. Colonization of vent structures is common at modern vents. For example, at the modern Lost City and Shinkai Seep hydrothermal deposits, microbial consortia colonize

intricate tube-shaped, 100 μm to millimeter-scale pores in aragonite-brucite buildups (Kelley et al., 2005; Okumura et al., 2016). There is evidence of encrustation of some filamentous micron-scale organisms. However, the dominant (>1 mm) porosity structure is governed by the diffuse fluid flow regime (Kelley et al., 2005; Ludwig et al., 2006; Okumura et al., 2016; Schrenk et al., 2004). The chemical gradients at the vent site, combined with a complicated porosity structure, allow microbial communities to take hold. It is not clear how extensive of a role the microbial community plays in nucleating minerals or modifying fluid flow to shape the large fluid conduits (Emerson and Moyer, 2002; Steen et al., 2016). A chemoautotrophic community—in this case, microbial sulfate reducers— likely colonized vents and increased the redox gradient to allow metal deposition during the Mesoproterozoic at Black Butte (Figure 9B).

In some cases, coarse marcasite overgrows the mottled and colloform pyrite in the tube structures (Figure 2D). Marcasite is a metastable polymorph of pyrite that forms below about pH 4 (Murowchick and Barnes, 1986), mostly likely from the oxidation of hydrogen sulfide on a colloidal precursor (Schoonen and Barnes, 1991). Perhaps some vents had sulfide oxidizing microbes colonizing the vent, allowing local lowering of pH in a microbial community and promoting marcasite deposition (Juniper et al., 1992; Schieber, 2011; White et al., 2013). If so, the depositional basin of the Newland Formation was at least episodically and transiently oxic.

Despite its intergrowth with mottled pyrite, the sulfur isotopic composition of colloform pyrite is much less variable (IQR=4.5‰), and is heavier (Figure 6F,G); the median value (9.2‰ V-CDT) is similar to the inferred composition of contemporaneous seawater sulfate. Colloform pyrite is also intimately associated with quartz (Figure 8B,C,D), and has an isotopic composition similar to later base metal minerals (Figure 6G). The colloform texture is associated with precipitation into open space at rates controlled by reactant supply (Anderson et al., 1998; Koski et al., 1994), and its isotopic composition is consistent with quantitative reduction of seawater sulfate. If seawater in the Helena Embayment were completely reduced, the isotopic composition of the sulfide would match that of seawater

sulfate, and microbial sulfate reducing communities would be less active. Complete reduction of seawater sulfate at the vent site would favor pyrite precipitation governed by iron supply from the vent, producing the colloform texture (Figure 9C). Resupply of sulfate to the water column by mixing or diffusion into the deep basin would lead to a rejuvenation of the microbial sulfate reducing community and renewed mottled pyrite deposition with variable isotopic composition.

Base metal mineralization

The mottled and colloform pyrite comprising the tube structures is overgrown by coarse pyrite, galena, and cupriferous minerals (Figure 6A, Figure 7), likely after burial of the structures (Graham et al., 2012; White et al., 2013). Graham et al. (2012) suggested that later mineralizing fluids at Black Butte were hotter or more oxidizing, allowing replacement of barite and transport of copper. The isotopic compositions of irregular and euhedral coarse pyrite are slightly depleted from contemporaneous seawater sulfate (mean $\delta^{34}S$=6.1‰, Table 4Table 4). Our limited analyses of chalcopyrite (mean $\delta^{34}S$=3.9‰) are heavier than the mottled pyrite and lighter than seawater sulfate, and consistent with data reported by Zieg and Leitch (1998) (-5.1 to 7.1‰, Figure 6J). The coarse pyrite and base metal sulfides paragenetically follow the massive barite that fills the pyrite-walled tube structures, which is isotopically similar to the early diagenetic bladed barite (Figure 6B, Gellatly and Lyons, 2005; Strauss, 1993; Strauss and Schieber, 1990; Zieg and Leitch, 1998).

Other sediment-hosted sulfide deposits similarly display two sulfur sources: a light and variable source interpreted as a biogenic result of microbial sulfate reduction, and a heavier and more homogenous source interpreted as leached from underlying rock units (Anderson et al., 1998; Blakeman et al., 2002; Eldridge et al., 1993; Ireland et al., 2004). While sulfide-rich fluids will easily transport barium, they should not transport significant copper unless they are hotter than about 250°C (Cooke et al., 2000; Hitzman et al., 2010; Xiao et al., 1998). Zieg and Leitch (1998) report a vein chalcopyrite-pyrite equilibrium temperature of 276°C. White et al. (2013) calculate lower deposition temperatures (<225°C) from the equilibrium stability of more minor cobalt, nickel, and zinc-bearing minerals, although variability in the composition of some minerals may allow for temperatures up to about 300°C. Therefore, if

sulfidic, the hydrothermal fluids must have been between 250° and 300°C, and deposition occurred by cooling to less than about 225°C. However, such temperatures are close to the saturation of cupriferous minerals (Xiao et al., 1998), predicting the formation of a significant mineralized feeder zone below sites of hydrothermal effluence (Cooke et al., 2000; Goodfellow et al., 1993; Large et al., 2005; Leach et al., 2005) that is not well-developed at Black Butte.

Instead, the presumed source for the base metals is the hematitic Neihart Formation (White et al., 2013; Zieg et al., 2013), which would have buffered any sulfur in the hydrothermal fluids to a sulfate-rich speciation that could not transport barium. Like the earlier mottled and colloform pyrite, coarse pyrite and base metal sulfides would have deposited upon meeting a reservoir of sulfide produced by sulfate reduction (Figure 9D). However, the latter phases would have precipitated deeper in the hydrothermal system (Dixon and Davidson, 1996; Gadd et al., 2016; Ireland et al., 2004; Large et al., 1998), where reduction of pre-existing early diagenetic barite may have provided sulfide for the coarse pyrite and base metal sulfides. The sulfur isotopic composition of barite, coarse pyrite, and base metal sulfides is consistent with thermal reduction, which would have produced sulfide that was 10-20‰ lower in $\delta^{34}S$ than the barite (Figure 6B,C,H-J) (Johnson et al., 2004; Kelley et al., 2004; Powell and Macqueen, 1984). Barium liberated from the reduction of early diagenetic barite would migrate up towards the base of the microbial sulfate reduction zone, creating a barite front in the hydrothermal system, as observed in modern and Phanerozoic hydrothermal barite deposits (Eickmann et al., 2014; Johnson et al., 2009). Addition of more sulfate migrating with the metalliferous fluids could also promote re-precipitation of barite, as observed in modern continental slope sediments (Feng and Roberts, 2011; Torres et al., 1996). While the sulfur isotopic composition of sulfate migrating with the metalliferous fluids at Black Butte is unknown, future examination of the oxygen isotopic composition and high precision measurement of all four stable sulfur isotopes may discern between these barite precipitation mechanisms (Feng and Roberts, 2011).

The relative transport rates of metalliferous brines and sulfur over the life of a long-lived hydrothermal system may have varied dramatically. Increasing temperatures at the trap site and temporally-variable fluid circulation could remobilize and isotopically homogenize the sulfide minerals. Such remobilization of sulfides by later, hotter fluids was invoked by Graham et al. (2012) to explain the unusual occurrence of chalcopyrite inclusions in barite. Temporally-variable transport of metals and sulfur results in variable redox conditions at the site of deposition, indicated by barite co-depositing or alternating paragenetically with sulfides (Graham et al., 2012; Huston et al., 2007; Samson and Russell, 1987).

Summary and conclusions

Tube structures at the sediment-hosted Black Butte Copper deposit are millimeter-scale porous networks of mottled and colloform pyrite that are overgrown by base metal sulfides. These structures precipitated at sites of diffuse hydrothermal venting by means of abiotic processes broadly similar those observed in modern hydrothermal seeps, thereby documenting the direct interaction of hydrothermal fluids with seawater. We suggest that pyrite in tube walls is syngenetic mineralization of tube-shaped fluid conduits, the shape of which was determined by low-buoyancy venting of the hydrothermal fluids. Mottled pyrite replaced an initial conduit composed of a metastable iron-sulfur colloid, carbonate, or hydroxide. During temporary periods of complete water column sulfate reduction, colloform pyrite overgrew the tube structures. After burial, the tube structures were overgrown by coarse pyrite, base metal sulfides, barite, and quartz or dolomite.

The tube structures formed in environments that had extensive diagenetic pyrite and barite precipitation, ultimately derived from seawater that had concentrations of sulfate ~2-6 mM or greater. The isotopic compositions of these minerals were controlled by kinetic effects associated with microbial sulfate reduction in sediments that left residual sulfate isotopically ^{34}S -enriched with respect to seawater sulfate. During deposition of the lower Newland Formation, we estimate that the $\delta^{34}S$ of seawater sulfate in the Helena Embayment was about 10‰ enriched in ^{34}S relative to V-CDT.

The mineralogy and sulfur isotopic composition of the tube structures suggests that bottom waters in the Helena Embayment during deposition of the Newland Formation may have had quite variable redox conditions. Large sulfur isotopic variation of mottled pyrite suggests sulfate-rich seawater being actively reduced under varying degrees of sulfate limitation. A more homogenous composition for the intergrown colloform pyrite suggests that, occasionally, much of the bottom water sulfate was reduced to sulfide. Finally, precipitation of marcasite, possible only under locally acidic conditions, suggests that some intervals were oxic, allowing sulfur-oxidizing communities to colonize the vents and seafloor. Base metal mineralization occurred deeper in the hydrothermal system, and deposition occurred by titration with sulfide derived from reductive remobilization of barite.

The recognition of diffuse hydrothermal vents in a sediment-hosted deposit provides a rare opportunity to examine the interaction between hydrothermal fluids, seawater, and benthic microbiota in Mesoproterozoic oceans. The close association with crinkly laminated pyrite suggests there may have been extensive microbial sulfate-reducing communities associated with vent sites. The particularly large sulfur isotopic range of mottled pyrite suggests, like in modern and fossilized diffuse vents, that the chimneys may have been colonized by sulfate reducers as well. It is unclear what role, besides providing sulfide to titrate the metals, the microbes played in modifying tube structure, fluid flow, or mineralogy. However, the dominant porosity structure of the tube structures reflects the diffuse effluence of buoyant fluids to the seafloor.

Acknowledgements

This project originated during the Agouron Institute Advanced Field Course during July 2013. Funding was provided by the Agouron Institute and the NASA Astrobiology Institute (NAI). We thank Tintina Resources, Inc., especially Chance Matthews, for access to drill core and outcrop associated with the Black Butte Copper Project. We also thank Tyler Mackey, James Wray, Ross Williams, Ken Williford, and Doug Archer for thoughtful discussion and field assistance, and especially Kirsten Siebach for excellent photos. We thank Peter Girguis and Roger Summons for samples of modern hydrothermal vents used in

the micro-CT analyses; Jess Adkins, Nathan Dalleska, Yunbin Guan, Jena Johnson, Guillaume Paris, and Jason Price for analytical support; and Michael Russell for help interpreting our data. We thank Peter McGoldrick, Garth Graham, and an additional anonymous reviewer for helpful and thoughtful reviews that greatly improved this submission. We thank the editors Aaron Cavosie, Fernando Corfu, and Cary Cosper for their help managing and preparing this manuscript.

Supplemental Figures and Data

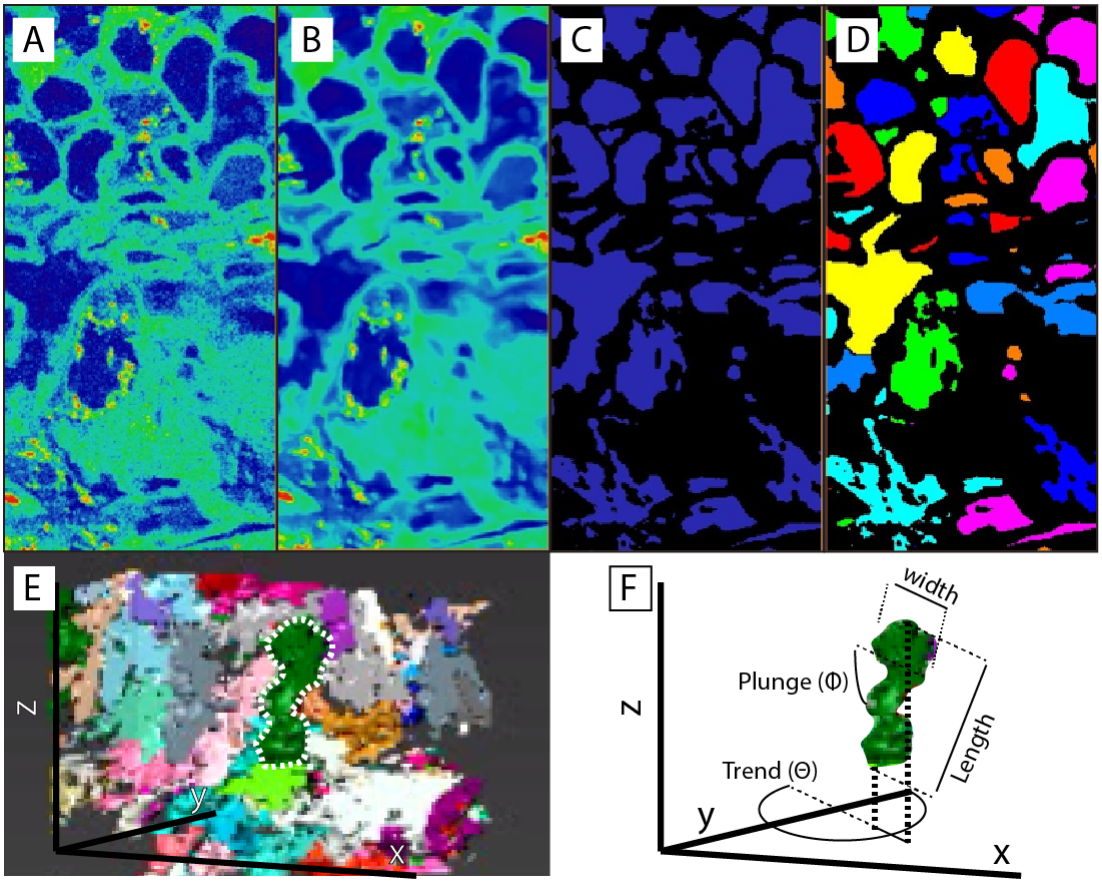

Supplemental Figure 1: Example of the workflow in Avizo Fire used to create pore data. (A) Raw micron-scale density data from a sub-volume of sample B1. (B) Three-dimensional image filtering result from the edge-preserving, curvature-driven smoothing parameter. (C) Result of the pore determination by an interactively-determined threshold density contrast with wall material. Black is all density values greater than a threshold. (D) Result of the labeling command to identify and separate individual pore volumes, which are now colored arbitrarily. (E) Three-dimensional view of the individually-labeled and colored pore volumes with a vertical z-axis and arbitrary horizontal x-y axes. (F) Quantifiable parameters describing each pore includes the volume, the longest and intermediate axes lengths of the pore (length and width), the aspect ratio (length/width), the angle between vertical and the long axis (plunge, Φ), and the trend direction (Θ) of the pore in the horizontal plane.

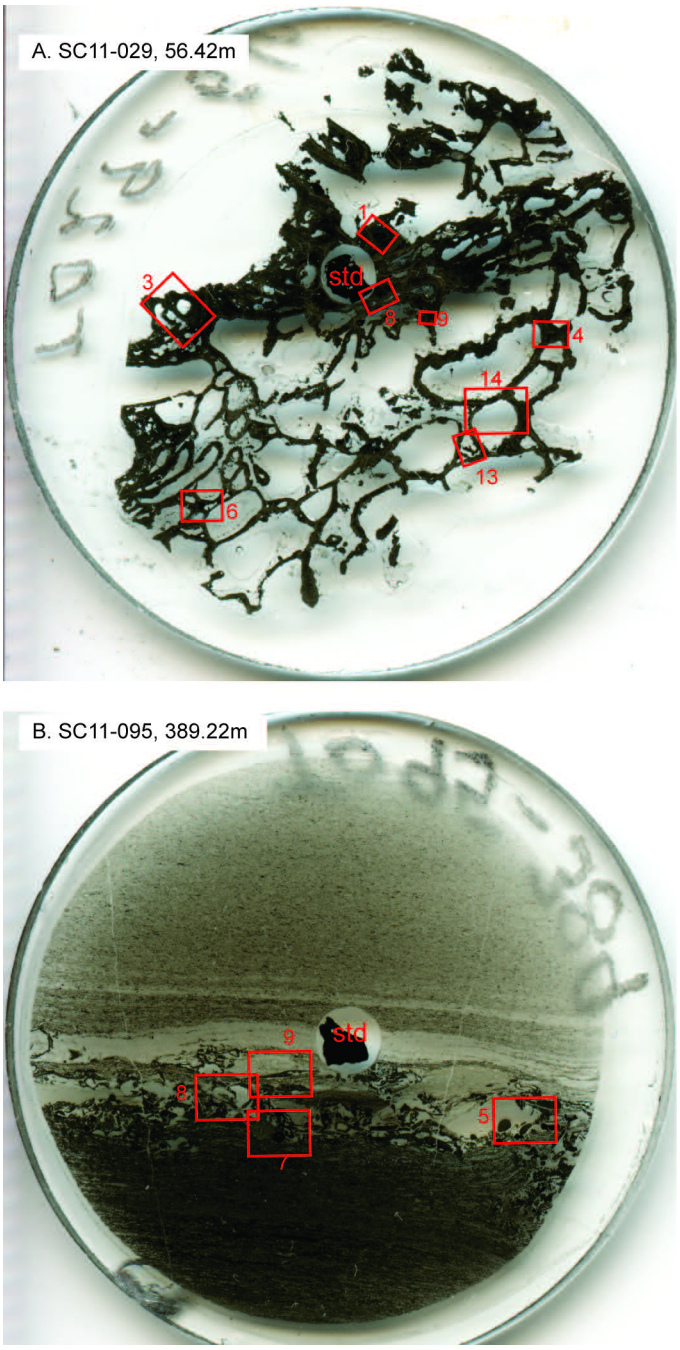

Supplemental Figure 2: One-inch (2.54 cm) round polished thick sections mounted with in-house pyrite analytical standard (std). *In situ* sulfide-sulfur analytical sites are boxed and numbered as in Figure 8 and Supplemental Figure 4. Thick sections are both cut perpendicular to bedding.

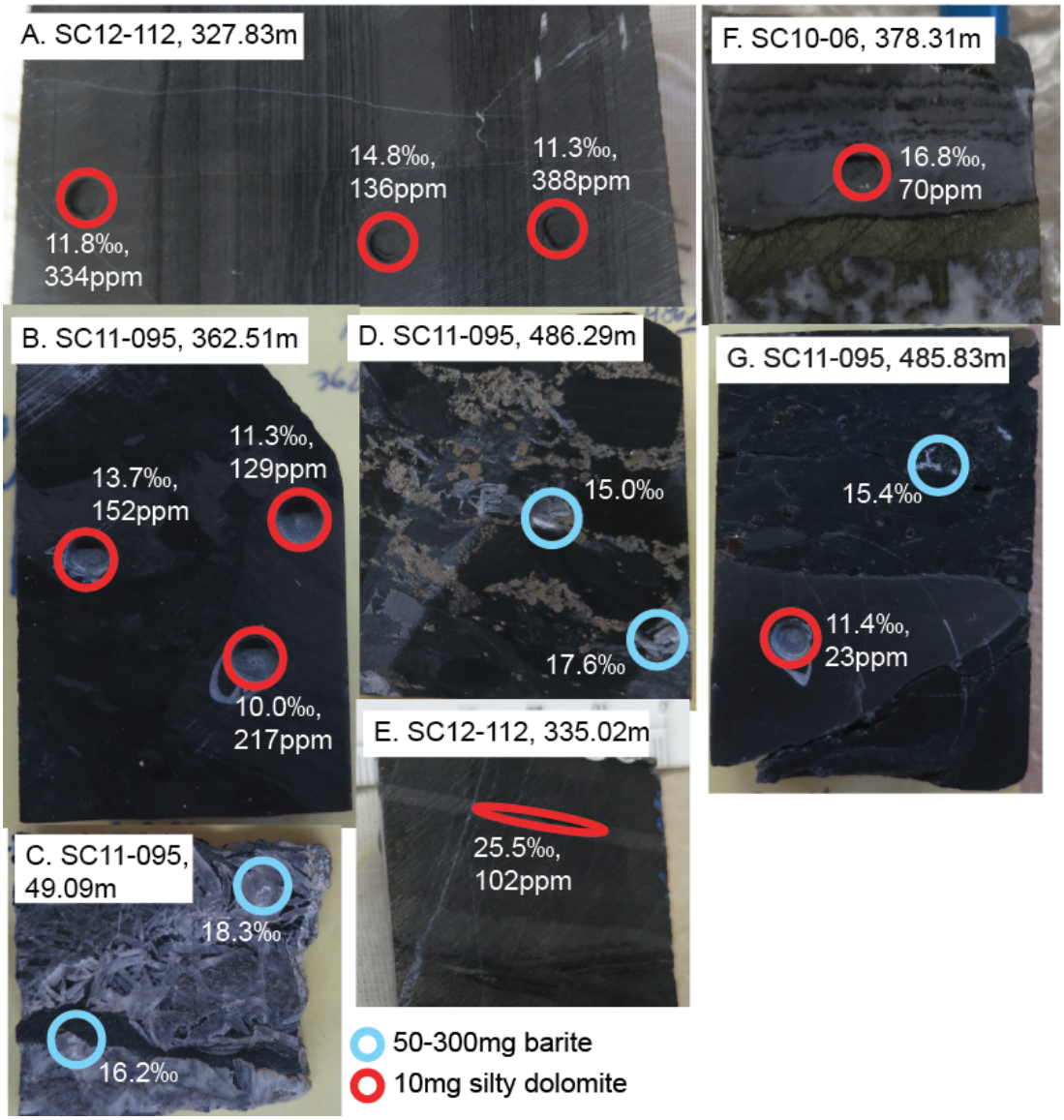

Supplemental Figure 3: Non-sulfide textures sampled for this study, in addition to the sample shown in Figure 5E. Silty dolomite CAS samples are circled in red, and barite samples are circled in blue. All samples are from 3 cm-wide quarter-core segments. (A) Dolomitic caps of graded laminations below the LSZ in laminated striped shale lithofacies from core SC12-112-327.83 m. (B) Dolostone clasts in clast-supported debris flow above the USZ, in a unit called Unit 0, from core SC11-095-362.51 m. (C) Synsedimentary barite lathes that precipitated prior to sediment compaction in the upper Newland Formation from core SC11-095-49.09 m. (D) Synsedimentary barite lathes being replaced by pyrite in the USZ from core SC11-095-486.29 m. (E) Dolomitic cap of graded lamination below the LSZ in laminated striped shale lithofacies from core SC12-112-335.02 m. (F) Dolostone clast in pyrite-cemented breccia in the MSZ from core SC10-06-378.31 m. (G) Dolostone clast and porosity-filling barite in clast-supported debris flow in the USZ from core SC11-095-485.83 m.

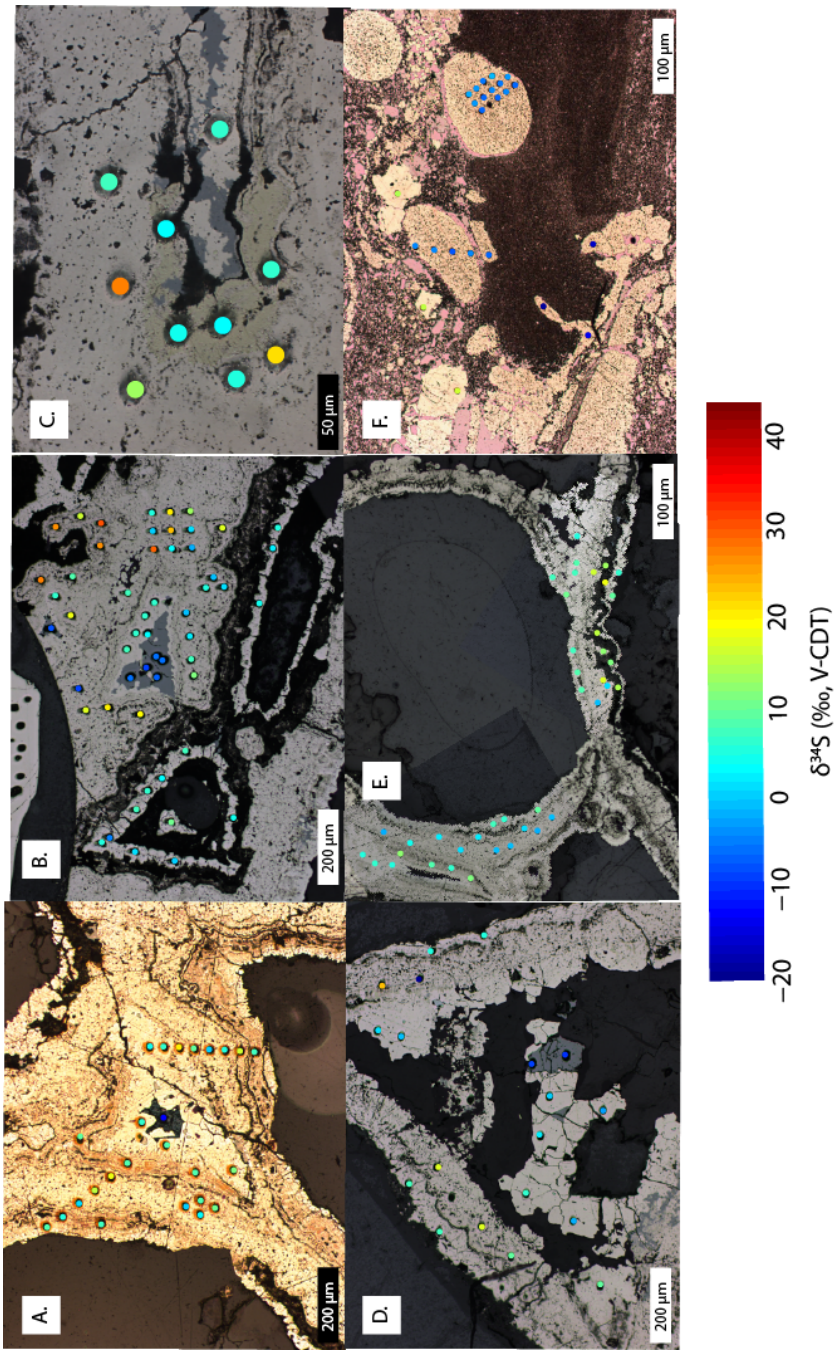

Supplemental Figure 4 Additional SIMS sulfide-sulfur $\delta^{34}S$ analysis pits colored by isotopic composition overlain on plain-polarized reflected light photomicrographs. (A) SC11-029-56.42 m, Site 4. (B) SC11-029-56.42 m, Site 8. (C) SC11-029-56.42 m, Site 9. (D) SC11-029-56.42 m, Site 13. (E) SC11-029-56.42 m, Site 14. (F) SC11-095-389.22 m, Site 5.

Supplemental Movie B1: USZ sample from Black Butte with pyrite walls and minimal porosity occlusion from drill core SC11-029-56.5 m (Figure 1C). The sample is approximately 2 x 3 x 6 cm. In the first 20 s, grayscale is proportional to density, with solid white indicating minor barite and middle gray indicating sulfide minerals. 0-6 s: perspective view of the exterior of sample, which is a quarter segment of drill core. 6-20 s: vertical slices through the sample. In the remainder of the video, individual pore volumes are colored and all material denser than a threshold value is removed. Separate pores sharing a color are not connected. 20-22 s: all pores with volume greater than 0.05 mm^3. 22 s-1 min: Pores are filtered to only show those oriented with plunge of 45° to 65°. Reconstruction is rotated to show three-dimensional shape of pores.

Supplemental Movie B3: Silica-replaced outcrop sample from 46° 46.368'N, 110° 52.843'W above USZ gossan (Figure 1A). Sample is approximately 1.5 x 3 x 2.5 cm. Grayscale is proportional to density, with solid white indicating the densest silica. Tube structure walls are missing, and therefore appear as black stringers most visible on the outer surface of the sample where weathering has accentuated the relief. 0-16 s: perspective view of the exterior of the sample, oriented up properly. 16-35 s: vertical slices through the sample. 35-49 s: horizontal slices through the sample.

Supplemental Movie LCL: Inactive carbonate-walled chimney from Lost City (sample 3871-1442 collected during *HOV Alvin* cruise AT-7-41). Sample is approximately 3.5 x 2 x 4.5 cm. Grayscale is proportional to density, with solid white indicating the densest carbonate. 0-6 s: perspective view of exterior of sample (no orientation information recorded on sample). 6-20 s: vertical slices through the sample. In the remainder of the video, individual pore volumes are colored and all material denser than a threshold value is removed. Separate pores sharing a color are not connected. 20-24 s: all pores with volume greater than 0.05 mm^3. 24-54 s: Pores are filtered to only show those oriented with trend of 98° to 204°. Reconstruction is rotated to show three-dimensional shape of pores.

Supplemental Movie LCM: Carbonate-walled flange from Lost City called "IMAX" on an active 53-60°C vent on the Poseidon structure (sample 3869-1404 collected at Marker 2 during *HOV Alvin* cruise AT-7-41). Sample is approximately 3 x 2 x 4.5 cm. Grayscale is proportional to density, with solid white indicating the densest carbonate. 0-6 s: perspective view of exterior of sample, oriented up properly. 6-15 s: vertical slices through the sample.

Supplemental Movie M1: Anhydrite-walled chimney from a 300-311°C vent called "Hot Harold" in the Mothra vent field on the Juan de Fuca Ridge (collected during *HOV Alvin* cruise AT-15-23 on September 9, 2007 at 47°55.425660'N, 129°6.491760'W, 2278 m depth). Sample is approximately 4 x 5.5 x 8.5 cm. Grayscale is proportional to density, with solid white indicating the densest anhydrite. 0-6 s: perspective view of exterior of sample, oriented up properly. 6-20 s: vertical slices through the sample. 20-28 s: all pores with pore volumes greater than 0.05 mm^3 are reconstructed within an interior volume. Individual pore volumes are colored and all material denser than a threshold value is removed. Separate pores sharing a color are not connected. Reconstruction is rotated to visualize three-dimensional shape.

Supplemental Table 1: SIMS sulfur isotope data

Filename	$\delta^{34}S$	std err	Site	Spot	Phase	Slide	
T095_389@1.asc	15.7	0.08	5	1	Pe	T095-389	
T095_389@2.asc	-4.8	0.07	5	2	Pn	T095-389	
T095_389@3.asc	-3.6	0.08	5	3	Pn	T095-389	
T095_389@4.asc	-6.0	0.12	5	4	Pn	T095-389	
T095_389@5.asc	-3.3	0.08	5	5	Pn	T095-389	
T095_389@6.asc	-2.8	0.07	5	6	Pn	T095-389	
T095_389@7.asc	15.2	0.09	5	7	Pe	T095-389	
T095_389@8.asc	-18.4	0.16	5	8	Pn	T095-389	
T095_389@9.asc	-12.9	0.11	5	9	Pn	T095-389	
T095_389@10.asc	-15.0	0.07	5	10	Pn	T095-389	
T095_389@12.asc	17.2	0.08	5	12	Pe	T095-389	
T095_389@13.asc	-4.8	0.12	5	13	Pn	T095-389	
T095_389@14.asc	-3.2	0.11	5	14	Pn	T095-389	
T095_389@15.asc	-5.3	0.08	5	15	Pn	T095-389	
T095_389@17.asc	-5.6	0.06	5	17	Pn	T095-389	
T095_389@18.asc	-2.2	0.09	5	18	Pn	T095-389	
T095_389@19.asc	-4.9	0.06	5	19	Pn	T095-389	
T095_389@20.asc	-3.4	0.09	5	20	Pn	T095-389	
T095_389@21.asc	-4.8	0.13	5	21	Pn	T095-389	
T095_389@22.asc	-2.1	0.10	5	22	Pn	T095-389	
T095_389@23.asc	-0.7	0.07	5	23	Pn	T095-389	
T095_389@24.asc	-3.9	0.07	5	24	Pn	T095-389	
T095_389@25.asc	-2.5	0.06	5	25	Pn	T095-389	
T095_389@26.asc	-1.5	0.09	5	26	Pn	T095-389	
T095_389@27.asc	10.5	32.26	7	27	Pn	T095-389	low counts
T095_389@28.asc	1.4	0.12	7	28	Pn	T095-389	
T095_389@29.asc	19.3	5.87	7	29	Pn	T095-389	low counts
T095_389@30.asc	-7.7	0.14	7	30	Pn	T095-389	
T095_389@31.asc	-8.1	0.14	7	31	Pn	T095-389	
T095_389@32.asc	-11.6	0.13	8	32	Pi	T095-389	
T095_389@33.asc	-12.6	0.13	8	33	Pn	T095-389	

Filename	$\delta^{34}S$	std err	Site	Spot	Phase	Slide	
T095_389@34.asc	-10.2	0.12	8	34	Pn	T095-389	
T095_389@35.asc	-4.3	0.15	8	35	Pn	T095-389	
T095_389@36.asc	-3.0	0.13	8	36	Pn	T095-389	
T095_389@37.asc	-3.9	0.13	8	37	Pn	T095-389	
T095_389@38.asc	-4.9	0.13	8	38	Pn	T095-389	
T095_389@39.asc	-2.3	0.15	8	39	Pn	T095-389	
T095_389@40.asc	-12.6	1.02	8	40	Pn	T095-389	low counts
T095_389@41.asc	1.7	0.15	8	41	Pn	T095-389	
T095_389@42.asc	-0.3	0.08	8	42	Pn	T095-389	
T095_389@43.asc	-8.9	0.09	8	43	Pn	T095-389	
T095_389@44.asc	-7.2	0.08	8	44	Pn	T095-389	
T095_389@45.asc	-8.9	0.14	8	45	Pn	T095-389	
T095_389@46.asc	-9.2	0.09	9	46	Pn	T095-389	
T095_389@47.asc	-6.6	0.31	9	47	Pn	T095-389	
T095_389@48.asc	-7.3	0.69	9	48	Pn	T095-389	
T095_389@49.asc	-5.5	0.43	9	49	Pn	T095-389	
T095_389@50.asc	-9.3	0.10	9	50	Pn	T095-389	
T095_389@51.asc	-8.5	0.08	9	51	Pn	T095-389	
T095_389@52.asc	-9.0	0.72	9	52	Pn	T095-389	
T095_389@53.asc	-5.0	0.10	9	53	Pn	T095-389	
T095_389@54.asc	-6.5	0.04	9	54	Pn	T095-389	
T095_389@55.asc	-6.5	0.07	9	55	Pn	T095-389	
T095_389@56.asc	-7.5	0.61	9	56	Pn	T095-389	
T095_389@57.asc	-6.0	0.04	9	57	Pn	T095-389	
T095_389@58.asc	-6.9	0.06	9	58	Pn	T095-389	
T095_389@59.asc	-8.1	0.18	9	59	Pn	T095-389	
T095_389@60.asc	-4.6	0.08	9	60	Pn	T095-389	
T095_389@61.asc	-5.5	0.09	9	61	Pn	T095-389	
T095_389@62.asc	-7.1	0.07	9	62	Pn	T095-389	
T095_389@63.asc	-5.2	0.09	9	63	Pn	T095-389	
T095_389@64.asc	-5.0	0.10	9	64	Pn	T095-389	
T095_389@65.asc	-5.5	0.04	9	65	Pn	T095-389	
T095_389@66.asc	-6.4	0.08	9	66	Pn	T095-389	

Filename	$\delta^{34}S$	std err	Site	Spot	Phase	Slide
T095_389@67.asc	-10.0	0.14	9	67	Pn	T095-389
Site8_0729@1.asc	-7.1	0.30	8	1	G	T029-56
Site8_0729@2.asc	-8.3	0.36	8	2	G	T029-56
Site8_0729@3.asc	-5.7	0.23	8	3	G	T029-56
Site8_0729@4.asc	-5.4	0.23	8	4	G	T029-56
Site8_0729@5.asc	6.3	0.21	8	5	Pe	T029-56
Site8_0729@6.asc	6.7	0.21	8	6	Pe	T029-56
Site8_0729@7.asc	6.7	0.21	8	7	Pe	T029-56
Site8_0729@8.asc	6.8	0.20	8	8	Pe	T029-56
Site8_0729@9.asc	11.2	0.26	8	9	Pm	T029-56
Site8_0729@10.asc	6.9	0.21	8	10	Pm	T029-56
Site8_0729@11.asc	2.1	0.21	8	11	Pm	T029-56
Site8_0729@12.asc	-1.2	0.21	8	12	Pm	T029-56
Site8_0729@13.asc	3.4	0.23	8	13	Cpy	T029-56
Site8_0729@14.asc	-6.0	0.24	8	14	G	T029-56
Site9_0729@15.asc	7.4	0.12	9	15	Pm	T029-56
Site9_0729@16.asc	3.2	0.15	9	16	Cpy	T029-56
Site9_0729@17.asc	27.0	0.12	9	17	Pm	T029-56
Site9_0729@18.asc	4.3	0.15	9	18	Cpy	T029-56
Site9_0729@19.asc	2.8	0.17	9	19	Cpy	T029-56
Site9_0729@20.asc	5.9	0.19	9	20	Cpy	T029-56
Site9_0729@21.asc	13.1	0.23	9	21	Pm	T029-56
Site9_0729@22.asc	5.3	0.25	9	22	Pm	T029-56
Site9_0729@23.asc	20.8	0.18	9	23	Pm	T029-56
Site9_0729@24.asc	6.1	0.15	9	24	Pi	T029-56
Site13_0729@25.asc	-2.9	0.23	13	25	Pe	T029-56
Site13_0729@26.asc	0.6	0.11	13	26	Pe	T029-56
Site13_0729@27.asc	2.3	0.11	13	27	Pe	T029-56
Site13_0729@28.asc	5.9	0.11	13	28	Pe	T029-56
Site13_0729@29.asc	-2.0	0.13	13	29	Pe	T029-56
Site13_0729@30.asc	-9.6	0.29	13	30	Ge	T029-56
Site13_0729@31.asc	-9.1	0.36	13	31	Ge	T029-56
Site13_0729@32.asc	8.9	0.13	13	32	Pe	T029-56

Filename	$\delta^{34}S$	std err	Site	Spot	Phase	Slide
Site13_0729@33.asc	9.1	0.20	13	33	Pm	T029-56
Site13_0729@34.asc	17.2	0.14	13	34	Pm	T029-56
Site13_0729@36.asc	7.5	0.33	13	36	Pi	T029-56
Site13_0729@37.asc	7.3	0.22	13	37	Pi	T029-56
Site13_0729@38.asc	16.9	0.37	13	38	Pm	T029-56
Site13_0729@39.asc	1.4	0.22	13	39	Pe	T029-56
Site13_0729@40.asc	-0.9	0.23	13	40	Pe	T029-56
Site13_0729@41.asc	23.5	0.26	13	41	Pm	T029-56
Site13_0729@42.asc	-20.2	0.30	13	42	Pm	T029-56
Site13_0729@43.asc	5.6	0.26	13	43	Pi	T029-56
Site13_0729@44.asc	5.5	0.26	13	44	Pi	T029-56
Site8_0729@45.asc	17.2	0.28	8	45	Pm	T029-56
Site8_0729@46.asc	5.5	0.32	8	46	Pi	T029-56
Site8_0729@47.asc	2.8	0.32	8	47	Pi	T029-56
Site8_0729@48.asc	4.1	0.29	8	48	Pi	T029-56
Site8_0729@49.asc	1.4	0.28	8	49	Pm	T029-56
Site8_0729@50.asc	4.9	0.30	8	50	Pm	T029-56
Site8_0729@51.asc	-0.3	0.27	8	51	Pm	T029-56
Site8_0729@52.asc	25.8	0.30	8	52	Pc	T029-56
Site8_0729@53.asc	16.4	0.32	8	53	Pc	T029-56
Site8_0729@54.asc	30.1	0.33	8	54	Pm	T029-56
Site8_0729@55.asc	26.6	0.34	8	55	Pm	T029-56
Site8_0729@56.asc	27.5	0.39	8	56	Pm	T029-56
Site8_0729@57.asc	8.1	0.32	8	57	Pm	T029-56
Site8_0729@58.asc	6.7	0.27	8	58	Pm	T029-56
Site8_0729@59.asc	18.3	0.33	8	59	Pm	T029-56
Site8_0729@60.asc	-7.9	0.32	8	60	G	T029-56
Site8_0729@61.asc	19.0	0.42	8	61	Pm	T029-56
Site8_0729@62.asc	19.7	0.31	8	62	Pm	T029-56
Site8_0729@63.asc	17.7	0.34	8	63	Pm	T029-56
Site8_0729@64.asc	-8.5	0.26	8	64	Pm	T029-56
Site8_0729@65.asc	7.5	0.22	8	65	Pi	T029-56
Site8_0729@66.asc	3.2	0.24	8	66	Pi	T029-56

Filename	$\delta^{34}S$	std err	Site	Spot	Phase	Slide
Site8_0729@67.asc	6.6	0.22	8	67	Pi	T029-56
Site8_0729@68.asc	7.0	0.29	8	68	Pi	T029-56
Site8_0729@69.asc	-4.3	0.72	8	69	Pi	T029-56
Site8_0729@70.asc	4.8	0.21	8	70	Pi	T029-56
Site8_0729@71.asc	10.3	0.22	8	71	Pi	T029-56
Site8_0729@72.asc	1.1	0.23	8	72	Pi	T029-56
Site8_0729@73.asc	0.3	0.26	8	73	Pi	T029-56
Site8_0729@74.asc	4.7	0.26	8	74	Pi	T029-56
Site8_0729@75.asc	-2.1	0.22	8	75	Pm	T029-56
Site8_0729@76.asc	3.4	0.23	8	76	Pm	T029-56
Site8_0729@77.asc	29.7	0.22	8	77	Pm	T029-56
Site8_0729@78.asc	0.5	0.27	8	78	Pm	T029-56
Site8_0729@79.asc	23.6	0.24	8	79	Pm	T029-56
Site8_0729@80.asc	1.0	0.25	8	80	Pm	T029-56
Site8_0729@81.asc	13.6	0.24	8	81	Pm	T029-56
Site8_0729@82.asc	19.7	0.25	8	82	Pm	T029-56
Site8_0729@83.asc	4.8	0.29	8	83	Pm	T029-56
Site8_0729@84.asc	6.8	0.21	8	84	Pi	T029-56
Site14_0730@85.asc	7.6	0.12	14	85	Pi	T029-56
Site14_0730@86.asc	6.2	0.13	14	86	Pi	T029-56
Site14_0730@87.asc	9.4	0.16	14	87	Pi	T029-56
Site14_0730@88.asc	2.3	0.12	14	88	Pm	T029-56
Site14_0730@89.asc	0.9	0.15	14	89	Pm	T029-56
Site14_0730@90.asc	2.5	0.19	14	90	Pm	T029-56
Site14_0730@91.asc	1.6	0.16	14	91	Pm	T029-56
Site14_0730@92.asc	-1.1	0.15	14	92	Pm	T029-56
Site14_0730@93.asc	-0.2	0.14	14	93	Pm	T029-56
Site14_0730@94.asc	-1.6	0.13	14	94	Pm	T029-56
Site14_0730@95.asc	-1.0	0.14	14	95	Pm	T029-56
Site14_0730@96.asc	4.5	0.14	14	96	Pm	T029-56
Site14_0730@97.asc	8.3	0.12	14	97	Pc	T029-56
Site14_0730@98.asc	6.7	0.12	14	98	Pc	T029-56
Site14_0730@99.asc	11.2	0.32	14	99	Pc	T029-56

Filename	$\delta^{34}S$	std err	Site	Spot	Phase	Slide
Site14_0730@100.asc	5.5	0.12	14	100	Pe	T029-56
Site14_0730@101.asc	6.2	0.13	14	101	Pe	T029-56
Site14_0730@102.asc	12.4	0.16	14	102	Pc	T029-56
Site14_0730@103.asc	5.7	0.12	14	103	Pe	T029-56
Site14_0730@104.asc	-1.4	0.11	14	104	Pm	T029-56
Site14_0730@105.asc	12.5	0.17	14	105	Pm	T029-56
Site14_0730@106.asc	1.0	0.18	14	106	Pm	T029-56
Site14_0730@107.asc	17.6	0.21	14	107	Pm	T029-56
Site14_0730@108.asc	-0.5	0.17	14	108	Pm	T029-56
Site14_0730@109.asc	11.2	1.20	14	109	DkGr	T029-56
Site14_0730@110.asc	13.9	1.36	14	110	DkGr	T029-56
Site14_0730@111.asc	8.3	0.17	14	111	Pi	T029-56
Site14_0730@112.asc	7.9	0.16	14	112	Pi	T029-56
Site14_0730@113.asc	7.1	0.18	14	113	Pi	T029-56
Site14_0730@114.asc	9.1	0.17	14	114	Pi	T029-56
Site14_0730@115.asc	15.7	0.29	14	115	DkGr	T029-56
Site14_0730@116.asc	6.5	0.17	14	116	Pi	T029-56
Site14_0730@117.asc	13.4	1.04	14	117	DkGr	T029-56
Site14_0730@118.asc	18.2	0.88	14	118	DkGr	T029-56
Site14_0730@119.asc	10.1	0.19	14	119	Pi	T029-56
Site14_0730@120.asc	7.2	0.26	14	120	Pi	T029-56
Site14_0730@121.asc	16.0	0.21	14	121	Pm	T029-56
Site14_0730@122.asc	7.4	0.18	14	122	Pi	T029-56
Site14_0730@123.asc	7.9	0.20	14	123	Pi	T029-56
Site14_0730@124.asc	5.7	0.16	14	124	Pe	T029-56
Site6_0730@125.asc	4.1	0.16	6	125	Pe	T029-56
Site6_0730@126.asc	4.3	0.15	6	126	Pe	T029-56
Site6_0730@127.asc	-13.0	0.27	6	127	Cov	T029-56
Site6_0730@128.asc	1.4	0.15	6	128	Pe	T029-56
Site6_0730@129.asc	2.4	0.14	6	129	Pe	T029-56
Site6_0730@130.asc	5.7	0.19	6	130	Pe	T029-56
Site6_0730@131.asc	-1.0	0.16	6	131	Pe	T029-56
Site6_0730@132.asc	-0.2	0.22	6	132	Pe	T029-56

Filename	$\delta^{34}S$	std err	Site	Spot	Phase	Slide
Site6_0730@133.asc	-1.2	0.28	6	133	Pm	T029-56
Site6_0730@134.asc	8.0	0.15	6	134	Pm	T029-56
Site6_0730@135.asc	13.6	0.22	6	135	hit qtz	T029-56
Site6_0730@136.asc	7.3	0.10	6	136	Pi	T029-56
Site6_0730@137.asc	9.4	0.08	6	137	Pi	T029-56
Site6_0730@138.asc	6.8	0.15	6	138	Pi	T029-56
Site6_0730@139.asc	5.0	0.10	6	139	Pm	T029-56
Site6_0730@140.asc	7.6	0.08	6	140	Pm	T029-56
Site6_0730@141.asc	1.1	0.12	6	141	Pe	T029-56
Site6_0730@142.asc	8.4	0.10	6	142	Pm	T029-56
Site6_0730@143.asc	10.4	0.30	6	143	Pm	T029-56
Site6_0730@144.asc	8.1	0.11	6	144	Pe	T029-56
Site1_0730@145.asc	41.1	0.14	1	145	Pm	T029-56
Site1_0730@146.asc	9.6	0.12	1	146	Pm	T029-56
Site1_0730@147.asc	11.6	0.14	1	147	Pm	T029-56
Site1_0730@148.asc	22.6	0.10	1	148	Pm	T029-56
Site1_0730@149.asc	3.2	0.10	1	149	Pm	T029-56
Site1_0730@150.asc	9.5	0.11	1	150	Pc	T029-56
Site1_0730@151.asc	8.2	0.10	1	151	Pc	T029-56
Site1_0730@152.asc	11.5	0.21	1	152	Pc	T029-56
Site1_0730@153.asc	8.4	0.10	1	153	Pc	T029-56
Site1_0730@154.asc	21.6	0.11	1	154	Pm	T029-56
Site1_0730@155.asc	8.7	0.09	1	155	Pm	T029-56
Site1_0730@156.asc	7.2	0.13	1	156	Pc	T029-56
Site1_0730@157.asc	6.9	0.09	1	157	Pi	T029-56
Site1_0730@158.asc	-1.8	0.18	1	158	Pc	T029-56
Site1_0730@159.asc	5.8	0.11	1	159	Pc	T029-56
Site1_0730@160.asc	5.4	0.13	1	160	Pi	T029-56
Site1_0730@161.asc	5.3	0.09	1	161	Pc	T029-56
Site1_0730@162.asc	7.4	0.10	1	162	Pc	T029-56
Site1_0730@163.asc	33.8	0.14	1	163	Pm	T029-56
Site1_0730@164.asc	9.2	0.09	1	164	Pc	T029-56
Site3_0731@165.asc	10.5	0.17	3	165	Pc	T029-56

Filename	$\delta^{34}S$	std err	Site	Spot	Phase	Slide
Site3_0731@166.asc	2.8	0.19	3	166	Pc	T029-56
Site3_0731@167.asc	2.8	0.17	3	167	Pc	T029-56
Site3_0731@168.asc	6.1	0.19	3	168	Pc	T029-56
Site3_0731@169.asc	8.4	0.16	3	169	Pc	T029-56
Site3_0731@170.asc	13.4	0.17	3	170	Pc	T029-56
Site3_0731@171.asc	43.6	0.15	3	171	Pm	T029-56
Site3_0731@172.asc	-3.3	0.20	3	172	Pm	T029-56
Site3_0731@173.asc	28.1	0.15	3	173	Pm	T029-56
Site3_0731@174.asc	7.6	0.19	3	174	Pc	T029-56
Site3_0731@175.asc	9.7	0.15	3	175	Pm	T029-56
Site3_0731@176.asc	-2.0	0.20	3	176	Pm	T029-56
Site3_0731@177.asc	2.9	0.15	3	177	Pc	T029-56
Site3_0731@178.asc	0.9	0.16	3	178	Pm	T029-56
Site3_0731@179.asc	10.3	0.16	3	179	Pc	T029-56
Site3_0731@180.asc	6.1	0.20	3	180	Pi	T029-56
Site3_0731@181.asc	0.3	0.28	3	181	Pm	T029-56
Site3_0731@182.asc	-1.6	0.15	3	182	Pm	T029-56
Site3_0731@183.asc	4.8	0.16	3	183	Pi	T029-56
Site3_0731@184.asc	13.9	0.15	3	184	Pc	T029-56
Site3_0731@185.asc	4.0	0.12	3	185	Pm	T029-56
Site3_0731@186.asc	-5.8	0.15	3	186	Pm	T029-56
Site3_0731@187.asc	3.9	0.12	3	187	Pi	T029-56
Site3_0731@188.asc	3.5	0.16	3	188	Pi	T029-56
Site3_0731@189.asc	5.7	0.13	3	189	Pi	T029-56
Site3_0731@190.asc	-4.5	0.11	3	190	Pm	T029-56
Site3_0731@191.asc	-3.1	0.10	3	191	Pm	T029-56
Site3_0731@192.asc	6.5	0.23	3	192	Pc	T029-56
Site3_0731@193.asc	-1.6	0.09	3	193	Pm	T029-56
Site3_0731@194.asc	-1.0	0.17	3	194	Pm	T029-56
Site3_0731@195.asc	0.2	0.10	3	195	Pm	T029-56
Site3_0731@196.asc	9.7	0.11	3	196	Pc	T029-56
Site3_0731@197.asc	1.2	0.12	3	197	Pm	T029-56
Site3_0731@198.asc	29.5	0.11	3	198	Pm	T029-56

Filename	$\delta^{34}S$	std err	Site	Spot	Phase	Slide
Site3_0731@199.asc	37.3	0.12	3	199	Pm	T029-56
Site3_0731@200.asc	1.4	0.11	3	200	Pm	T029-56
Site3_0731@201.asc	1.9	0.09	3	201	Pc	T029-56
Site3_0731@202.asc	-3.8	1.60	3	202	Pc	T029-56
Site3_0731@203.asc	7.3	0.10	3	203	Pc	T029-56
Site3_0731@204.asc	9.8	0.21	3	204	Pc	T029-56
T029-56@11.asc	-2.1	0.17	1	-11	Tenn	T029-56
T029-56@12.asc	4.0	0.16	1	-12	Pm	T029-56
T029-56@13.asc	13.1	0.22	1	-13	Pm	T029-56
T029-56@14.asc	27.0	0.18	1	-14	Pm	T029-56
T029-56@15.asc	45.2	0.17	1	-15	Pm	T029-56
T029-56@16.asc	6.5	0.16	1	-16	Pi	T029-56
T029-56@17.asc	7.3	0.17	1	-17	Pi	T029-56
T029-56@18.asc	6.8	0.16	1	-18	Pi	T029-56
T029-56@19.asc	6.3	0.16	1	-19	Pc	T029-56
T029-56@20.asc	7.8	0.22	1	-20	Pc	T029-56
T029-56@21.asc	6.6	0.16	1	-21	Pi	T029-56
T029-56@22.asc	11.9	0.16	1	-22	Pc	T029-56
T029-56@23.asc	-12.5	0.33	4	-23	Cov	T029-56
T029-56@24.asc	12.5	0.28	4	-24	Pe	T029-56
T029-56@25.asc	6.4	0.28	4	-25	Pe	T029-56
T029-56@26.asc	5.2	0.28	4	-26	Pe	T029-56
T029-56@27.asc	8.5	0.28	4	-27	Pc	T029-56
T029-56@28.asc	9.2	0.29	4	-28	Pc	T029-56
T029-56@29.asc	9.7	0.32	4	-29	Pc	T029-56
T029-56@30.asc	10.9	0.29	4	-30	Pm	T029-56
T029-56@31.asc	8.7	0.30	4	-31	Pm	T029-56
T029-56@32.asc	3.4	0.28	4	-32	Pm	T029-56
T029-56@33.asc	0.7	0.29	4	-33	Pm	T029-56
T029-56@34.asc	8.3	0.30	4	-34	Pc	T029-56
T029-56@35.asc	8.1	0.26	3	-35	Pi	T029-56
T029-56@36.asc	7.6	0.27	3	-36	Pc	T029-56
T029-56@37.asc	9.9	0.27	3	-37	Pc	T029-56

Filename	$\delta^{34}S$	std err	Site	Spot	Phase	Slide
T029-56@38.asc	-1.8	0.26	3	-38	Pm	T029-56
T029-56@39.asc	11.4	0.28	3	-39	Pc	T029-56
T029-56@40.asc	9.5	0.28	3	-40	Pc	T029-56
T029-56@41.asc	28.0	0.29	3	-41	Pm	T029-56
T029-56@42.asc	31.7	0.28	3	-42	Pm	T029-56
T029-56@43.asc	8.9	0.28	3	-43	Pc	T029-56
T029-56@44.asc	8.7	0.26	3	-44	Pi	T029-56
T029-56@45.asc	8.8	0.27	3	-45	Pc	T029-56
T029-56@46.asc	31.9	0.27	3	-46	Pm	T029-56
T029-56@47.asc	3.4	0.28	3	-47	Pm	T029-56
T029-56@48.asc	8.7	0.27	3	-48	Pc	T029-56
T029-56@49.asc	7.7	0.26	3	-49	Pi	T029-56
T029-56@50.asc	7.9	0.26	3	-50	Pi	T029-56
T029-56@51.asc	2.3	0.29	3	-51	Pi	T029-56
T029-56@52.asc	1.0	0.26	3	-52	Pi	T029-56
T029-56@53.asc	8.4	0.27	3	-53	Pi	T029-56
T029-56@54.asc	22.0	0.29	3	-54	Pc	T029-56
T029-56@55.asc	19.8	0.28	3	-55	Pc	T029-56
T029-56@56.asc	34.1	0.29	3	-56	Pc	T029-56
T029-56@57.asc	9.9	0.26	3	-57	Pi	T029-56
T029-56@58.asc	11.0	0.26	3	-58	Pi	T029-56
T029-56@59.asc	16.3	0.27	3	-59	Pc	T029-56
T029-56@60.asc	28.9	0.29	3	-60	Pc	T029-56
T029-56@61.asc	8.1	0.13	3	-61	Pi	T029-56
T029-56@62.asc	7.3	0.13	3	-62	Pc	T029-56
T029-56@63.asc	27.0	0.15	3	-63	Pc	T029-56
T029-56@64.asc	-1.1	0.15	3	-64	Pm	T029-56
T029-56@65.asc	28.5	0.14	3	-65	Pc	T029-56
T029-56@66.asc	6.8	0.14	3	-66	Pc	T029-56
T029-56@67.asc	6.4	0.14	3	-67	Pi	T029-56
T029-56@68.asc	3.8	0.15	3	-68	Pi	T029-56
T029-56@69.asc	10.4	0.16	3	-69	Pc	T029-56
T029-56@70.asc	11.7	0.15	3	-70	Pc	T029-56

Filename	$\delta^{34}S$	std err	Site	Spot	Phase	Slide
T029-56@71.asc	9.4	0.10	4	-71	Pe	T029-56
T029-56@72.asc	19.0	0.12	4	-72	Pm	T029-56
T029-56@73.asc	16.3	0.11	4	-73	Pm	T029-56
T029-56@74.asc	2.2	0.11	4	-74	Pm	T029-56
T029-56@75.asc	6.1	0.17	4	-75	Pc	T029-56
T029-56@76.asc	8.8	0.10	4	-76	Pi	T029-56
T029-56@77.asc	7.0	0.10	4	-77	Pe	T029-56
T029-56@78.asc	21.2	0.11	4	-78	Pc	T029-56
T029-56@79.asc	10.0	0.23	4	-79	Pm	T029-56
T029-56@80.asc	0.8	0.10	4	-80	Pm	T029-56
T029-56@81.asc	5.8	0.09	4	-81	Pm	T029-56
T029-56@82.asc	17.5	0.12	4	-82	Pc	T029-56
T029-56@83.asc	7.4	0.12	4	-83	Pc	T029-56
T029-56@1.asc	12.1	0.44	1	-1	Pi	T029-56
T029-56@2.asc	9.9	0.41	1	-2	Pc	T029-56
T029-56@3.asc	9.1	0.48	1	-3	Pi	T029-56
T029-56@4.asc	5.4	0.46	1	-4	Pi	T029-56
T029-56@5.asc	16.9	0.45	1	-5	Pi	T029-56
T029-56@6.asc	17.6	0.44	1	-6	Pc	T029-56
T029-56@7.asc	10.9	0.58	1	-7	Pm	T029-56
T029-56@8.asc	38.6	0.63	1	-8	Pm	T029-56
T029-56@9.asc	12.5	0.43	1	-9	Pi	T029-56
T029-56@10.asc	9.7	0.45	1	-10	Pm	T029-56

BIBLIOGRAPHY

Adams, D.D., Hurtgen, M.T., Sageman, B.B., 2010. Volcanic triggering of a biogeochemical cascade during Oceanic Anoxic Event 2. Nat. Geosci. 3, 201–204. https://doi.org/10.1038/Ngeo743

Adams, J.E., Rhodes, M.L., 1960. Dolomitization by seepage refluxion. AAPG Bull. 44, 1912–1920.

Al-Aasm, I.S., Veizer, J., 1982. Chemical stabilization of low-Mg calcite; an example of brachiopods. J. Sediment. Res. 52, 1101–1109. https://doi.org/10.1306/212f80e4-2b24-11d7-8648000102c1865d

Aleinikoff, J.N., Lund, K., Fanning, C.., 2015. SHRIMP U–Pb and REE data pertaining to the origins of xenotime in Belt Supergroup rocks: evidence for ages of deposition, hydrothermal alteration, and metamorphism. Can. J. Earth Sci. 52, 722–745.

Algeo, T., Luo, G., Song, H., Lyons, T., Canfield, D., 2015. Reconstruction of secular variation in seawater sulfate concentrations. Biogeosciences 12, 2131–2151.

Alt, J.C., 1995. Sulfur isotopic profile through the oceanic crust: Sulfur mobility and seawater-crustal sulfur exchange during hydrothermal alteration. Geology 23, 585–588. https://doi.org/10.1130/0091-7613(1995)023<0585:siptto>2.3.co;2

Anderson, I.K., Ashton, J.H., Boyce, A.J., Fallick, A.E., Russell, M.J., 1998. Ore depositional process in the Navan Zn-Pb deposit, Ireland. Econ. Geol. 93, 535–563. https://doi.org/10.2113/gsecongeo.93.5.535

Arp, G., Hofmann, J., Reitner, J., 1998. Microbial fabric formation in spring mounds ("microbialites") of alkaline salt lakes in the Badain Jaran sand sea, PR China. PALAIOS 13, 581–592. https://doi.org/10.1043/0883-1351(1998)013<0581:mffism>2.0.co;2

Arp, G., Ostertag-Henning, C., YÜCekent, S., Reitner, J., Thiel, V., 2008. Methane-related microbial gypsum calcitization in stromatolites of a marine evaporative setting (Münder Formation, Upper Jurassic, Hils Syncline, north Germany). Sedimentology 55, 1227–1251. https://doi.org/10.1111/j.1365-3091.2007.00944.x

Ault, W.U., Kulp, J.L., 1959. Isotopic geochemistry of sulphur. Geochim. Cosmochim. Acta 16, 201–235. https://doi.org/10.1016/0016-7037(59)90112-7

Babcock, J.A., Yurewicz, D.A., 1989. The Massive Facies of the Capitan Limestone, Guadalupe Mountains, Texas and New Mexico, in: Harris, P.M., Grover, G.A. (Eds.), Subsurface and Outcrop Examination of the Capitan Shelf Margin, Northern Delaware Basin: SEPM Core Workshop No. 13. SEPM, San Antonio, pp. 365–371.

Balan, E., Aufort, J., Pouillé, S., Dabos, M., Blanchard, M., Lazzeri, M., Rollion-Bard, C., Blamart, D., 2017. Infrared spectroscopic study of sulfate-bearing calcite from deep-sea bamboo coral. Eur. J. Mineral. 29,

397–408. https://doi.org/10.1127/ejm/2017/0029-2611

Balan, E., Blanchard, M., Pinilla, C., Lazzeri, M., 2014. First-principles modeling of sulfate incorporation and 34S/32S isotopic fractionation in different calcium carbonates. Chem. Geol. 374–375, 84–91. https://doi.org/10.1016/j.chemgeo.2014.03.004

Baldermann, A., Deditius, A.P., Dietzel, M., Fichtner, V., Fischer, C., Hippler, D., Leis, A., Baldermann, C., Mavromatis, V., Stickler, C.P., Strauss, H., 2015. The role of bacterial sulfate reduction during dolomite precipitation: Implications from Upper Jurassic platform carbonates. Chem. Geol. 412, 1–14. https://doi.org/10.1016/j.chemgeo.2015.07.020

Banks, D.A., 1985. A fossil hydrothermal worm assemblage from the Tynagh lead–zinc deposit in Ireland 313, 128–131. https://doi.org/10.1038/313128a0

Barbieri, R., Cavalazzi, B., 2005. Microbial fabrics from Neogene cold seep carbonates, Northern Apennine, Italy. Palaeogeogr. Palaeoclimatol. Palaeoecol. 227, 143–155. https://doi.org/10.1016/j.palaeo.2005.04.026

Beaudoin, G., Taylor, B.E., Rumble, III, D., Thiemens, M., 1994. Variations in the sulfur isotope composition of troilite from the Cation Diablo iron meteorite. Geochim. Cosmochim. Acta 3.

Bebout, D.G., Kerans, C., 1993. Guide to the Permian Reef Geology Trail, McKittrick Canyon, Guadalupe Mountains National Park, Texas.

Bergmann, K.D., Finnegan, S., Creel, R.C., Eiler, J.M., Hughes, N.C., Popov, L.E., Fischer, W.W., 2018. A paired apatite and calcite clumped isotope thermometry approach to estimating Cambro-Ordovician seawater temperatures and isotopic composition. Geochim. Cosmochim. Acta 224, 18–41. https://doi.org/10.1016/j.gca.2017.11.015

Bergström, S.M., Chen, X., Gutiérrez-Marco, J.C., Dronov, A., 2009. The new chronostratigraphic classification of the Ordovician System and its relations to major regional series and stages and to δ13C chemostratigraphy. Lethaia 42, 97–107. https://doi.org/10.1111/j.1502-3931.2008.00136.x

Bergström, S.M., Schmitz, B., Saltzman, M.R., Huff, W.D., 2010a. The Upper Ordovician Guttenberg δ13C excursion (GICE) in North America and Baltoscandia: Occurrence, chronostratigraphic signifi cance, and paleoenvironmental relationships. GSA Spec. Pap. 466 34.

Bergström, S.M., Young, S., Schmitz, B., 2010b. Katian (Upper Ordovician) δ13C chemostratigraphy and sequence stratigraphy in the United States and Baltoscandia: A regional comparison. Palaeogeogr. Palaeoclimatol. Palaeoecol. 296, 217–234. https://doi.org/10.1016/j.palaeo.2010.02.035

Bernasconi, S.M., Meier, I., Wohlwend, S., Brack, P., Hochuli, P.A., Bläsi, H., Wortmann, U.G., Ramseyer, K., 2017. An evaporite-based high-resolution sulfur isotope record of Late Permian and Triassic seawater sulfate. Geochim. Cosmochim. Acta 204, 331–349.

https://doi.org/10.1016/j.gca.2017.01.047

Berner, E.K., Berner, R.A., 2012. Global environment: water, air, and geochemical cycles. Princeton University Press.

Berner, R.A., 1984. Sedimentary pyrite formation: An update. Geochim. Cosmochim. Acta 48, 605–615. https://doi.org/10.1016/0016-7037(84)90089-9

Berner, R.A., 1978. Sulfate reduction and the rate of deposition of marine sediments. Earth Planet. Sci. Lett. 37, 492–498. https://doi.org/10.1016/0012-821X(78)90065-1

Bickert, T., Pätzold, J., Samtleben, C., Munnecke, A., 1997. Paleoenvironmental changes in the Silurian indicated by stable isotopes in brachiopod shells from Gotland, Sweden. Geochim. Cosmochim. Acta 61, 2717–2730. https://doi.org/10.1016/S0016-7037(97)00136-1

Bishop, J.K.B., 1988. The barite-opal-organic carbon association in oceanic particulate matter. Nature 332, 341–343. https://doi.org/10.1038/332341a0

Blakeman, R.J., Ashton, J.H., Boyce, A.J., Fallick, A.E., Russell, M.J., 2002. Timing of Interplay between Hydrothermal and Surface Fluids in the Navan Zn + Pb Orebody, Ireland: Evidence from Metal Distribution Trends, Mineral Textures, and δ34S Analyses. Econ. Geol. 97, 73. https://doi.org/10.2113/gsecongeo.97.1.73

Borer, J., Harris, P., 1991. Lithofacies and Cyclicity of the Yates Formation, Permian Basin: Implications for Reservoir Heterogeneity. AAPG Bull. 75, 726–779.

Bottcher, M.E., Smock, A.M., Cypionka, H., 1998. Sulfur isotope fractionation during experimental precipitation of ironžII/ and manganesežII/ sulfide at room temperature. Chem. Geol. 146, 127–134.

Bottrell, S.H., Newton, R.J., 2006. Reconstruction of changes in global sulfur cycling from marine sulfate isotopes. Earth-Sci. Rev. 75, 59–83. https://doi.org/10.1016/j.earscirev.2005.10.004

Bowles, M.W., Mogollón, J.M., Kasten, S., Zabel, M., Hinrichs, K.-U., 2014. Global rates of marine sulfate reduction and implications for sub–sea-floor metabolic activities. Science 344, 889. https://doi.org/10.1126/science.1249213

Boyce, A., Coleman, M., Russell, M., 1983. Formation of fossil hydrothermal chimneys and mounds from Silvermines, Ireland. Nature 306, 545–550.

Boyce, A.J., Little, C.T.S., Russell, M.J., 2003. A new fossil vent biota in the Ballynoe barite deposit, Silvermines, Ireland: Evidence for intracratonic sea-floor hydrothermal activity about 352 Ma. Econ. Geol. 98, 649. https://doi.org/10.2113/gsecongeo.98.3.649

Brabec, M.Y., Lyons, T.W., Mandernack, K.W., 2012. Oxygen and sulfur isotope fractionation during sulfide oxidation by anoxygenic phototrophic bacteria. Geochim. Cosmochim. Acta 83, 234–251. https://doi.org/10.1016/j.gca.2011.12.008

Bradley, A.S., 2008. Organic geochemical biosignatures in alkaline hydrothermal systems.

Massachusetts Institute of Technology, Cambridge, MA.

Bradley, A.S., Hayes, J.M., Summons, R.E., 2009. Extraordinary 13C enrichment of diether lipids at the Lost City Hydrothermal Field indicates a carbon-limited ecosystem. Geochim. Cosmochim. Acta 73, 102–118. https://doi.org/10.1016/j.gca.2008.10.005

Brand, U., Veizer, J., 1981. Chemical diagenesis of a multicomponent carbonate system; 2, Stable isotopes. J. Sediment. Res. 51, 987–997. https://doi.org/10.1306/212f7df6-2b24-11d7-8648000102c1865d

Brand, U., Veizer, J., 1980. Chemical diagenesis of a multicomponent carbonate system; 1, Trace elements. J. Sediment. Res. 50, 1219–1236. https://doi.org/10.1306/212f7bb7-2b24-11d7-8648000102c1865d

Breier, J.A., White, S.N., German, C.R., 2010. Mineral–microbe interactions in deep-sea hydrothermal systems: a challenge for Raman spectroscopy. Philos. Trans. R. Soc. Math. Phys. Eng. Sci. 368, 3067. https://doi.org/10.1098/rsta.2010.0024

Breit, G.N., Simmons, E.C., Goldhaber, M.B., 1985. Dissolution of barite for the analysis of strontium isotopes and other chemical and isotopic variations using aqueous sodium carbonate. Chem. Geol. Isot. Geosci. Sect. 52, 333–336. https://doi.org/10.1016/0168-9622(85)90043-0

Brenchley, P.J., Marshall, J.D., Carden, G.A.F., Robertson, D.B.R., 1994. Bathymetric and isotopic evidence for a short-lived Late Ordovician glaciation in a greenhouse period. Geology 22, 295–298.

Brown, A., 1996. Position of the Polydiexodina last-occurrence datum in Guadalupian strata: Revised correlations at McKittrick Canyon, in: DeMis, W.D., Cole, A.G. (Eds.), The Brushy Canyon Play in Outcrop and Subsurface: Concepts and Examples, Permian Basin Section SEPM Publication 96-38. Permian Basin Section SEPM, Midland, TX, pp. 75–84.

Brunner, B., Bernasconi, S.M., 2005. A revised isotope fractionation model for dissimilatory sulfate reduction in sulfate reducing bacteria. Geochim. Cosmochim. Acta 69, 4759–4771. https://doi.org/10.1016/j.gca.2005.04.015

Budd, D.A., Frost, E.L., Huntington, K.W., Allwardt, P.F., 2013. Syndepositional Deformation Features In High-Relief Carbonate Platforms: Long-Lived Conduits for Diagenetic Fluids. J. Sediment. Res. 83, 12–36. https://doi.org/10.2110/jsr.2013.3

Burdett, J.W., Arthur, M.A., Richardson, M., 1989. A Neogene seawater sulfur isotope age curve from calcareous pelagic microfossils. Earth Planet. Sci. Lett. 94, 189–198. https://doi.org/10.1016/0012-821x(89)90138-6

Burke, A., Present, T.M., Paris, G., Rae, E.C.M., Sandilands, B.H., Gaillardet, J., Peucker-Ehrenbrink, B., Fischer, W.W., McClelland, J.W., Spencer, R.G.M., Voss, B.M., Adkins, J.F., 2018. Sulfur isotopes in rivers: Insights into global weathering budgets, pyrite oxidation, and the modern sulfur cycle. Earth Planet. Sci. Lett. https://doi.org/10.1016/j.epsl.2018.05.022

Busenberg, E., Plummer, N.L., 1985. Kinetic and thermodynamic factors

controlling the distribution of SO42− and Na+ in calcites and selected aragonites. Geochim. Cosmochim. Acta 49, 713–725. https://doi.org/10.1016/0016-7037(85)90166-8

Cady, S.L., Farmer, J.D., Grotzinger, J.P., Schopf, J.W., Steele, A., 2003. Morphological biosignatures and the search for life on Mars. Astrobiology 3, 351–368.

Calner, M., Jeppsson, L., Munnecke, A., 2004. The Silurian of Gotland—Part I: Review of the stratigraphic framework, event stratigraphy, and stable carbon and oxygen isotope development. Erlanger Geol. Abh. Sonderband 5, 113–131.

Came, R.E., Eiler, J.M., Veizer, J., Azmy, K., Brand, U., Weidman, C.R., 2007. Coupling of surface temperatures and atmospheric CO2 concentrations during the Palaeozoic era. Nature 449, 198–201. https://doi.org/10.1038/nature06085

Campbell, K.A., Farmer, J.D., Des Marais, D., 2002. Ancient hydrocarbon seeps from the Mesozoic convergent margin of California: carbonate geochemistry, fluids and palaeoenvironments. Geofluids 2, 63–94. https://doi.org/10.1046/j.1468-8123.2002.00022.x

Canfield, D.E., 2004. The evolution of the Earth surface sulfur reservoir. Am. J. Sci. 304, 839–861. https://doi.org/10.2475/ajs.304.10.839

Canfield, D.E., 2001. Isotope fractionation by natural populations of sulfate-reducing bacteria. Geochim. Cosmochim. Acta 65, 1117–1124. https://doi.org/10.1016/S0016-7037(00)00584-6

Canfield, D.E., Farquhar, J., Zerkle, A.L., 2010. High isotope fractionations during sulfate reduction in a low-sulfate euxinic ocean analog. Geology 38, 415. https://doi.org/10.1130/G30723.1

Canfield, D.E., Raiswell, R., 1999. The evolution of the sulfur cycle. Am. J. Sci. 299, 697–723. https://doi.org/10.2475/ajs.299.7-9.697

Canfield, D.E., Teske, A., 1996. Late Proterozoic rise in atmospheric oxygen concentration inferred from phylogenetic and sulphur-isotope studies. Nature 382, 11.

Canfield, D.E., Thamdrup, B., 1994. The production of 34S-depleted sulfide during bacterial disproportionation of elemental sulfur. Science 266, 1973–1975. https://doi.org/10.1126/science.11540246

Chen, D., Wang, J., Racki, G., Li, H., Wang, C., Ma, X., Whalen, M.T., 2013. Large sulphur isotopic perturbations and oceanic changes during the Frasnian–Famennian transition of the Late Devonian. J. Geol. Soc. 170, 465–476. https://doi.org/10.1144/jgs2012-037

Chow, T.J., Goldberg, E.D., 1960. On the marine geochemistry of barium. Geochim. Cosmochim. Acta 20, 192–198. https://doi.org/10.1016/0016-7037(60)90073-9

Church, T.M., Wolgemuth, K., 1972. Marine barite saturation. Earth Planet. Sci. Lett. 15, 35–44. https://doi.org/10.1016/0012-821X(72)90026-X

Claypool, G.E., Holser, W.T., Kaplan, I.R., Sakai, H., Zak, I., 1980. The age curves of sulfur and oxygen isotopes

in marine sulfate and their mutual interpretation. Chem. Geol. 28, 199–260. https://doi.org/10.1016/0009-2541(80)90047-9

Cohen, K., Finney, S., Gibbard, P., Fan, J.-X., 2013. The ICS international chronostratigraphic chart. Episodes 36, 199–204.

Cooke, D.R., Bull, S.W., Large, R.R., McGoldrick, P.J., 2000. The Importance of Oxidized Brines for the Formation of Australian Proterozoic Stratiform Sediment-Hosted Pb-Zn (Sedex) Deposits. Econ. Geol. 95, 1–18. https://doi.org/10.2113/gsecongeo.95.1.1

Coplen, T.B., Krouse, H.R., 1998. Sulphur isotope data consistency improved. Nature 392, 32. https://doi.org/10.1038/32080

Copper, P., Jin, J., 2014. The revised Lower Silurian (Rhuddanian) Becscie Formation, Anticosti Island, eastern Canada records the tropical marine faunal recovery from the end-Ordovician Mass Extinction. Newsl. Stratigr. 47, 61–83. https://doi.org/10.1127/0078-0421/2014/0040

Copper, P., Jin, J., Desrochers, A., 2013. The Ordovician-Silurian boundary (late Katian-Hirnantian) of western Anticosti Island: revised stratigraphy and benthic megafaunal correlations. Stratigraphy 10, 213–227.

Cramer, B.D., Loydell, D.K., Samtleben, C., Munnecke, A., Kaljo, D., Männik, P., Martma, T., Jeppsson, L., Kleffner, M.A., Barrick, J.E., Johnson, C.A., Emsbo, P., Joachimski, M.M., Bickert, T., Saltzman, M.R., 2010. Testing the limits of Paleozoic chronostratigraphic correlation via high-resolution (<500 k.y.) integrated conodont, graptolite, and carbon isotope (δ13Ccarb) biochemostratigraphy across the Llandovery–Wenlock (Silurian) boundary: Is a unified Phanerozoic time scale achievable? Geol. Soc. Am. Bull. 17.

Crémière, A., Strauss, H., Sebilo, M., Hong, W.-L., Gros, O., Schmidt, S., Tocny, J., Henry, F., Gontharet, S., Laverman, A.M., 2017. Sulfur diagenesis under rapid accumulation of organic-rich sediments in a marine mangrove from Guadeloupe (French West Indies). Chem. Geol. 454, 67–79. https://doi.org/10.1016/j.chemgeo.2017.02.017

Cuif, J.-P., Dauphin, Y., Doucet, J., Salome, M., Susini, J., 2003. XANES mapping of organic sulfate in three scleractinian coral skeletons. Geochim. Cosmochim. Acta 67, 75–83. https://doi.org/10.1016/S0016-7037(02)01041-4

Cummins, R.C., Finnegan, S., Fike, D.A., Eiler, J.M., Fischer, W.W., 2014. Carbonate clumped isotope constraints on Silurian ocean temperature and seawater δ18O. Geochim. Cosmochim. Acta 140, 241–258. https://doi.org/10.1016/j.gca.2014.05.024

Cusack, M., Dauphin, Y., Cuif, J.-P., Salomé, M., Freer, A., Yin, H., 2008. Micro-XANES mapping of sulphur and its association with magnesium and phosphorus in the shell of the brachiopod, Terebratulina retusa. Chem. Geol. 253, 172–179. https://doi.org/10.1016/j.chemgeo.2008.05.007

Dauphin, Y., Cuif, J.-P., Salomé, M., Susini, J., 2005. Speciation and distribution of sulfur in a mollusk shell as revealed by in situ maps using X-ray

absorption near-edge structure (XANES) spectroscopy at the S K-edge. Am. Mineral. 90, 1748. https://doi.org/10.2138/am.2005.1640

Davies, G.R., Krouse, H.R., 1975. Sulphur isotope distribution in Paleozoic sulphate evaporites, Canadian Arctic Archipelago. Geol. Surv. Can. Pap. 75–1 Part B, 221–225.

DeFord, R.K., Riggs, G.D., 1941. Tansill formation, west Texas and southeastern New Mexico. AAPG Bull. 25, 1713–1728.

Delaney, J.R., Robigou, V., McDuff, R.E., Tivey, M.K., 1992. Geology of a vigorous hydrothermal system on the Endeavour Segment, Juan de Fuca Ridge. J. Geophys. Res. Solid Earth 97, 19663–19682.

Desrochers, A., Farley, C., Achab, A., Asselin, E., Riva, J.F., 2010. A far-field record of the end Ordovician glaciation: The Ellis Bay Formation, Anticosti Island, Eastern Canada. Palaeogeogr. Palaeoclimatol. Palaeoecol. 296, 248–263. https://doi.org/10.1016/j.palaeo.2010.02.017

Desrochers, A., Gauthier, É.L., 2009. Carte géologique de l'île d'Anticosti (1/250 000), DV 2009-03.

Dewing, K., Nowlan, G., 2012. The Lower Cambrian to Lower Ordovician Carbonate Platform and Shelf Margin, Canadian Arctic Islands, in: Derby, J.R., Fritz, R.D., Longacre, S.A., Morgan, W.A., Stembach, C.A. (Eds.), The Great American Carbonate Bank: The Geology and Economic Resources of the Cambrian – Ordovician Sauk Megasequence of Laurentia: AAPG Memoir 98. pp. 627–647.

Dixon, G., Davidson, G.J., 1996. Stable isotope evidence for thermochemical sulfate reduction in the Dugald river (Australia) strata-bound shale-hosted zinc□ead deposit. Chem. Geol. 129, 227–246. https://doi.org/10.1016/0009-2541(95)00177-8

Dogramaci, S.S., Herczeg, A.L., Schiff, S.L., Bone, Y., 2001. Controls on δ34S and δ18O of dissolved sulfate in aquifers of the Murray Basin, Australia and their use as indicators of flow processes. Appl. Geochem. 16, 475–488. https://doi.org/10.1016/S0883-2927(00)00052-4

Dunham, R.J., 1972. Capitan Reef, New Mexico and Texas: facts and questions to aid interpretation and group discussion, Permian Basin Section SEPM Publication 72-14. Permian Basin Section SEPM, Midland, TX.

Dunster, J.N., 1997. The Lady Loretta Formation: sedimentology and stratiform sediment-hosted base metal mineralisation. University of Tasmania.

Eickmann, B., Thorseth, I.H., Peters, M., Strauss, H., Bröcker, M., Pedersen, R.B., 2014. Barite in hydrothermal environments as a recorder of subseafloor processes: a multiple-isotope study from the Loki's Castle vent field. Geobiology 12, 308–321. https://doi.org/10.1111/gbi.12086

Eldridge, C.S., Williams, N., Walshe, J.L., 1993. Sulfur isotope variability in sediment-hosted massive sulfide deposits as determined using the ion microprobe SHRIMP; II, A study of the H.Y.C. Deposit at McArthur River, Northern Territory, Australia. Econ. Geol. 88, 1–26.

https://doi.org/10.2113/gsecongeo.88.1.1

Elliott, W.C., Aronson, J.L., 1993. The timing and extent of illite formation in Ordovician K-bentonites at the Cincinnati Arch, the Nashville Dome and north-eastern Illinois basin. Basin Res. 5, 125–135. https://doi.org/10.1111/j.1365-2117.1993.tb00061.x

Ellwood, B.B., Brett, C.E., MacDonald, W.D., 2007. Magnetostratigraphy susceptibility of the Upper Ordovician Kope Formation, northern Kentucky. Palaeogeogr. Palaeoclimatol. Palaeoecol. 243, 42–54. https://doi.org/10.1016/j.palaeo.2006.07.003

Emerson, D., Moyer, C.L., 2002. Neutrophilic Fe-Oxidizing Bacteria Are Abundant at the Loihi Seamount Hydrothermal Vents and Play a Major Role in Fe Oxide Deposition. Appl. Environ. Microbiol. 68, 3085–3093. https://doi.org/10.1128/aem.68.6.3085-3093.2002

Epstein, A.G., Epstein, J.B., Harris, L.D., 1977. Conodont Color Alteration- an Index to Organic Metamorphism. Geol. Surv. Prof. Pap. 995, 31.

Esteban, M., Pray, L., 1983. Pisoids and pisolite facies (Permian), Guadalupe Mountains, New Mexico and West Texas, in: Coated Grains. pp. 503–537.

Farquhar, J., Wu, N., Canfield, D.E., Oduro, H., 2010. Connections between Sulfur Cycle Evolution, Sulfur Isotopes, Sediments, and Base Metal Sulfide Deposits. Econ. Geol. 105, 509–533. https://doi.org/10.2113/gsecongeo.105.3.509

Fedonkin, M.A., Yochelson, E.L., 2002. Middle Proterozoic (1.5 Ga) Horodyskia moniliformis Yochelson and Fedonkin, the oldest known tissue-grade colonial eucaryote. Smithson. Contrib. Paleobiology 94, 1–29.

Feng, D., Peng, Y., Bao, H., Peckmann, J., Roberts, H.H., Chen, D., 2016. A carbonate-based proxy for sulfate-driven anaerobic oxidation of methane. Geology 44, 999–1002. https://doi.org/10.1130/G38233.1

Feng, D., Roberts, H.H., 2011. Geochemical characteristics of the barite deposits at cold seeps from the northern Gulf of Mexico continental slope. Earth Planet. Sci. Lett. 309, 89–99. https://doi.org/10.1016/j.epsl.2011.06.017

Fernández-Díaz, L., Fernández-González, Á., Prieto, M., 2010. The role of sulfate groups in controlling CaCO3 polymorphism. Geochim. Cosmochim. Acta 74, 6064–6076. https://doi.org/10.1016/j.gca.2010.08.010

Fichtner, V., Strauss, H., Immenhauser, A., Buhl, D., Neuser, R.D., Niedermayr, A., 2017. Diagenesis of carbonate associated sulfate. Chem. Geol. 463, 61–75. https://doi.org/10.1016/j.chemgeo.2017.05.008

Fichtner, V., Strauss, H., Mavromatis, V., Dietzel, M., Huthwelker, T., Borca, C.N., Guagliardo, P., Kilburn, M.R., Göttlicher, J., Pederson, C.L., Griesshaber, E., Schmahl, W.W., Immenhauser, A., 2018. Incorporation and subsequent diagenetic alteration of sulfur in Arctica islandica. Chem. Geol. 482, 72–90. https://doi.org/10.1016/j.chemgeo.2018.01.035

Fike, D.A., Grotzinger, J., 2010. A δ34SSO4 approach to reconstructing biogenic pyrite burial in carbonate-evaporite basins: An example from the Ara Group, Sultanate of Oman. Geology 38, 371–374.

Fike, D.A., Grotzinger, J.P., 2008. A paired sulfate–pyrite δ34S approach to understanding the evolution of the Ediacaran–Cambrian sulfur cycle. Geochim. Cosmochim. Acta 72, 2636–2648. https://doi.org/10.1016/j.gca.2008.03.021

Finnegan, S., Bergmann, K., Eiler, J.M., Jones, D.S., Fike, D.A., Eisenman, I., Hughes, N.C., Tripati, A.K., Fischer, W.W., 2011. The Magnitude and Duration of Late Ordovician–Early Silurian Glaciation. Science 331, 903–906.

Finnegan, S., Heim, N.A., Peters, S.E., Fischer, W.W., 2012. Climate change and the selective signature of the Late Ordovician mass extinction. Proc. Natl. Acad. Sci. 109, 6829–6834.

Fischer, W.W., Fike, D.A., Johnson, J.E., Raub, T.D., Guan, Y., Kirschvink, J.L., Eiler, J.M., 2014. SQUID–SIMS is a useful approach to uncover primary signals in the Archean sulfur cycle. Proc. Natl. Acad. Sci. 111, 5468–5473. https://doi.org/10.1073/pnas.1322577111

Flugel, E., Munnecke, A., 2010. Microfacies of carbonate rocks: analysis, interpretation and application. Springer-Verlag.

Föllmi, K.B., 1996. The phosphorus cycle, phosphogenesis and marine phosphate-rich deposits. Earth-Sci. Rev. 40, 55–124. https://doi.org/10.1016/0012-8252(95)00049-6

Fouke, B.W., Farmer, J.D., Des Marais, D.J., Pratt, L., Sturchio, N.C., Burns, P.C., Discipulo, M.K., 2000. Depositional Facies and Aqueous-Solid Geochemistry of Travertine-Depositing Hot Springs (Angel Terrace, Mammoth Hot Springs, Yellowstone National Park, U.S.A.). J. Sediment. Res. 70, 565–585. https://doi.org/10.1306/2dc40929-0e47-11d7-8643000102c1865d

Froelich, P.N., Klinkhammer, G.P., Bender, M.L., Luedtke, N.A., Heath, G.R., Cullen, D., Dauphin, P., Hammond, D., Hartman, B., Maynard, V., 1979. Early oxidation of organic matter in pelagic sediments of the eastern equatorial Atlantic: suboxic diagenesis. Geochim. Cosmochim. Acta 43, 1075–1090. https://doi.org/10.1016/0016-7037(79)90095-4

Frost, E.L., Budd, D.A., Kerans, C., 2012. Syndepositional Deformation In A High-Relief Carbonate Platform and Its Effect On Early Fluid Flow As Revealed By Dolomite Patterns. J. Sediment. Res. 82, 913–932. https://doi.org/10.2110/jsr.2012.74

Früh-Green, G.L., Kelley, D.S., Bernasconi, S.M., Karson, J.A., Ludwig, K.A., Butterfield, D.A., Boschi, C., Proskurowski, G., 2003. 30,000 Years of Hydrothermal Activity at the Lost City Vent Field. Science 301, 495–498. https://doi.org/10.1126/science.1085582

Fry, B., Ruf, W., Gest, H., Hayes, J.M., 1988. Sulfur isotope effects associated with oxidation of sulfide by O2 in aqueous solution. Chem. Geol. Isot. Geosci. Sect. 73, 205–210. https://doi.org/10.1016/0168-9622(88)90001-2

Gadd, M.G., Layton-Matthews, D., Peter, J.M., Paradis, S.J., 2016. The world-class Howard's Pass SEDEX Zn-Pb district, Selwyn Basin, Yukon. Part I: trace element compositions of pyrite record input of hydrothermal, diagenetic, and metamorphic fluids to mineralization. Miner. Deposita 51, 319–342. https://doi.org/10.1007/s00126-015-0611-2

Gamo, T., Sakai, H., Kim, E.-S., Shitashima, K., Ishibashi, J., 1991. High alkalinity due to sulfate reduction in the CLAM hydrothermal field, Okinawa Trough. Earth Planet. Sci. Lett. 107, 328–338. https://doi.org/10.1016/0012-821X(91)90080-2

Garber, R.A., Grover, G.A., Harris, P.M., 1989. Geology of the Capitan Shelf Margin - Subsurface Data from the Northern Delaware Basin, in: Harris, P.M., Grover, G.A. (Eds.), Subsurface and Outcrop Examination of the Capitan Shelf Margin, Northern Delaware Basin: SEPM Core Workshop No. 13. SEPM, San Antonio, pp. 3–272.

Garrels, R.M., Lerman, A., 1984. Coupling of the sedimentary sulfur and carbon cycles; an improved model. Am. J. Sci. 284, 989–1007. https://doi.org/10.2475/ajs.284.9.989

Garrels, R.M., Lerman, A., 1981. Phanerozoic cycles of sedimentary carbon and sulfur. Proc. Natl. Acad. Sci. 78, 4652–4656.

Gartman, A., Luther, G.W., 2014. Oxidation of synthesized sub-micron pyrite (FeS 2) in seawater. Geochim. Cosmochim. Acta 144, 96–108. https://doi.org/10.1016/j.gca.2014.08.022

Gellatly, A.M., Lyons, T.W., 2005. Trace sulfate in mid-Proterozoic carbonates and the sulfur isotope record of biospheric evolution. Geochim. Cosmochim. Acta 69, 3813–3829. https://doi.org/10.1016/j.gca.2005.01.019

Gill, B.C., Lyons, T.W., Frank, T.D., 2008. Behavior of carbonate-associated sulfate during meteoric diagenesis and implications for the sulfur isotope paleoproxy. Geochim. Cosmochim. Acta 72, 4699–4711. https://doi.org/10.1016/j.gca.2008.07.001

Gill, B.C., Lyons, T.W., Jenkyns, H.C., 2011a. A global perturbation to the sulfur cycle during the Toarcian Oceanic Anoxic Event. Earth Planet. Sci. Lett. 312, 484–496. https://doi.org/10.1016/j.epsl.2011.10.030

Gill, B.C., Lyons, T.W., Saltzman, M.R., 2007. Parallel, high-resolution carbon and sulfur isotope records of the evolving Paleozoic marine sulfur reservoir. Palaeogeogr. Palaeoclimatol. Palaeoecol. 256, 156–173. https://doi.org/10.1016/j.palaeo.2007.02.030

Gill, B.C., Lyons, T.W., Young, S.A., Kump, L.R., Knoll, A.H., Saltzman, M.R., 2011b. Geochemical evidence for widespread euxinia in the Later Cambrian ocean. Nature 469, 80–83.

Given, R.K., Lohmann, K.C., 1986. Isotopic evidence for the early meteoric diagenesis of the reef facies, Permian Reef Complex of west Texas and New Mexico. J. Sediment. Res. 56, 183–193. https://doi.org/10.1306/212f88b4-2b24-11d7-8648000102c1865d

Given, R.K., Lohmann, K.C., 1985. Derivation of the original isotopic composition of Permian marine cements. J. Sediment. Res. 55, 430–439.

Glenn, C.R., Föllmi, K.B., Riggs, S., Baturin, G., Grimm, K., Trappe, J., Abed, A., Galli-Olivier, C., Garrison, R., Ilyin, A., Jehl, C., Rohrlich, V., Sadaqah, R., Schidlowski, M., Sheldon, R., Siegmund, H., 1994. Phosphorus and phosphorites: Sedimentology and environments of formation. Eclogae Geol. Helvetie 87, 747–788.

Glickson, D.A., Kelley, D.S., Delaney, J.R., 2007. Geology and hydrothermal evolution of the Mothra Hydrothermal Field, Endeavour Segment, Juan de Fuca Ridge. Geochem. Geophys. Geosystems 8, n/a-n/a. https://doi.org/10.1029/2007GC001588

Godlewski, D., Zieg, G., 1984. Stratigraphy and depositional setting of the Precambrian Newland Limestone, in: Hobbs, S. (Ed.), The Belt, Abstracts and Summaries Belt Symposium II, 1983, Montana Bureau of Mines and Geology, Special Publication. pp. 2–4.

Goldberg, T., Poulton, S.W., Strauss, H., 2005. Sulphur and oxygen isotope signatures of late Neoproterozoic to early Cambrian sulphate, Yangtze Platform, China: Diagenetic constraints and seawater evolution. Precambrian Res. 137, 223–241. https://doi.org/10.1016/j.precamres.2005.03.003

Goldhaber, M.B., Kaplan, I.R., 1980. Mechanisms of sulfur incorporation and isotope fractionation during early diagenesis in sediments of the gulf of California. Mar. Chem. 9, 95–143. https://doi.org/10.1016/0304-4203(80)90063-8

Goldhammer, R.K., Dunn, P.A., Hardie, L.A., 1990. Depositional cycles, composite sea-level changes, cycle stacking patterns, and the hierarchy of stratigraphic forcing: Examples from Alpine Triassic platform carbonates. GSA Bull. 102, 535–562. https://doi.org/10.1130/0016-7606(1990)102<0535:DCCSLC>2.3.CO;2

Gomes, M.L., Hurtgen, M.T., 2015. Sulfur isotope fractionation in modern euxinic systems: Implications for paleoenvironmental reconstructions of paired sulfate–sulfide isotope records. Geochim. Cosmochim. Acta 157, 39–55. https://doi.org/10.1016/j.gca.2015.02.031

Gomes, M.L., Hurtgen, M.T., Sageman, B.B., 2016. Biogeochemical sulfur cycling during Cretaceous oceanic anoxic events: A comparison of OAE1a and OAE2. Paleoceanography 31, 2015PA002869. https://doi.org/10.1002/2015PA002869

Goodfellow, W., Lydon, J., Turner, R., 1993. Geology and genesis of stratiform sediment-hosted (SEDEX) zinc-lead-silver sulphide deposits. Geol. Assoc. Can. Spec. Pap. 40, 201–251.

Gorjan, P., Kaiho, K., Fike, D.A., Xu, C., 2012. Carbon- and sulfur-isotope geochemistry of the Hirnantian (Late Ordovician) Wangjiawan (Riverside) section, South China: Global correlation and environmental event interpretation. Palaeogeogr. Palaeoclimatol. Palaeoecol. 337–338, 14–22. https://doi.org/10.1016/j.palaeo.2012.03.021

Gradstein, F.M., Ogg, J.G., Schmitz, M., Ogg, G., 2012. The Geologic Time Scale 2012. Elsevier.

Graham, G., Hitzman, M.W., Zieg, J., 2012. Geologic Setting, Sedimentary Architecture, and Paragenesis of the Mesoproterozoic Sediment-Hosted Sheep Creek Cu-Co-Ag Deposit, Helena Embayment, Montana. Econ. Geol. 107, 1115–1141.

Gregory, D.D., Large, R.R., Halpin, J.A., Steadman, J.A., Hickman, A.H., Ireland, T.R., Holden, P., 2015. The chemical conditions of the late Archean Hamersley basin inferred from whole rock and pyrite geochemistry with Δ33S and δ34S isotope analyses. Geochim. Cosmochim. Acta 149, 223–250. https://doi.org/10.1016/j.gca.2014.10.023

Grobe, M., 2000. Distribution and thickness of salt within the Devonian Elk Point Group, Western Canada Sedimentary Basin. Earth Sci. Rep. 2, 1–12.

Grossman, E.L., Mii, H.-S., Yancey, T.E., 1993. Stable isotopes in Late Pennsylvanian brachiopods from the United States: Implications for Carboniferous paleoceanography. Geol. Soc. Am. Bull. 105, 1284–1296. https://doi.org/10.1130/0016-7606(1993)105<1284:siilpb>2.3.co;2

Grotzinger, J.P., Knoll, A.H., 1999. Stromatolites in Precambrian carbonates: evolutionary mileposts or environmental dipsticks? Annu. Rev. Earth Planet. Sci. 27, 313–358.

Grotzinger, J.P., Knoll, A.H., 1995. Anomalous Carbonate Precipitates: Is the Precambrian the Key to the Permian? PALAIOS 10, 578–596. https://doi.org/10.2307/3515096

Guo, H., Du, Y., Kah, L.C., Hu, C., Huang, J., Huang, H., Yu, W., Song, H., 2015. Sulfur isotope composition of carbonate-associated sulfate from the Mesoproterozoic Jixian Group, North China: Implications for the marine sulfur cycle. Precambrian Res. 266, 319–336. https://doi.org/10.1016/j.precamres.2015.05.032

Habicht, K.S., Canfield, D.E., 1997. Sulfur isotope fractionation during bacterial sulfate reduction in organic-rich sediments. Geochim. Cosmochim. Acta 61, 5351–5361. https://doi.org/10.1016/S0016-7037(97)00311-6

Halevy, I., Peters, S.E., Fischer, W.W., 2012. Sulfate Burial Constraints on the Phanerozoic Sulfur Cycle. Science 337, 331–334. https://doi.org/10.1126/science.1220224

Hammarlund, E.U., Dahl, T.W., Harper, D.A.T., Bond, D.P.G., Nielsen, A.T., Bjerrum, C.J., Schovsbo, N.H., Schönlaub, H.P., Zalasiewicz, J.A., Canfield, D.E., 2012. A sulfidic driver for the end-Ordovician mass extinction. Earth Planet. Sci. Lett. 331–332, 128–139. https://doi.org/10.1016/j.epsl.2012.02.024

Hannington, M.D., Jonasson, I.R., Herzig, P.M., Petersen, S., 1995. Physical and Chemical Processes of Seafloor Mineralization at Mid-Ocean Ridges, in: Humphris, S.E., Zierenberg, R.A., Mullineaux, L.S., Thomson, R.E. (Eds.), Seafloor Hydrothermal Systems: Physical, Chemical, Biological, and Geological Interactions. American Geophysical Union, pp. 115–157. https://doi.org/10.1029/GM091p0115

Hardie, L.A., 1984. Evaporites; marine or non-marine? Am. J. Sci. 284, 193–240.

https://doi.org/10.2475/ajs.284.3.193

Harrison, A.G., Thode, H.G., 1958. Mechanism of the bacterial reduction of sulphate from isotope fractionation studies. Trans. Faraday Soc. 54, 84. https://doi.org/10.1039/tf9585400084

Haymon, R.M., 1983. Growth history of hydrothermal black smoker chimneys. Nature 301, 695–698. https://doi.org/10.1038/301695a0

Haymon, R.M., Kastner, M., 1981. Hot spring deposits on the East Pacific Rise at 21°N: preliminary description of mineralogy and genesis. Earth Planet. Sci. Lett. 53, 363–381. https://doi.org/10.1016/0012-821X(81)90041-8

Haymon, R.M., Koski, R.A., Sinclair, C., 1984. Fossils of Hydrothermal Vent Worms from Cretaceous Sulfide Ores of the Samail Ophiolite, Oman. Science 223, 1407–1409. https://doi.org/10.1126/science.223.4643.1407

Hill, C.A., 1990. Sulfuric Acid Speleogenesis of Carlsbad Cavern and Its Relationship to Hydrocarbons, Delaware Basin, New Mexico and Texas (1). AAPG Bull. 74, 1685–1694.

Himes, M., Peterson, E., 1990. Geological and Mineralogical Characteristics of the Sheep Creek Copper-Cobalt Sediment-hosted Stratabound Sulfide Deposit, Meagher County, Montana, in: Hausen, D., Halbe, D., Peterson, E., Tafuri, W. (Eds.), Gold '90; Proceedings of the Gold '90 Symposium, Salt Lake City, Utach, February 26 to March 1, 1990. Society for Mining, Metallurgy, and Exploration, Inc., Littleton, Colorado, pp. 533–546.

Hitzman, M.W., Selley, D., Bull, S., 2010. Formation of sedimentary rock-hosted stratiform copper deposits through Earth history. Econ. Geol. 105, 627–639.

Hofmann, B.A., Farmer, J.D., 2000. Filamentous fabrics in low-temperature mineral assemblages: are they fossil biomarkers? Implications for the search for a subsurface fossil record on the early Earth and Mars. Planet. Space Sci. 48, 1077–1086. https://doi.org/10.1016/S0032-0633(00)00081-7

Holland, H.D., 1973. Systematics of the isotopic composition of sulfur in the oceans during the Phanerozoic and its implications for atmospheric oxygen. Geochim. Cosmochim. Acta 37, 2605–2616. https://doi.org/10.1016/0016-7037(73)90268-8

Holland, S.M., 1993. Sequence stratigraphy of a carbonate-clastic ramp: The Cincinnatian Series (Upper Ordovician) in its type area. GSA Bull. 105, 306–322. https://doi.org/10.1130/0016-7606(1993)105<0306:SSOACC>2.3.CO;2

Holland, S.M., Patzkowsky, M.E., 1996. Sequence stratigraphy and long-term paleoceanographic change in the Middle and Upper Ordovician of the eastern United States. Spec. Pap.-Geol. Soc. Am. 117–130.

Holmden, C., Braun, W.K., Patterson, W.P., Eglington, B.M., Prokopiuk, T.C., Whittaker, S., 2006. Carbon isotope chemostratigraphy of Frasnian sequences in Western Canada. Sask. Geol. Surv. Summ. Investig. 1, 1–6.

Holser, W., Maynard, J., Cruikshank, K., 1989. Modelling the natural cycle of sulphur through Phanerozoic time.

Evol. Glob. Biogeochem. Sulphur Cycle Wiley N. Y. 21–56.

Holser, W.T., 1977. Catastrophic chemical events in the history of the ocean. Nature 267, 403–408.

Holser, W.T., Kaplan, I.R., 1966. Isotope geochemistry of sedimentary sulfates. Chem. Geol. 1, 93–135. https://doi.org/10.1016/0009-2541(66)90011-8

Horner, T.J., Pryer, H.V., Nielsen, S.G., Crockford, P.W., Gauglitz, J.M., Wing, B.A., Ricketts, R.D., 2017. Pelagic barite precipitation at micromolar ambient sulfate. Nat. Commun. 8, 1342. https://doi.org/10.1038/s41467-017-01229-5

Horodyski, R.J., 1993. Paleontology of Proterozoic shales and mudstones: examples from the Belt Supergroup, Chuar Group and Pahrump Group, western USA. Precambrian Res. 61, 241–278.

Hough, M.L., Shields, G.A., Evins, L.Z., Strauss, H., Henderson, R.A., Mackenzie, S., 2006. A major sulphur isotope event at c. 510 Ma: a possible anoxia–extinction–volcanism connection during the Early–Middle Cambrian transition? Terra Nova 18, 257–263. https://doi.org/10.1111/j.1365-3121.2006.00687.x

Hurtgen, M.T., Pruss, S.B., Knoll, A.H., 2009. Evaluating the relationship between the carbon and sulfur cycles in the later Cambrian ocean: An example from the Port au Port Group, western Newfoundland, Canada. Earth Planet. Sci. Lett. 281, 288–297. https://doi.org/10.1016/j.epsl.2009.02.033

Huston, D.L., Maas, R., Czarnota, K., 2007. The age and genesis of the Nifty copper deposit: back to the future. Geosci. Aust. Prof. Opin. Canberra 22.

Ireland, T., Large, R.R., McGoldrick, P., Blake, M., 2004. Spatial distribution patterns of sulfur isotopes, nodular carbonate, and ore textures in the McArthur River (HYC) Zn-Pb-Ag deposit, Northern Territory, Australia. Econ. Geol. 99, 1687–1709.

Jacquet, S.H.M., Henjes, J., Dehairs, F., Worobiec, A., Savoye, N., Cardinal, D., 2007. Particulate Ba-barite and acantharians in the Southern Ocean during the European Iron Fertilization Experiment (EIFEX). J. Geophys. Res. Biogeosciences 112. https://doi.org/10.1029/2006JG000394

Jarvis, I., Burnett, W.., Nathan, Y., Almbaydin, F. s. ., Attia, A. k. ., Castrol, L.., Flicoteaux, R., Hilmy, M.., Husain, V., Qutawnah, A., Serjani, A., Zanin, Y.., 1994. Phosphorite geochemistry: State of the art and environmental concerns. Eclogae Geol. Helvetie 87, 643–700.

Jenkyns, H.C., 1988. The early Toarcian (Jurassic) anoxic event; stratigraphic, sedimentary and geochemical evidence. Am. J. Sci. 288, 101–151. https://doi.org/10.2475/ajs.288.2.101

Jenkyns, H.C., 1980. Cretaceous anoxic events: from continents to oceans. J. Geol. Soc. 137, 171–188.

Jeppsson, L., 1990. An oceanic model for lithological and faunal changes tested on the Silurian record. J. Geol. Soc. 147, 663–674. https://doi.org/10.1144/gsjgs.147.4.0663

Jeppsson, L., 1983. Silurian conodont faunas from Gotland. Foss. Strata 15, 121–144.

John, E.H., Wignall, P.B., Newton, R.J., Bottrell, S.H., 2010. δ34SCAS and δ18OCAS records during the Frasnian–Famennian (Late Devonian) transition and their bearing on mass extinction models. Chem. Geol. 275, 221–234. https://doi.org/10.1016/j.chemgeo.2010.05.012

John, S.G., Adkins, J.F., 2010. Analysis of dissolved iron isotopes in seawater. Mar. Chem. 119, 65–76.

Johnson, C.A., Emsbo, P., Poole, F.G., Rye, R.O., 2009. Sulfur- and oxygen-isotopes in sediment-hosted stratiform barite deposits. Geochim. Cosmochim. Acta 73, 133–147. https://doi.org/10.1016/j.gca.2008.10.011

Johnson, C.A., Kelley, K.D., Leach, D.L., 2004. Sulfur and Oxygen Isotopes in Barite Deposits of the Western Brooks Range, Alaska, and Implications for the Origin of the Red Dog Massive Sulfide Deposits. Econ. Geol. 99, 1435–1448. https://doi.org/10.2113/gsecongeo.99.7.1435

Johnson, J.E., Webb, S.M., Thomas, K., Ono, S., Kirschvink, J.L., Fischer, W.W., 2013. Manganese-oxidizing photosynthesis before the rise of cyanobacteria. Proc. Natl. Acad. Sci. 110, 11238–11243. https://doi.org/10.1073/pnas.1305530110

Johnston, D.T., Gill, B.C., Masterson, A., Beirne, E., Casciotti, K.L., Knapp, A.N., Berelson, W., 2014. Placing an upper limit on cryptic marine sulphur cycling. Nature advance online publication. https://doi.org/10.1038/nature13698

Jones, B., de Ronde, C.E.J., Renaut, R.W., 2008. Mineralized microbes from Giggenbach submarine volcano. J. Geophys. Res. Solid Earth 113, B08S05. https://doi.org/10.1029/2007JB005482

Jones, D.S., Fike, D.A., 2013. Dynamic sulfur and carbon cycling through the end-Ordovician extinction revealed by paired sulfate–pyrite δ34S. Earth Planet. Sci. Lett. 363, 144–155.

Jones, D.S., Fike, D.A., Finnegan, S., Fischer, W.W., Schrag, D.P., McCay, D., 2011. Terminal Ordovician carbon isotope stratigraphy and glacioeustatic sea-level change across Anticosti Island (Québec, Canada). Geol. Soc. Am. Bull. 123, 1645–1664. https://doi.org/10.1130/b30323.1

Jørgensen, B.B., 1990. A Thiosulfate Shunt in the Sulfur Cycle of Marine Sediments. Science 249, 152–154.

Jørgensen, B.B., 1982. Mineralization of organic matter in the sea bed- the role of sulphate reduction. Nature 296, 643–645.

Jørgensen, B.B., 1979. A theoretical model of the stable sulfur isotope distribution in marine sediments. Geochim. Cosmochim. Acta 43, 363–374. https://doi.org/10.1016/0016-7037(79)90201-1

Juniper, S.K., Jonasson, I.R., Tunnicliffe, V., Southward, A.J., 1992. Influence of a tube-building polychaete on hydrothermal chimney mineralization. Geology 20, 895–898. https://doi.org/10.1130/0091-7613(1992)020<0895:ioatbp>2.3.co;2

Kah, L.C., Lyons, T.W., Frank, T.D., 2004. Low marine sulphate and protracted oxygenation of the Proterozoic biosphere. Nature 431, 834–838.

Kah, L.C., Thompson, C.K., Henderson, M.A., Zhan, R., 2016. Behavior of marine sulfur in the Ordovician.

Palaeogeogr. Palaeoclimatol. Palaeoecol. 458, 133–153. https://doi.org/10.1016/j.palaeo.2015.12.028

Kaiho, K., Kajiwara, Y., Chen, Z.-Q., Gorjan, P., 2006. A sulfur isotope event at the end of the Permian. Chem. Geol. 235, 33–47. https://doi.org/10.1016/j.chemgeo.2006.06.001

Kaiho, K., Kajiwara, Y., Nakano, T., Miura, Y., Kawahata, H., Tazaki, K., Ueshima, M., Chen, Z., Shi, G.R., 2001. End-Permian catastrophe by a bolide impact: Evidence of a gigantic release of sulfur from the mantle. Geology 29, 815–818. https://doi.org/10.1130/0091-7613(2001)029<0815:epcbab>2.0.co;2

Kaiho, K., Kajiwara, Y., Tazaki, K., Ueshima, M., Takeda, N., Kawahata, H., Arinobu, T., Ishiwatari, R., Hirai, A., Lamolda, M.A., 1999. Oceanic primary productivity and dissolved oxygen levels at the Cretaceous/Tertiary boundary: their decrease, subsequent warming, and recovery. Paleoceanography 14, 511–524.

Kamber, B.S., Whitehouse, M.J., 2007. Micro-scale sulphur isotope evidence for sulphur cycling in the late Archean shallow ocean. Geobiology 5, 5–17. https://doi.org/10.1111/j.1472-4669.2006.00091.x

Kampschulte, A., Bruckschen, P., Strauss, H., 2001. The sulphur isotopic composition of trace sulphates in Carboniferous brachiopods: implications for coeval seawater, correlation with other geochemical cycles and isotope stratigraphy. Chem. Geol. 175, 149–173. https://doi.org/10.1016/s0009-2541(00)00367-3

Kampschulte, A., Strauss, H., 2004. The sulfur isotopic evolution of Phanerozoic seawater based on the analysis of structurally substituted sulfate in carbonates. Chem. Geol. 204, 255–286. https://doi.org/10.1016/j.chemgeo.2003.11.013

Kaplan, I.R., Emery, K.O., Rittenberg, S.C., 1963. The distribution and isotopic abundance of sulphur in recent marine sediments off southern California. Geochim. Cosmochim. Acta 27, 297–331. https://doi.org/10.1016/0016-7037(63)90074-7

Kaplan, I.R., Rittenberg, S.C., 1964. Microbiological Fractionation of Sulphur Isotopes. Microbiology 34, 195–212. https://doi.org/10.1099/00221287-34-2-195

Kelley, D.S., Delaney, J.R., Yoerger, D.R., 2001a. Geology and venting characteristics of the Mothra hydrothermal field, Endeavour segment, Juan de Fuca Ridge. Geology 29, 959–962. https://doi.org/10.1130/0091-7613(2001)029<0959:GAVCOT>2.0.CO;2

Kelley, D.S., Karson, J.A., Blackman, D.K., Fruh-Green, G.L., Butterfield, D.A., Lilley, M.D., Olson, E.J., Schrenk, M.O., Roe, K.K., Lebon, G.T., Rivizzigno, P., the AT3-60 Shipboard Party, 2001b. An off-axis hydrothermal vent field near the Mid-Atlantic Ridge at 30o N. Nature 412, 145–149. https://doi.org/10.1038/35084000

Kelley, D.S., Karson, J.A., Früh-Green, G.L., Yoerger, D.R., Shank, T.M., Butterfield, D.A., Hayes, J.M.,

Schrenk, M.O., Olson, E.J., Proskurowski, G., Jakuba, M., Bradley, A., Larson, B., Ludwig, K., Glickson, D., Buckman, K., Bradley, A.S., Brazelton, W.J., Roe, K., Elend, M.J., Delacour, A., Bernasconi, S.M., Lilley, M.D., Baross, J.A., Summons, R.E., Sylva, S.P., 2005. A Serpentinite-Hosted Ecosystem: The Lost City Hydrothermal Field. Science 307, 1428–1434. https://doi.org/10.1126/science.1102556

Kelley, K.D., Leach, D.L., Johnson, C.A., Clark, J.L., Fayek, M., Slack, J.F., Anderson, V.M., Ayuso, R.A., Ridley, W.I., 2004. Textural, Compositional, and Sulfur Isotope Variations of Sulfide Minerals in the Red Dog Zn-Pb-Ag Deposits, Brooks Range, Alaska: Implications for Ore Formation. Econ. Geol. 99, 1509–1532. https://doi.org/10.2113/gsecongeo.99.7.1509

Kendall, A.C., Harwood, G.M., 1989. Shallow-Water Gypsum in the Castile Formation - Significance and Implications, in: Harris, P.M., Grover, G.A. (Eds.), Subsurface and Outcrop Examination of the Capitan Shelf Margin, Northern Delaware Basin: SEPM Core Workshop No. 13. SEPM, San Antonio, pp. 451–457.

Kerans, C., Kempter, K., 2002. Hierarchical stratigraphic analysis of a carbonate platform: Permian of the Guadalupe Mountains [CD-ROM], AAPG/Datapages Discovery Series. Bureau of Economic Geology, The University of Texas at Austin, Austin, TX.

Kerans, C., Tinker, S.W., 1999. Extrinsic stratigraphic controls on development of the Capitan Reef Complex.

Kim, S.-T., Coplen, T.B., Horita, J., 2015. Normalization of stable isotope data for carbonate minerals: Implementation of IUPAC guidelines. Geochim. Cosmochim. Acta 158, 276–289. https://doi.org/10.1016/j.gca.2015.02.011

King, P.B., 1948. Geology of the Southern Guadalupe Mountains, Texas (USGS Numbered Series No. 215), Professional Paper. U.S. Geological Survey.

King, P.B., 1942. Permian of west Texas and southeastern New Mexico in DeFord and Lloyd, eds., West Texas-New Mexico symposium. AAPG Bull. 26, 535–763.

King, P.B., Newell, N.D., 1956. McCombs Limestone Member of Bell Canyon Formation, Guadalupe Mountains, Texas: GEOLOGICAL NOTES. AAPG Bull. 40, 386–387.

Kirkland, D.W., Denison, R.E., Dean, W.E., 2000. Parent Brine of the Castile Evaporites (Upper Permian), Texas and New Mexico. J. Sediment. Res. 70, 749. https://doi.org/10.1306/2DC40935-0E47-11D7-8643000102C1865D

Kontrec, J., Kralj Damir, Brečević Ljerka, Falini Giuseppe, Fermani Simona, Noethig-Laslo Vesna, Mirosavljević Krunoslav, 2004. Incorporation of Inorganic Anions in Calcite. Eur. J. Inorg. Chem. 2004, 4579–4585. https://doi.org/10.1002/ejic.200400268

Korte, C., Jasper, T., Kozur, H.W., Veizer, J., 2005. δ18O and δ13C of Permian brachiopods: A record of seawater evolution and continental glaciation. Palaeogeogr. Palaeoclimatol.

Palaeoecol. 224, 333–351. https://doi.org/10.1016/j.palaeo.2005.03.015

Koski, R.A., Jonasson, I.R., Kadko, D.C., Smith, V.K., Wong, F.L., 1994. Compositions, growth mechanisms, and temporal relations of hydrothermal sulfide-sulfate-silica chimneys at the northern Cleft segment, Juan de Fuca Ridge. J. Geophys. Res. Solid Earth 99, 4813–4832. https://doi.org/10.1029/93JB02871

Kozdon, R., Kita, N.T., Huberty, J.M., Fournelle, J.H., Johnson, C.A., Valley, J.W., 2010. In situ sulfur isotope analysis of sulfide minerals by SIMS: Precision and accuracy, with application to thermometry of ~3.5Ga Pilbara cherts. Chem. Geol. 275, 243–253. https://doi.org/10.1016/j.chemgeo.2010.05.015

Kumar, S., 1995. Megafossils from the Mesoproterozoic Rohtas Formation (the Vindhyan Supergroup), Katni area, central India. Precambrian Res. 72, 171–184. https://doi.org/10.1016/0301-9268(94)00085-6

Kump, L.R., 1989. Alternative modeling approaches to the geochemical cycles of carbon, sulfur, and strontium isotopes. Am J Sci 289, 390–410.

Kump, L.R., Arthur, M.A., Patzkowsky, M.E., Gibbs, M.T., Pinkus, D.S., Sheehan, P.M., 1999. A weathering hypothesis for glaciation at high atmospheric pCO2 during the Late Ordovician. Palaeogeogr. Palaeoclimatol. Palaeoecol. 152, 173–187. https://doi.org/10.1016/S0031-0182(99)00046-2

Kump, L.R., Garrels, R.M., 1986. Modeling atmospheric O 2 in the global sedimentary redox cycle. Am. J. Sci. 286, 337–360. https://doi.org/10.2475/ajs.286.5.337

Kurtz, A.C., Kump, L.R., Arthur, M.A., Zachos, J.C., Paytan, A., 2003. Early Cenozoic decoupling of the global carbon and sulfur cycles. Paleoceanography 18, 1090. https://doi.org/10.1029/2003PA000908

Lambert, L.L., Wardlaw, B.R., Nestell, M.K., Nestell, G.P., 2002. Latest Guadalupian (Middle Permian) conodonts and foraminifers from West Texas. Micropaleontology 48, 343–364. https://doi.org/10.1661/0026-2803(2002)048[0343:LGMPCA]2.0.CO;2

Lang, W.B., 1937. The Permian Formations of the Pecos Valley of New Mexico and Texas. AAPG Bull. 21, 833–898.

Large, R.R., Bull, S.W., Cooke, D.R., McGoldrick, P.J., 1998. A genetic model for the H.Y.C. Deposit, Australia; based on regional sedimentology, geochemistry, and sulfide-sediment relationships. Econ. Geol. 93, 1345–1368. https://doi.org/10.2113/gsecongeo.93.8.1345

Large, R.R., Bull, S.W., McGoldrick, P.J., Walters, S., 2005. Stratiform and strata-bound Zn-Pb-Ag deposits in Proterozoic sedimentary basins, northern Australia. Econ. Geol. 100, 931–963.

Larter, R.C.L., Boyce, A.J., Russell, M.J., 1981. Hydrothermal pyrite chimneys from the Ballynoe baryte deposit, Silvermines, County Tipperary, Ireland. Miner. Deposita 16, 309–317. https://doi.org/10.1007/BF00202742

Leach, D., Marsh, E., Bradley, D., Gardoll, S., Huston, D., 2005. The distribution of SEDEX Pb-Zn deposits through Earth history, in: Mao, J., Bierlein, F. (Eds.), Mineral Deposit Research: Meeting the Global Challenge. Springer Berlin Heidelberg, pp. 145–148. https://doi.org/10.1007/3-540-27946-6_38

Leach, D.L., Bradley, D.C., Huston, D., Pisarevsky, S.A., Taylor, R.D., Gardoll, S.J., 2010. Sediment-hosted lead-zinc deposits in Earth history. Econ. Geol. 105, 593–625.

Lees, J.M., 2014. RFOC: Graphics for Spherical Distributions and Earthquake Focal Mechanisms. R package version 3.3-3 156.

Leslie, A.B., Harwood, G.M., Kendall, A.C., 1997. Geochemical variations within a laminated evaporite deposit: evidence for brine composition during formation of the Permian Castile Formation, Texas and New Mexico, USA. Sediment. Geol. 110, 223–235. https://doi.org/10.1016/S0037-0738(96)00087-5

Li, J., Kusky, T.M., 2007. World's largest known Precambrian fossil black smoker chimneys and associated microbial vent communities, North China: Implications for early life. Gondwana Res. 12, 84–100. https://doi.org/10.1016/j.gr.2006.10.024

Li, P., Huang, J., Chen, M., Bai, X., 2009. Coincident negative shifts in sulfur and carbon isotope compositions prior to the end-Permian mass extinction at Shangsi Section of Guangyuan, South China. Front. Earth Sci. China 3, 51–56. https://doi.org/10.1007/s11707-009-0018-4

Lin, T.J., Ver Eecke, H.C., Breves, E.A., Dyar, M.D., Jamieson, J.W., Hannington, M.D., Dahle, H., Bishop, J.L., Lane, M.D., Butterfield, D.A., Kelley, D.S., Lilley, M.D., Baross, J.A., Holden, J.F., 2016. Linkages between mineralogy, fluid chemistry, and microbial communities within hydrothermal chimneys from the Endeavour Segment, Juan de Fuca Ridge. Geochem. Geophys. Geosystems 17, 300–323. https://doi.org/10.1002/2015GC006091

Little, C.T., Herrington, R.J., Maslennikov, V.V., Morris, N.J., Zaykov, V.V., 1997. Silurian hydrothermal-vent community from the southern Urals, Russia. Nature 385, 146.

Little, C.T.S., Cann, J.R., Herrington, R.J., Morisseau, M., 1999a. Late Cretaceous hydrothermal vent communities from the Troodos ophiolite, Cyprus. Geology 27, 1027–1030. https://doi.org/10.1130/0091-7613(1999)027<1027:lchvcf>2.3.co;2

Little, C.T.S., Herrington, R.J., Haymon, R.M., Danelian, T., 1999b. Early Jurassic hydrothermal vent community from the Franciscan Complex, San Rafael Mountains, California. Geology 27, 167–170. https://doi.org/10.1130/0091-7613(1999)027<0167:ejhvcf>2.3.co;2

Little, C.T.S., Herrington, R.J., Maslennikov, V.V., Zaykov, V.V., 1998. The fossil record of hydrothermal vent communities, in: Mills, R., Harrison, K. (Eds.), Modern Ocean Floor Processes and the Geological Record, Special Publication. Geological Society, London, pp.

259–270. https://doi.org/10.1144/GSL.SP.1998.148.01.14

Love, L.G., 1971. Early diagenetic polyframboidal pyrite, primary and redeposited, from the Wenlockian Denbigh Grit Group, Conway, North Wales, U.K. J. Sediment. Res. 41, 1038–1044. https://doi.org/10.1306/74d723ec-2b21-11d7-8648000102c1865d

Lowenstein, T.K., Hardie, L.A., 2006. Criteria for the recognition of salt-pan evaporites. Sedimentology 32, 627–644. https://doi.org/10.1111/j.1365-3091.1985.tb00478.x

Loyd, S.J., Berelson, W.M., Lyons, T.W., Hammond, D.E., Corsetti, F.A., 2012a. Constraining pathways of microbial mediation for carbonate concretions of the Miocene Monterey Formation using carbonate-associated sulfate. Geochim. Cosmochim. Acta 78, 77–98. https://doi.org/10.1016/j.gca.2011.11.028

Loyd, S.J., Dickson, J.A.D., Scholle, P.A., Tripati, A.K., 2013. Extensive, uplift-related and non-fault-controlled spar precipitation in the Permian Capitan Formation. Sediment. Geol. 298, 17–27. https://doi.org/10.1016/j.sedgeo.2013.10.001

Loyd, S.J., Marenco, P.J., Hagadorn, J.W., Lyons, T.W., Kaufman, A.J., Sour-Tovar, F., Corsetti, F.A., 2012b. Sustained low marine sulfate concentrations from the Neoproterozoic to the Cambrian: Insights from carbonates of northwestern Mexico and eastern California. Earth Planet. Sci. Lett. 339–340, 79–94. https://doi.org/10.1016/j.epsl.2012.05.032

Lu, F.H., Meyers, W.J., 2003. Sr, S, and OSO4 Isotopes and the Depositional Environments of the Upper Miocene Evaporites, Spain. J. Sediment. Res. 73, 444–450. https://doi.org/10.1306/093002730444

Ludwig, K.A., Kelley, D.S., Butterfield, D.A., Nelson, B.K., Früh-Green, G., 2006. Formation and evolution of carbonate chimneys at the Lost City Hydrothermal Field. Geochim. Cosmochim. Acta 70, 3625–3645.

Luepke, J.J., Lyons, T.W., 2001. Pre-Rodinian (Mesoproterozoic) supercontinental rifting along the western margin of Laurentia: geochemical evidence from the Belt-Purcell Supergroup. Precambrian Res. 111, 79–90. https://doi.org/10.1016/S0301-9268(01)00157-7

Luo, G., Ono, S., Huang, J., Algeo, T.J., Li, C., Zhou, L., Robinson, A., Lyons, T.W., Xie, S., 2015. Decline in oceanic sulfate levels during the early Mesoproterozoic. Precambrian Res. 258, 36–47. https://doi.org/10.1016/j.precamres.2014.12.014

Lydon, J.W., 1996. Sedimentary exhalative sulphides (SEDEX), in: Eckstrand, O.R., Sinclair, W.D., Thorpe, R.I. (Eds.), Geology of Canadian Mineral Deposit Types. Geological Survey of Canada, Geology of Canada, no. 8, pp. 130–152.

Lyons, T.W., Frank, T.D., Schreiber, M.E., Winston, D., Lohmann, K.C., 1993. Geochemical Constraints on Paleoenvironments within the Belt Supergroup (Middle Proterozoic), Montana, in: Berg, R.B. (Ed.), Special Publication 112: Belt Symposium III.

Montana Bureau of Mines and Geology, Whitefish, Montana, pp. 190–201.

Lyons, T.W., Gellatly, A.M., McGoldrick, P.J., Kah, L.C., 2006. Proterozoic sedimentary exhalative (SEDEX) deposits and links to evolving global ocean chemistry. Mem.-Geol. Soc. Am. 198, 169–184.

Lyons, T.W., Luepke, J.J., Schreiber, M.E., Zieg, G.A., 2000. Sulfur geochemical constraints on Mesoproterozoic restricted marine deposition: lower Belt Supergroup, northwestern United States. Geochim. Cosmochim. Acta 64, 427–437. https://doi.org/10.1016/S0016-7037(99)00323-3

Lyons, T.W., Walter, L.M., Gellatly, A.M., Martini, A.M., Blake, R.E., 2004. Sites of anomalous organic remineralization in the carbonate sediments of South Florida, USA: The sulfur cycle and carbonate-associated sulfate, in: Sulfur Biogeochemistry - Past and Present: Geological Society of America Special Paper 379. pp. 161–176.

Marenco, P.J., Corsetti, F.A., Hammond, D.E., Kaufman, A.J., Bottjer, D.J., 2008a. Oxidation of pyrite during extraction of carbonate associated sulfate. Chem. Geol. 247, 124–132.

Marenco, P.J., Corsetti, F.A., Kaufman, A.J., Bottjer, D.J., 2008b. Environmental and diagenetic variations in carbonate associated sulfate: An investigation of CAS in the Lower Triassic of the western USA. Geochim. Cosmochim. Acta 72, 1570–1582.

Marenco, P.J., Marenco, K.N., Lubitz, R.L., Niu, D., 2013. Contrasting long-term global and short-term local redox proxies during the Great Ordovician Biodiversification Event: A case study from Fossil Mountain, Utah, USA. Palaeogeogr. Palaeoclimatol. Palaeoecol. 377, 45–51. https://doi.org/10.1016/j.palaeo.2013.03.007

Marenco, P.J., Martin, K.R., Marenco, K.N., Barber, D.C., 2016. Increasing global ocean oxygenation and the Ordovician Radiation: Insights from Th/U of carbonates from the Ordovician of western Utah. Palaeogeogr. Palaeoclimatol. Palaeoecol. 458, 77–84. https://doi.org/10.1016/j.palaeo.2016.05.014

Marin-Carbonne, J., Rollion-Bard, C., Bekker, A., Rouxel, O., Agangi, A., Cavalazzi, B., Wohlgemuth-Ueberwasser, C.C., Hofmann, A., McKeegan, K.D., 2014. Coupled Fe and S isotope variations in pyrite nodules from Archean shale. Earth Planet. Sci. Lett. 392, 67–79. https://doi.org/10.1016/j.epsl.2014.02.009

Mazumdar, A., Goldberg, T., Strauss, H., 2008. Abiotic oxidation of pyrite by Fe(III) in acidic media and its implications for sulfur isotope measurements of lattice-bound sulfate in sediments. Chem. Geol. 253, 30–37. https://doi.org/10.1016/j.chemgeo.2008.03.014

Mazzullo, S.J., 1999. Paleoenvironments, Cyclicity, and Diagenesis in the Outer Shelf Tansill Formation in the Carlsbad Embayment (Dark Canyon), Northern Guadalupe Mountains, New Mexico.

Mazzullo, S.J., 1980. Calcite pseudospar replacive of marine acicular aragonite, and implications for aragonite cement diagenesis. J. Sediment. Res. 50, 409–422.

https://doi.org/10.1306/212f7a18-2b24-11d7-8648000102c1865d

Mazzullo, S.J., Cys, J.M., 1977. Submarine cements in Permian boundstones and reef-associated rocks, Guadalupe Mountains, west Texas and southeastern New Mexico, in: Hileman, M.E., Mazzullo, S.J. (Eds.), Upper Guadalupian Facies, Permian Reef Complex, Guadalupe Mountains, New Mexico and West Texas, 1977 Field Conference Guidebook, v. 1, Permian Basin Section SEPM, Publication 77-16. Permian Basin Section SEPM, Midland, TX, pp. 151–200.

McGoldrick, P., 1999. Northern Australian'Sedex'deposits: microbial oases in Proterozoic seas, in: Stanley, C. (Ed.), Mineral Deposits: Processes to Processing. Presented at the Fifth Biennial SGA Meeting and Tenth Quadrennial International Association on the Genesis of Ore Deposits Symposium, CRC Press, Rotterdam, pp. 885–888.

McGoldrick, P., 1998. Halo model for the Grevillea Prospect, in: Leaman, D., Bull, S., Winefield, P., Selley, D., Scott, R., Cooke, D., McGoldrick, P., Large, R., Garven, G. (Eds.), Sediment-Hosted Base Metal Deposits: Project Outcomes Report. AMIRA/ARC Project P384A. Center for Ore Deposit Research (CODES SRC), University of Tasmania, Hobart, Tasmania, pp. 157–167.

McGoldrick, P., Zieg, J., 2004. Massive microbes from the MesoProterozoic of Montana? Presented at the Geological Society of Australia Abstracts, p. 100.

Mekhtiyeva, V., 1974. Sulfur isotopic composition of fossil molluscan shells as an indicator of hydrochemical conditions in ancient basins. Geochem. Int. 11, 1188–1192.

Melim, L.A., Scholle, P.A., 2002. Dolomitization of the Capitan Formation forereef facies (Permian, west Texas and New Mexico): seepage reflux revisited. Sedimentology 49, 1207–1227. https://doi.org/10.1046/j.1365-3091.2002.00492.x

Melim, L.A., Scholle, P.A., 1999. Diagenesis of the Capitan Formation forereef facies (Permian, west Texas and New Mexico), in: Geologic Framework of the Capitan Reef.

Meybeck, M., 2003. Global occurrence of major elements in rivers. Treatise Geochem. 5, 207–223.

Mills, J.V., Gomes, M.L., Kristall, B., Sageman, B.B., Jacobson, A.D., Hurtgen, M.T., 2017. Massive volcanism, evaporite deposition, and the chemical evolution of the Early Cretaceous ocean. Geology 45, 475–478. https://doi.org/10.1130/G38667.1

Moore, D.W., Young, L.E., Modene, J.S., Plahuta, J.T., 1986. Geologic setting and genesis of the Red Dog zinc-lead-silver deposit, western Brooks Range, Alaska. Econ. Geol. 81, 1696–1727. https://doi.org/10.2113/gsecongeo.81.7.1696

Mruk, D.H., 1989. Diagenesis of the Capitan limestone, upper Permian, McKittrick canyon, west Texas, in: Harris, P.M., Grover, G.A. (Eds.), Subsurface and Outcrop Examination of the Capitan Shelf Margin, Northern Delaware Basin: SEPM Core Workshop No. 13. SEPM, San Antonio, pp. 387–406.

Munnecke, A., Samtleben, C., Bickert, T., 2003. The Ireviken Event in the

lower Silurian of Gotland, Sweden – relation to similar Palaeozoic and Proterozoic events. Palaeogeogr. Palaeoclimatol. Palaeoecol. 195, 99–124. https://doi.org/10.1016/S0031-0182(03)00304-3

Murowchick, J.B., Barnes, H.L., 1986. Marcasite precipitation from hydrothermal solutions. Geochim. Cosmochim. Acta 50, 2615–2629. https://doi.org/10.1016/0016-7037(86)90214-0

Mutti, M., Simo, J.A., 1994. Distribution, petrography and geochemistry of early dolomite in cyclic shelf facies, Yates Formation (Guadalupian), Captain Reef Complex, USA, in: Purser, B., Tucker, M., Zenger, D. (Eds.), Dolomites, Special Publication of the International Association of Sedimentologists. Blackwell Scientific, Oxford, pp. 91–107.

Mutti, M., Simo, J.A., 1993. Stratigraphic Patterns and Cycle-Related Diagenesis of Upper Yates Formation, Permian, Guadalupe Mountains, in: Loucks, R.G., Sarg, J.F. (Eds.), Carbonate Sequence Stratigraphy: Recent Developments and Applications, AAPG Memoir. The American Association of Petroleum Geologists, Tulsa, Oklahoma, pp. 515–534.

Neese, D.A., Schwartz, A.H., 1977. Origin of the pisolite facies of the shelf crest, in: Hileman, M.E., Mazzullo, S.J. (Eds.), Upper Guadalupian Facies, Permian Reef Complex, Guadalupe Mountains, New Mexico and West Texas, 1977 Field Conference Guidebook, v. 1, Permian Basin Section SEPM, Publication 77-16. Permian Basin Section SEPM, Midland, TX, pp. 437–450.

Newell, N.D., Rigby, J.K., Fischer, A.G., Whiteman, A.J., Hickox, J.E., Bradley, J.S., 1953. The Permian Reef Complex of the Guadalupe Mountains Region, Texas and New Mexico: A Study in Paleoecology. W. H. Freeman & Company, San Francisco, CA.

Newton, R.J., Pevitt, E.L., Wignall, P.B., Bottrell, S.H., 2004. Large shifts in the isotopic composition of seawater sulphate across the Permo–Triassic boundary in northern Italy. Earth Planet. Sci. Lett. 218, 331–345. https://doi.org/10.1016/S0012-821X(03)00676-9

Newton, R.J., Reeves, E.P., Kafousia, N., Wignall, P.B., Bottrell, S.H., Sha, J., 2011. Low marine sulfate concentrations and the isolation of the European epicontinental sea during the Early Jurassic. Geology 39, 7–10. https://doi.org/10.1130/g31326.1

Nielsen, He., 1989. Local and global aspects of the sulphur isotope age curve of oceanic sulphate. Evol. Glob. Biogeochem. Sulphur Cycle Wiley N. Y. 57–64.

Oehler, J.H., Logan, R.G., 1977. Microfossils, cherts, and associated mineralization in the Proterozoic McArthur (H.Y.C.) lead-zinc-silver deposit. Econ. Geol. 72, 1393–1409. https://doi.org/10.2113/gsecongeo.72.8.1393

Ohkouchi, N., Kawamura, K., Kajiwara, Y., Wada, E., Okada, M., Kanamatsu, T., Taira, A., 1999. Sulfur isotope records around Livello Bonarelli (northern Apennines, Italy) black shale at the Cenomanian-Turonian boundary. Geology 27, 535–538. https://doi.org/10.1130/0091-7613(1999)027<0535:siralb>2.3.co;2

Okumura, T., Ohara, Y., Stern, R., Yamanaka, T., Onishi, Y., Watanabe, H., Chen, C., Bloomer, S., Pujana, I., Sakai, S., 2016. Brucite chimney formation and carbonate alteration at the Shinkai Seep Field, a serpentinite-hosted vent system in the southern Mariana forearc. Geochem. Geophys. Geosystems 17, 3775–3796. https://doi.org/10.1002/2016GC006449

Osleger, D.A., 1998. Sequence architecture and sea-level dynamics of Upper Permian shelfal facies, Guadalupe Mountains, southern New Mexico. J. Sediment. Res. 68, 327–346. https://doi.org/10.2110/jsr.68.327

Osleger, D.A., Tinker, S.W., 1999. Three-Dimensional Architecture of Upper Permian High-Frequency Sequences, Yates-Capitan Shelf Margin, Permian Basin, U.S.A., in: Harris, P.M. (Mitch), Simo, J.A. (Toni) (Eds.), Advances in Carbonate Sequence StratigraphyApplication to Reservoirs, Outcrops and Models. Geological Society of America.

Owens, J.D., Gill, B.C., Jenkyns, H.C., Bates, S.M., Severmann, S., Kuypers, M.M.M., Woodfine, R.G., Lyons, T.W., 2013. Sulfur isotopes track the global extent and dynamics of euxinia during Cretaceous Oceanic Anoxic Event 2. Proc. Natl. Acad. Sci. 110, 18407–18412. https://doi.org/10.1073/pnas.1305304110

Pancost, R.D., Freeman, K.H., Patzkowsky, M.E., 1999. Organic-matter source variation and the expression of a late Middle Ordovician carbon isotope excursion. Geology 27, 1015. https://doi.org/10.1130/0091-7613(1999)027<1015:OMSVAT>2.3.CO;2

Paris, G., Adkins, J.F., Sessions, A.L., Webb, S.M., Fischer, W.W., 2014a. Neoarchean carbonate–associated sulfate records positive Δ33S anomalies. Science 346, 739–741. https://doi.org/10.1126/science.1258211

Paris, G., Fehrenbacher, J.S., Sessions, A.L., Spero, H.J., Adkins, J.F., 2014b. Experimental determination of carbonate-associated sulfate δ34S in planktonic foraminifera shells. Geochem. Geophys. Geosystems 15, 1452–1461. https://doi.org/10.1002/2014GC005295

Paris, G., Sessions, A.L., Subhas, A.V., Adkins, J.F., 2013. MC-ICP-MS measurement of δ34S and Δ33S in small amounts of dissolved sulfate. Chem. Geol. 345, 50–61. https://doi.org/10.1016/j.chemgeo.2013.02.022

Patzkowsky, M.E., Slupik, L.M., Arthur, M.A., Pancost, R.D., Freeman, K.H., 1997. Late Middle Ordovician environmental change and extinction: Harbinger of the Late Ordovician or continuation of Cambrian patterns? Geology 25, 911. https://doi.org/10.1130/0091-7613(1997)025<0911:LMOECA>2.3.CO;2

Paytan, A., Kastner, M., Campbell, D., Thiemens, M.H., 2004. Seawater Sulfur Isotope Fluctuations in the Cretaceous. Science 304, 1663–1665. https://doi.org/10.1126/science.1095258

Paytan, A., Kastner, M., Campbell, D., Thiemens, M.H., 1998. Sulfur Isotopic Composition of Cenozoic Seawater Sulfate. Science 282, 1459–

1462. https://doi.org/10.1126/science.282.5393.1459

Paytan, A., Kastner, M., Martin, E.E., Macdougall, J.D., Herbert, T., 1993. Marine barite as a monitor of seawater strontium isotope composition. Nature 366, 445–449.

Paytan, A., Mearon, S., Cobb, K., Kastner, M., 2002. Origin of marine barite deposits: Sr and S isotope characterization. Geology 30, 747–750. https://doi.org/10.1130/0091-7613(2002)030<0747:oombds>2.0.co;2

Perrin, J., Rivard, C., Vielzeuf, D., Laporte, D., Fonquernie, C., Ricolleau, A., Cotte, M., Floquet, N., 2017. The coordination of sulfur in synthetic and biogenic Mg calcites: The red coral case. Geochim. Cosmochim. Acta 197, 226–244. https://doi.org/10.1016/j.gca.2016.10.017

Pingitore, J., Nicholas E., Meitzner, G., Love, K.M., 1995. Identification of sulfate in natural carbonates by x-ray absorption spectroscopy. Geochim. Cosmochim. Acta 59, 2477–2483. https://doi.org/10.1016/0016-7037(95)00142-5

Pisarchik, Y.K., Golubchina, M.N., 1975. On isotope ratios of sulfur in the Cambrian sulfatic limestones of the Siberian platform. Geochem. Int. 12, 227–230.

Pisarchik, Y.K., Golubchina, M.N., Toksubayev, A.I., 1977. Isotopic composition of sulfur in calcium sulfates from the Cambrina Upper Lena Formation (Siberian Platform). Geochem. Int. 14, 182–185.

Planavsky, N.J., McGoldrick, P., Scott, C.T., Li, C., Reinhard, C.T., Kelly, A.E., Chu, X., Bekker, A., Love, G.D., Lyons, T.W., 2011. Widespread iron-rich conditions in the mid-Proterozoic ocean. Nature 477, 448–451.

Playà, E., Cendón, D.I., Travé, A., Chivas, A.R., García, A., 2007. Non-marine evaporites with both inherited marine and continental signatures: The Gulf of Carpentaria, Australia, at ~70 ka. Sediment. Geol. 201, 267–285. https://doi.org/10.1016/j.sedgeo.2007.05.010

Pope, M.C., Read, J.F., 1997. High-Resolution Stratigraphy of the Lexington Limestone (Late Middle Ordovician), Kentucky, U.S.A.: A Cool-Water Carbonate-Clastic Ramp in a Tectonic Ally Active Foreland Basin, in: James, N.P., Clarke, J.A.D. (Eds.), Cool-Water Carbonates, Special Publication. SEPM (Society for Sedimentary Geology), Tulsa, Oklahoma, pp. 411–429.

Popp, B., 1986. The record of carbon, oxygen, sulfur, and strontium isotopes and trace elements in late Paleozoic brachiopods [Ph. D. thesis]: Urbana.

Poulton, S.W., Henkel, S., März, C., Urquhart, H., Flögel, S., Kasten, S., Damsté, J.S.S., Wagner, T., 2015. A continental-weathering control on orbitally driven redox-nutrient cycling during Cretaceous Oceanic Anoxic Event 2. Geology 43, 963–966. https://doi.org/10.1130/G36837.1

Powell, T.G., Macqueen, R.W., 1984. Precipitation of Sulfide Ores and Organic Matter: Sulfate Reactions at Pine Point, Canada. Science 224, 63. https://doi.org/10.1126/science.224.4644.63

Present, T.M., Paris, G., Burke, A., Fischer, W.W., Adkins, J.F., 2015. Large

Carbonate Associated Sulfate isotopic variability between brachiopods, micrite, and other sedimentary components in Late Ordovician strata. Earth Planet. Sci. Lett. 432, 187–198. https://doi.org/10.1016/j.epsl.2015.10.005

Price, F.T., Shieh, Y.N., 1979. Fractionation of sulfur isotopes during laboratory synthesis of pyrite at low temperatures. Chem. Geol. 27, 245–253. https://doi.org/10.1016/0009-2541(79)90042-1

R Core Team, 2015. R: A language and environment for statistical computing. R Foundation for Statistical Computing, Vienna, Austria.

Raab, M., Spiro, B., 1991. Sulfur isotopic variations during seawater evaporation with fractional crystallization. Chem. Geol. Isot. Geosci. Sect. 86, 323–333. https://doi.org/10.1016/0168-9622(91)90014-N

Raven, M.R., Sessions, A.L., Fischer, W.W., Adkins, J.F., 2016. Sedimentary pyrite δ34S differs from porewater sulfide in Santa Barbara Basin: Proposed role of organic sulfur. Geochim. Cosmochim. Acta 186, 120–134. https://doi.org/10.1016/j.gca.2016.04.037

Rees, C.E., Jenkins, W.J., Monster, J., 1978. The sulphur isotopic composition of ocean water sulphate. Geochim. Cosmochim. Acta 42, 377–381. https://doi.org/10.1016/0016-7037(78)90268-5

Reitner, J., Peckmann, J., Reimer, A., Schumann, G., Thiel, V., 2005. Methane-derived carbonate build-ups and associated microbial communities at cold seeps on the lower Crimean shelf (Black Sea). Facies 51, 66–79. https://doi.org/10.1007/s10347-005-0059-4

Rennie, V.C.F., Paris, G., Sessions, A.L., Abramovich, S., Turchyn, A.V., Adkins, J.F., 2018. A novel Cenozoic record of seawater sulfur isotopes from foramiferal calcite. Nat. Geosci.

Rennie, V.C.F., Turchyn, A.V., 2014. The preservation of and in carbonate-associated sulfate during marine diagenesis: A 25 Myr test case using marine sediments. Earth Planet. Sci. Lett. 395, 13–23. https://doi.org/10.1016/j.epsl.2014.03.025

Riccardi, A.L., Arthur, M.A., Kump, L.R., 2006. Sulfur isotopic evidence for chemocline upward excursions during the end-Permian mass extinction. Geochim. Cosmochim. Acta 70, 5740–5752.

Rickard, D., 1995. Kinetics of FeS precipitation: Part 1. Competing reaction mechanisms. Geochim. Cosmochim. Acta 59, 4367–4379. https://doi.org/10.1016/0016-7037(95)00251-T

Rickard, D., Luther, G.W., 1997. Kinetics of pyrite formation by the H2S oxidation of iron (II) monosulfide in aqueous solutions between 25 and 125°C: The mechanism. Geochim. Cosmochim. Acta 61, 135–147. https://doi.org/10.1016/S0016-7037(96)00322-5

Rodgers, J., 1971. The Taconic Orogeny. Geol. Soc. Am. Bull. 82, 1141. https://doi.org/10.1130/0016-7606(1971)82[1141:TTO]2.0.CO;2

Rohrlach, B.D., Fu, M., Clarke, J.D.A., 1998. Geological setting, paragenesis and fluid history of the Walford Creek Zn-Pb-Cu-Ag prospect, Mt Isa

Basin, Australia. Aust. J. Earth Sci. 45, 63–81. https://doi.org/10.1080/08120099808728367

Rohrssen, M., Love, G.D., Fischer, W., Finnegan, S., Fike, D.A., 2013. Lipid biomarkers record fundamental changes in the microbial community structure of tropical seas during the Late Ordovician Hirnantian glaciation. Geology 41, 127–130. https://doi.org/10.1130/g33671.1

Root, S., Onasch, C.M., 1999. Structure and tectonic evolution of the transitional region between the central Appalachian foreland and interior cratonic basins. Tectonophysics 305, 205–223. https://doi.org/10.1016/S0040-1951(99)00022-0

Rush, J., Kerans, C., 2010. Stratigraphic Response Across a Structurally Dynamic Shelf: The Latest Guadalupian Composite Sequence at Walnut Canyon, New Mexico, U.S.A. J. Sediment. Res. 80, 808–828. https://doi.org/10.2110/jsr.2010.073

Russell, M., Solomon, M., Walshe, J., 1981. The genesis of sediment-hosted, exhalative zinc+ lead deposits. Miner. Deposita 16, 113–127.

Russell, M.J., Hall, A., 1997. The emergence of life from iron monosulphide bubbles at a submarine hydrothermal redox and pH front. J. Geol. Soc. 154, 377–402.

Russell, M.J., Hall, A.J., Turner, D., 1989. In vitro growth of iron sulphide chimneys: possible culture chambers for origin-of-life experiments. Terra Nova 1, 238–241. https://doi.org/10.1111/j.1365-3121.1989.tb00364.x

Ryan, W.B.F., Carbotte, S.M., Coplan, J.O., O'Hara, S., Melkonian, A., Arko, R., Weissel, R.A., Ferrini, V., Goodwillie, A., Nitsche, F., Bonczkowski, J., Zemsky, R., 2009. Global Multi-Resolution Topography synthesis. Geochem. Geophys. Geosystems 10. https://doi.org/10.1029/2008GC002332

Sakai, H., 1972. Oxygen isotopic ratios of some evaporites from Precambrian to Recent ages. Earth Planet. Sci. Lett. 15, 201–205. https://doi.org/10.1016/0012-821X(72)90061-1

Saltzman, M.R., Young, S.A., 2005. Long-lived glaciation in the Late Ordovician? Isotopic and sequence-stratigraphic evidence from western Laurentia. Geology 33, 109–112.

Samson, I.M., Russell, M.J., 1987. Genesis of the Silvermines zinc-lead-barite deposit, Ireland; fluid inclusion and stable isotope evidence. Econ. Geol. 82, 371–394.

Samtleben, C., Munnecke, A., Bickert, T., Pätzold, J., 1996. The Silurian of Gotland (Sweden): facies interpretation based on stable isotopes in brachiopod shells. Geol. Rundsch. 85, 278–292. https://doi.org/10.1007/BF02422234

Sangster, D.F., 2002. The role of dense brines in the formation of vent-distal sedimentary-exhalative (SEDEX) lead–zinc deposits: field and laboratory evidence. Miner. Deposita 37, 149–157. https://doi.org/10.1007/s00126-001-0216-9

Sarg, J.F., 1981. Petrology of the carbonate-evaporite facies transition of the Seven Rivers Formation (Guadalupian, Permian), southeast New Mexico. J. Sediment. Res. 51.

Schieber, J., 2011. Marcasite in Black Shales—a Mineral Proxy for Oxygenated Bottom Waters and Intermittent Oxidation of Carbonaceous Muds. J. Sediment. Res. 81, 447–458. https://doi.org/10.2110/jsr.2011.41

Schieber, J., 1990. Pyritic shales and microbial mats: Significant factors in the genesis of stratiform Pb-Zn deposits of the Proterozoic? Miner. Deposita 25, 7–14.

Schieber, J., 1989a. Pyrite mineralization in microbial mats from the mid-Proterozoic Newland Formation, Belt Supergroup, Montana, USA. Sediment. Geol. 64, 79–90.

Schieber, J., 1989b. The origin of the Neihart Quartzite, a basal deposit of the mid-Proterozoic Belt Supergroup, Montana, USA. Geol. Mag. 126, 271–281.

Schieber, J., 1989c. Facies and origin of shales from the mid-Proterozoic Newland Formation, Belt Basin, Montana, USA. Sedimentology 36, 203–219.

Schippers, A., Jørgensen, B.B., 2002. Biogeochemistry of pyrite and iron sulfide oxidation in marine sediments. Geochim. Cosmochim. Acta 66, 85–92. https://doi.org/10.1016/S0016-7037(01)00745-1

Schmalz, R.F., 1969. Deep-Water Evaporite Deposition: A Genetic Model. AAPG Bull. 53, 798–823.

Schmidt, V., 1977. Inorganic and organic reef growth and subsequent diagenesis in the Permian Capitan Reef Complex, Guadalupe Mountains, Texas, New Mexico, in: Hileman, M.E., Mazzullo, S.J. (Eds.), Upper Guadalupian Facies, Permian Reef Complex, Guadalupe Mountains, New Mexico and West Texas, 1977 Field Conference Guidebook, v. 1, Permian Basin Section SEPM, Publication 77-16. Permian Basin Section SEPM, Midland, TX, pp. 93–131.

Schobben, M., Stebbins, A., Algeo, T.J., Strauss, H., Leda, L., Haas, J., Struck, U., Korn, D., Korte, C., 2017a. Volatile earliest Triassic sulfur cycle: A consequence of persistent low seawater sulfate concentrations and a high sulfur cycle turnover rate? Palaeogeogr. Palaeoclimatol. Palaeoecol., The Palaeozoic-Mesozoic Transition in South China: Oceanic Environments and Life from Late Permian to Late Triassic 486, 74–85. https://doi.org/10.1016/j.palaeo.2017.02.025

Schobben, M., Stebbins, A., Algeo, T.J., Strauss, H., Leda, L., Haas, J., Struck, U., Korn, D., Korte, C., 2017b. Volatile earliest Triassic sulfur cycle: A consequence of persistent low seawater sulfate concentrations and a high sulfur cycle turnover rate? Palaeogeogr. Palaeoclimatol. Palaeoecol. https://doi.org/10.1016/j.palaeo.2017.02.025

Schobben, M., Stebbins, A., Ghaderi, A., Strauss, H., Korn, D., Korte, C., 2015. Flourishing ocean drives the end-Permian marine mass extinction. Proc. Natl. Acad. Sci. 112, 10298–10303. https://doi.org/10.1073/pnas.1503755112

Scholle, P.A., Ulmer, D.S., Melim, L.A., 1992. Late-stage calcites in the Permian Capitan Formation and its equivalents, Delaware Basin margin, west Texas and New Mexico: evidence for replacement of precursor evaporites. Sedimentology

39, 207–234. https://doi.org/10.1111/j.1365-3091.1992.tb01035.x

Schoonen, M.A.A., Barnes, H.L., 1991. Reactions forming pyrite and marcasite from solution: II. Via FeS precursors below 100°C. Geochim. Cosmochim. Acta 55, 1505–1514. https://doi.org/10.1016/0016-7037(91)90123-M

Schreiber, B.C., Tabakh, M.E., 2000. Deposition and early alteration of evaporites. Sedimentology 47, 215–238.

Schrenk, M.O., Kelley, D.S., Bolton, S.A., Baross, J.A., 2004. Low archaeal diversity linked to subseafloor geochemical processes at the Lost City Hydrothermal Field, Mid-Atlantic Ridge. Environ. Microbiol. 6, 1086–1095.

Schröder, S., Schreiber, B.C., Amthor, J.E., Matter, A., 2004. Stratigraphy and environmental conditions of the terminal Neoproterozoic–Cambrian Period in Oman: evidence from sulphur isotopes. J. Geol. Soc. 161, 489–499. https://doi.org/10.1144/0016-764902-062

Sears, J.W., Chamberlain, K.R., Buckley, S.N., 1998. Structural and U-Pb geochronological evidence for 1.47 Ga rifting in the Belt basin, western Montana. Can. J. Earth Sci. 35, 467–475. https://doi.org/10.1139/e97-121

Seguin, M.K., Petryk, A.A., 1986. Paleomagnetic study of the Late Ordovician–Early Silurian platform sequence of Anticosti Island, Quebec. Can. J. Earth Sci. 23, 1880–1890. https://doi.org/10.1139/e86-176

Shapiro, R., Fricke, H., 2002. Tepee Buttes: Fossilized methane-seep ecosystems. Field Guid. 3, 94–101. https://doi.org/10.1130/0-8137-0003-5.94

Shields, G.A., Kimura, H., Yang, J., Gammon, P., 2004. Sulphur isotopic evolution of Neoproterozoic-Cambrian seawater: new francolite-bound sulphate δ34S data and a critical appraisal of the existing record. Chem. Geol. 204, 163–182. https://doi.org/10.1016/j.chemgeo.2003.12.001

Shields, G.A., Strauss, H., Howe, S.S., Siegmund, H., 1999. Sulphur isotope compositions of sedimentary phosphorites from the basal Cambrian of China: implications for Neoproterozoic-Cambrian biogeochemical cycling. J. Geol. Soc. 156, 943–955. https://doi.org/10.1144/gsjgs.156.5.0943

Silver, B.A., Todd, R.G., 1969. Permian cyclic strata, northern Midland and Delaware Basins, west Texas and southeastern New Mexico. AAPG Bull. 53, 2223–2251.

Sim, M.S., Bosak, T., Ono, S., 2011a. Large Sulfur Isotope Fractionation Does Not Require Disproportionation. Science 333, 74–77. https://doi.org/10.1126/science.1205103

Sim, M.S., Ono, S., Donovan, K., Templer, S.P., Bosak, T., 2011b. Effect of electron donors on the fractionation of sulfur isotopes by a marine Desulfovibrio sp. Geochim. Cosmochim. Acta 75, 4244–4259. https://doi.org/10.1016/j.gca.2011.05.021

Sim, M.S., Ono, S., Hurtgen, M.T., 2015. Sulfur isotope evidence for low and fluctuating sulfate levels in the Late

Devonian ocean and the potential link with the mass extinction event. Earth Planet. Sci. Lett. 419, 52–62. https://doi.org/10.1016/j.epsl.2015.03.009

Slotznick, S.P., Zieg, J., Webb, S.M., Kirschvink, J.L., Fischer, W.W., 2015. Iron mineralogy and redox chemistry of the Mesoproterozoic Newland Formation in the Helena embayment, Belt Supergroup, Montana. Northwest Geol. 44, 55–72.

Song, Huyue, Tong, J., Algeo, T.J., Song, Haijun, Qiu, H., Zhu, Y., Tian, L., Bates, S., Lyons, T.W., Luo, G., Kump, L.R., 2014. Early Triassic seawater sulfate drawdown. Geochim. Cosmochim. Acta 128, 95–113. https://doi.org/10.1016/j.gca.2013.12.009

Sperling, E.A., Rooney, A.D., Hays, L., Sergeev, V., Vorob'eva, N., Sergeeva, N., Selby, D., Johnston, D.T., Knoll, A.H., 2014. Redox heterogeneity of subsurface waters in the Mesoproterozoic ocean. Geobiology 12, 373–386.

Stanton, R.J., Pray, L.C., 2004. Skeletal-Carbonate Neptunian Dikes of the Capitan Reef: Permian, Guadalupe Mountains, Texas, U.S.A. J. Sediment. Res. 74, 805. https://doi.org/10.1306/042704740805

Staudt, W.J., Schoonen, M.A.A., 1995. Sulfate Incorporation into Sedimentary Carbonates, in: Geochemical Transformations of Sedimentary Sulfur, ACS Symposium Series. American Chemical Society, pp. 332–345. https://doi.org/10.1021/bk-1995-0612.ch018

Stearns, R.G., Reesman, A.L., 1986. Cambrian to Holocene Structural and Burial History of Nashville Dome. AAPG Bull. 70, 143–154.

Steen, I.H., Dahle, H., Stokke, R., Roalkvam, I., Daae, F.-L., Rapp, H.T., Pedersen, R.B., Thorseth, I.H., 2016. Novel Barite Chimneys at the Loki's Castle Vent Field Shed Light on Key Factors Shaping Microbial Communities and Functions in Hydrothermal Systems. Front. Microbiol. 6, 1–13. https://doi.org/10.3389/fmicb.2015.01510

Strauss, H., 1997. The isotopic composition of sedimentary sulfur through time. Palaeogeogr. Palaeoclimatol. Palaeoecol. 132, 97–118. https://doi.org/10.1016/s0031-0182(97)00067-9

Strauss, H., 1993. The sulfur isotopic record of Precambrian sulfates: new data and a critical evaluation of the existing record. Precambrian Res. 63, 225–246. https://doi.org/10.1016/0301-9268(93)90035-z

Strauss, H., Schieber, J., 1990. A Sulfur Isotope Study of Pyrite Genesis - the Mid-Proterozoic Newland Formation, Belt Supergroup, Montana. Geochim. Cosmochim. Acta 54, 197–204. https://doi.org/10.1016/0016-7037(90)90207-2

Takano, B., 1985. Geochemical implications of sulfate in sedimentary carbonates. Chem. Geol. 49, 393–403. https://doi.org/10.1016/0009-2541(85)90001-4

Theiling, B.P., Coleman, M., 2015. Refining the extraction methodology of carbonate associated sulfate: Evidence from synthetic and natural carbonate samples. Chem. Geol. 411, 36–48.

https://doi.org/10.1016/j.chemgeo.2015.06.018

Thode, H.G., Monster, J., 1970. Sulfur Isotope Abundances and Genetic Relations of Oil Accumulations in Middle East Basin. AAPG Bull. 54, 627–637.

Thode, H.G., Monster, J., 1965. Sulfur-Isotope Geochemistry of Petroleum, Evaporites, and Ancient Seas, in: Young, A., Galley, J.E. (Eds.), AAPG Memoir 4: Fluids in Subsurface Environments. American Association of Petroleum Geologists, Tulsa, Oklahoma, pp. 367–377.

Thode, H.G., Monster, J., Dunford, H.B., 1961. Sulphur isotope geochemistry. Geochim. Cosmochim. Acta 25, 159–174. https://doi.org/10.1016/0016-7037(61)90074-6

Thode, H.G., Monster, J., Dunford, H.B., 1958. Sulphur Isotope Abundances in Petroleum and Associated Materials. AAPG Bull. 42, 2619–2641.

Thompson, C.K., Kah, L.C., 2012. Sulfur isotope evidence for widespread euxinia and a fluctuating oxycline in Early to Middle Ordovician greenhouse oceans. Palaeogeogr. Palaeoclimatol. Palaeoecol. 313–314, 189–214. https://doi.org/10.1016/j.palaeo.2011.10.020

Tinker, S.W., 1998. Shelf-to-basin facies distributions and sequence stratigraphy of a steep-rimmed carbonate margin; Capitan depositional system, McKittrick Canyon, New Mexico and Texas. J. Sediment. Res. 68, 1146–1174.

Tivey, M.K., 2007. Generation of seafloor hydrothermal vent fluids and associated mineral deposits. Oceanography 20, 50.

Tivey, M.K., 1995. Modeling Chimney Growth and Associated Fluid Flow at Seafloor Hydrothermal Vent Sites, in: Humphris, S.E., Zierenberg, R.A., Mullineaux, L.S., Thomson, R.E. (Eds.), Seafloor Hydrothermal Systems: Physical, Chemical, Biological, and Geological Interactions, Geophysical Monograph 91. American Geophysical Union, pp. 158–177. https://doi.org/10.1029/GM091p0158

Torres, M.E., Brumsack, H.J., Bohrmann, G., Emeis, K.C., 1996. Barite fronts in continental margin sediments: a new look at barium remobilization in the zone of sulfate reduction and formation of heavy barites in diagenetic fronts. Chem. Geol. 127, 125–139. https://doi.org/10.1016/0009-2541(95)00090-9

Tostevin, R., Turchyn, A.V., Farquhar, J., Johnston, D.T., Eldridge, D.L., Bishop, J.K.B., McIlvin, M., 2014. Multiple sulfur isotope constraints on the modern sulfur cycle. Earth Planet. Sci. Lett. 396, 14–21. https://doi.org/10.1016/j.epsl.2014.03.057

Tucker, M.E., 1991. Sequence stratigraphy of carbonate-evaporite basins: models and application to the Upper Permian (Zechstein) of northeast England and adjoining North Sea. J. Geol. Soc. 148, 1019–1036. https://doi.org/10.1144/gsjgs.148.6.1019

Turchyn, A.V., Schrag, D.P., 2004. Oxygen Isotope Constraints on the Sulfur Cycle over the Past 10 Million Years. Science 303, 2004–2007. https://doi.org/10.1126/science.1092296

Turchyn, A.V., Schrag, D.P., Coccioni, R., Montanari, A., 2009. Stable isotope analysis of the Cretaceous sulfur cycle. Earth Planet. Sci. Lett. 285, 115–123. https://doi.org/10.1016/j.epsl.2009.06.002

Tyrrell Jr, W.W., 1969. Criteria useful in interpreting environments of unlike but time-equivalent carbonate units (Tansill-Capitan-Lamar), Capitan reef complex, West Texas and New Mexico, in: Friedman, G.M. (Ed.), SEPM Special Publication 14: Depositional Environments in Carbonate Rock. pp. 80–97. https://doi.org/10.2110/pec.69.03.0080

Utrilla, R., Pierre, C., Orti, F., Pueyo, J.J., 1992. Oxygen and sulphur isotope compositions as indicators of the origin of Mesozoic and Cenozoic evaporites from Spain. Chem. Geol. 102, 229–244. https://doi.org/10.1016/0009-2541(92)90158-2

Vredenburgh, L.D., Cheney, E.S., 1971. Sulfur and carbon isotopic investigation of petroleum, Wind River basin, Wyoming. AAPG Bull. 55, 1954–1975.

Walker, J.C., 1986. Global geochemical cycles of carbon, sulfur and oxygen. Mar. Geol. 70, 159–174.

Walter, M., Du, R., Horodyski, R.J., 1990. Coiled carbonaceous megafossils from the Middle Proterozoic of Jixian (Tianjin) and Montana. Am. J. Sci. 290-A, 133–148.

Ward, R.F., Kendall, C.G.S.C., Harris, P.M., 1986. Upper Permian (Guadalupian) facies and their association with hydrocarbons--Permian basin, west Texas and New Mexico. AAPG Bull. 70, 239–262.

Warren, J.K., 2010. Evaporites through time: Tectonic, climatic and eustatic controls in marine and nonmarine deposits. Earth-Sci. Rev. 98, 217–268. https://doi.org/10.1016/j.earscirev.2009.11.004

Whalen, M.T., Eberli, G.P., van Buchem, F.S., Mountjoy, E.W., 2000. Facies models and architecture of Upper Devonian carbonate platforms (Miette an Ancient wall), Alberta, Canada. Genet. Stratigr. Explor. Prod. Scales Mém. 24, 139–178.

White, J., Gammons, C.H., Zieg, G.A., 2013. Paragenesis of cobalt and nickel in the Black Butte shale-hosted copper deposit, Belt Basin, Montana, USA. Miner. Deposita 49, 335–351. https://doi.org/10.1007/s00126-013-0492-1

Wignall, P.B., Hallam A., Newton R. J., Sha J. G., Reeves E., Mattioli E., Crowley S., 2006. An eastern Tethyan (Tibetan) record of the Early Jurassic (Toarcian) mass extinction event. Geobiology 4, 179–190. https://doi.org/10.1111/j.1472-4669.2006.00081.x

Wilde, G.L., Rudine, S.F., Lambert, L.L., 1999. Formal designation: Reef Trail Member, Bell Canyon Formation, and its significance for recognition of the Guadalupian-Lopingian boundary.

Wilkinson, B.H., 1979. Biomineralization, paleoceanography, and the evolution of calcareous marine organisms. Geology 7, 524–527. https://doi.org/10.1130/0091-7613(1979)7<524:bpateo>2.0.co;2

Winston, D., Link, P., 1993. Middle Proterozoic rocks of Montana, Idaho and eastern Washington: the Belt Supergroup. Precambrian

Conterminous US Geol. N. Am. 2, 487–517.

Witts, J.D., Newton, R.J., Mills, B.J.W., Wignall, P.B., Bottrell, S.H., Hall, J.L.O., Francis, J.E., Alistair Crame, J., 2018. The impact of the Cretaceous–Paleogene (K–Pg) mass extinction event on the global sulfur cycle: Evidence from Seymour Island, Antarctica. Geochim. Cosmochim. Acta. https://doi.org/10.1016/j.gca.2018.02.037

Wortmann, U.G., Chernyavsky, B.M., 2007. Effect of evaporite deposition on Early Cretaceous carbon and sulphur cycling. Nature 446, 654–656.

Wortmann, U.G., Paytan, A., 2012. Rapid Variability of Seawater Chemistry Over the Past 130 Million Years. Science 337, 334–336. https://doi.org/10.1126/science.1220656

Wotte, T., Shields-Zhou, G.A., Strauss, H., 2012a. Carbonate-associated sulfate: Experimental comparisons of common extraction methods and recommendations toward a standard analytical protocol. Chem. Geol. 326–327, 132–144. https://doi.org/10.1016/j.chemgeo.2012.07.020

Wotte, T., Strauss, H., Fugmann, A., Garbe-Schönberg, D., 2012b. Paired δ34S data from carbonate-associated sulfate and chromium-reducible sulfur across the traditional Lower–Middle Cambrian boundary of W-Gondwana. Geochim. Cosmochim. Acta 85, 228–253. https://doi.org/10.1016/j.gca.2012.02.013

Wotte, T., Strauss, H., Sundberg, F. A., 2011. Carbon and Sulfur Isotopes from the Cambrian Series 2-Cambrian Series 3 of Laurentia and Siberia, in: Hollingsworth, J.S., Sundberg, Frederick A., Foster, J.R. (Eds.), Museum of Northern Arizona Bulletin 67: Cambrian Stratigraphy and Paleontology of Northern Arizona and Southern Nevada: The 16th Field Conference of the Cambrian Stage Subdivision Working Group, International Subcommission on Cambrian Stratigraphy, Flagstaff, Arizona, and Southern Nevada, United States. Museum of Northern Arizona, Flagstaff, Arizona, pp. 43–63.

Wu, N., 2013. Sulfur isotopic evolution of Phanerozoic and Ediacaran seawater sulfate. University of Maryland, College Park, Md.

Wu, N., Farquhar, J., Strauss, H., 2014. δ34S and Δ33S records of Paleozoic seawater sulfate based on the analysis of carbonate associated sulfate. Earth Planet. Sci. Lett. 399, 44–51. https://doi.org/10.1016/j.epsl.2014.05.004

Wu, N., Farquhar, J., Strauss, H., Kim, S.-T., Canfield, D.E., 2010. Evaluating the S-isotope fractionation associated with Phanerozoic pyrite burial. Geochim. Cosmochim. Acta 74, 2053–2071. https://doi.org/10.1016/j.gca.2009.12.012

Xiao, Z., Gammons, C.H., Williams-Jones, A.E., 1998. Experimental study of copper(I) chloride complexing in hydrothermal solutions at 40 to 300°C and saturated water vapor pressure. Geochim. Cosmochim. Acta 62, 2949–2964. https://doi.org/10.1016/S0016-7037(98)00228-2

Yan, D., Chen, D., Wang, Q., Wang, J., Wang, Z., 2009. Carbon and sulfur isotopic anomalies across the Ordovician–Silurian boundary on the

Yangtze Platform, South China. Palaeogeogr. Palaeoclimatol. Palaeoecol. 274, 32–39. https://doi.org/10.1016/j.palaeo.2008.12.016

Yan, D., Zhang, L., Qiu, Z., 2013. Carbon and sulfur isotopic fluctuations associated with the end-Guadalupian mass extinction in South China. Gondwana Res. 24, 1276–1282. https://doi.org/10.1016/j.gr.2013.02.008

Yeremenko, N.A., Pankina, R.G., 1972. Variations of 34S in Sulfates of Recent and Ancient Marine Basins of the Soviet Union. Geochem. Int. 10, 45–54.

Young, S.A., Gill, B.C., Edwards, C.T., Saltzman, M.R., Leslie, S.A., 2016. Middle–Late Ordovician (Darriwilian–Sandbian) decoupling of global sulfur and carbon cycles: Isotopic evidence from eastern and southern Laurentia. Palaeogeogr. Palaeoclimatol. Palaeoecol. 458, 118–132. https://doi.org/10.1016/j.palaeo.2015.09.040

Young, S.A., Saltzman, M.R., Bergström, S.M., 2005. Upper Ordovician (Mohawkian) carbon isotope (δ13C) stratigraphy in eastern and central North America: Regional expression of a perturbation of the global carbon cycle. Palaeogeogr. Palaeoclimatol. Palaeoecol. 222, 53–76. https://doi.org/10.1016/j.palaeo.2005.03.008

Yurewicz, D.A., 1977. The origin of the massive facies of the lower and middle Capitan Limestone (Permian), Guadalupe Mountains, New Mexico and west Texas, in: Hileman, M.E., Mazzullo, S.J. (Eds.), Upper Guadalupian Facies, Permian Reef Complex, Guadalupe Mountains, New Mexico and West Texas, 1977 Field Conference Guidebook, v. 1, Permian Basin Section SEPM, Publication 77-16. Permian Basin Section SEPM, Midland, TX, pp. 45–92.

Zhang, G., Zhang, X., Li, D., Farquhar, J., Shen, S., Chen, X., Shen, Y., 2015. Widespread shoaling of sulfidic waters linked to the end-Guadalupian (Permian) mass extinction. Geology 43, 1091–1094. https://doi.org/10.1130/G37284.1

Zhang, L., Zhao, L., Chen, Z.-Q., Algeo, T.J., Li, Y., Cao, L., 2015. Amelioration of marine environments at the Smithian–Spathian boundary, Early Triassic. Biogeosciences 12, 1597–1613.

Zhang, T., Shen, Y., Zhan, R., Shen, S., Chen, X., 2009. Large perturbations of the carbon and sulfur cycle associated with the Late Ordovician mass extinction in South China. Geology 37, 299–302. https://doi.org/10.1130/g25477a.1

Zieg, G., Leitch, C.H., 1998. The geology of the Sheep Creek copper deposit, Meagher County, Montana, in: Berg, R. (Ed.), Belt Symposium III Abstracts, Montana Bureau of Mines and Geology Open-File Report MBMG 381. pp. 67–69.

Zieg, G.A., 1986. Stratigraphy and sedimentology of the Middle Proterozoic upper Newland Limestone. Belt Supergroup Guide Proterozoic Rocks West. Mont. Adjac. Areas Mont. Bur. Mines Geol. Spec. Publ. 94, 125–141.

Zieg, G.A., Scartozzi, V., Chutas, N., Albers, D., Gostomski, K., Jones, J., 2013. Black Butte Copper Deposits, Lower Belt Supergroup, Montana. Northwest Geol. 42, 131–148.

Zou, C., Qiu, Z., Poulton, S.W., Dong, D., Wang, H., Chen, D., Lu, B., Shi, Z., Tao, H., 2018. Ocean euxinia and climate change "double whammy" drove the Late Ordovician mass extinction. Geology. https://doi.org/10.1130/G40121.1

APPENDIX A

Table A1: References for $\delta^{34}S$ data included in compilation in Chapter I; number of CAS, evaporite, and barite analyses in each reference; and description of age assignments for the data.

Reference	CAS	Evap.	Bar.	Age Model
Adams et al., Nat. Geo., 2010	16			Ages linearly interpolated between Ar/Ar dates in provided in Figure 1 in paper
Arp et al., Sedimentology, 2008	6			Assigned age of 146 Ma for the latest Tithonian
Ault & Kulp, GCA, 1959		12		Evaporite ages updated at stage scale to latest stratigraphy, and tied to ICS2016/04
Balderer et al., 1991		11		Data compiled with age model by Bernasconi et al., GCA, 2017
Baldermann et al., Chem. Geo., 2015	8			Linear interpoloation of stratigraphic height between Rb/Sr ages in paper
Bernasconi et al., GCA, 2017		282		Age model provided in paper, which matches ICS2016/04 except for age of Smithian-Spathian boundary
Boschetti et al. 2011		5		Data compiled with age model by Bernasconi et al., GCA, 2017
Burdett et al., EPSL, 1989	56	25		Ages provided in a paper using Berggren et al. (1985) timescale
Chen et al., J. Geol. Soc., 2013	71			Linear interpolation of stratigraphic height between conodont zone age constraints from Kaufmann (2006), updated to GSSP ages in ICS2016/04
Claypool et al., Chem. Geo., 1980		272		Evaporite ages updated at stage scale to latest stratigraphy, and tied to ICS2016/04
Cortecci et al. 1981		20		Used age model in Bernasconi et al., GCA, 2017
Davies & Krosue, Geol. Surv. Can. Paper 75-1, 1975		23		Evaporite ages updated at stage scale to latest stratigraphy, and tied to ICS2016/04
Fanlo & Ayora 1998		26		Data compiled with age model by Bernasconi et al., GCA, 2017
Fike & Grotzinger, GCA, 2008	157			Ages provided in Fike et al., Annu. Rev. Earth. Planet. Sci., 2015
Gill et al., EPSL, 2011	105			Linear interpolation of stratigraphic height between stage boundaries using ICS2016/04, assigning Calcari Maculati to Bajocian stage

Reference	CAS	Evap.	Bar.	Age Model
Gill et al., Nature, 2011	111			Linear interpolation of stratigraphic height between stage boundaries using ICS2016/04
Gill et al., PPP, 2007	74			Linear interpolation of stratigraphic height between stage boundaries using ICS2016/04
Gomes et al., Paleocean. & Paleoclim., 2016	115			Ages provided in paper on GTS2012 time scale, which matches ICS2016/04 in the Cretaceous
Holser & Kaplan, Chem. Geol., 1966		49		Evaporite ages updated at stage scale to latest stratigraphy, and tied to ICS2016/04
Horacek et al. 2010		6		Data compiled with age model by Bernasconi et al., GCA, 2017
Hurtgen et al., EPSL, 2009	30			At Felix Cove, carbon isotope maxima in SPICE is set as base of Steptoean (Saltzman et al., 2004). In other sections, biomere event at onset of SPICE is set as base of Steptoean. March Pt. Formation includes *Bolaspidella* trilobites (Upper Middle Cambrian), and total deposition likely 5-10Ma; the lowest sample in the March Pt. Formation is set as the base of the Marjuman
Insalaco et al., 2006		17		Data compiled with age model by Bernasconi et al., GCA, 2017
John et al., Chem. Geo., 2010	34			Linear interpolation of stratigraphic height between conodont zone age constraints from Kaufmann (2006), updated to GSSP ages in ICS2016/04
Jones & Fike, EPSL, 2013	42			Linearly interpolated between stage boundaries using ICS2016/04. Hirnantian and Ordovician-Silurian boundary placed based on carbon isotope stratigraphy, not biostratigraphy, in text.
Kah et al., PPP, 2016	42			Ages provided in Fig 9, using ICS2016/04 ages at the tie points
Kaiho et al., Chem. Geo., 2006	11			Approximated age model as described for Schobben et al., PPP, 2017
Kaiho et al., Geology, 2001	12			Meishan section bed ages and accumulation rates from Burgess et al., 2014
Kaiho et al., Paleoceanography, 1999	18			K-Pg boundary set at ICS2016/04 age, and sedimentation rates from paper
Kampschulte & Strauss, Chem. Geo, 2004	244			Ages updated by interpolation to ICS2016/04 from Harland 1989 timescale
Kramm & Wedopohl, Chem. Geol., 1991		9		Zechstein evaporites tied to ICS2016/04 using ~1Myr/unit starting at the bottom of the Lopingian (Stollhofen et al., 2009)

Reference	CAS	Evap.	Bar.	Age Model
Li et al., Front. Earth Sci. China, 2009	27			Bed 27/28 boundary is proposed Permian-Triassic Boundary; using age from Burgess 2014. Maokou/Wujiaping Fm. boundary is Guadalupian-Lopingian Boundary according to Yadong (2008); using age from ICS2016/04
Longinelli and Flora 2007		8		Data compiled with age model by Bernasconi et al., GCA, 2017
Loyd et al., EPSL, 2012	63			Linear interpolation of stratigraphic height between stage boundaries using ICS2016/04
Lu & Meyers, J. Sed. Res., 2003		16		Middle Messinian age assigned in ICS2016/04
Marenco et al., GCA, 2008	25	9		Section correlated using flooding surfaces and Sr isotope data, and linearly interpolating ages of the Spathian/Anisian and Smithian/Spathian boundaries from Burgess et al., 2014
Marenco et al., PPP, 2013	27			Linear interpolation of stratigraphic height using stratigraphy published in Marenco et al., 2016, which uses ages in ICS2016/04
Marenco et al., PPP, 2016				Linear interpolation of stratigraphic height between stage boundaries in Fig 2, using ages from Kah et al., 2016, which match ICS2016/04
Mills et al., Geology, 2017	114			Age model developed in paper on GTS2012 time scale, which matches ICSv2016/04 in the Cretaceous
Newton et al., EPSL, 2004	32			Linear interpolation of stratigraphic height over the extinction interval using ages from Burgess et al., 2014, and age of 251.5 Ma for top of Tesero Ooilite set as the age at which the d13C returns to a "flat" value at the Meishan GSSP
Newton et al., Geology, 2011	85			Linear interpolation of stratigraphic height between stage boundaries using ICS2016/04 for Yorkshire section, and correlated Tibet strata using chemostratigraphy preferred by the authors
Ohkouchi et al., Geology, 1999	27			Age model based on Al accumulation provided in paper, and shifted +0.29Myr to agree with ICS2016/04 Cenomanian-Turonian boundary age of 93.9Ma
Owens et al., PNAS, 2013	216			Eastbourne section sedimentation rates between carbon isotope excursion features from Voigt et al. (2008) astrochronology tied to ICS2016/04 time scale using Cenomanian-Turonian GSSP. South Ferriby and Trunch sections tied to ages of CIE calculated for Eastbourne section and linearly interpolated stratigraphic height. Raia del Pedale section height linearly interpolated between CIE ages from Eastbourne and stage boundaries.
Pankina et al., Geochem. Int., 1975		18		Evaporite ages updated at stage scale to latest stratigraphy, and tied to ICS2016/04

Reference	CAS	Evap.	Bar.	Age Model
Paytan et al., Science, 1998			69	Ages updated to ICS2016/04 from those provided in Kurtz (2004), which uses Berggren, SEPM SP54 (1995) timescale
Paytan et al., Science, 2004			123	Ages updated to GTS2004 by Prokoph et al. (2008), and then interpolated to ICS2016/04
Pisarchik & Golubchina, Geochem. Int, 1975		26		Evaporite ages updated at stage scale to latest stratigraphy, and tied to ICS2016/04
Playà et al., Sed. Geol., 2007		10		Age of 70 kyr given in text
Poulton et al., Geology, 2015	24			Sedimentation rates from Kolonic et al., Paleo., (2005), rescaled to reflect obliquity-controlled cycles instead of eccentricity, as the authors prefer, citing Meyers et al., (2012). Cenomanian-Turonian boundary shifted from GTS2004 age in Kolonic et al. to ICS2016/04.
Present et al., EPSL, 2015	77			Ages determined by linearly interpolating stage boundaries to ICS2016/04, which are placed with carbon isotope stratigraphy as described by Jones & Fike (2013)
Present, Ph.D. Ch. 3, 2018	52			ICS2016/04 ages used to interpolate biostratigraphy and carbon isotope stratigraphy in Bergstrom (2009) and Cramer (2010)
Present, Ph.D. Ch. 4, 2018	255			Assigned base of Triplet Member to base of Middle Capitanian, 262Ma, and assumed each High Frequency Sequence deposited in 500kyr
Rennie & Turchyn, EPSL, 2014	56			Site 807A to 362.8m: Martin & Scher (2004); Site 807A below 362.8m: Schrag et al. (1995); Site 821A: Wei & Gartner (1993); Site 1003A: Wright & Kroon (2000)
Riccardi et al., GCA, 2006	102			Used Burgess (2014) ages for Meishan section and extinction interval at Shangsi, and for Dienerian base. Used Algeo (2013) age for Changhsingian base. Used Bowring (1998) age for base of Meishan bed #7.
Sakai, EPSL, 1972		13		Evaporite ages updated at stage scale to latest stratigraphy, and tied to ICS2016/04
Schobben et al., PNAS, 2015	74			Ages provided in paper using Burgess (2014) dates
Schobben et al., PPP, 2017	19			Assigned approximate mid-Griesbachian age of 251.50Ma to uppermost Balvany East strata, and linearly interpolated stratigraphic height to Permian-Triassic Boundary at base of Gerennavar Fm., neglecting missing section between Balvany East and Balvany North; used same accumulation rate for limestones in Nagyvisnyo Fm. anchored at EPME and apportioned remaining time in the Boundary Shale beds between top of limestones and P-Tr. Boundary
Schroder et al. 2004		29		Ages provided in Fike et al., Annu. Rev. Earth. Planet. Sci., 2015

Reference	CAS	Evap.	Bar.	Age Model
Sim et al., EPSL, 2015	68			Ages provided in paper using Kaufmann (2006) time scale updated to GSSP ages in ICS2016/04
Song et al., GCA, 2014	202			Age model is from Figure 4 (tie points are in bold), using dates from Burgess 2014 and ICS2016/04; interpolated linearly in between tie points; Composite height is linking of sections by the C-isotope tie points in Figures 3 and 4: Daijang 400m = Lower Guandau 135m (N3); Lower Guandau 225m = Upper Guandau 10m (P4). Adjusted Daijang B by 18m to approx. bring in line with Daijang A, as in Fig 3
Spötl, 1998		8		Used age model in Bernasconi et al., GCA, 2017
Thode & Monster, AAPG Memoir 4, 1965		68		Evaporite ages updated at stage scale to latest stratigraphy, and tied to ICS2016/04
Thode & Monster, AAPG Bull., 1970		17		Evaporite ages updated at stage scale to latest stratigraphy, and tied to ICS2016/04
Thode et al., AAPG Bull., 1958		5		Assigned to upper Frasnian (Hearn et al., 2011)
Thompson & Kah, PPP, 2012	235			Ages provided in paper using U/Pb dates in Thompson et al., PPP, 2012
Turchyn et al., EPSL, 2009	39		39	Ages updated by interpolation to ICS2016/04 from GTS2004
Utrilla et al., Chem. Geo., 1992		62		Listed formations assigned by stage to ICS2016/04 ages
Vredenburgh & Cheney, AAPG Bull., 1971		16		Evaporite ages updated at stage scale to latest stratigraphy, and tied to ICS2016/04
Witts et al., GCA, 2018	41			Linearly interpolated GTS2012 magnetochron age assignments using stratigraphic heights; GTS2012 matches ICS2016/04 in Cretaceous and Paleogene
Worden et al., 1997		11		Used age model in Bernasconi et al., GCA, 2017
Wotte et al., GCA, 2012	85			Linear interpolation of stratigraphic height between stage boundaries using ICS2016/04
Wotte et al., Mus. Northern. Ari. Bull., 2011	69			Linear interpolation of stratigraphic height between stage boundaries using ICS2016/04, using Susan Duster Limestone sedimentation rate for Molodo River and Ulakhan-Kyyry-Taas sections
Wu et al., EPSL, 2014	214		66	Ages updated by interpolation to ICS2016/04 from GTS2004
Yan et al., Gond. Res., 2013	27			Guadalupian-Lopingian boundary set at base of *C.p.p.* based on ICS2016/04; Sed rates from Qiu (2015) indicate 0.04cm/kyr in the bedded chert relative to bentonite (257Ma) at top of *C.p.p* zone, so base of bedded chert is 258.6Ma.; Applied this sed rate down through the limestone

Reference	CAS	Evap.	Bar.	Age Model
Yeremenko & Pankina, Geochem. Int., 1972		17		Evaporite ages updated at stage scale to latest stratigraphy, and tied to ICS2016/04
Young et al., PPP, 2016	68			Linear interpolation of stratigraphic height between stage boundaries in Fig 2 and 3 using ICS2016/04 ages
Zhang et al., Biogeosci., 2015	15			Used Smithian/Spathian boundary ages from Burgess et al., 2014, and sedimentation rates provided in Figure 3 of paper

APPENDIX B

Table B 1: Sample locations, descriptions, and geochemical data from Chapter 4. Mineralogy: Cc = calcite, Dol = dolomite, Cements: p = poikilitic calcite, d = drusy calcite, i = isopachous cement, b = botryoidal cement. Facies codes are from Tinker (1998). Textures: MS = mudstone, WS = wackestone, PS = packstone, GS = grainstone, gdPS = grain-dominated packstone, RS = rudstone, BS = boundstone. Grain sizes: s = silt, vf = very fine, f = fine, m = medium, c = coarse, vc = very coarse.

Sample	Date collected	UTM Grid Ref.	Ht. (m)	Polished Slab Description
	McKittrick Canyon Limestone			
MC-005	6-Dec-13	13R 523003 3538231	0	normally-graded gray skeletal-lithoclast lime PS/WS fine from granule/small pebble to vf sand; convoluted base/flame structures; lithoclasts are vf lime WS; skeletal clasts include broken echinoderm discs & spines, bryozoans, tabulate corals, encrusting forams; WS includes broken vf forams and sponge spicules
MC-006	6-Dec-13	13R 523003 3538231	0.2	normally-graded laminated lime skeletal-lithoclast PS (pebble c. skeletal WS and *Archaelithoporella-Tubiphytes* BS lithoclasts) and silty lime MS with twinned prismatic or bladed ferric oxy-hydroxides (oxidizes on cut surface to yellow-green)
MC-008	6-Dec-13	13R 523003 3538231	0.4	convolutedly-laminated dark gray/brown skeletal lime MS/WS and skeletal-lithoclast PS with clast of boundstone; skeletal clasts in WS are vf broken forams, spicules, and angular debris
MC-012	6-Dec-13	13R 523036 3538230	0.8	skeletal-lithoclast lime GS, partly silicified skeletal-lithoclast gdPS, and normally-graded skeletal-lithoclast lime PS; skeletal fragments include crinoid discs, brachiopods, algal fragments; lithoclasts are vf skeletal WS, tabular *Archaelithoporella* BS fragments, and skeletal GS
MC-013	6-Dec-13	13R 523036 3538230	1.4	wavy and ripple-laminated vf peloid-foram-ostrocod lime PS/WS
MC-014	6-Dec-13	13R 523036 3538230	1.8	thick graded lamina of f/vf peloid-spicule-*Tubiphytes* PS/WS; partially silicified; <10um disseminated pyrite; wavy laminated dark MS

Sample	Date collected	UTM Grid Ref.	Ht. (m)	Polished Slab Description
MC-015	6-Dec-13	13R 523036 3538230	2.3	f. bioclast-lithoclast PS, including spicules, *Tubiphytes* fragments, and bryozoan fragments
MC-016	6-Dec-13	13R 523055 3538214	2.5	poorly sorted, lithoclast-bioclast GS; minor chert replacement; compaction indicated by broken brachiopods and suturing of skeletal clasts with lithoclasts; lithoclasts are skeletal WS
MC-017	6-Dec-13	13R 523055 3538214	3.1	skeletal-lithoclast PS; bryozoans, brachiopod (secondary fibrous Cc partially-preserved), *Tubiphytes* fragments; milky chert fills vugs
MC-018	6-Dec-13	13R 523055 3538214	3.5	vc lithoclast-skeletal fragment PS, including mollusk, *Tubiphytes*, and WS clasts
MC-019	6-Dec-13	13R 523055 3538214	3.68	laminated f. skeletal fragment GS; forams, *Tubiphytes*, spicules, bryozoans
MC-020	6-Dec-13	13R 523055 3538214	3.9	partly silicified skeletal-lithoclast gdPS; lithoclasts of WS and BS; skeletal fragments include bryozoans, brachiopods; overlies graded bed of spicule-Tubiphytes lime PS/WS/MS
	Wilderness Ridge Graben Triplet section			
MC-031	9-Dec-13	13R 522442 3540127	13.1	Subrounded bioclast aggregate grains up to 4mm and foram/mollusk bioclast PS/GS with isopachous cement on some aggregate grains and blocky interparticle pore-filling calcite between grains in grainstones
MC-032	9-Dec-13	13R 522453 3540138	14.2	Thickly laminated intraclast-algal GS with *Mizzia*
MC-033	9-Dec-13	13R 522453 3540138	16	Heavily recrystallized MS with blocky calcite-filled ovoid to irregular porosity; possibly evaporite molds
MC-034	9-Dec-13	13R 522453 3540138	16.4	Fenestral med. PS with tabular gray intraclasts (or maybe Phylloid algae?) and larger *mollusk*/brachiopod fragments replaced by biomoldic clear Cc; fenestrae filled with blocky white or clear Cc
MC-035	9-Dec-13	13R 522445 3540147	17.5	Blocky calcite-filled solution-enlarged vug in fenestral PS. Gray-brown, inclusion-rich exterior of vug, with white-clear poikilitic interior; minor pendant cements overgrow poikilitic calcite

Sample	Date collected	UTM Grid Ref.	Ht. (m)	Polished Slab Description
MC-036	9-Dec-13	13R 522445 3540147	19.1	Coated grain-algal GS, with clear Cc interparticle and biomoldic cement; subrounded c/vc ooids and 2-3mm oncoids; algal bioclasts include *Mizzia* with cloudy intraparticle Cc
MC-037	9-Dec-13	13R 522445 3540147	19.6	Pink coated grain-algal GS; grains coated with clear isopachous bladed cement, and blocky Cc interparticle cement; biomoldic porosity occasionally has pendant cements
MC-038	9-Dec-13	13R 522445 3540147	19.7	Brecciated pink ooid-algal-aggregate grain dol. GS with poikilitic Cc cement; algal grains mainly dasyclads (probably *Mizzia*), minor foraminifera; phylloid algae biomoldic Cc
MC-040	9-Dec-13	13R 522439 3540147	21.4	Carbonate-cemented very fine subangular to subrounded sandstone grades up to quartz sand/peloid GS
MC-041	10-Dec-13	13R 522439 3540147	21.7	Peloid-vf quartz sand-bioclast GS, with bryozoans and dasyclad algae
MC-042	10-Dec-13	13R 522439 3540147	22.3	Fenestral, ooid-oncoid-bioclast (foram, dasyclad) PS/GS; isopachous-bladed cement on grains; interparticle pendant cements and clear blocky Cc; cavities filled by drusy bladed and blocky Cc
MC-043	10-Dec-13	13R 522439 3540147	22.5	f. peloid-bioclast (foram/algae) PS; pendant cements; white equant Cc in 2^{o} porosity/fenestrae
MC-044	10-Dec-13	13R 522439 3540147	23.1	ooid-oncoid-algal GS; some oncoid cores replaced by sparry Cc; pendant cements
MC-045	10-Dec-13	13R 522439 3540147	23.5	peloid/bioclast gdPS and fenestral peloid-bioclast GS; botryoidal pendant cements & cloudy isopachous cements fill fenestrae, followed by clear Cc
MC-046	10-Dec-13	13R 522439 3540147	24.4	Algal-aggregate grain-foram gdPS; grains lined with isopachous bladed cement; interparticle porosity filled with cloudy microcrystalline dol, drusy dol, and blocky Cc
MC-047	10-Dec-13	13R 522438 3540148	25	Oncoid gdPS with two generations of isopachous cements on grains and two generations of interparticle calcite. Matrix peloid-algae-foram PS. Oncoid cores often replaced by sparry Cc
MC-049	10-Dec-13	13R 522438 3540148	26	Thickly interlaminated oncoid RS, peloid PS, and oncoid gdPS; GS cemented by isopachous cements
MC-050	10-Dec-13	13R 522438 3540148	26.6	

Sample	Date collected	UTM Grid Ref.	Ht. (m)	Polished Slab Description
				lithoclast-oncoid-algal gdPS overlain by ooid-peloid PS and lithoclast-skeletal PS; gdPS grains coated with cloudy isopachous cement and filled with cloudy equant Cc; karsted and filled with sparry Cc and vf brown s.s.
MC-051	10-Dec-13	13R 522438 3540148	27.5	Heavily recrystallized dasyclad-lithoclast-foram WS; allochems are up to 1mm
MC-052	10-Dec-13	13R 522438 3540148	27	Cross bedded oncoid RS overlying vf peloid-ooid-lithoclast-foram GS; oncoid cores are peloid-algal PS or dasyclads (often dissolved), and are clotted/poorly-laminated; interparticle porosity filled by isopachous fibrous gray dolomite, isopachous drusy-bladed Cc, and sparry Cc; vf coated grain GS grains have isopachous and blocky interparticle dol cement
MC-055	10-Dec-13	13R 522433 3540147	29.4	laminated peloid GS in sheet crack
MC-056	10-Dec-13	13R 522433 3540147	29.4	ooid-oncoid GS grades up to gdPS and peloid PS; sheet crack geopetal fill grades up from m. peloid GS to vf peloid PS; oncoids are finely laminated isopachous dol, often on lithoclasts; cement sometimes crinkly; gray isopachous cement on GS grains
MC-057	10-Dec-13	13R 522433 3540147	30.1	ooid-oncoid-lithoclast-bioclast gdPS/RS overlain by ooid-oncoid-algal RS; sheet crack with laminated peloid GS, possibly replaced botryoidal and isopachous fibrous pendants
MC-058	10-Dec-13	13R 522417 3540160	30.2	c. bioclast-intraclast GS (algal fragments, forams) with isopachous dol on many grains and drusy/blocky Cc interparticle cements
MC-059	10-Dec-13	13R 522417 3540160	30.7	ooid-bioclast (dasyclad/gastropod/mollusk) GS with cloudy gray interparticle cement
MC-060	10-Dec-13	13R 522417 3540160	31.1	lithoclast-bioclast RS overlain by fenestral MS; GS has cloudy gray interparticle cement; possible horizon with Cc-filled selenite molds
MC-061	10-Dec-13	13R 522422 3540162	32.4	ooid-oncoid-algal GS; clear sparry and equant white Cc interparticle cement
	McKittrick Peak Triplet section			
MC-258	28-Apr-16	13R 522536 3540077	6.5	reddish-brown f ooid-peloid GS with Cc-replaced mollusk fragments
MC-259	28-Apr-16	13R 522536 3540077	8.3	fenestral, tan crystalline algal-ooid GS with beige cement

Sample	Date collected	UTM Grid Ref.	Ht. (m)	Polished Slab Description
MC-260	28-Apr-16	13R 522568 3540063	10.3	poorly sorted vc ooid/g oncoid-algal GS; oncoids are tan in a gray vf-vc grain & cement matrix
MC-261	28-Apr-16	13R 522568 3540063	12	gray granule (2-3mm) oncoid-intraclast RS w/ beige isopachous dol & drusy interparticle Cc
MC-262	28-Apr-16	13R 522534 3540080	12.8	gray granule (2-3mm) oncoid-intraclast RS w/ beige isopachous dol & drusy interparticle Cc
MC-263	28-Apr-16	13R 522534 3540080	13.1	f/m algal-ooid GS
MC-264	28-Apr-16	13R 522534 3540080	14.8	coarsening-upwards oncoid-*Mizzia* RS with isopachous dol and drusy Cc interparticle cements; vertical burrow (?) filled with m. GS
MC-265	28-Apr-16	13R 522507 3540073	16.4	vf peloid GS; overlain by thick lamination of oncoid-peloid GS; overlain by c. oncoid BS with uneven, gray laminated top; overlain by more peloid GS
MC-266	28-Apr-16	13R 522507 3540073	17.8	coarsening-upwards pelleted oncoid-mollusk RS; gastropods & bivalve fragments replaced by sparry Cc and overgrown by isopachous dol, isopachous fibrous cements, and drusy Cc
MC-267	28-Apr-16	13R 522507 3540073	18	m/c *Mizzia*-mollusk GS w/ isopachous dol and isopachous fibrous/drusy Cc; 2-3mm thick small sheet cracks filled by isopachous cements and purple/green calcite
MC-269	28-Apr-16	13R 522545 3540087	20.1	cross-lam. Lithoclast-algal-peloid pebble RS and peloid-algal GS cemented by sparry Cc
	McKittrick Peak Hairpin section			
MC-161	22-Apr-16	13R 522565 3539985	1.4	dolomitic sponge-Tubiphytes-*Archaelithoporella* lime BS with isopachous bladed, drusy, and equant cements
MC-162	22-Apr-16	13R 522565 3539985	2.2	clear Cc spar
MC-163	22-Apr-16	13R 522556 3540000	2.6	skeletal-lithoclast lime PS with *Polydiexodina* and mollusk fragments; vf spicule/pellet matrix

Sample	Date collected	UTM Grid Ref.	Ht. (m)	Polished Slab Description
MC-165	22-Apr-16	13R 522556 3540000	4.6	sponge-bryozoan BS with fusilinid-skeletal PS (possibly lithoclast w/ *Polydiexodina*) in interstices and above
MC-166	22-Apr-16	13R 522556 3540000	5.3	Tubiphytes-sponge-*Archaelithoporella* lime BS with dolomitized gray botryoids, *Archaelithoporella* intergrown with botryoids, and brown botryoidal fibrous cement replaced by drusy Cc
MC-167	22-Apr-16	13R 522591 3539997	6.2	clear Cc spar
MC-168	22-Apr-16	13R 522591 3539997	8.3	sponge BS with isopachous bladed Cc intergrown with brown *Archaelithoporella*
MC-169	22-Apr-16	13R 522591 3539997	9.2	sponge-bryozoan BS with skeletal GS in interstices
MC-170	22-Apr-16	13R 522546 3540010	10.7	*Archaelithoporella*-sponge BS
MC-171	22-Apr-16	13R 522546 3540010	12.8	*Archaelithoporella*-encrusted sponge-bryozoan BS with fine skeletal/peloid GS in interstices; gray isopachous bladed, white equant, and clear drusy Cc in framework
MC-172	22-Apr-16	13R 522546 3540010	14.9	*Archaelithoporella*-encrusted sponges/bryozoan lime BS with fine rhombohedral dol replecement
MC-173	22-Apr-16	13R 522554 3540017	15.3	sparry Cc
MC-177	23-Apr-16	13R 522553 3540021	20	coarsely crystalline vc/g sponge-algal dol GS
MC-178	23-Apr-16	13R 522550 3540034	21.5	peloid-bioclast PS (silt algal matrix) with forams & ostracods; fenestral/brecciated with drusy Cc
MC-179	23-Apr-16	13R 522550 3540034	23	peloid-bioclast f/m GS with spicules, forams and ostracod tests; occ. MS lithoclast
MC-180	23-Apr-16	13R 522594 3540036	28	Pisoid-*Polydiexodina* RS; interparticle isopachous cloudy fibrous Cc, and clear drusy Cc

Sample	Date collected	UTM Grid Ref.	Ht. (m)	Polished Slab Description
MC-181	23-Apr-16	13R 522568 3540037	30.2	Oncoid-*Polydiexodina*-lithoclast RS; coatings are discontinuous with dol. pellets, unlike pisoids
MC-182	23-Apr-16	13R 522550 3540034	32	block: f-c peloid-algal gdPS with oncoids that have *Polydiexodina* and peloid aggregate nuclei; piece 1: c algal-gastropod GS; piece 2: c/vc algal-gastropod GS, many with lumpy coatings; piece 3: c algal-gastropod GS. RS/GS have drusy calcite interparticle cement, often with rusty (silt?) grains near bottom, possibly geopetal; brown cloudy Cc around GS grains, and gray drusy Cc in interparticle voids/fracture porosity
MC-183	23-Apr-16	13R 522538 3540013	37.5	fenestral, laminated f-c peloid GS
MC-184	23-Apr-16	13R 522538 3540013	37.8	wavy laminated very fine quartz arenite in base of sheet crack
MC-185	23-Apr-16	13R 522538 3540013	38	laminated f-c peloid GS in sheet crack; laminations separated by microcrystalline crenulated/tufted dolomite; more clear drusy Cc at base
MC-186	23-Apr-16	13R 522538 3540013	38.2	beige algal-coated grain m-vc GS/RS with cloudy drusy Cc interparticle cement that is clear in larger voids; 1cm-thick sheet crack at bottom filled with geopetal peloid GS; radial bladed clear Cc floor and pendant cements separate at least two generations of peloid GS
MC-187	23-Apr-16	13R 522559 3540017	39.4	large brown botryoidal fibrous cements coated by beige isopachous dolomite and filled by drusy sparry Cc; some botryoids replaced by beige dolomite and partially dissolved

Sample	Date collected	UTM Grid Ref.	Ht. (m)	Polished Slab Description
MC-188	23-Apr-16	13R 522559 3540017	42.2	wavy laminated dol. MS overlain by equant Cc cements brecciating peloid-bioclast PS; subvertical fractures filled by sparry Cc (possibly replacing evaporite veins, cf Harris & Grover Fig 48B); evaporite casts replaced by equant Cc
MC-189	23-Apr-16	13R 522559 3540017	42.5	ooid-oncoid granule RS overlain by tan vf pellet WS(?)-GS(?)
MC-190	23-Apr-16	13R 522595 3540055	45.1	1-3cm brown botryoidal acicular and fibrous pendant cements, partially replaced by gray dolomite; more replacement near top, which also has additional clear Cc replacement
MC-191	23-Apr-16	13R 522595 3540055	45.5	chambered calcareous sponge-algae-*mollusk* RS
MC-192	23-Apr-16	13R 522595 3540055	48.6	pink algal-foram m/c GS with 1cm gray oncoids
MC-193	23-Apr-16	13R 522534 3540035	54	fenestral vc peloid/1-2cm oncoid GS/RS; oncoid cores are *Polydiexodina* and *mollusk*s; fenestrae have isopachous and pendant cements
MC-194	23-Apr-16	13R 522534 3540035	56	cross-bedded *Mizzia-Polydiexodina* vc GS overlying clear to cloudy fine-grained Cc that replaces platy algal fragments *(Archaelithophyllum* sp.?), which in turn overlie tan crenulated isopachous microcrystalline calcite
MC-195	23-Apr-16	13R 522551 3540067	57.5	thickly laminated/thinly bedded oncoid RS and vc peloid/ooid GS; sparry Cc between oncoids that also fills brecciation of GS, possibly after anhydrite as seen in core
MC-197	23-Apr-16	13R 522551 3540067	60.5	interlocked oncoid RS/BS; nuclei are vc to g ooid/oncoid GS; cortices are isopachous and discontinuous, with peloids caught in them; vertical brecciation filled by drusy and poikilitic Cc (replacing botryoids?), and isopachous bladed dolomite

Sample	Date collected	UTM Grid Ref.	Ht. (m)	Polished Slab Description
	Capitan Formation samples (no measured section)			
MC-093	12-Dec-13	13R 522851 3539812		tan, dolomitic, crystalline bioclast WS/vf GS; rare quartz vf sand; vugs filled with bladed and drusy Cc, and calcite pellet silt
MC-095	12-Dec-13	13R 522940 3539787		bioclast lime GS; coarse matrix of spicule/foram/algal(?) fragments with cm fragments of sponge/bryozoan/phylloid algae (?); large intraclasts?
MC-096	12-Dec-13	13R 522920 3539774		bioturbated bioclast lime WS/GS; coarse matrix of spicule/foram/algal(?) fragments with cm fragments of *Tubiphytes* and bryozoans w/ encrusting fistuliporoid bryozoans
MC-097	12-Dec-13	13R 522902 3539785		brecciated lime WS with bryozoan/*Archaelithoporella*-encrusted sponge fragments and drusy Cc-filled cement
MC-098	12-Dec-13	13R 522877 3539775		shattered bioclast lime WS with equant Cc in vug
MC-099	12-Dec-13	13R 522856 3539789		cement-sponge-*Tubiphytes* BS
MC-100	12-Dec-13	13R 522836 3539806		light gray vf skeletal-intraclast PS grades up to peloid PS/GS; pebbles of *Archaelithoporella*-sponge BS, *Archaelithoporella*-bryozoan BS, and *Archaelithoporella*-Tubiphytes/*Archaelithoporella*-bryozoan BS pebble WS in lower part of skeletal PS; articulate ostracods and brachiopods with shelter porosity; secondary (?) porosity filled by isopachous-fibrous gray cement and drusy calcite
MC-101	12-Dec-13	13R 522820 3539820		*Tubiphytes* FS with vf spicule GS matrix and cement-filled voids; minor *Archaelithoporella* encrustation on Tubiphytes and on walls of voids
MC-102	12-Dec-13	13R 522800 3539851		

Sample	Date collected	UTM Grid Ref.	Ht. (m)	Polished Slab Description
				fabric destructive dolomite with clasts of bladed calcite-fossil fragment RS; crystalline dolomite is replacing silt-sized quartz and feldspar cemented by micrite
MC-103	12-Dec-13	13R 522772 3539843		brown calcite fibrous cement BS with pellet GS internal sediment and dolomitic *Archaelithoporella*
	Triplet slope section			
MC-198	24-Apr-16	13R 522735 3539707	1	white blocky Cc between boulders
MC-199	24-Apr-16	13R 522735 3539707	2	large lithoclast of sponge-botryoid-bryozoan-*Archaelithoporella* BS
MC-200	24-Apr-16	13R 522735 3539707	1.7	silty (?) orange, brecciated, dolomitic, heavily recrystallized skeletal lime WS; fossils (bryozoan?) highlighted by white ghosts; white rims along fracture porosity and solution-enlarged vug, which has meteoric pendant cements; blocky calcite in breccia fracture porosity
MC-201	24-Apr-16	13R 522735 3539707	2.8	brecciated, silty(?) bryozoan-intraclast dol. PS; cemented by partially-dolomitized fine grained blocky Cc; poikilitic Cc in fracture porosity
MC-202	24-Apr-16	13R 522750 3539698	4.8	orange recrystallized intraclast-skeletal lime RS; allochems up to ~1cm; matrix silt/vf Cc cemented by dol, with minor (authigenic?) anatase and hematite; soft white dickite in moldic and vuggy porosity
MC-203	24-Apr-16	13R 522750 3539698	5	orange & purple recrystallized intraclast-skeletal lime RS; calcareous sponge, bryozoan, intraclast allochems up to ~2cm, with moldic porosity of calcareous sponges; matrix silt/vf Cc cemented by dol, with minor orthoclase & muscovite silt
MC-204	24-Apr-16	13R 522750 3539698	5.5	

Sample	Date collected	UTM Grid Ref.	Ht. (m)	Polished Slab Description
				recrystallized dolomitic skeletal lime PS with (silty?) blocky Cc matrix; anhydrite molds (?) with coarse sparry Cc; skeletal molds of brachiopods, bryozoans, and sponges
MC-205	24-Apr-16	13R 522767 3539698	6.4	matrix-supported lithoclast-skeletal lime RS; lithoclasts are intraclast-skeletal lime WS; intraclasts in the lithoclasts are *Archaelithoporella*-sponge-encrusting bryozoan BS, and skeletal fragments in the lithoclasts are mollusks, bryozoans, and *Tubiphytes;* RS matrix is vf foram-spicule PS
MC-206	24-Apr-16	13R 522767 3539698	10	dolomitic coarse sub-rounded lithoclast-skeletal GS; isopachous dog-tooth dol on partially-dolomitized lithoclasts; clear Cc interparticle cement
MC-207	24-Apr-16	13R 522767 3539698	11.5	subrounded lithoclast-skeletal dolomite GS with isopachous dol and poikilitic Cc interparticle cement
MC-208	24-Apr-16	13R 522767 3539698	14	bioclast-peloid-lithoclast dolomite RS with poikilitic Cc
MC-209	24-Apr-16	13R 522786 3539671	17.5	f-vc (up to 1cm) skeletal-lithoclast lime gdPS; dolomitized bryozoan & foram fragments; angular lithoclasts composed of lime MS/WS; crinoids and *mollusk*s replaced by cloudy Cc
MC-210	24-Apr-16	13R 522786 3539671	18.5	c-vc skeletal-lithoclast lime PS; dolomitized bryozoan & foram fragments; angular lime MS/WS lithoclasts; crinoids replaced by cloudy Cc
MC-211	24-Apr-16	13R 522786 3539671	19.5	vc-g skeletal-lithoclast dol. PS; lithoclasts are dol. skeletal WS
MC-212	24-Apr-16	13R 522786 3539671	21.5	foram-lithoclast-*Tubiphytes* lime gdPS; lithoclasts are spicule lime WS and *Archaelithoporella* BS; isopachous bladed Cc on allochems where not filled by s/vf WS matrix, with remaining porosity occluded by specular blocky/drusy Cc
MC-213	24-Apr-16	13R 522795 3539679	22.5	matrix-supported lithoclast dol. RS; lithoclasts of *Archaelithoporella* lime BS, m skeletal dol. GS, vf spicule-peloid lime GS; dolomite-cemented siltstone (quartz + rutile, with Cc-filled molds) matrix; blocky Cc in anhydrite cast (?) and fractures

Sample	Date collected	UTM Grid Ref.	Ht. (m)	Polished Slab Description
MC-215	24-Apr-16	13R 522795 3539663	27.5	clast-supported lithoclast-skeletal dolomitic RS with peloidal dol PS matrix; isopachous fibrous Cc with dol inclusions (after HMC?) on lithoclasts, and coarse blocky Cc between some clasts

Sample	Drilled Sample		Facies/cement	Min	$\delta^{13}C$	$\delta^{18}O$	[SO4] (ppm)	$\delta^{34}S$	1σ
MC-005	A	lithoclast pebble of vf lime WS in PS lamina	S3	Cc	5.5	-2.2	1424	17.85	0.06
	B	skeletal lime WS	S3	Cc	4.8	-3.1	2068	17.91	0.08
	C	skeletal-lithoclast lime PS	S3	Cc	4.1	-3.7	2079	17.52	0.07
MC-006	A	darker MS lamination with little heavy minerals	S3	Cc	4.7	-3.3	938	11.17	0.07
MC-008	A	lithoclast pebble of lime BS	S3	Cc	6.1	-1.4	3535	18.58	0.07
	B	skeletal PS	S3	Cc	5.3	-2.7	2794	17.34	0.07
	C	skeletal WS	S3	Cc	4.7	-4.5	2560	13.43	0.07
MC-012	A	skeletal-lithoclast lime PS	S3	Cc	5.9	-2.0	3052	17.60	0.08
	B	skeletal-lithoclast lime GS	S3	Cc	5.9	-1.5	3454	17.12	0.07
MC-013	A	peloid-skeletal WS	S3	Cc	4.7	-3.0	1607	13.85	0.06
MC-014	A	f base of graded PS/WS lamination bed	S3	Cc	6.2	-1.5	4205	17.51	0.08
	B	vf top of graded PS/WS lamination	S3	Cc	6.2	-2.2	3478	15.11	0.07
	C	dark MS	S3	Cc	6.4	-2.2	2706	14.82	0.06

Sample	Drilled Sample		Facies/cement	Min	$\delta^{13}C$	$\delta^{18}O$	[SO4] (ppm)	$\delta^{34}S$	1σ
MC-015	A	bioclast PS	S3	Cc	6.3	-1.8	3096	17.33	0.07
MC-016	A	lithoclasts and intergranular cement	S3	Cc	5.6	-4.6	1894	16.88	0.08
MC-017	A	WS lithoclast	S3	Cc	4.8	-5.3	1155	17.13	0.07
	B	bryozoan fragment	S3	Cc	5.0	-4.7	1445	16.44	0.09
MC-018	A	lithoclast-skeletal fragment PS	S3	Cc	5.0	-3.3	2025	16.73	0.08
MC-019	A	skeletal GS	S3	Cc	6.2	-1.9	3190	17.34	0.07
MC-020	A	skeletal gdPS	S3	Cc	5.3	-2.6	4353	15.81	0.07
	B	lithoclasts of lime WS	S3	Cc	5.3	-2.6	2923	15.87	0.06
MC-031	A	Bioclast aggregate RS	OS8	Dol	4.8	1.6	606	9.69	0.07
	B	Bioclast PS (drill between agg. grains)	OS8	Dol	6.2	1.6	86		
	C	Bioclast aggregate PS (drill right on agg.)	OS8	Dol			1047	8.31	0.29
	D	Blocky intergrain calcite cement	d	Cc	-7.8	-6.2	160	12.01	0.45
MC-032	A	Bioclast GS; rustier-colored grains than rest of slab	OS9	Dol	4.8	0.3	653	9.57	0.08
	B	Intraclast GS; minimal interparticle cement	OS9	Dol	6.1	2.3	797	9.84	0.10
	C	Intraclast-algal GS; more cement than B	OS9	Dol	3.5	-0.3	720		
MC-033	A	Tan recrystallized MS	SC5	Dol	6.0	2.9	383	8.68	0.07
	B	White/tan recrystallized MS with irregular Cc-filled pores	SC5	Dol	-0.7	-0.6	606	21.50	0.08
	C	Yellowish recrystallized MS near ovoid Cc-filled pores	SC5	Dol	5.8	2.0	287	9.25	0.10
MC-034	A	Intraclast PS grain	SC5	Dol	5.9	2.5	565	7.36	0.07
	B	fenestral medium-grained PS	SC5	Dol			454	7.22	0.07
MC-035	A	White poikilitic interior	p	Cc	-3.1	-13.3	367	18.36	0.08
	B	Gray drusy exterior	d	Cc	-7.0	-5.8	176	-4.66	0.21
MC-036	A	Ooid GS	OS7	Dol	5.7	1.9	296	8.25	0.08
	B	Algal/oncoid/ooid RS	OS8	Dol	5.0	1.9	313	7.57	0.08

Sample	Drilled Sample		Facies/cement	Min	$\delta^{13}C$	$\delta^{18}O$	[SO4] (ppm)	$\delta^{34}S$	1σ
MC-037	A	Ooid/algal RS	OS8	Dol	5.8	2.7	449	9.50	0.07
	B	Large round grain, prob. recrystallized dasyclad	OS8	Dol	5.6	2.1	479	9.47	0.08
MC-038	A	Clear, coarse, poikilitic Cc	p	Cc	0.6	-12.4	140	22.07	0.12
	B	Ooid-algal dol GS	OS9	Dol	5.3	1.3	434	9.50	0.08
	C	Oncoid with algal nucleus	OS9	Dol	6.1	2.7	752	9.84	0.08
MC-040	A	Carbonate-cemented very fine sandstone	OS1	Dol	3.2	0.7	290	8.22	0.08
	B	Peloid-quartz sand GS	OS2	Dol	6.3	3.2	681	6.53	0.07
MC-041	A	Peloid-algal GS	OS2	Dol	6.1	3.1	708	8.89	0.10
MC-042	A	oncoid/bioclast RS	SC4	Dol	5.5	1.9	373	7.25	0.09
	B	darker bioclast/ooid PS matrix	SC5	Dol	6.1	3.1	556	8.28	0.08
MC-043	A	Peloid PS	SC5	Dol	6.0	2.7	416	7.43	0.07
MC-044	A	ooid-oncoid GS	SC4	Dol	5.3	2.2	702	3.86	0.09
MC-045	A	peloid-bioclast gdPS	SC4	Dol	5.8	2.2	293	9.27	0.05
	B	fenestral peloid-bioclast GS	SC5	Dol	3.8	-0.4	371	9.23	0.11
MC-046	A	muddier PS region	SC7	Dol	6.3	2.4	530	9.32	0.09
	B	algal GS	SC7	Dol	6.2	2.3	474	8.92	0.05
MC-047	A	Peloid PS matrix	SC6	Dol	5.9	2.1	434	9.37	0.05
	B	Oncoid	SC6	Dol	6.1	1.9	344	9.61	0.09
	C	Grains and isopachous cements	SC6	Dol	6.3	2.6	459	9.58	0.04
MC-049	A	oncoid RS	SC6	Dol	6.4	2.2	439	8.92	0.05
	B	peloid PS	SC6	Dol	6.4	2.1	357	8.81	0.09
	C	peloid PS	SC6	Dol	6.4	2.0	339	9.14	0.05
MC-050	A	lithoclast-oncoid-algal gdPS and cements	SC6	Dol	6.2	2.6	31		
	B	peloid PS	SC6	Dol	6.3	2.6	517	8.80	0.04
	C	lithoclast-skeletal PS	SC6	Dol	6.5	2.2	499	8.62	0.06
MC-051	A	skeletal-lithoclast WS	SC7	Dol	5.2	2.4	633	12.33	0.10
MC-052	A	oncoid RS with a lot of isopachous cement	SC7	Dol	6.2	2.6	536	9.22	0.06
	B	oncoid core	SC7	Dol	6.2	1.7	372	9.14	0.09

Sample	Drilled Sample		Facies/cement	Min	$\delta^{13}C$	$\delta^{18}O$	[SO4] (ppm)	$\delta^{34}S$	1σ
	C	vf coated grain GS	SC6	Dol	6.4	2.2			
	D	isopachous cement on oncoid GS and sparry Cc	i	Cc	-0.8	-2.6	643	9.96	0.09
MC-055	A	sheet crack peloid GS	SC7	Dol	6.6	2.9	474	9.42	0.10
MC-056	A	sheet crack peloid GS	SC7	Dol	6.2	2.6	435	9.02	0.11
	B	ooid-oncoid gdPS matrix	SC6	Dol	6.4	2.9	862	9.53	0.08
	C	peloid PS with abundant secondary porosity	SC7	Dol	5.8	3.0	771	9.44	0.04
	D	oncoid RS (laminated dol oncoids & interpart. cements)	SC7	Dol	5.4	2.1	538	9.41	0.11
MC-057	A	sheet crack peloid GS	SC7	Dol	6.6	2.9	613	9.68	0.05
	B	sheet crack isopachous pendant cement	i	Dol	5.6	2.0	249	9.46	0.08
	C	coated grain RS	SC8	Dol	5.6	1.5	445	8.83	0.10
	D	GS interparticle gray cement	SC8	Dol	5.3	0.3	481	9.69	0.10
MC-058	A	GS with low-Fe isopachous dol	SC4	Dol	6.8	2.6	553	10.18	0.07
	B	GS with low-Fe isopachous dol and high-Fe blocky Cc	SC4	Dol	5.5	-3.2	253	10.16	0.07
MC-059	A	ooid GS	SC4	Dol	6.2	2.2	733	9.03	0.05
MC-060	A	fenestral MS	SC5	Dol	6.3	1.4	1335	9.39	0.13
	B	lithoclast-bioclast RS	SC7	Dol	6.4	2.0	482	8.91	0.05
MC-061	A	coated grain GS	SC6	Dol	5.0	1.3	40		
MC-258	A	ooid-peloid GS	OS7	Dol	5.70	3.47	565	9.85	0.05
MC-259	A	fenestral algal-ooid GS	SC6	Dol	4.11	-0.17	719	11.21	0.05
MC-260	A	c/vc ooid GS and vf-vc grain matrix	OS8	Dol	1.14	-3.02	196	11.37	0.04
MC-261	A	oncoid-intraclast RS	OS8	Dol	5.98	3.74	389	8.63	0.03
MC-262	A	oncoid-intraclast RS	OS8	Dol	5.15	2.99	368	7.83	0.02
MC-263	A	f/m algal-ooid GS	OS5	Dol	5.87	3.11	237	7.73	0.04

Sample	Drilled Sample		Facies/cement	Min	$\delta^{13}C$	$\delta^{18}O$	[SO4] (ppm)	$\delta^{34}S$	1σ
MC-264	A	oncoids with minor interparticle cement	SC6	Dol	6.34	2.55	221	7.91	0.06
MC-265	A	lower vf peloid GS (bottom)	OS7	Dol	6.04	3.33	336	8.94	0.04
	B	oncoid-peloid GS (upper)	OS8	Dol	5.45	2.76	363	9.16	0.06
MC-266	A	oncoids and isopachous cements (upper-left)	OS8	Dol	5.91	3.30	344	9.07	0.04
	B	oncoids, isopach. cements, and drusy Cc (lower-right)	OS8	Dol	3.69	-1.54	257	8.17	0.04
MC-267	A	*Mizzia-mollusk* GS	SC7	Dol	5.34	2.77	455	8.83	0.04
	B	small sheet crack with purple/green Cc	i	Cc	3.18	0.46	294	1.41	0.06
MC-269	A	beige interior of lithoclast	OS9	Dol	4.61	2.04	551	9.46	0.10
	B	pink lithoclast granules with some sparry cement	OS9	Dol	3.61	0.41	432	10.81	0.10
MC-161	A	coarse Cc spar	p	Cc	-1.22	-16.02	201	19.32	0.10
	B	smooth tan part of sponge BS	OS0	Cc	4.76	-3.90	153	11.94	0.15
	C	cloudy crystalline white part of sponge BS	OS0	Cc	4.86	-2.89	541	12.80	0.14
	D	dolomitic *Archaelithoporella* & drusy cement	OS0	Cc	5.50	-2.11	332	10.17	0.17
	E	replaced botryoidal cement	b	Cc	1.79	-2.93	648	11.92	0.18
MC-162	A	clear Cc spar	p	Cc	0.62	-13.27	32	17.04	0.25
MC-163	A	vf spicule-pellet matrix	S4	Cc	3.24	-3.73	291	12.87	0.12
	B	lithoclast of WS/PS or sponge fragment	S4	Cc	3.56	-3.86	132	19.30	0.14
MC-165	A	skeletal PS fill	OS0	Cc	2.12	-3.99	213	13.56	0.12
	B	sponge BS	OS0	Cc	2.38	-5.08	314	13.05	0.18
MC-166	A	gray, partially dolomitized botryoid	b	Cc	5.33	-2.10	635	12.07	0.17
	B	brown small botryoids intergrown with *Archaelithoporella*	b	Cc	4.30	-2.77	748	15.31	0.10
	C	Tubiphytes-*Archaelithoporella* BS	OS0	Cc	4.08	-4.05	316	12.76	0.09
	D	larger brown partially dolomitized botryoids	b	Cc	3.33	-4.13	637	14.96	0.10
	E	drusy Cc replacing larger brown botryoids	d	Cc	-0.24	-4.55	407	15.45	0.13
MC-167	A	clear Cc spar	p	Cc	-4.90	-16.28	168	20.25	0.36

Sample	Drilled Sample		Facies/cement	Min	$\delta^{13}C$	$\delta^{18}O$	[SO4] (ppm)	$\delta^{34}S$	1σ
MC-168	A	isopachous bladed and drusy Cc	i	Cc	-1.71	-6.09	255	13.12	0.22
MC-169	A	skeletal GS in between sponges	OS0	Cc	4.96	-2.43	291	13.15	0.11
	B	spar-replaced sponge	OS0	Cc	0.51	-4.09	212	13.49	0.22
	C	tan sponge BS, less spar	OS0	Cc	3.63	-3.34	417	12.76	0.12
MC-170	A	dolomitic small gray botryoids	b	Cc	2.75	-2.72	494	13.43	0.11
	B	equant crystalline sponge BS	OS0	Cc	5.34	-2.19	358	15.02	0.11
	C	tan sponge BS	OS0	Cc	5.03	-3.17	314	13.56	0.13
MC-171	A	fine skeletal/peloid GS fill	OS0	Cc	4.77	-2.97	549	11.39	0.15
	B	coarse cloudy sparry Cc	OS0	Cc	5.47	-3.82	240	13.17	0.11
	C	isopachous bladed and drusy Cc	OS0	Cc	1.88	-7.12	495	15.18	0.09
	D	dolomitic bryozoan BS	OS0	Cc	4.54	-4.77	367	14.53	0.04
MC-172	A	sponge BS	OS0	Cc	3.88	-4.51	367	14.48	0.04
MC-173	A	sparry Cc	p	Cc	-3.50	-12.00	172	23.94	0.13
MC-177	A	coarsely crystalline GS	OS5	Dol	5.79	1.86	515	10.30	0.11
MC-178	A	peloid-bioclast PS	SC4	Cc	3.25	-3.07	267	12.86	0.10
MC-179	A	peloid-bioclast GS	SC4	Cc	3.20	-2.50	405	12.76	0.12
MC-180	A	Polydiexodina nucleus of a pisoid	SC8	Dol	3.51	-2.64	404	13.54	0.11
	B	pisoid RS	SC8	Cc	4.28	-1.64	517	14.29	0.11
MC-181	A	clotted, dolomitic coating of oncoid	OS9	Dol	5.23	-1.69	419	12.88	0.13
	B	pellet GS	OS9	Dol	5.22	-1.55	388	13.14	0.12
	C	Polydiexodina nucleus of an oncoid	OS9	Dol	4.89	-2.33	429	13.03	0.11
MC-182	A	peloid PS (cross-bedded?) from block top	SC6	Dol	6.67	2.49	275	8.79	0.12
	B	peloid GS from block top	SC6	Dol	6.29	1.96	404	7.11	0.21
	C	pellet-oncoid gdPS from block top	SC6	Dol	6.33	1.89	273	5.23	0.12
	D	oncoid with peloid aggregate nucleus from block top	SC6	Dol	6.53	2.43	630	9.89	0.10
	E	oncoid with Polydiexodina nucleus from block top	SC6	Dol	6.32	2.48	235	7.42	0.12
	F	peloid GS w/ cloudy Cc from block bottom	d	Dol	-6.35	-7.15	106	17.21	0.20
	G	peloid GS from piece 3	SC6	Dol	6.41	2.27	356	8.22	0.11

Sample	Drilled Sample		Facies/cement	Min	$\delta^{13}C$	$\delta^{18}O$	[SO4] (ppm)	$\delta^{34}S$	1σ
MC-183	A	peloid GS	SC5	Dol	4.69	-1.86	339	10.86	0.12
MC-184	A	dolomite-cemented arenite	SC1	Dol	2.49	-1.18	278	10.52	0.13
MC-185	A	peloid GS	SC5	Dol	4.96	-0.94	334	11.01	0.15
	B	dolomite lamination-rich area	SC5	Dol	4.91	-1.29	375	10.52	0.13
MC-186	A	oncoid-aggregate grain RS	SC7	Dol	6.17	2.25	516	8.37	0.12
	B	peloid GS in small sheet crack	SC7	Dol	6.41	3.02	447	8.45	0.16
MC-187	A	dolomitized and dissolved small botryoids	b	Dol	4.55	-0.74	401	9.62	0.10
	B	partially dolomitized large brown botryoids	b	Cc	5.79	-1.14	534	9.53	0.13
	C	large brown botryoids	b	Cc	5.47	-1.83	421	9.89	0.11
	D	large brown botryoid with drusy Cc replacement	b	Cc	0.39	-3.96	283	13.09	0.13
	E	poikilitic sparry Cc	p	Cc	-2.26	-11.22	301	25.16	0.12
	F	isopachous fibrous Cc	i	Cc	3.64	-2.04	346	10.86	0.11
	G	dolomitized botryoid	b	Dol	5.88	-0.44	319	9.93	0.13
	H	partially dolomitized large brown botryoids	b	Dol	6.38	-0.48	228	9.32	0.12
	I	dolomitized botryoid	b	Dol	4.50	-0.93	190	9.96	0.11
	J	partially dolomitized large brown botryoids	b	Cc	5.78	-1.50	595	9.88	0.12
MC-188	A	laminated dol. MS	SC5	Dol	6.28	2.72	738	9.59	0.23
	B	equant Cc-filled evaporite mold in brecciated PS	d	Dol	-3.21	-3.94	242	10.06	0.27
	C	peloid-bioclast PS	SC4	Dol	5.26	2.04	721	10.04	0.28
MC-189	A	pellet GS	SC4	Dol	6.46	1.65	324	8.63	0.14
	B	ooid-oncoid RS	SC7	Dol	5.74	0.96	332	8.50	0.14
MC-190	A	dolomitized small botryoids	b	Dol	3.39	-1.85	557	12.08	0.12
	B	dolomitized botryoids mostly replaced by equant Cc	b	Cc	1.98	-3.04	323	10.07	0.11
	C	brown fibrous botryoidal calcite	b	Cc	5.40	-1.50	742	10.45	0.12
	D	grayer dolomitic fibrous botryoidal calcite	b	Cc	5.44	-1.70	594	10.77	0.06
	E	brown fibrous botryoidal calcite with drusy Cc	b	Cc	4.88	-3.07	492	10.59	0.12
MC-191	A	poikilitic sparry Cc (after anh?)	p	Cc	0.73	-12.24	250	21.01	0.11
	B	sponge-algal RS	SC4	Dol	6.18	0.71	505	9.05	0.12
MC-192	A	gray oncoid	SC6	Dol	6.70	1.77	489	8.91	0.12

Sample	Drilled Sample		Facies/cement	Min	$\delta^{13}C$	$\delta^{18}O$	[SO4] (ppm)	$\delta^{34}S$	1σ
	B	pink GS with yellow calcite	SC6	Dol	2.32	-0.81	805	10.58	0.10
	C	pink GS	SC6	Dol	6.84	1.85	535	7.76	0.14
MC-193	A	fenestral ooid-peloid GS	SC6	Dol	6.14	1.12	91	15.12	0.29
	B	oncoid; core is a possibly heavily recrystallized sponge	SC7	Dol	6.77	2.19	624	8.82	0.14
MC-194	A	poikilitic coarse sparry Cc	p	Cc	-4.10	-13.49	73	23.53	0.28
	B	heavily recrystallized algal (*Archaelith*. sp.?) GS	SC5	Dol	4.20	-0.13	518	10.96	0.04
	C	*Polydiexodina* fragment	SC5	Dol	6.56	2.84	737	9.43	0.06
	D	vc algal GS	SC5	Dol	6.35	2.62	679	10.44	0.09
	E	microcrystalline tan, isopachous, crenulated cement	SC5	Dol	5.37	1.29	844	6.04	0.16
MC-195	A	poikilitic coarse sparry Cc	p	Cc	0.30	-12.49	230	9.64	0.14
	B	peloid/ooid GS	SC6	Dol	6.89	2.76	806	8.58	0.12
MC-197	A	ooid GS nucleus of large oncoid	SC8	Dol	6.23	3.24	606	9.85	0.07
	B	isopachous laminations on oncoid	i	Dol	5.72	2.65	703	10.50	0.04
	C	poikilitic coarse sparry Cc (replacing anh?)	p	Cc	-3.49	-13.22	174	15.62	0.09
MC-093	A	lime very fine tube matrix	OS1	Cc	5.46	-1.24	350	13.92	0.08
	B	dolomitic, crystalline matrix	OS1	Cc	3.43	-2.81	317	14.16	0.18
MC-095	A	coarse spicule/foram/algal GS matrix	OS4	Cc	3.80	-2.34	382	14.14	0.08
MC-096	A	lighter fine GS	OS4	Cc	4.99	-1.07	376	11.61	0.07
	B	fine WS	OS4	Cc	4.14	-2.48	318	12.59	0.09
MC-097	A	light gray MS	OS3	Cc	4.61	-2.87	329	12.80	0.09
	B	fine WS	OS3	Cc	4.58	-2.96	408	12.89	0.11
	C	poikilitic Cc in vugg	p	Cc	-1.51	-15.86	214	18.71	0.14
	D	drusy Cc cementing breccia clasts	d	Cc	-4.34	-9.02	100	14.15	0.24
MC-098	A	lime MS	OS3	Cc	5.57	-0.56	354	13.10	0.08
	B	equant Cc in vugg	d	Cc	3.64	-2.94	331	13.69	0.15
	C	lime WS	OS3	Cc	4.76	-1.53	447	13.60	0.08

Sample	Drilled Sample		Facies/cement	Min	$\delta^{13}C$	$\delta^{18}O$	[SO4] (ppm)	$\delta^{34}S$	1σ
MC-099	A	replaced/dissolved botryoidal cements	b	Cc	2.67	-3.21	531	14.72	0.09
	B	isopachous fibrous Cc	i	Cc	4.61	-2.29	864	14.00	0.08
	C	radial fibrous Cc pseudospar	b	Cc	5.13	-2.37	1214	15.45	0.08
	D	clear drusy Cc	d	Cc	-1.82	-5.52	159	12.36	0.13
MC-100	A	sponge BS pebble	OS0	Cc	4.80	-1.37	419	13.03	0.10
	B	spicule-echinoderm PS/GS matrix	OS0	Cc	4.50	-1.95	416	14.41	0.12
	C	peloid GS	OS0	Cc	4.66	-1.60	311	13.08	0.13
MC-101	A	*Tubiphytes* stalk	OS0	Cc	4.74	-1.75	387	13.29	0.10
	B	spicule GS matrix	OS0	Cc	4.45	-2.39	470	14.11	0.11
	C	fibrous Cc	i	Cc	5.19	-1.16	426	12.61	0.10
MC-102	A	recrystallized calcareous sponge filled by white cement	OS0	Dol	2.55	-2.66	169	12.08	0.11
	B	dolomitic matrix (replacing qtz-fsp sltst)	OS2	Dol	5.57	-0.86	346	9.54	0.11
	C	diagenetic pellet GS	OS0	Dol	5.15	-0.50	250	13.39	0.14
	D	fibrous isopachous cement	i	Dol	5.82	0.77	382	9.41	0.10
	E	coarse clear poikilitic Cc	p	Cc	0.99	-11.34	78	13.65	0.23
MC-103	A	tan vf pellet GS ?	OS0	Cc	4.49	-2.83	421	12.92	0.12
	B	gray-brown vf pellet GS and fibrous cements	OS0	Cc	4.82	-1.89	537	13.77	0.12
MC-198	A	white blocky Cc	p	Cc	-0.82	-13.50	408	18.80	0.15
MC-199	A	brown botryoidal calcite, slight dolomitization along crystal domain boundaries	b	Cc	4.10	-4.55	381	12.83	0.11
	B	light gray lime MS with mm-scale dol. domains	S5	Cc	5.07	-2.64	380	11.55	0.10
	C	dolomitized/Cc-replaced/dissolved *Archaelithoporella*+small botryoids	b	Dol	5.85	-0.91	458	10.38	0.10
	D	clear brown calcite (sponge?)	d	Cc	4.67	-3.12	416	11.85	0.10
MC-200	A	orange, dolomitic skeletal lime WS with Fe-oxides	S5	Dol	-7.03	-7.84	33	13.72	0.18
	B	blocky calcite	p	Cc	0.15	-13.45	50	18.05	0.13
	C	white (reduced) skeletal lime WS	S5	Cc	-7.94	-7.91	25	11.73	0.32

Sample	Drilled Sample		Facies/cement	Min	$\delta^{13}C$	$\delta^{18}O$	[SO4] (ppm)	$\delta^{34}S$	1σ
	D	sparry Cc between clasts	p	Cc	0.13	-12.60	131	21.84	0.10
MC-201	A	white recrystallized dol. bryozoan fossil	S4	Dol	5.41	1.36	408	10.13	0.11
	B	fabric-destructively dolomitized intraclast	S4	Dol	5.32	1.53	435	10.04	0.12
MC-202	A	orange lime MS intraclast	S4	Cc	-6.69	-6.69	31		
	B	dolomitic s/vf blocky Cc matrix	d	Dol	-4.00	-8.33	89	17.73	0.11
MC-203	A	coarse sparry Cc in fracture/mold	p	Cc	-1.83	-14.22	659	22.00	0.14
	B	orange vf blocky Cc matrix w/ dol cement	S1	Dol	-4.83	-6.36	55	10.55	0.17
	C	beige vf blocky Cc matrix on other side of redox front w/ dol cement	S1	Dol	-2.60	-4.76	90	10.84	0.16
	D	gray MS intraclast	S1	Cc	-3.02	-4.69	73	9.27	0.21
MC-204	A	coarse sparry Cc in fracture/mold	p	Cc	-1.77	-13.69	358	23.76	0.11
	B	dolomitic blocky Cc matrix	d	Cc	-5.92	-7.90	66	16.02	0.17
	C	more allochem-rich part of PS	S4	Cc	-6.37	-7.40	43	13.55	0.14
MC-205	A	foram-spicule PS matrix of RS	S4	Cc	2.63	-4.50	225	12.34	0.11
	B	spicule WS matrix of WS lithoclast	S4	Cc	2.63	-4.78	257	12.69	0.10
	C	*Archaelithoporella* encrustation in intraclast in lithoclast (drilled out spar to get to encrustation)	S4	Cc	0.92	-6.08	221		
MC-206	A	lithoclast-skeletal GS in Cc-rich region	S5	Cc	2.15	-7.55	235	13.74	0.12
	B	dolomitic intraclast and minor Cc cement	S5	Dol	0.47	-6.21	275	13.20	0.14
MC-207	A	dolomitic intraclast and isopachous dol cement	S5	Dol	5.12	0.56	259	10.15	0.11
MC-208	A	poikilitic Cc	p	Cc	-0.04	-13.45	86	23.11	0.11
	B	fabric-destructively dolomitized lithoclast	S5	Dol	5.86	0.35	241	8.20	0.11
	C	dolomitized peloid matrix	S5	Dol	5.76	-0.21	309	8.60	0.14
MC-209	A	lime MS lithoclast	S4	Cc	3.40	-4.47	245	12.01	0.09
	B	finer, more limestone-rich part of gdPS	S4	Cc	3.65	-3.73	243	11.24	0.09
	C	larger dol. bryozoan allochem in lime gdPS	S4	Dol	3.38	-3.88	230	11.26	0.10
MC-210	A	skeletal-lithoclast lime PS with dolomitized allochems	S4	Cc	3.46	-3.66	217	11.03	0.13

Sample	Drilled Sample		Facies/cement	Min	$\delta^{13}C$	$\delta^{18}O$	[SO4] (ppm)	$\delta^{34}S$	1σ
MC-211	A	skeletal-lithoclast dol PS, mostly matrix	S4	Dol	5.15	-0.77	353	6.11	0.17
	B	dolomitized skeletal WS lithoclast	S4	Dol	5.79	0.08	338	7.68	0.09
MC-212	A	clear drusy interparticle Cc	d	Cc	-1.02	-7.15	199	11.46	0.14
	B	s/vf peloid (?) WS matrix	S5	Cc	3.65	-2.36	373	11.96	0.11
	C	*Archaelithoporella* BS lithoclast	S5	Cc	3.29	-2.76	240	12.69	0.11
MC-213	A	dol. cemented sltst matrix with Cc-filled molds	S1	Dol	3.58	-3.61	117	10.47	0.11
	B	blocky Cc (after anhydrite?)	p	Cc	-0.92	-13.62	227	18.84	0.16
	C	dol peloid (?) PS lithoclast	S1	Dol	4.01	-2.28	125	9.68	0.12
	D	dol MS lithoclast	S1	Dol	5.65	-0.20	167	8.64	0.13
	E	*Archaelithoporella* BS lithoclast	S1	Cc	3.98	-2.44	189	12.07	0.11
	F	skeletal GS lithoclast	S1	Cc	4.49	-1.97	180	12.10	0.12
MC-215	A	poikilitic blocky Cc between lithoclasts	p	Cc	0.24	-12.00	82	19.29	0.18
	B	isopachous Cc between lithoclasts	i	Cc	0.34	-8.22	39	9.73	0.10
	C	beige dolomitic peloid GS matrix	S5	Dol	5.42	0.31	106	7.37	0.10
	D	lithoclast of f/m peloid-spicule-intraclast GS	S5	Cc	2.25	-6.01	170	18.69	0.15
	E	pink/gray dolomitic skeletal-peloid GS matrix	S5	Cc	1.76	-5.49	176	15.55	0.11